KONA

POWDER SCIENCE AND TECHNOLOGY IN JAPAN

No. 6 (1988)
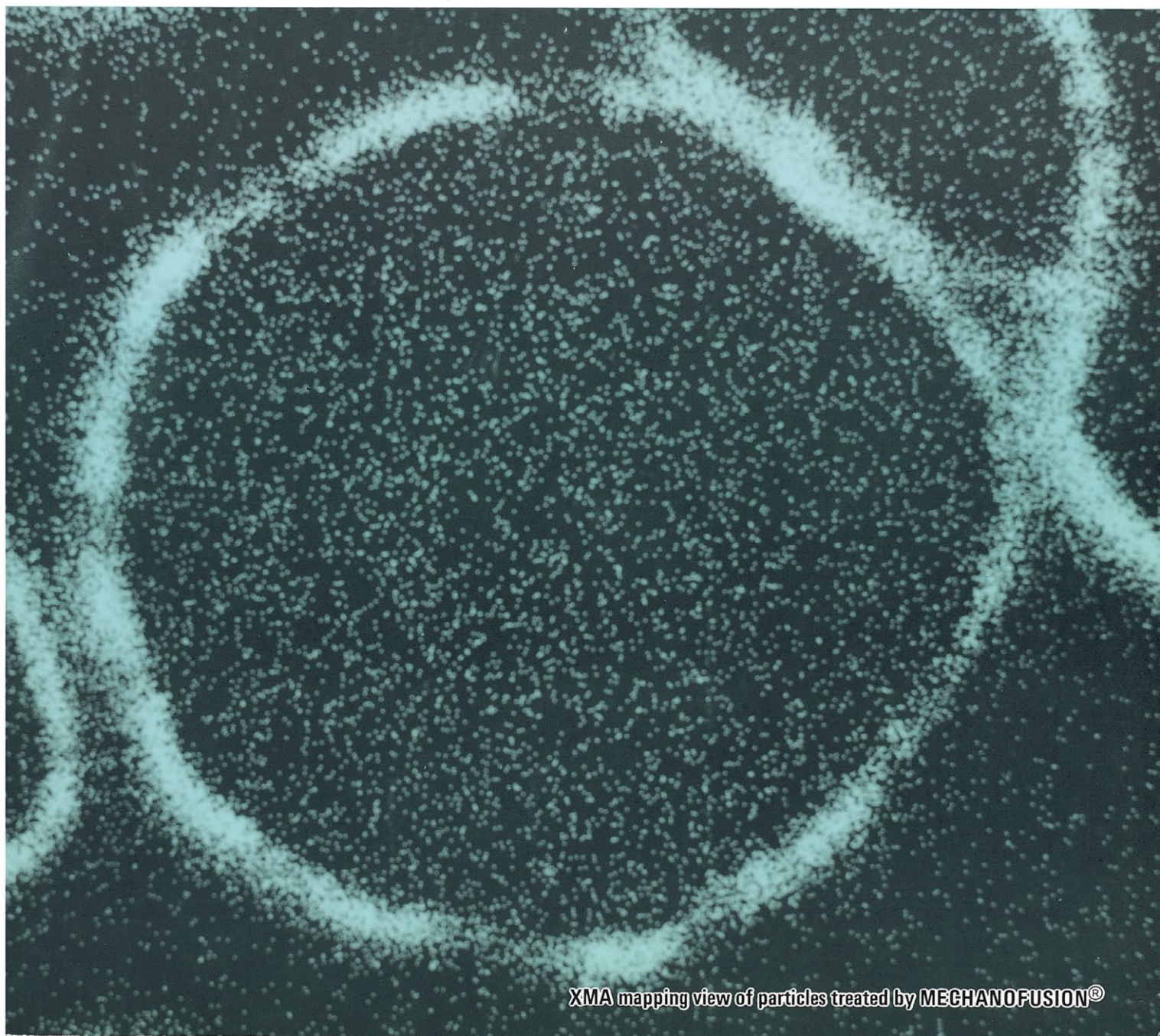
XMA mapping view of particles treated by MECHANOFUSION®

KONA is aimed, as its subtitle indicates, to introduce annually the recent works on powder science and technology in Japan to the interested parties in the world. It consists of the English version of reports and reviews carefully selected out of the latest papers which were originally written in Japanese.

KONA is distributed without charge to senior researchers, institutions and libraries in this field throughout the world under the sponsorship of Hosokawa Micron Corporation. Within these limits the editors are always glad to consider the addition of names to the mailing list.
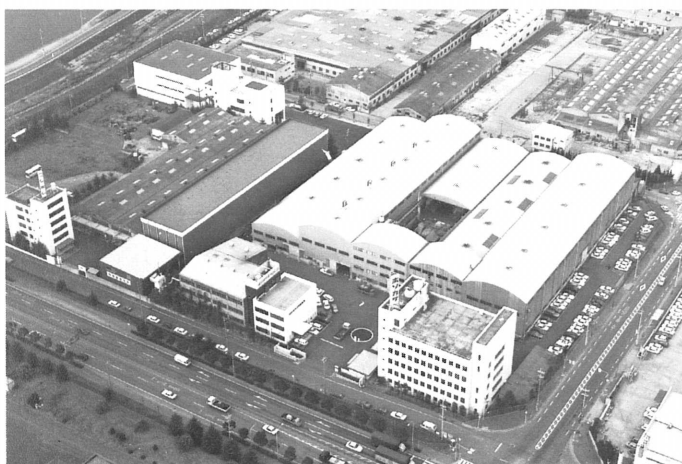
Explanation of the Cover

" 粉 "; This Chinese character is pronounced as "KONA" in Japanese and means "Powder".
" 拡 " on the front page was written by the late Mr. Eiichi Hosokawa, founder of Hosokawa Micron Corporation.

Hosokawa Micron Corporation and its R&D Center
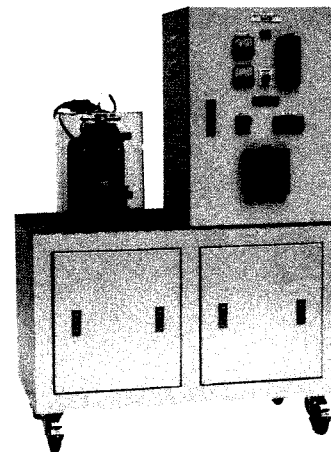
MECHANOFUSION®

Tomorrow's Technology Today!

In recent years, research and development activities for creating powder materials with new features have been increasing in many leading-edge technical fields, such as fine ceramics and electronic parts. These powder materials are expected to function as composite materials or high-performance materials, with new characteristics.

HOSOKAWA MICRON CORP. has developed the MECHANO-FUSION® system, a dry-type powder treatment device with epoch-making mechanism, as part of the above-mentioned research.

MECHANOFUSION® is a novelty technology for creation of new particulate materials. By applying a certain mechanical energy and generating mechano-chemical reaction upon two or more materials, they turn out to be a new material that has new physical and chemical properties. Mechanofusion process

Laboratory Model

can be applied for a variety of combination of particulate materials. Example photographs of composite particles produced using the Mechanofusion System are shown below.

Photos 1 (a) through 1 (c) show SEM pictures of one example, where copper particles of approximately 40 microns in diameter is mechanofused with tin to a ratio of 3% by means of mechanofusion treatment. **Photo 1 (a)** shows the tin powder used as the raw material. **Photo 1 (b)** shows the copper powder used as the core particles. **Photo 1 (c)** shows the product particles. **Photo 2** shows a cross-sectional view of a product particle. The copper particle surface is mechanofused with tin (green). **Photo 3** (the same photo as on the cover page), shows the mapping view of tin obtained using an X-ray microanalyzer, clearly indicating the tin element fused onto the copper surface.

(a)
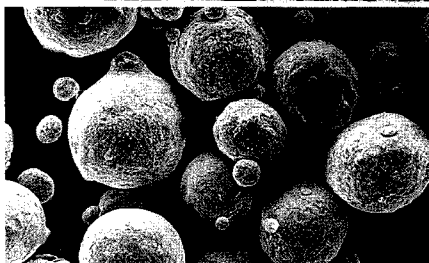
(b)
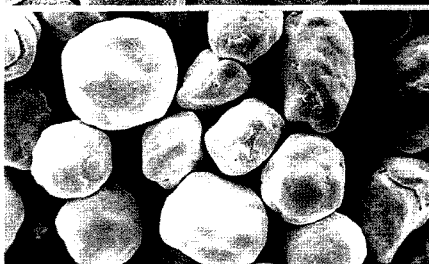
(c)
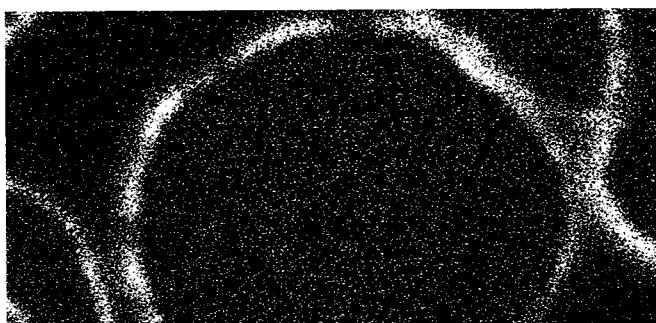
Photo 1

Photo 2

Photo 3
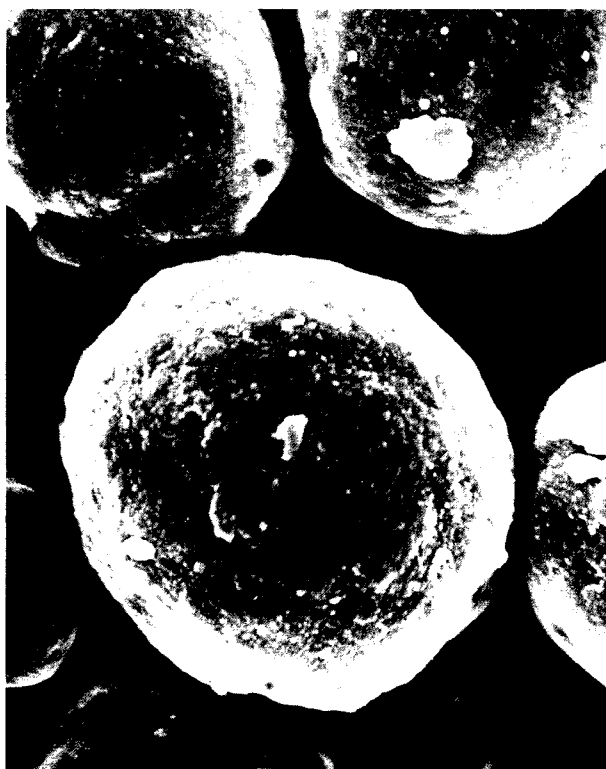
Photo 4 : SEM picture of particles treated by mechanofusion with PMMA (particle dia. about 5 μm) and TiO_2 particles.

Photo 5 : TEM picture of a cross-sectional view of the particles shown on the photograph left. TiO_2 layer, seen black, has about 0.5 μm thickness.

● 10 μm
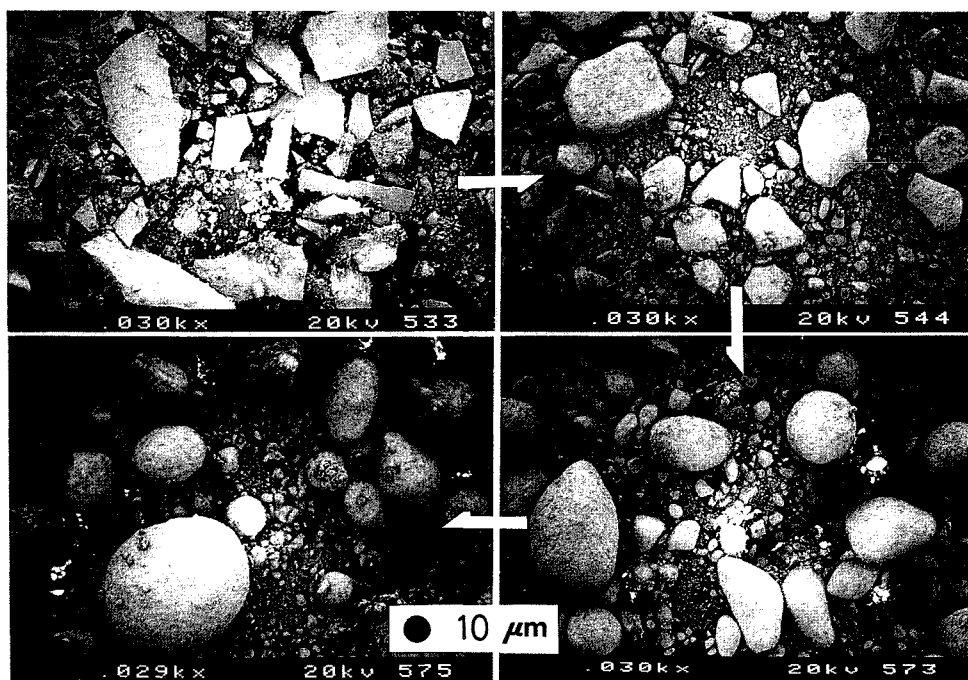
Photo 6 : Example of mono-component mechanofusion. Photographs show the process of particle shape control. Iron particles shown in the picture on upper left are spherical and uniform according to increase of progress time.

Contents

< Original Report >

Shape Analysis of Particles by an Image Scanner and a Microcomputer: Application to Agglomerated Aerosol Particles

Susumu Tohno and Kanji Takahashi

*Institute of Atomic Energy,
Kyoto University* *

Abstract

Algorithms are presented for feature extraction of the geometrical shape of particles. The system consists of a microcomputer and an image scanner which scans the micrograph of particles and transmits the compressed image data. Methods for shape analysis are: 1) calculation of fundamental particle shape parameters (Feret diameter, area, perimeter, first moment, second moment), 2) fractal analysis, 3) opening method and 4) separation of circular primary particles from an agglomerate. The connectivity of particle boundary is recognized for five cases (continuation, termination, creation, split and merge), and the fundamental shape features are calculated according to it. The validity and accuracy of these methods are examined by comparing the calculated and theoretical shape parameters for standard figures. A new index is proposed for the description of the structuring elements number of a two-dimensional particle shape in opening analysis.

These methods are applied to the shape analysis of agglomerated aerosol particles generated from an electric furnance and by the CVD method, and it is shown that the fractal dimension as a particle distribution is useful for the quantitative description of shape.

1. Introduction

Agglomerated aerosol particles are found in various fields, such as coal combustion, diesel exhaust gases and nuclear reactor safety. They have complicated shapes like chain or cluster aggregates. Investigation of the dynamic behavior of these agglomerated particles is required for evaluating the measurements on these aerosols or their effects on human health. The relationship between the geometrical shape and the dynamics of a non-spherical particle has not yet been studied sufficiently, except for particles having simple configurations. It is necessary to find a shape parameter (or parameters) that can clearly explain the relation between the geometrical shape and the dynamic behavior of irregular-shaped particles. Quantification of the geometrical shape of aerosol particles is performed mainly for two-dimensional microscopic images. Computer image processing is indispensable for the morphological analysis of a particle having a complicated shape.

Recently, image processing technology has significantly advanced so that even bad quality image can be processed at a high-speed using image signal processors. These commercially available image processing instruments are very expensive and cannot be used easily, while the image scanner, which is used for inputting images, such as drawings into a microcomputer, is relatively inexpensive. Moreover, it has the advantages of low image distortion and high resolution due to the use of Charge Coupled Devices (CCD). Therefore, the scanner is effective for processing micrograph images of particles with a microcomputer.

This paper discusses the methods for calculating various shape parameters from micrographs using an image scanner and a microcomputer. The methods are then applied to the shape analysis of agglomerated aerosol particles.

2. Image Processing Using Image Scanner

2.1 Calculation of fundamental particle shape parameters

The calculation of particle shape parameters is performed for a binary coded image that is converted from the gray picture of an original micrograph. The threshold value for binary coding is set at an appropriate level by changing the preset level of the image scanner (PC-IN501, NEC), and the binary coded images are displayed on a CRT by the microcomputer (PC-9801, NEC). The scanner reads the image data of a particle micrograph in the horizontal direction using CCD and transmits the compressed binary image data to the microcomputer by sliding the micrograph in the vertical direction with a roller. We have adopted sequential method for processing an image because the scanner transmits data, scanning the field of view in a raster scan mode, and the method also saves data storage area.

The following conditions should be satisfied for the 8-connected continuation of one pair of points (start point $S_k(i)$ and end point $E_k(i)$ of the k-th edge points) detected on the scan line i, and the h-th edge points on the scan line $(i-1)$:

$$S_h(i-1) \leqq E_k(i) \qquad (1)$$

$$S_k(i) \qquad \leqq E_h(i-1) \qquad (2)$$

The connectivity at each edge point is recognized as one of five cases shown in **Fig. 1**.

(1) Creation

No edge points on the scan line $(i-1)$ are continuous to the ones on line i, and the object on line i is designated with a new label.

(2) Termination

No edge points on the scan line $(i+1)$ are continuous to the ones on line i.

(3) Continuation

Only one pair of edge points on the scan line $(i-1)$ are continuous to the ones on line i, and the object on line i is designated with the same label as the one on
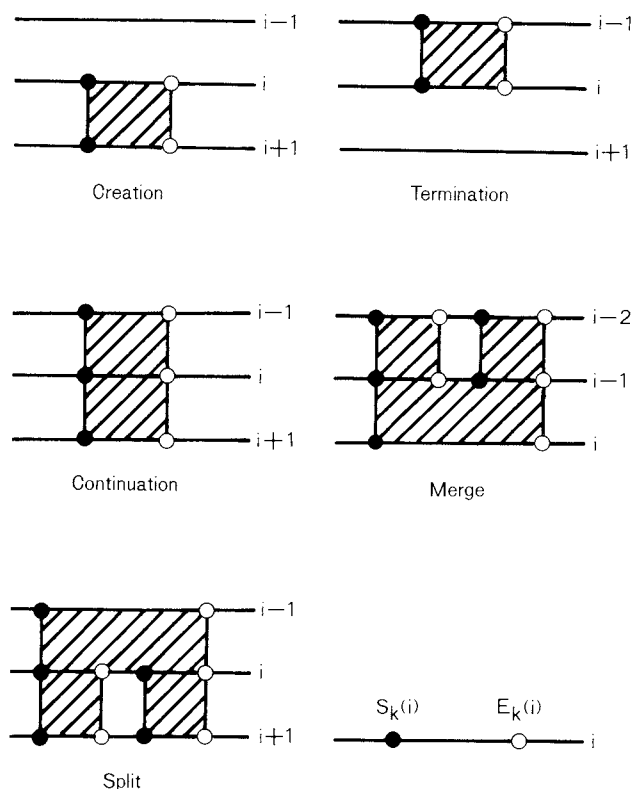
Fig. 1 Illustration of the connectivity of particle boundary at the scan line i.

line $(i-1)$.

(4) Merge

Two or more pairs of edge points on the scan line $(i-1)$ are continuous to the single pair of edge points on line i, and the same label is reassigned to the corresponding objects.

(5) Split

Two or more pairs of edge points on the scan line i are continuous to the single pair of edge points on line $(i-1)$, and the label of the object on line $(i-1)$ are assigned to the ones on line i.

Based on the recognition described above, we can calculate the fundamental particle shape parameters, such as horizontal or vertical Feret diameter, area, perimeter, first moment and second moment.

(a) Horizontal Feret diameter:

$$F_h = \max(_jE - _jS) \qquad (3)$$

where $_jS$ and $_jE$ are the edge points designated label j.

(b) Vertical Feret diameter:

$$F_v = \max(Y_t) - \max(Y_c) \qquad (4)$$

where Y_c and Y_t are the scan line numbers (Y coordinate) when conditions (1) and (2) are satisfied, respectively.

(c) Area: $A = \Sigma \{E(i) - S(i)\} \qquad (5)$

(d) Perimeter:

$$P = \Sigma [1 + \{S(i) - S(i-1)\}^2]^{\frac{1}{2}}$$
$$+ \Sigma [1 + \{E(i) - E(i-1)\}^2]^{\frac{1}{2}} \qquad (6)$$

The correction method proposed by Taniguchi[1] is adopted to reduce errors caused by digitization of the image in the diagonal direction.

(e) First moment:

$$G_x = \Sigma \{E(i) - S(i)\} y \qquad (7)$$

$$G_y = \Sigma \{S(i) + \cdots + E(i)\} \qquad (8)$$

(f) Second moment:

$$I_x = \Sigma \{E(i) - S(i)\} y^2 \qquad (9)$$

$$I_y = \Sigma \{S(i)^2 + \cdots + E(i)^2\} \qquad (10)$$

$$I_{xy} = \Sigma [\{S(i) + \cdots + E(i)\} y] \qquad (11)$$

Using these fundamental shape parameters, we can calculate diameter of the circle of equal projected area, diameter of the circle of equal perimeter, center of gravity, radius of gyration, direction of major axis, circularity, anisometry and bulkiness. In cases of Merge and Split, the basic parameters are corrected. The number of particles equals the difference between the total event number of Creation and that of Merge for particle boundaries having different labels.

2. 2 Fractal dimension

The shape parameters described in Section 2. 1 cannot completely reflect the two structural characteristics of an agglomerated particle profile, that is, the boundary consists of fine primary particles and macro-scale irregular form. Kaye[2] applied the concept of "fractal" proposed by Mandelbrodt[3] to the shape analysis of powders and analyzed the structures using the structured walk method. To apply that concept to this image processing system, a new calculation method has been examined.

If the length of a particle boundary is measured with scale λ_n and n steps are required for measurement, the length L_n of the boundary is given by

$$L_n = \lambda_n \cdot n \qquad (12)$$

When a straight line is measured for several values of λ_n, a linear relationship holds between L_n and λ_n. If the length of complicated boundary, such as a coastline, is measured in the same manner, the length increases with the shortening of λ_n because the fine structure of the boundary appears. This relationship can be expressed as,

$$L_n = \alpha \lambda_n{}^\beta \qquad (13)$$

for fractal boundaries, where α is constant, and β is negative value. With Eq. (12) = Eq. (13), the following equation is obtained:

$$n = \alpha \lambda_n{}^{-(1-\beta)} = \alpha \lambda_n{}^{-d} \qquad (14)$$

A log-log plot of n versus λ_n generates a linear line. The fractal dimension d represented below can be obtained from the slope of the line:

$$d = 1 - \beta \qquad (15)$$

The fractal dimension is calculated by the following procedures which are different from the sequential method in Section 2. 1.

a) First, a particle binary image is stored in the VRAM (resolution: 640×400) of the microcomputer, and the outline is extracted.

b) The profile can be extracted by detecting the edge points on a specific line and carrying out a logical operation between the image data on the specific scan line and on the upper one, as well as on the lower one.

c) Next, grid length λ_n is chosen as a basic value for scale conversion.

d) The number N of the intersection points of the particle boundary and grid lines (X and Y axes) is counted, as shown in **Fig. 2**, for a series of lengths λ_n.

e) The fractal dimension d is obtained as the absolute value of the slope of the line in the log-log graph of N versus λ_n.

However, N should be corrected to unity within specific grid interval if the boundary intersects two or more times.

A one-dimensional measure is used to determine the fractal dimension of a particle boundary, as shown in **Fig. 2**. If open space, such as a netlike agglomerate, exists in the particle, the
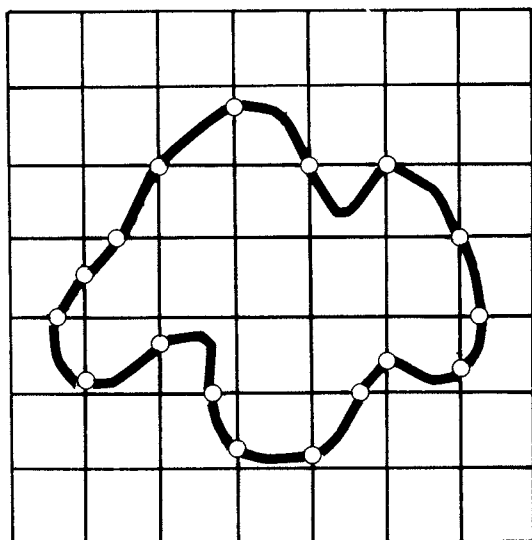
Fig. 2 Counting the points of intersection of particle boundary and grid lines.

following procedure can be applied in order to obtain the porosity, that is, the fractal dimension for a two-dimensional measure.

The gravity center of a particle image is picked, and then a series of nested squares of different sizes are placed around it. The number of particle pixels in each square is counted[4].

2. 3 Opening method

Fractal dimension is effective for quantitatively describing the properties of the complicated boundary of an aerosol particle. However, the dimension cannot express the isotropic properties of a two-dimensional shape or the elemental particle numbers of agglomerated particle. To measure particle size distribution, Matheron has mathematically developed the concept "opening" (refer to reference 5 for details). Domon[6] has applied this for quantitatively describing the morphology of mouse parotid glands.

Since a square lattice is used in this system, $n/2$ operations of the erosion-dilation processing to a binary coded image on square grids can be considered as the opening process of size n. If the total pixel number of binary images is $P(n)$, the pixel number of particles for the opening size n is given by $D(n) = P(n-1) - P(n)$. A two-dimensional image can be expressed using the number distribution of particles, that is, the distribution of $D(n)$.

For instance, the distribution $D(n)$ of a figure consisting of only one structuring element (a square in this system) has only one peek at n which corresponds to its side. The distribution has some peaks if the figure consists of some elements having different sizes, like chain agglomerates.

In practical processing, binary image data is stored in the VRAM of the microcomputer, and the number of pixels are counted after activating erosion-dilation operations n times.

2. 4 Primary particle separation from an agglomerated particle

The method of erosion-dilation processing described in Section 2. 3 can be applied to estimate original primary particles from the two-dimensional image of an agglomerated aerosol particle which consists of fine spherical particles if the degree of particle overlapping is slight. When the degree is significant, the separation is impossible using this method. The iterative method[7] or the method for feature extraction and hierarchical decomposition for a closed curve using averaging operations[8] has been applied to separate the above with satisfactory results[9]. If these methods were to be applied to our system, all calculations would have to be processed by the software of the microcomputer, resulting in an overloading. Then, we have examined a new processing method.

When primary particles are assumed to be spherical, the coordinates of centers and radii must be determined. To obtain these, a part of their arcs should be estimated from the agglomerated particle. First, an outline of the two-dimensional image is extracted by the operation described in Section 2. 2. The curvature of the boundary changes abruptly on the intersection points where different circles meet. This can be expressed by the tangent angle becoming negative at the points. Therefore, we calculate the tangent angles at each discrete outline point with the boundary following, and select the candidate points for calculating parameters of circles during positive tangent angles.

To reduce the effects of digitization errors, the original image is subjected to one dilation-erosion process, and the coordinates of the

boundary points are smoothed by the interpolation using the gravity center of three points. Next, three parameters (the coordinates of the center and the radius of a circle) are estimated by the non-linear least squares method. The initial value of each parameter is obtained as follows: the center is the intersection point of the perpendicular bisectors of two chords (one is formed by candidate points having an initial number and an intermediate number; the other is formed by candidate points having a final number and an intermediate number), the radius is the distance between the center and the candidate point having intermediate number.

In case that the parameters obtained by the above-mentioned steps should indicate a circle, the program may sometimes recognize them as indicating different circles. We define the distance function P, which depends on the distance between centers of each circle Δr, written in

$$P = 1 - \Delta r/d_{th} \qquad (\Delta r \leqq d_{th}) \qquad (16)$$

$$P = 0 \qquad (\Delta r > d_{th}) \qquad (17)$$

A threshold value of P is determined by the discriminant analysis method[10] in order to judge that some pairs of circles indicate an identical circle. If the pair of circles indicate an identical circle, the parameters are recalculated by reorganizing the candidate points on the boundary. In our calculation d_{th} is assumed to be 10. If a large circle should include a smaller one, another judgement is done in order to reorganize the parameters.

The programs described in Section 2. 1 are written in the assembly language when the programs (for controlling input/output to or from the image scanner and VRAM) require high-speed processing, and the others are in the C language. These programs are modularized.

3. Measurement Results for Standard Figures

3. 1 Fundamental shape parameters

The measurement accuracy depends on two kinds of errors: one is caused by the algorithm itself, and the other is due to binary coding. The latter is attributed to the photographic contrast or the characteristics of the image scanner.

A study on the accuracy of the algorithm
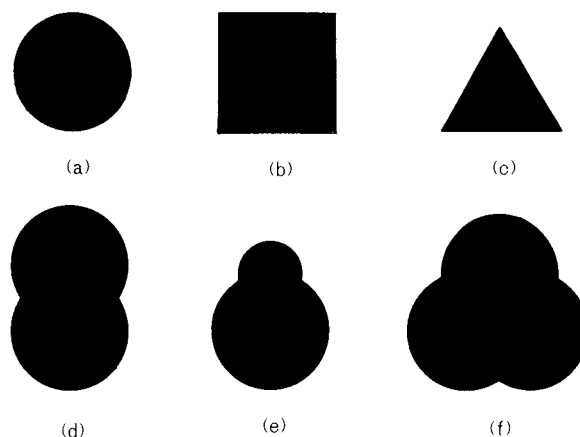
Fig. 3 Standard figures for evaluating measurement accuracy. (a) circle, (b) square, (c) equilateral triangle, (d) doublet (same size), (e) doublet (different size), (f) triplet.

was carried out by Kuga[11] and the authors[12] using model images generated by a computer. They have reported that the largest error occurs in perimeter measurement. Since the threshold level of the image scanner can be only changed into 8 levels, we used photographs having higher contrast. In the following, we have discussed the errors caused by the fluctuation of light source and electrical circuits.

As shown in **Fig. 3**, the standard figures have been created and the shape parameters of these figures have been calculated. The sizes of figures were changed into 4 or 5 levels, and the average values of 20 measurements were obtained. The figures, except for a circle, are input by rotating them to some degree. **Tables 1** and **2** list the mean ratio of the measured to theoretical shape parameter and the coefficients of variation. The perimeter and the area represent the diameter equivalent to the circle perimeter and the area, respectively. The sizes shown in **Tables 1** and **2** represent the pixel numbers equivalent to: the circle diameter; the side of a square and triangle; the diameter of the structuring element circle for a doublet and triplet (same size); and the smaller circle diameter for a doublet (different size). In this case, the diameter of the larger circle is twice that of the smaller one.

Table 1 shows that accuracy increases with the increase in the figure size. When the number of pixels exceeds 70, the difference be-

Table 1　Mean ratio of measured to theoretical shape parameters and coefficient of variation for three standard figures

Figure	Size	Area	Perimeter	Radius of gyration
Circle	11	1.05±0.030	1.04±0.027	1.05±0.028
	20	1.01±0.012	1.01±0.015	1.01±0.012
	38	1.01±0.0061	1.01±0.0080	1.01±0.0059
	73	1.01±0.0046	1.01±0.0066	1.01±0.0045
	127	1.00±0.0023	1.00±0.0032	1.00±0.0020
Square	10	1.02±0.019	1.03±0.026	1.03±0.018
	19	1.01±0.011	0.98±0.027	1.01±0.012
	37	1.00±0.0055	0.98±0.031	1.00±0.0054
	72	1.01±0.0053	1.00±0.025	1.01±0.0052
	128	1.01±0.0037	0.99±0.035	1.01±0.0033
Triangle	11	1.09±0.020	0.95±0.023	1.06±0.021
	19	1.07±0.017	0.99±0.020	1.06±0.016
	38	1.02±0.0068	0.98±0.0096	1.02±0.0068
	72	1.01±0.0072	1.01±0.0069	1.03±0.0069
	130	1.01±0.0045	1.00±0.0051	1.01±0.0041

Table 2　Mean ratio of measured to theoretical shape parameters and coefficient of variation for simple agglomerate models

Figure	Size	Area	Perimeter
Doublet (same size)	10	1.02±0.020	0.98±0.026
	19	1.01±0.0082	1.00±0.010
	37	1.01±0.011	1.01±0.019
	72	1.01±0.0019	1.01±0.0064
Doublet (different size)	8	1.02±0.015	0.99±0.026
	15	1.02±0.0139	1.00±0.019
	29	1.01±0.0046	1.01±0.0070
	57	1.01±0.0042	1.01±0.0058
Triplet	10	1.02±0.017	0.99±0.018
	19	1.01±0.012	0.99±0.015
	37	1.01±0.0054	1.00±0.0080
	73	1.01±0.0028	1.01±0.0043

tween the measured and theoretical shape parameters (excluding the radius of gyration of triangles) are lower than 1%, and the coefficients of variation are stable. The error increases for pixel numbers below 20. Especially for a triangle, the rotation of the figure causes significant digitization errors in the diagonal direction, and the relative error of the area reaches approximately 10% for 10 pixels. However, as real particles seldom have such shapes, the relative errors of measured shape parameters are estimated to be about 5% or less for 20 pixels picture.

Table 2 shows the accuracy for simple agglomerated models. In this case, the error between the measured and theoretical shape parameters of the area is larger than that of the perimeter. For the agglomerate whose elemental particles have the same size (pixels = 10), the relative errors of the measured shape parameters are smaller than that of the elemental circle, and those errors become at the same level as the pixel number increases. This indicates that the errors caused by drawing the figure cannot be negligible, and the agglomerate is considered to be a circle whose diameter is bigger than that of the elemental circle due to the larger degree of fusion of the elemental circles. On the other hand, the relative error in the doublet consisting of different sized circles depends mainly on the larger circle.

3. 2　Fractal dimension

In the same manner as in Section 3. 1, standard figures are created, and image data is input by the image scanner to obtain the fractal dimension of the boundary. **Figure 4** shows the results of some examples. In this graph, the abscissa indicates the grid length normalized by the horizontal Feret diameter. The theoretical dimensions of the circle and triadic Koch curve are 1 and 1.2618, respectively. The dimension of the figure shown in (c) is 1.11, obtained by Kaye's method. Our calculation results are in good agreement with the above theoretical or measured values. For the other figures that Kaye used, our results agree with findings obtained by Kaye within a maximum error of 2%.

The Koch curve has an infinite self-similarity, however, a lower limit exists for drawing the figure or resolution of the computer display. Therefore, the fractal dimension is defined for the range that is larger than the lower limit mentioned above. The dimension is unity for the range below the lower limit. It should be noted that the fractal dimension is defined within a specific finite range because a figure has a finite scale.

3. 3　Opening method

Figure 5 shows the results of a circle, square and rectangle with an aspect ratio of 2, obtained by the opening method. The abscissa indicates the size of opening normalized by the side length (square root of the area) of the square that is equivalent to the area of the tar-
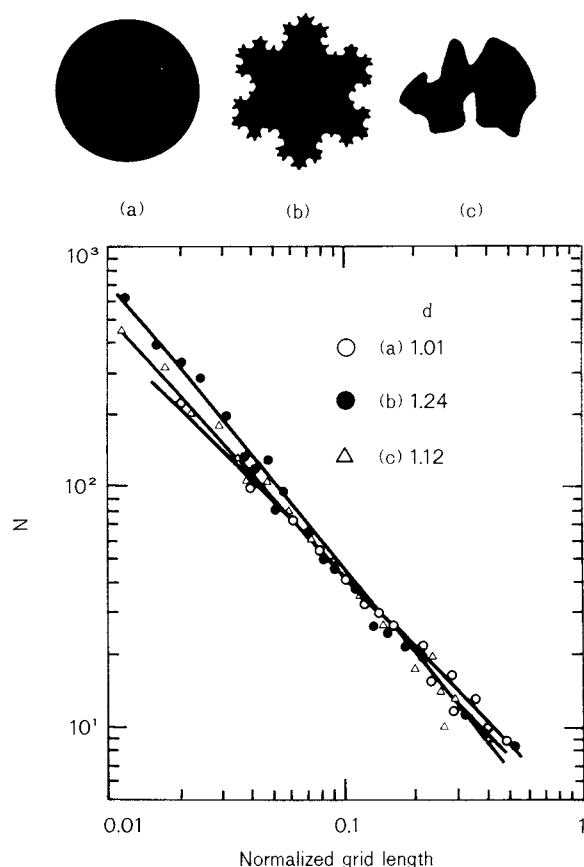
Fig. 4 Plot of the normalized grid length by horizontal
Feret diameter vs. N for standard figures;
(a) circle, (b) triadic Koch curve, (c) test
powder[2].

get figure. The ordinate $D(\lambda)$ is normalized with the area of the target figure and $n(\lambda)$ indicates the number of squares of side λ. These have the following relationship: $n(\lambda) = D(\lambda)/\lambda^2$ where $D(\lambda)$ is not normalized with the area of the target figure.

By comparing the data of squares which are smoothed and not smoothed, shown in **Fig. 5** (the square includes some ruggedness that cannot be shown in the figure), a peak in the number distribution of the smallest size is found in the graph for the unsmoothed square. This indicates that the smoothing operation is effective in reducing the effects of the digitization noise.

After the opening operation, the peak in the distribution for a square appears at the value of λ corresponding to the length of its side ($\lambda = 1$). The peak for a rectangle appears at the size of its shorter side. The number distribution shows a good agreement with the theoretical value. The maximum opening size is the side length of the inscribed square for a circle, and the distribution of squares is determined so as to fill the remaining portion of the circle. Consequently, the squares distribute over a relatively wide range of size that is smaller than its peak position, as shown in **Fig. 5**.
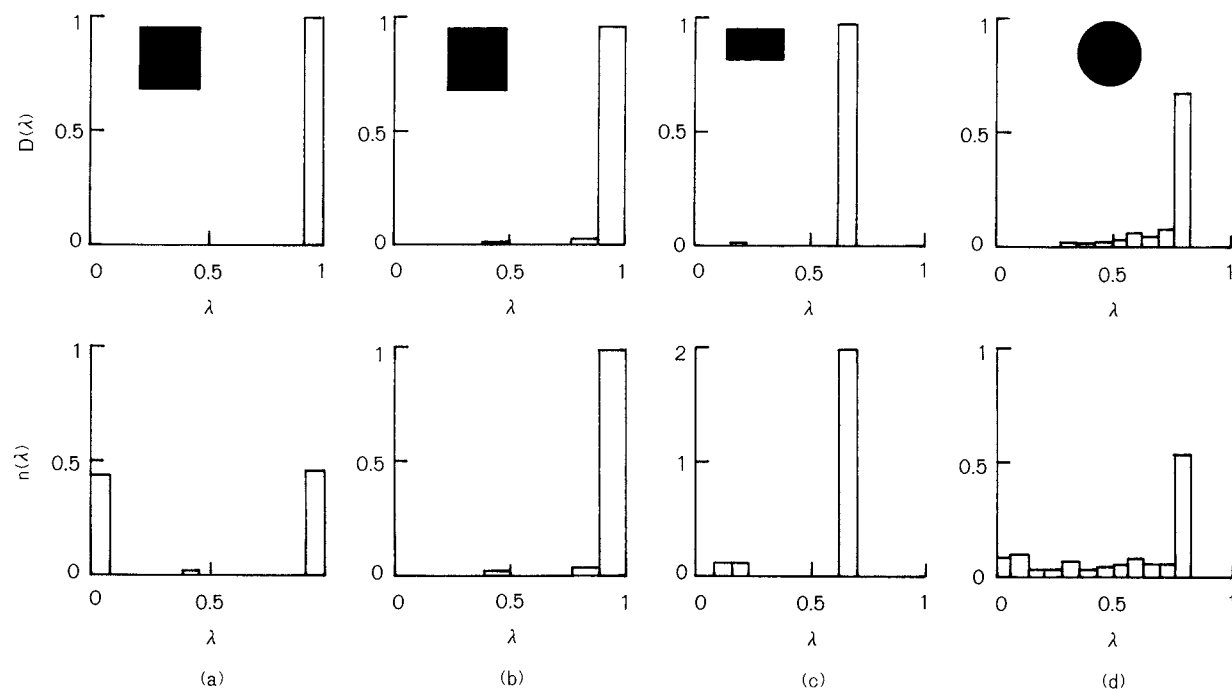
Fig. 5 Area and number distributions of openings for standard figures, (a) square (not smoothed),
(b) square (after smoothing), (c) rectangle, (d) circle.
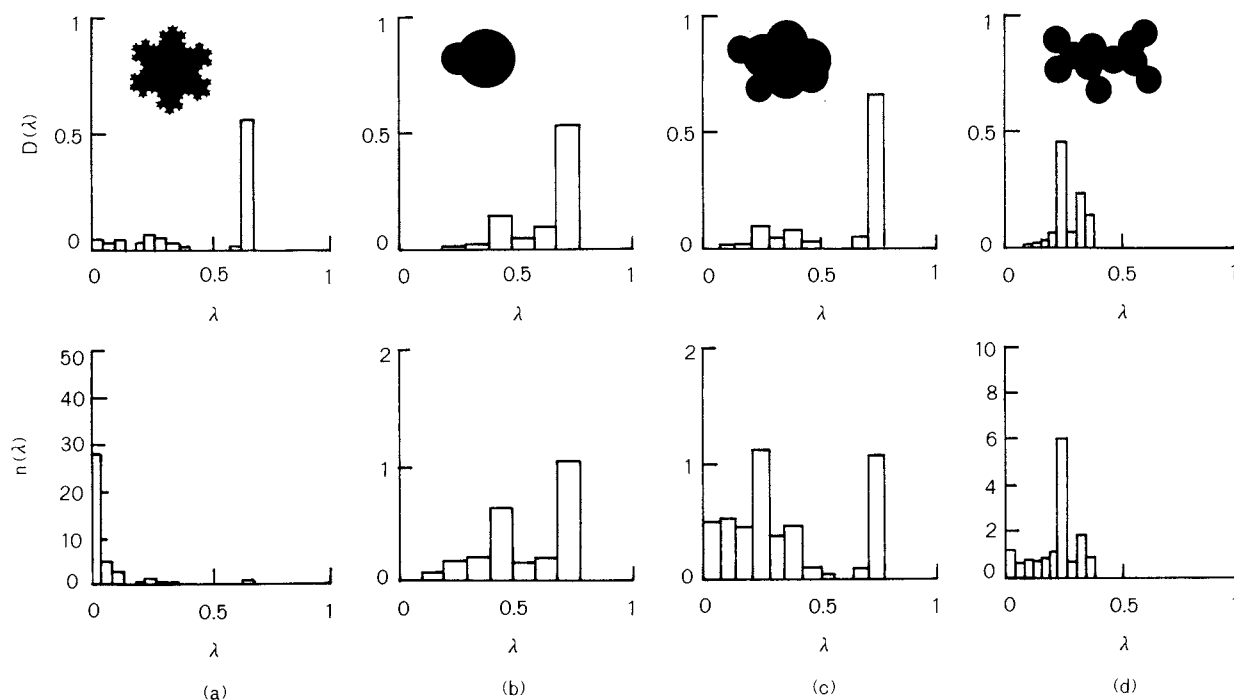
Fig. 6 Area and number distributions of openings for triadic Koch island and three agglomerates.

To evaluate the effectiveness of the opening method that divides a two-dimensional figure into structuring elements, it was applied to a triadic Koch island, to model figures of agglomerates, and to test powders that Kaye used to calculate fractal dimensions. As shown in **Fig. 6**, it was revealed for the Koch island that many smaller squares distribute around the central largest one, and the number of those smaller squares rapidly increases with the decrease in size. The results of the model figures of agglomerates shown in **Fig. 6** indicate that the
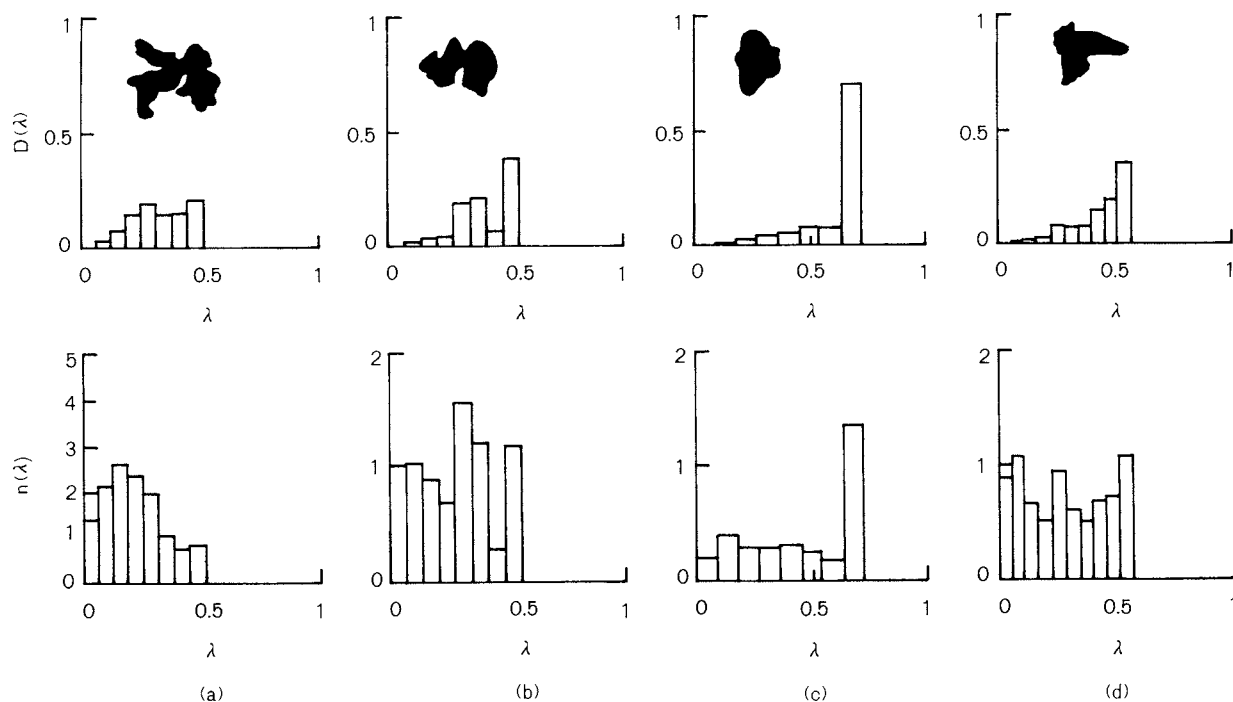
Fig. 7 Area and number distributions of openings for test powders[2].
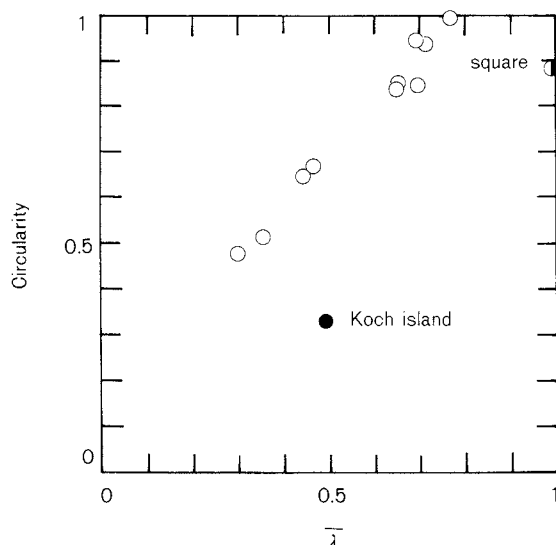
Fig. 8 Relationship between circularity and area weighted average of opening size.

Table 3 Index of structuring element number and total element number for various figures

Figure	Fig. No.	ρ	$N = \Sigma n$
Square	5 (b)	1.07	1.11
Rectangle	5 (c)	1.16	2.32
Circle	5 (d)	2.04	2.19
Triadic Koch island	6 (a)	1.46	38.9
Aggregate	6 (b)	2.44	2.57
Aggregate	6 (c)	4.23	4.59
Aggregate	6 (d)	2.42	14.6
Powder	7 (a)	5.08	13.2
Powder	7 (b)	5.03	7.98
Powder	7 (c)	2.46	3.33
Powder	7 (d)	7.11	7.78

agglomerates are divided into their structuring elements. For the strongly fused agglomerate consisting of many structuring elements, a peak appears at a point which corresponds to the largest circle of the fused portion. The results shown in **Fig. 7** also indicate that the test powders are satisfactorily divided into their structuring elements according to their shapes.

The area-weighted average of opening sizes is considered to represent a "squareness" using a standard figure as the quantitative evaluation of shape. **Figure 8** indicates the average, except for the Koch island, shows a good relationship to the circularity that is generally used. By considering the ratio of the total number N of distributed figures to the peak value n_p, an index as to the structuring elements of a figure,

$$\rho = N/n_p \qquad (18)$$

can offer the measure of structuring elements number with the total number N as shown in **Table 3**. For instance, when the agglomerates (c) and (d) in **Fig. 6** are compared, the fractal dimension of agglomerate (d) is larger than that of (c), and ρ of (c) is larger than that of (d), indicating that figure (c) includes more structuring elements than (d). N of (d) is larger than that of (c). This fact indicates that agglomerate (c) consists of more elements of the same size than (d).

3. 4 Separation of primary particles from an agglomerate

As described in Section 3. 3, the opening method can estimate the size and the number of primary particles, but the method is not effective in estimating primary particles when they are strongly fused. **Figure 9** illustrates the estimated results of structuring element circles from agglomerate models according to the method in Section 2. 4. In each model, the estimated results are satisfactory, and the estimation error of the radius is within 2%. However, some circles are not identical, though their arcs are on the same circumference. This was considered to be caused by the digitization errors resulting from the input condition. Therefore, we had to dialogically change the threshold value in the discriminant analysis in Section 2. 4.

4. Application to Agglomerated Aerosol Particles

4. 1 Particles generated by an electric furnance

A boat containing a granular lead with no silver was fed into an electric furnance. The generated aerosol particles were guided into a coagulation chamber by flowing N_2 gas, thereby obtaining agglomerated aerosol particles[13]. Since the generated aerosol particles were of a chain structure consisting of spherical primary particles, we applied the separation method described in Section 2. 4.

As shown in **Fig. 10**, the size distribution of primary particles is log-normal, having a geometric mean diameter of $0.205\,\mu$m and a geometric standard deviation of 1.46. On the other hand, the measurements of about 500 primary
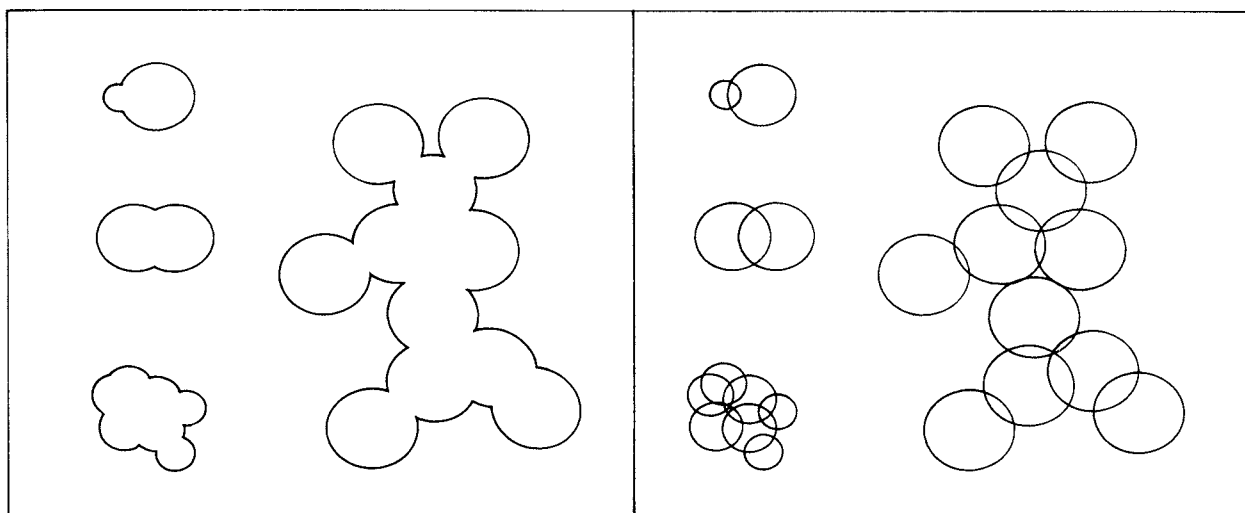
Fig. 9 Outlines of agglomerate models (left) and estimated primary circles (right).

Particle diameter (μm)
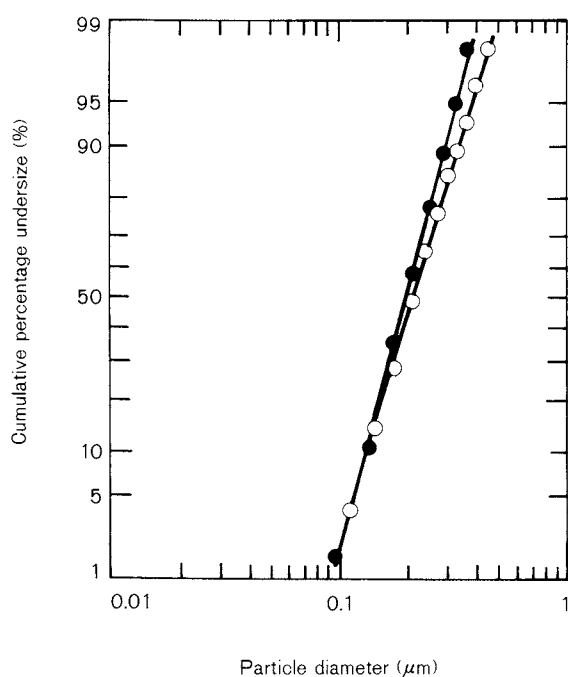
Fig. 10 Cumulative size distributions of primary particles; separation method in this study (○), visual method (●). Material: Pb, temperature of electric furnance: 1050°C, N$_2$ flow rate: 16.7 cm^3/s.

particle diameters using calipers show a geometric mean diameter of 0.195 μm and a geometric standard deviation of 1.41. This difference suggests that the number of larger diameter particles decreased more than the result obtained by the separation method. This is caused by the following: the parameter estimation was difficult or the estimated diameter

was larger than the real diameter because only a small numbers of pixels of an arc were used for estimation, or the change in curvature was too small as shown in **Fig. 11**. As a result, the discriminant function for reforming the arcs did not work effectively. It is required to en-
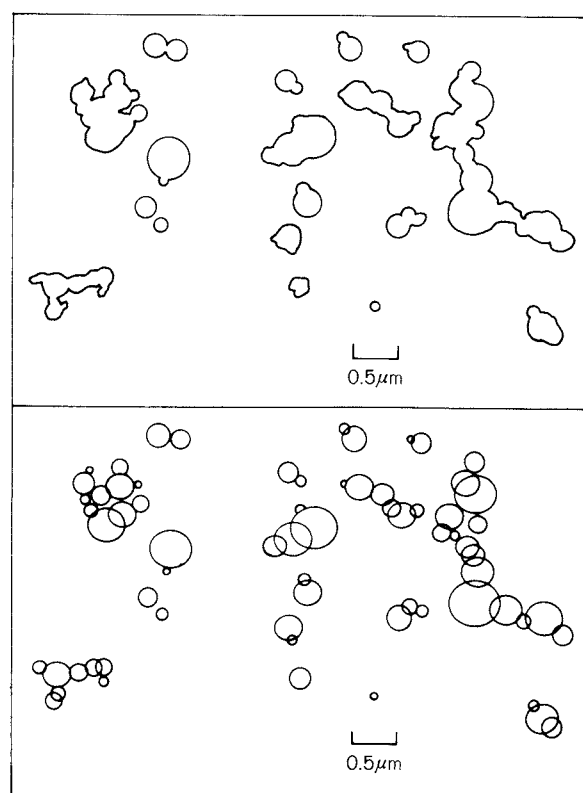
Fig. 11 Outlines of Pb fume generated from electric furnance (upper) and estimated primary particles (lower). Experimental condition is the same as in Fig. 10.
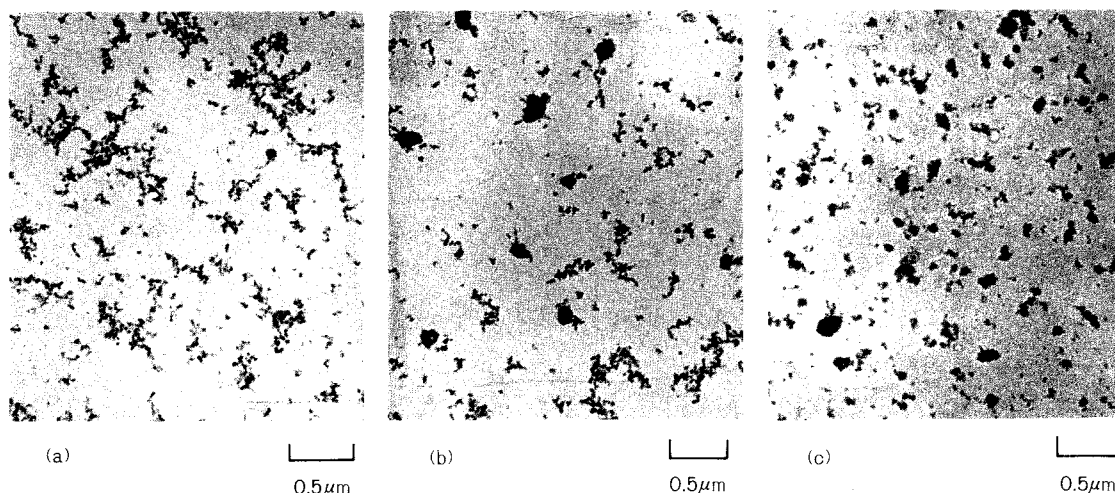
Fig. 12 TEM micrographs of aerosol particles generated by CVD method.
AlAA concentration: 10 mol/m^3, equivalence ratio: 2.5,
CO flow rate: (a) 8.33, (b) 12.5, (c) 16.7 cm^3/s.

hance the resolution ability of the image scanner or to manually eliminate excessively large circles to analyze particles that were not separated sufficiently.
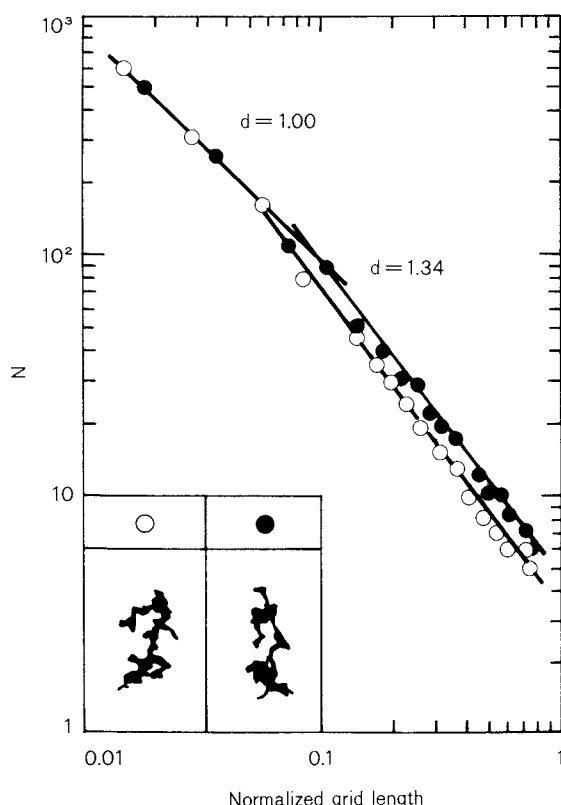
Fig. 13 Plot of the normalized grid length by horizontal Feret diameter vs. N for agglomerated aerosol particles generated by CVD method. AlAA concentration: 20 mol/m^3, equivalence ratio: 1, CO flow rate: 8.33 cm^3/s.

4. 2 Particles generated by the CVD method

We also applied the above described method to the shape analysis of aerosol particles generated by the CVD (Chemical Vapor Deposition) method. The aerosol particles are generated as follows: the Al$_2$O$_3$ aerosol particles were generated using oxidation of aluminium acetylacetonate (AlAA) in CO-O$_2$ flame. AlAA is introduced into the flame in a finely sprayed ethanol solution by a ultrasonic nebulizer with CO. Clean air flowed from the peripheral portion of the burner to introduce the particles into the plenum chamber for stabilization. The aerosol particles were sampled using thermopositor and subjected to observation using an electron microscope. **Figure 12** shows an example of TEM micrographs of the generated particles. The primary particles are approximately spherical in shape, and the size distribution is log-normal, having a geometrical mean diameter of 5 $\sim$ 9 nm and a geometrical standard deviation of 1.2 $\sim$ 1.3.

As shown in **Fig. 13**, the fractal dimension of the generated aerosol particle changes significantly at the point that corresponds to the size of the primary particles. This indicates that there are two shape structures of the agglomerated particle, i.e. the Euclidean boundary ($d=1$) of the spherical primary particle and the complicated boundary ($d=1.34$) of the entire agglomerated particle.

If the concentration of the solution and the equivalence ratio are constant, the particle

Fig. 14 Relationship between CO flow rate and shape factors of agglomerated aerosol particles generated by CVD method. ψ: arithmetic mean circularity, d: fractal dimension. AlAA concentration: 10 mol/m^3 (o), 20 mol/m^3 (●).

Fig. 15 Relationship between radius of gyration and diameter of the circle of equal perimeter for agglomerated aerosol particles generated by CVD method. CO flow rate: 8.33 cm^3/s, equivalence ratio: 2.5, AlAA concentration: 10 mol/m^3.
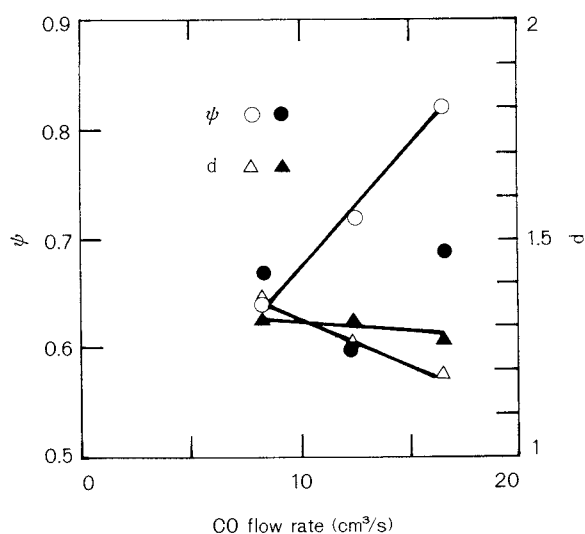
shape shifts from web to cluster aggregates with the increase in the CO flow rate. Circularity can be used as an index for quantifying such difference in shape of agglomerated particles. The circularity, however, is calculated for a single particle and has a specific distribution for each condition of particle generation. Thus, the obtained data was summarized using an arithmetic mean of circularities for $300 \sim 500$ particles as shown in **Fig. 14**. When AlAA concentration is 10 mol/m^3, the circularity is proportional to the CO flow rate, coinciding with the visual recognition. However, for the concentration of 20 mol/m^3, the circularity is not proportional to the CO flow rate. When the number percentage of fine particles is large on a micrograph, significant error in the digital image processing occurs because of poor resolution. As a result, the percentage of particles having a circularity of nearly unity increases, hence the mean value of circularities cannot completely express shape irregularity. This leads to possible disparity with the visual recognition result.

The size distribution of primary particles is relatively monodisperse, so agglomerated particles are considered to be self-similar as a group. We select radius of gyration r_g of an agglomerated particle as a basic scale, and perimeter P or area A as a measurement quantity. Then for the agglomerated particles, the relationship between r_g and P (or A) can be expressed as,

$$P \text{ (or } A) \propto r_g{}^d \tag{19}$$

as shown in **Fig. 15**. Here, d is the fractal dimention for a particle size distribution. This method can improve upon the lack of information, and it can eliminate erroneous information on the shapes of fine particles. The fractal dimensions in **Fig. 14** are obtained from the relationship between the perimeter (in this case, diameter of the circle of equal perimeter) and the radius of gyration. The results show that the method can quantitatively represent the characteristics of shape that cannot be described with circularity. The dimension agrees satisfactorily with that obtained from a single agglomerate in **Fig. 13**, and this indicates the consistency of both methods.

5. Conclusions

By using an image scanner and a microcomputer, shape analysis of particles was performed relatively inexpensively for the microscopic images. The calculation of fundamental shape parameters from a micrograph containing many particles was sequentially carried out by com-

bining the classification of the connectivity of the particle boundary and the conventional calculation algorithm of shape parameters. The accuracy of this method is of approximately 2% error when the number of pixels is 40 or more. We have developed the fractal and opening analysis method of a single particle, and the separation method of spherical primary particles from an agglomerate particle. Moreover, the particle shape can be described by parameters that relate to the index of structuring elements number proposed in the opening analysis. In the applications of these methods to agglomerated aerosol particles generated by the two methods, we introduced the fractal dimension for particle groups, which is obtained for the entire range of the particle size distribution. The fractal dimension, in this case, is determined from the relationship between the radius of gyration of a single particle as a standard scale and the perimeter as a measurement value. The dimension can quantitatively express the characteristic change of shape caused by the different conditions of generation, while it cannot be described with the mean value of circularities.

Nomenclature

A	:	area	(m^2)
$D(n)$	:	number of pixels of particles for opening size n	$(-)$
d	:	fractal dimension	$(-)$
d_{th}	:	threshold level	$(-)$
$E_k(i)$	:	k-th end (right) edge point at the scan line i	$(-)$
F_h	:	horizontal Feret diameter	(m)
F_v	:	vertical Feret diameter	(m)
G	:	first moment	(m^3)
I	:	second moment	(m^4)
L	:	length of perimeter	(m)
N	:	total number of structuring elements	$(-)$
n	:	number, size	$(-)$
P	:	perimeter, distance function defined in Eqs. (16) and (17)	$(m, -)$
$P(n)$	:	total number of pixels after opening for size n	$(-)$
r	:	normalized distance	$(-)$
r_g	:	radius of gyration	(m)
$S_k(i)$	:	k-th start (left) edge point at the scan line i	$(-)$
x	:	abscissa	$(-)$
y	:	ordinate	$(-)$
α	:	constant	$(-)$
β	:	$1-d$	$(-)$
λ	:	opening size	$(-)$
ρ	:	index of structuring element number	$(-)$

References

1) Taniguchi, K. and Y. Nakano: *Denshi-Tsushin-Gakkai-Ronbun-Shi (Trans. Inst. Electron, Commun. Eng. Japan)*, **D58**, 651-652 (1975) (in Japanese).

2) Kaye, B.H.: *Part. Charact.*, **1**, 14-21 (1984).

3) Mandelbrodt, B.B.: "Fractal: Form, Chance and Dimension", W.H. Freeman & Co. (1977).

4) Forrest, S.R. and T.A. Witten, Jr.: *J. Phys. A*, **12**, L109-L117 (1979).

5) Serra, J.: "Image Analysis and Mathematical Morphology", p. 333, Academic Press (1982).

6) Domon, M: Preprint of the 5th Symposium of Science on Form, p. 12 (1986) (in Japanese).

7) Sakaue, K. and M. Takagi: *Gyohoshori-Gakkai-Kenkyukai-Shiryo (Paper of Tech. Group on Computer Vision, Information Proc. Soc. Japan)*, CV6-3 (1980) (in Japanese).

8) Matsuyama, T., H. Yonezawa and K. Azuma: *ibid*, CV36-4 (1985) (in Japanese).

9) Kimura, A., K. Tanabe, R. Yamamoto and T. Arai: *Funtai-Kogakkai-Shi (J. Soc. Powder Technol., Japan)*, **22**, 820-826 (1985) (in Japanese).

10) Otsu, N.: *IEEE Trans. Syst., Man, Gybern.*, **SMC-9**, 62-66 (1979).

11) Kuga, Y., S. Endoh, J. Koga and K. Yamaguchi: *Funtai-Kogakkai-Shi (J. Soc. Powder Technol., Japan)*, **19**, 171-181 (1982) (in Japanese).

12) Konishi, K., S. Tohno and K. Takahashi: *Kyoto-Daigaku-Genshi-Enerugi-Kenkyusho-Iho (Bull. Inst. Atomic Energy, Kyoto Univ.)*, **63**, 40 (1983) (in Japanese).

13) Hattori, N: "Experimental Study on Dynamic Mobility of Agglomerated Aerosol Particles", Master's Thesis, Kyoto University (1986) (in Japanese).

Comparing the Flow Properties of Bulk Solids by Tri-axial Shear, Unconfined Yield and Direct Shear Tests[†]

Hiroshi Tsunakawa and Daizo Kunii
Dept. of Chemical Engineering
Yokohama National University*

Fumito Takagi and Minoru Sugita
Institute of Technology, Shimizu
Construction Co., Ltd.**

Tomio Tamura and Hideto Haze
Technical Research Institute,
Mitsui Construction Co., Ltd.***

Abstract

This paper discusses a comparison of the data of experiments obtained by using different shear tests methods in order to examine the confidence in the results of experiments on the flow properties of a bulk solid.

The angle of internal friction of dry granular materials, which has been measured by both a tri-axial shear tester and a fixed volume direct shear tester, increases with a decrease in the voidage of the specimen. Except for the extremely dense and loosely packed states, the experimental results of the angle of internal friction agree within about 3 degrees. There is however a difference of 3 to 5 degrees for a material in which the particle shape is deflective.

The flowability index of cohesive powders and wet materials is expressed by a ratio of the unconfined yield strength to the bulk density. The results of experiments on the flowability index are independent of the unconfined yield and direct shear tests.

1. Introduction

The flow properties of a bulk solid are important factors in designing various processes and operations relative to its use, as well as in evaluating its flowability. The flow properties are expressed in various ways, and the method and apparatus for their measurement are employed according to their relevance to the objective. From the viewpoint of designing processes, therefore, the data on the flow properties must be handled in light of objectivity and confidence. That is to say, where a flow property is measured by differing devices, whether the results agree or differ is an important question.

In this paper, a comparison is made between the data obtained by three different research institutions with respect to the flow properties of common or similar samples subject to tri-axial shear tests, unconfined yield tests, and direct shear tests.

2. Subjects and organization of studies

The flow properties of a bulk solid are basically represented by a family of linear yield loci. However, it is not convenient to deal with the linear yield loci themselves as an object relevant to comparison of the data of the flow properties.

---

* 156, Tokiwadai, Hodogaya-ku, Yokohama, 240
TEL. 045 (335) 1451

** 3-4-7, Etchujima, Koto-ku, Tokyo, 135
TEL. 03 (643) 4311

*** 518-1, Komaki, Nagareyama, Chiba, 270-01
TEL. 0471 (55) 4611

† This report was originally printed in *J. Soc. Powder Technology, Japan,* **23**, 678-684 (1986) in Japanese, before being translated into English with the permission of the editorial committee of the Soc. Powder Technology, Japan.

Table 1 The system of the present study

Material	Flow property	Testing method	Research institute
Dry granule	Angle of internal friction	Tri-axial shear test	Shimizu Construction Co., Ltd.
		Direct shear test	Yokohama National University
Powder and wet granule	Flowability (a ratio of uncon-fined yield strength to bulk density)	Unconfined yield test	Mitsui Construction Co., Ltd. and Yokohama National University
		Direct shear test	Yokohama National University

Since the yield locus of a dry granular material generally assumes a straight line, it is convenient to deal with the angle of internal friction, which is the inclination formed by the line, as an object of comparison in considering the data of flow properties. However, with respect to a powder or wet granular material, the yield locus forms a curve. The flow properties cannot be represented singly by the angle of internal friction. The flow properties then characteristically include an unconfined yield strength into which the intergranular frictional force and cohesion are integrated. The flowability index, which is defined as a ratio of the unconfined yield strength to the bulk density, typically represents the flow properties of a cohesive bulk solid and must be dealt with by mutual comparison.

The test of the flow properties were undertaken by the three research institutions specified in **Table 1**. The data on the angle of internal friction of the dry granules was obtained by both tri-axial and direct shear tests, whereas the flowability indices of cohesive granules and powders were determined by unconfined yield and direct shear tests.

3. The angle of internal friction of dry granules

The reader is referred to the published related literature[1] or reference book[2] for details about the tri-axial shear test, since this

Table 2 The conditions of the experiment of the tri-axial shear tests and the direct shear tests

Condition	Tri-axial	Direct
Specimen size [mm]	$50^D \times 100^H$	$100^D \times 10^H$
Stress range [kPa]	$100 \sim 1900$	$0 \sim 100$
Strain rate [%/min]	< 0.5	2.22

Table 3 The dry granules used in both the tri-axial and the direct shear tests

Material	Density $[t/m^3]$	Particle size [mm]
Soma sand	2.65	$0.59 \sim 0.84$
Yamakawa sand	2.64	$0.35 \sim 0.84$
Toyoura sand	2.64	$0.105 \sim 0.297$ $(0.21 \sim 0.25)^*$
Silicon carbide	3.20	0.21 (average)
Glass beads	2.50	$0.177 \sim 0.25$ $(0.21 \sim 0.25)^*$

*) These samples were used in direct shear tests.

test is widely used mainly in the field of soil engineering, and the testing method and devices applied are standardized. On the other hand, the direct shear test is carried out by various types of devices and has not yet been standardized yet. The test is limited to the fixed volume direct shear tester used in the present experiments. The testing method and devices used are described in the literature[3,4].

Table 2 shows the main conditions of the experiment under which the tri-axial shear tests and the fixed volume direct shear tests were carried out. These conditions had no special features in common. **Table 3** shows the five kinds of dry granules and their physical features that were subjected to the measurement of the angle of internal friction. Common samples were employed for the two testing methods with respect to Soma sand, Yamakawa sand, and silicon carbide, but the samples of Toyoura sand and glass beads used in the two tests were a little different in grain size.

Figure 1 shows the results obtained from the tri-axial shear tests on Toyoura sand. The specimens had a voidage at the initial packing ϵ_0 of 0.463. The minor principal stress (lateral pressure) σ_3 had four values — 0.098, 0.196, 0.294,
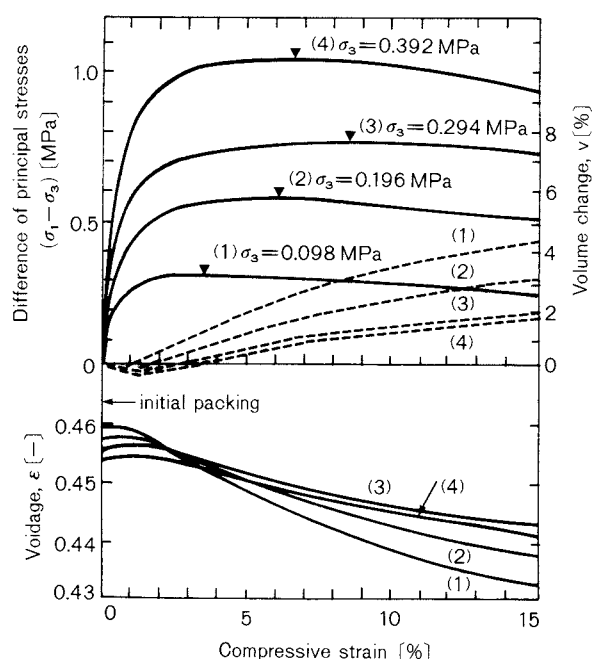
Fig. 1 The result of the tri-axial shear tests on Toyoura sand

Fig. 2 The yield locus of Toyoura sand obtained from the tri-axial shear tests

Table 4 The results of the tri-axial shear tests

| Material | Voidage | | Angle of internal friction δ [deg.] |
	at initial packing ϵ_0 [−]	at failure (average) ϵ [−]	
Soma sand	0.463	0.449	32.0
	0.433	0.417	36.0
	0.376	0.354	39.5
	0.354	0.329	40.25
Yamakawa sand	0.434	0.420	33.75
	0.417	0.400	34.5
	0.365	0.348	38.5
	0.357	0.335	40.0
Toyoura sand	0.482	0.470	34.0
	0.463	0.449	35.0
	0.405	0.387	39.75
	0.395	0.375	40.25
Silicon carbide	0.519	0.509	31.5
	0.496	0.483	32.0
	0.427	0.408	35.5
	0.415	0.393	36.25
Glass beads	0.408	0.408	23.0*

*) Quick test

and 0.392 MPa. These values were common to each of the tests. The difference in the principal stress, change in the volume, and change in the voidage were each plotted in relationship to the compressive strain. The voidage during failure was calculated by the equation.

$$\epsilon = 1 - (1 - \epsilon_0)/(1 - v_0)(1 - v) \qquad (1)$$

In this equation, ϵ_0 represents the voidage at the initial packing, v_0 is the change in the volume after consolidation (when only σ_3 is applied), and v is the change in the volume at the time of failure.

Upon determination of the maximum difference in principal stress as marked by ▼ in **Fig. 1**, Mohr's stress circles can be drawn as shown in **Fig. 2**. The straight line passing through the origin of the coordinates and tangent to the stress circles in the figure represents a yield locus. The angle of internal friction is represented as 35° in **Fig. 2**. With respect to the voidage corresponding to the maximum difference in the principal stress, the values differ slightly from one another with the change in σ_3, as shown in **Fig. 1**. Thus, the voidages are shown as 0.452, 0.449, 0.448, and 0.447 in the figure. It is a defect of the tri-axial shear testing method that the voidage cannot be made exactly the same for all tests. There-
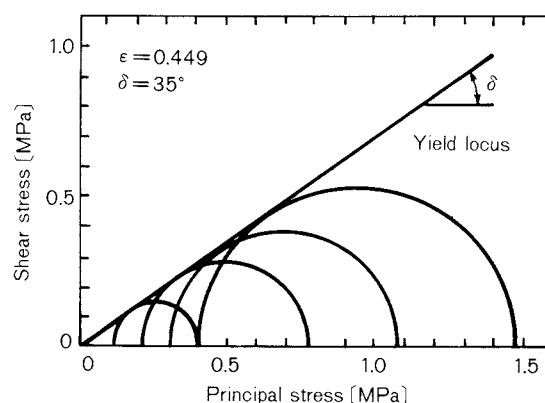
fore, the mean value of the voidages is used as the voidage during failure in the processing data. **Table 4** shows both the voidages and angles of internal friction obtained from the tri-axial shear tests.

Figure 3 shows a yield locus of Toyoura sand obtained by a fixed volume direct shear test. The yield locus can be determined by a single shear test where the vertical and horizontal components of the force generated at the step of shearing a specimen are simultaneously
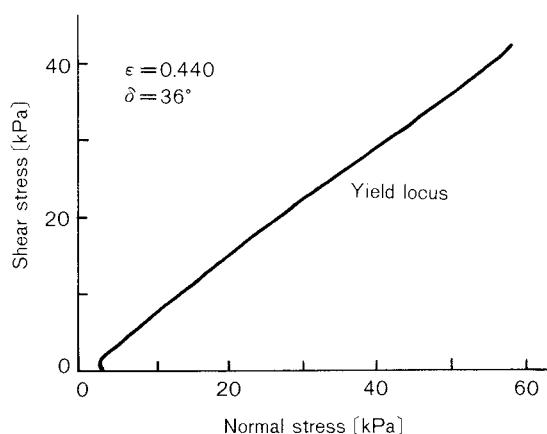
Fig. 3 The yield locus of Toyoura sand measured by the fixed volume direct shear tester

Fig. 4 A comparison of the angle of internal friction obtained from the tri-axial shear tests and the fixed volume direct shear tests

detected and output on an X-Y recorder. A yield locus can be regarded as forming a straight line passing through the origin. In **Fig. 3**, the angle of internal friction is shown as 36°. The voidage of the specimen at the initial packing ϵ_0 is shown as 0.440. In a fixed volume shear test, the voidage does not change during failure but remains the same as the value at the initial packing.

A comparison of the test results in **Figs. 2** and **3** shows that even though there is a great difference in the ranges of the stresses applied for the measurement, the angles of internal friction show closeness in values due to the virtual uniformity of the voidage.

Figure 4 shows a comparison of the results obtained by tri-axial shear tests with those obtained by fixed volume direct shear tests on the relationship between the voidage and the angle of internal friction. In past tri-axial shear tests, the angle of internal friction was considered in relationship to the voidage at the initial packing ϵ_0, but since the voidage during failure changes with compressive strain, as shown in **Fig. 1**, the voidage corresponding to the maximum difference in the principal stress must be considered.

The angle of internal friction increases with a decrease in the voidage independent of the testing methods. The results of two types of tests on Soma sand, Toyoura sand, and glass beads agree in the range from medium to loose in the packed state, but the values obtained by the direct shear tests are larger than those obtained by the other tests in the densely packed
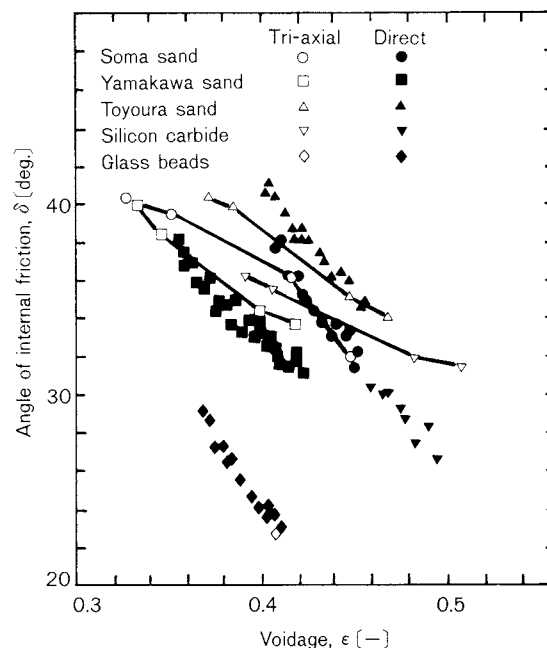
range. With respect to Yamakawa sand, the results agree on the whole, but there is a difference of up to 3° in the loosely packed range.

With respect to silicon carbide, however, the values obtained clearly show differnces of 3° ∼ 5° between the tri-axial shear tests and the fixed volume direct shear tests. The specimen of silicon carbide is a pulverized product, and the particles include those shaped almost like needles and flat particles. The distinct differences in the values obtained are considered to be due to a difference in how the shearing direction bears upon the disposition of the packed particles of the specimen between the two testing methods.

In **Fig. 5**, the results of shearing tests[5] carried out extensively by the Soil Engineering Society on sand (obtained at Onahama beach in Fukushima Prefecture, Japan) are shown as a relationship of the angle of internal friction to the initial void ratio. The sand had particle sizes of 0.1 ∼ 0.5 mm, and with the 50% diameter of 0.22 mm, if somewhat resembled Toyoura sand. **Figure 5** also shows the test results of Toyoura sand in the present study for comparison. Although the angles of internal friction differ slightly because of differences in the samples used, a close similarity is observed
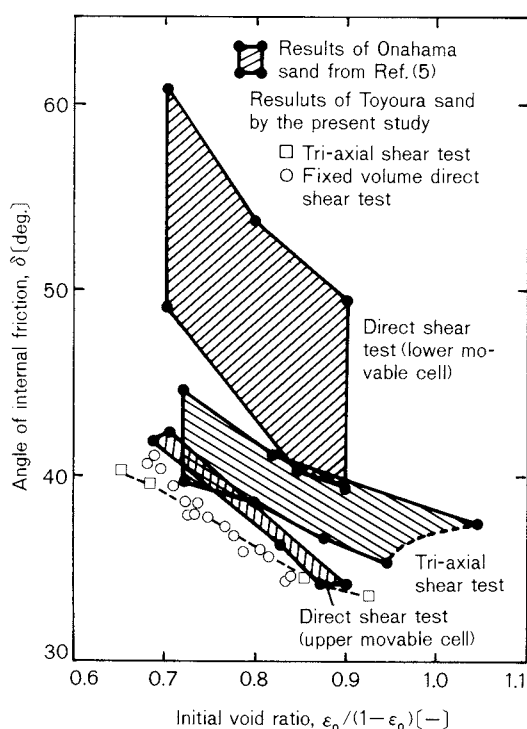
Fig. 5 A comparison of the angle of internal friction for Onahama sand and Toyoura sand measured by various types of shear testers

between the results of the Society's tests and those obtained in the present study for both the tri-axial and direct shear tests (the results of the Society's tests being based on upper-movable cells). Therefore, it is considered that there were no technical problems relating to the measurement in the present experiments.

It is said[5] that in the Society's extensive tests the results obtained by the use of lower-movable cell type devices for the direct shear tests showed larger deviations than all of the other comparable results, as well as a large degree of scatter, but the results were found

lacking in confidence. The device used for the fixed volume direct shear tests in the present experiments was also of the lower-movable cell type, but the obtained results were similar to those obtained by the tri-axial shear tests and the upper-movable cell-based direct shear tests.

Whether the shearing cell is of the upper-movable type or of the lower-movable type does not seem to significantly affect the results of the direct shear tests. The problem is considered to lie in the structure of the testing device, or in the dimensions of the shearing cells, etc.

4. The flowability of cohesive powder and granules

The unconfined yield strength of a cohesive powder or granular material is an important property to consider[6,7] when a storage vessel for it is designed. This is because this property is closely related to blocking which occurs at or near the outlet of the vessel. The most direct method for measuring the unconfined yield strength is the unconfined yield test, which is standardized mainly in the field of soil engineering. It is also possible to obtain the unconfined yield strength from the data of a yield locus measured by the direct shear test. Next, a comparison is made of the results obtained from the two testing methods.

Table 5 shows the samples and dimensions of the specimens, etc. which were used in the experiments. Common samples were employed in the two testing methods with respect to calcium carbonate, limestone, and coal (A), whereas the samples of coal (B) used for the two respective testing methods were similar but differed in particle size and free moisture.

Figure 6 shows a record of the compressive

Table 5 The conditions of the experiment and materials used in the unconfined yield tests and the direct shear tests

Material Condition	Calcium carbonate		Lime stone		Coal (A)		Coal (B)	
Testing method	U.Y.T.	D.S.T.	U.Y.T.	D.S.T.	U.Y.T.	D.S.T.	U.Y.T.	D.S.T.
Particle size	$2.6\ \mu m$	$2.6\ \mu m$	< 3 mm	< 3mm	< 3mm	< 3mm	< 10 mm	< 5.6 mm
Free moisture (%)	0.20	0.18	4.1	4.07	12.6	12.6	8.3	7.8
Specimen size [mm]	$18.8^D \times 50^H$	$100^D \times 10^H$	$50^D \times 100^H$	$100^D \times 10^H$	$50^D \times 100^H$	$100^D \times 10^H$	$100^D \times 200^H$	$100^D \times 10^H$

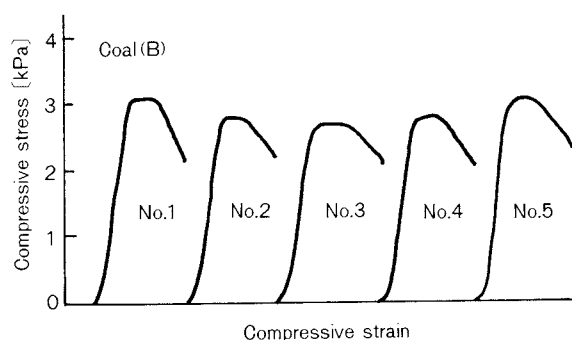(Note: U.Y.T. shows the unconfined yield test and D.S.T. the direct shear test)
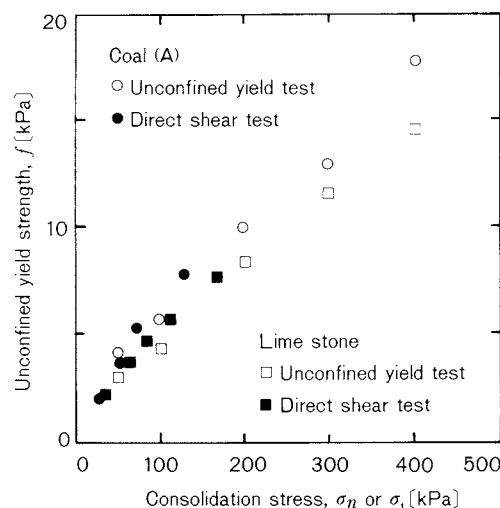
Fig. 6 Record of unconfined yield tests for coal (B)

Fig. 8 A comparison of the unconfined yield strength of coal (A) and limestone obtained from the unconfined yield tests and the direct shear tests

stress applied to the coal (B) in an unconfined yield test. The peak value of the compressive stress was regarded as the unconfined yield strength f. The test was carried out five times, more or less, for the same bulk density, and then it was repeated likewise for a different bulk density. The specimens were composed of three to five vertical layers. The specimens had different sizes depending on the particle size, as shown in **Table 5**. The relationship between the consolidation stress and the bulk density was examined by a separate measurement. The details of the testing method are described in the literature[7].

Figure 7 shows a yield locus of the coal (B) obtained by a direct shear test. From the end point of the preliminary shearing step of a specimen, a continuous line representing the relationship between the normal stress and the shear stress was recorded to show the yield locus. The unconfined yield stress f can be obtained as the diameter of the Mohr circle that

passes through the origin of the coordinates and meets the yield locus at one point. The major consolidation stress σ_1 is shown by the Mohr circle which meets the yield locus at the end point. The bulk density is calculated from the packed volume and the mass of the specimen at the time when the preliminary shearing has ended. The details of the testing method etc. are described in the literature[3].

Figure 8 shows the unconfined yield strength of the coal (A) and limestone obtained by both the unconfined yield and direct shear tests. In this figure, the results of the unconfined yield tests are shown as the relationship of the unconfined yield strength f to the consolidation stress σ_n, and the results of the direct shear
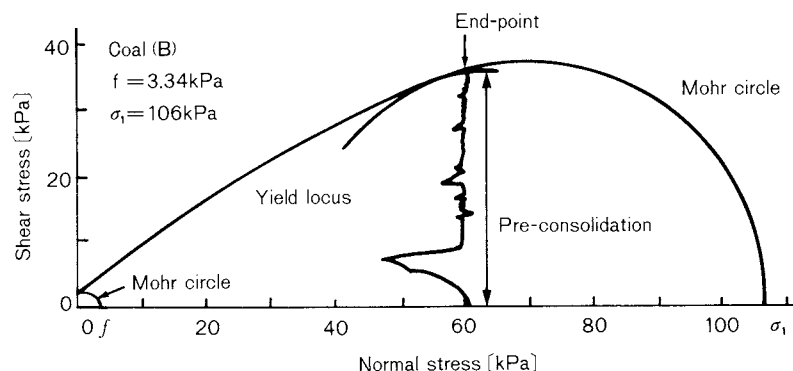

Fig. 7 The yield locus of coal (B) measured by the direct shear tester, and determination of the unconfined yield strength, f, and the major consolidation stress, σ_1
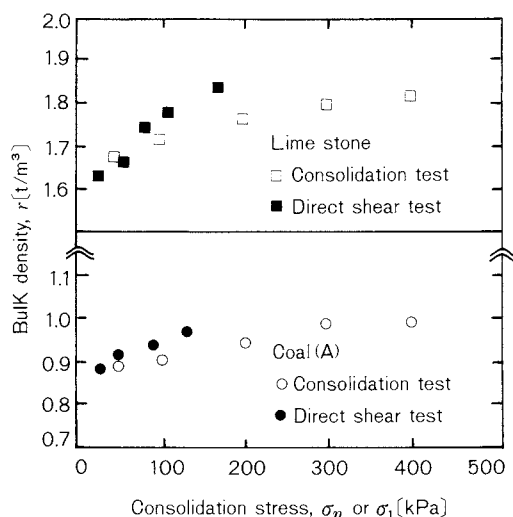
Fig. 9 A comparison of the bulk density of coal (A) and limestone obtained from the consolidation tests and the direct shear tests

Fig. 10 A comparison of the flowability of calcium carbonate obtained from the unconfined yield tests and the direct shear tests
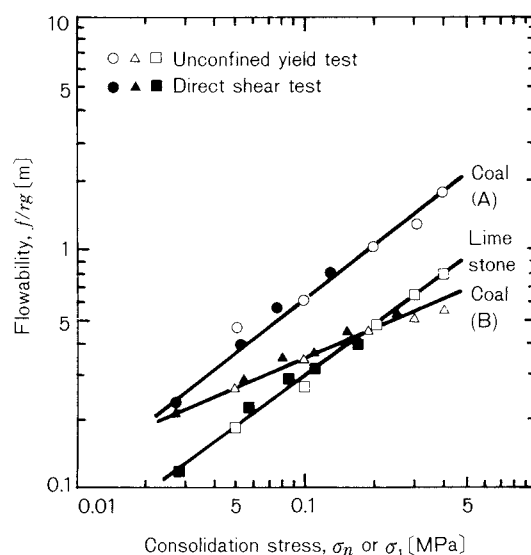
Fig. 11 A comparison of the flowability of wet coals and limestone obtained from both the unconfined yield tests and the direct shear tests

tests are shown as the relationship of the unconfined yield strength f to the major consolidation stress σ_1. The results of the two testing methods were relatively close, with the values obtained from the direct shear tests being slightly larger on the whole than those obtained from the other tests. This difference is considered to be due to shearing at the unconfined state of one method and a difference in the molding method for the specimens between the two testing methods. The latter reason lies in the fact that whereas the specimens used in the unconfined yield tests were molded by simple compression, those for the direct shear tests were molded through preliminary shearing.

Figure 9 shows the results of the bulk density γ of coal (A) and limestone, obtained by the two testing methods. It is shown that the bulk density was larger, and the specimens were packed more densely for the direct shear test than for the unconfined yield test. As a result, the unconfined yield strength is considered to have shown a larger value during the direct shear test.

It was already reported[3] that the flowability of a cohesive powder or granular material can be evaluated by a flowability index expressed as $f/\gamma g$. This flowability index means the critical height up to which a molded body of powder maintains its shape and an increase in the value, which occurs with an increase in

the cohesive force and frictional force between particles, signifies a degradation in the flowing property. The respective flowability indices obtained from both the unconfined yield and direct shear tests are shown in **Figs. 10** and **11** for comparison. Although they show some scatter, the results of calcium carbonate, are almost in agreement for both testing methods. The unconfined yield tests of calcium carbonate were carried out by Yokohama National University, and those of the other three kinds of specimens were done by Mitsui Construction Co.

The flowability indices obtained by the unconfined yield tests in **Fig. 11** represent the averages of the results of tests carried out five times, as shown in **Fig. 6**. In **Fig. 11**, a fairly good agreement can be observed between the results obtained by the two testing methods with respect to the flowability of wet coals and limestone.

The relationship between the flowability index and the major compressive stress in the results of direct shear tests can be represented by Eq. (2), as already reported[3,8]

$$f/\gamma g = a\sigma_1{}^b \qquad (2)$$

where a and b are coefficients proper to a powder, and g is the acceleration of gravity.

As is clear from **Fig. 11**, Eq. (2) is also applicable to the results of unconfined yield tests if the compressive stress σ_n is substituted for the major compressive stress σ_1. From the results obtained by the two testing methods, it is seen that Eq. (2) is valid for σ_1 or σ_n in a range of approximately $20 \sim 500$ kPa. If the results previously discussed[3,8] are also taken into consideration, Eq. (2) is valid for a range of $1 \sim 500$ kPa.

5. Summary

With a view to examining the results of differing testing methods in terms of their consistency, tri-axial shear tests were compared with fixed volume direct shear tests in the measurement of the angle of internal friction of dry granules. Unconfined yield tests were compared with direct shear tests in the measurement of the flowability indices of cohesive powder and granules. As a result, it was found that:

1) whereas the angle of internal friction of dry granules is dependent on the voidage, the values obtained by the two testing methods agree to within a difference of about $3°$, except for the extremes of the voidage range where, even though the specimen grains have exceptional shapes, a difference of more than $3°$ may arise depending on the testing method.

2) with respect to the flowability index of cohesive powder or granules, the values obtainable by the two testing methods agree relatively well. The flowability index can be expressed by Eq. (2) for the compressive stress or major compressive stress in the range of up to 500 kPa.

Nomenclature

a	: coefficient in Eq. (2)	[−]
b	: coefficient in Eq. (2)	[−]
f	: unconfined yield strength	[kPa]
g	: acceleration due to gravity	[m/s^2]
v	: volume change during failure	[%]
v_0	: initial volume change	[%]
γ	: bulk density	[t/m^3]
δ	: angle of internal friction	[deg]
ϵ	: voidage during failure	[−]
ϵ_0	: voidage at initial packing	[−]
σ_1	: major stress	[kPa]
σ_3	: minor stress	[kPa]
σ_n	: compressive stress	[kPa]

References

1) Takagi, F. and M. Sugita: *J. Soc. Powder Technol., Japan*, **16**, 277 (1979).
2) Soc. Soil Mecha. and Fund. Eng.: "Doshitsu Shiken-Ho" (1979).
3) Tsunakawa, H.: *J. Soc. Powder Technol., Japan*, **19**, 516 (1982).
4) Tsunakawa, H.: *Powder Technol.*, **33**, 249 (1982).
5) Yamada, K.: *Tsuchi To Kiso*, **13**, 89 (1965).
6) Tsunakawa, H.: *J. Soc. Powder Technol., Japan*, **18**, 405 (1981).
7) Tamura, T., H. Haze, M. Kato and T. Yamada: *J. Soc. Powder Technol., Japan*, **22**, 511 (1985).
8) Tsunakawa, H.: Preprints of CHISA '84 Congress, Prauge (1984).

The Aggregate Structure of Fine Particles and Compacting Process[†]

Masafumi Arakawa, Takeshi Kitamura,
Yoshinori Tokuoka, Hiroshi Morii
and Hitoyoshi Kinoshita
Faculty of Engineering and Design
*Kyoto Institute of Technology**

Abstract

The compacting characteristic of fine particles is greatly affected by the aggregate structure of particles. Several kinds of silicon nitrides, which are different from each other in particle shape, size and bulk density, were compacted in a uniaxial direction under various conditions, and the behavior of the particles during compaction was analyzed and compared by using Cooper's equation. It was found that the difference in the kind of samples and the condition of their pretreatment resulted in considerably different behaviors during compaction, and that the apparent volume reduction rate under pressure was remarkably different at low and high pressures.

The aggregate structure of each sample was estimated based on the above results together with the result of the measurement of the compaction structure of the molded bodies.

1. Introduction

Although many formulas have been proposed to represent the compaction characteristics of powders, strongly-cohesive fine particles assume an aggregate structure of such a high order and so complicated a phenomenon during compaction that the existing formulas are not readily applicable to such powders. Guided by the applicability of Cooper's formula, in which particle deformation is considered, to the compaction of the fine particles under study, the authors, through a study of silicon nitrides with respect to changes in the compacting characteristics caused by pretreatment, pointed out that a wetted powder containing a suitable quantity of liquid medium exhibits an improvement in its compacting characteristic. "Compacting characteristic" refers to the degree of ease with which a powder material can be compacted, that is, the quality of a powder material that permits the material to be compacted into a dense homogeneous body.

In this paper, the effect of pretreatment, under various conditions, on the compacting characteristic is studied with respect to several kinds of industrially used silicon nitrides. These nitrides differ from each other in their method of fabrication, particle size, and shape etc. By analyzing the behavior of powders under compaction, the aggregate structure that fine particles assume can be estimated.

2. Experiments

2. 1 Samples

Table 1 lists the physical properties and methods of fabrication with respect to the silicon nitrides that were employed in the present experiments.

The particles of Sample A each resembled a thick rectangular plate in shape and had a fairly broad particle size distribution, whereas those of Sample D were each an amorphous mass. They were also the most irregular in particle size of all the samples employed. The particles of all three samples of the U series

Table 1 Characteristics of sample powder

Sample code	Surface area m^2/g	Particle size μm	Fabricat.	Compaction pattern
A	8.5	0.38	SiO_2-N_2	B
D	20.7	0.15	Si-N_2	A
U-02	1.2	2.65	imide	C
U-05	3.3	0.96	imide	C
U-10	12.4	0.26	imide	C

Fig. 1 Variation in kneading torque with increasing liquid content

were each almost cube-shaped and were virtually uniform in particle size.

Butanol was used as the wetting medium.

2. 2 Method and apparatus

Each of the cylindrical molds with a cross-sectional area of 0.5 cm² was filled with a sample in the form of dry powder or with a wetted preparation of a sample prepared by mixing it with butanol at a suitable volume percentage and by kneading the two together. The sample in the mold was compacted under a pressure of up to 1,000 kg/cm² by means of an Autograph S-500 to form a cylindrical specimen several centimeters long. The relationship between the applied pressure and the apparent volume during compaction was analyzed using Cooper's formula. The cylindrical specimen was also longitudinally divided into three approximately equal parts, and the pore distribution of each part was measured by means of a mercury porosimeter so as to determine the degree of homogeneity of the compacted body.

To mix a sample with the liquid medium, a laboplastomill and a biaxial continuous kneader were used. The degree to which the kneading was performed was shown by the time with respect to the use of the batch-based labo-plastomill (hereafter abbreviated as LPM) or by the number of times of repeated kneading with respect to the use of a continuous biaxial kneader (hereafter abbreviated as KRC).

3. Results

3. 1 Optimum volume percentage of the wetted powder
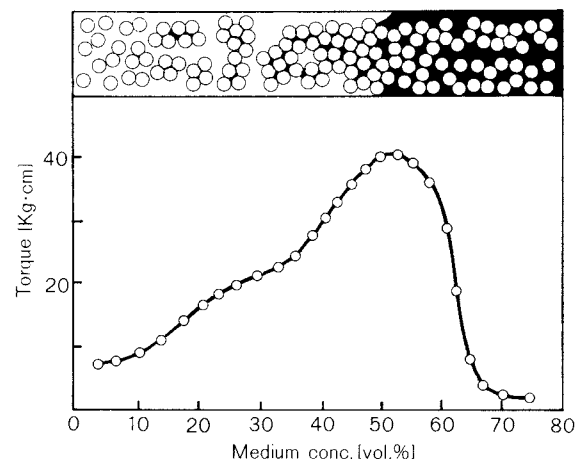
The optimum percentage of volume of a

wetted powder was determined in the following manner. A dry sample powder was kneaded by stirring in the LPM with the gradual addition of butanol in small quantities as a liquid medium, and the relationship of the kneading torque to the content of the liquid medium was obtained as shown in **Fig. 1**. The kneading torque changed only slightly while the powder was dry or while the aggregates of the particles with the liquid medium were so small as to be able to move freely. However, the kneading torque increased as the aggregates became so large as to exceed the interval between the stirring vanes. This is because of the need to deform and break the aggregates. The torque reached its peak when all the particles assumed their most close-packed structure in which the pores were filled with the liquid medium, and it then decreased as the content of the liquid was increased further. This happened because the volume of the pores (filled with the liquid medium) in which particles could move freely increased. Assuming that the conditions for obtaining a dense, homogeneous compacted body were for the aggregates of particles to be capable of being deformed and for the porosity to be minimal, as previously reported, the optimal content of the liquid was considered to be the volume percentage that was slightly larger than the content at the peak of the kneading torque. Samples wetted at differing volume percentages about the optimal value were compacted, and the respective mean pore
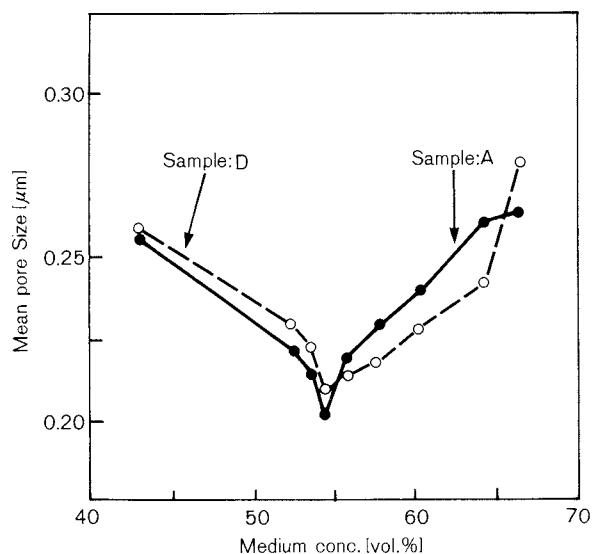
24

Fig. 2 The change in mean pore size with liquid
content

Fig. 3 The variation in the packing fraction of
the compacted body with column length

size was obtained from the pore distribution,
as shown in **Fig. 2**. The volume percentage of
the liquid medium at which the mean pore size
was the smallest was regarded as the optimal
content.

Samples wetted with butanol at the optimal
volume percentage were kneaded well in a
mortar, LPM, or KRC, and then compacted
into specimens of various thicknesses by the
application of 1,000 kg/cm^2 of pressure. Of
all the specimens thus prepared, those kneaded
by KRC showed the packing fraction to be
highest and the changes with column length to
be relatively small. Therefore, KRC was mainly
employed for kneading in the present experi-
ments.

3. 2 Behavior of particles during compaction

A. R. Cooper[2] divided the behavior of pow-
der particles during compaction into two
stages, one characterized by the packing of
particles and the other characterized by the
deformation of the individual particles that
causes disappearance of the pores. Equation (1)
was then proposed.

$$\frac{V_0 - V}{V_0 - V_s} = \alpha_1 e^{k_1/P} + \alpha_2 e^{k_2/P} \qquad (1)$$

where V_0 and V represent the apparent volume
of a powder before and at the application of
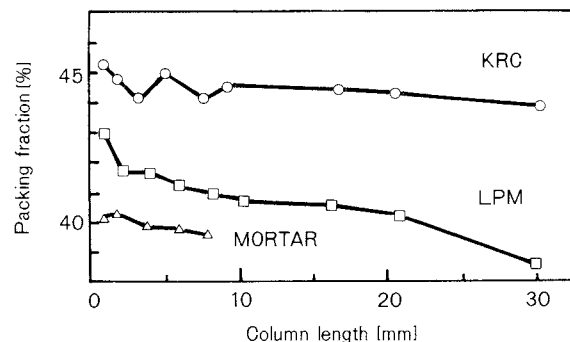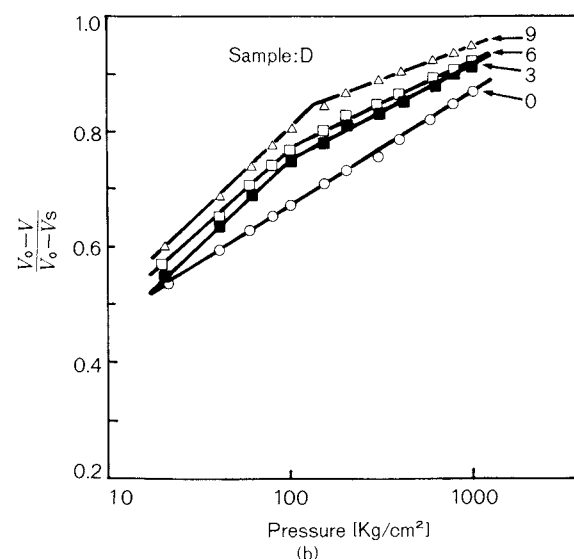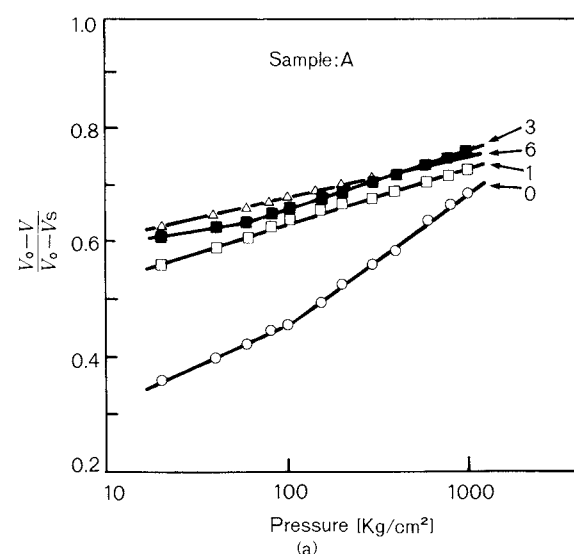pressure P, respectively, and α_1, α_2, k_1, and k_2

Fig. 4 The relationship between the fractional volume
compaction and pressure for variously kneaded
powders. The numeral shows repeat times.
(a): Sample A, (b): Sample D

are experimentally obtainable constants. V_s represents the specific volume of a material, i.e. the volume that particles assume when they have become consolidated into a single solid mass with no pores through deformation of the particles by compaction. Since, however, it is hardly possible for inorganic fine particles to be deformed by compaction under general conditions, V_s is dealt with in this paper as the apparent volume of a group of most close-packed (to a porosity of 0.26) uniform globular particles.

Changes in the apparent volume reduction rate $(V_0 - V)/(V_0 - V_s)$ under pressure (hereafter referred to as the "Cooper plot") obtained with respect to each sample listed in **Table 1** are represented by straight lines each deflected at a certain pressure, as shown in **Fig. 4**, that corroborate Eq. (1). The slopes k_1 and k_2 of these straight lines vary with changes in the kind of sample, and kneading conditions, etc.

3. 3 The relationship to column length

Changes in the Cooper plot of the compacted bodies for differing column lengths were examined for differing samples and for differing kneading machines. **Figure 5** shows an example of the results. With respect to Sample A, consideration of the changes in k_1 and k_2 in relationship to the column length shows that,
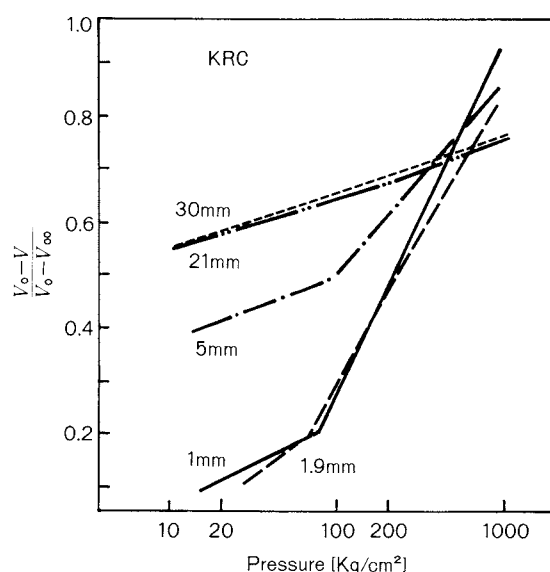

Fig. 6 The change of k_1, k_2 with column length
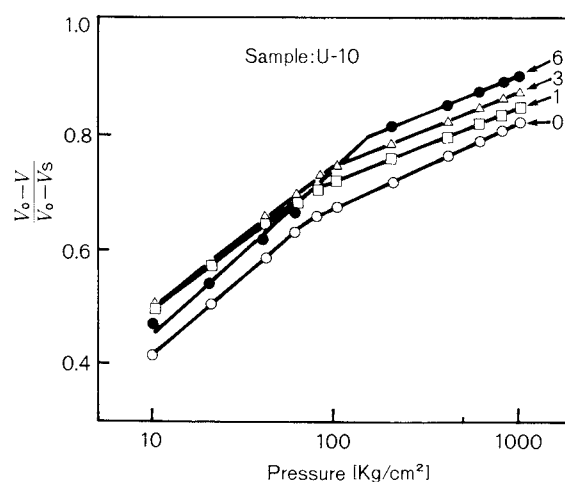
Fig. 7 The Cooper plot of Sample U-10 under repeat kneading

as seen in **Fig. 6**, k_2 mainly assumes a larger value with an increase in the column length until eventually k_1 and k_2 coincide, i.e. k_1 and k_2 are then represented by a straight line. With respect to the samples in which $k_1 > k_2$, such as the samples of the U series, little change is observed, but a parallel relationship is maintained, as shown in **Fig. 7**.

4. Discussion

The Cooper plots of silicon nitrides, as shown in **Figs. 4** and **5**, can be classified into the three types — Type A ($k_1 < k_2$), Type B ($k_1 > k_2$), and Type C ($k_1 = k_2$) — illustrated in **Fig. 8**. The pressure dependency of the apparent volume reduction rate is represented key k_1 and k_2, k_1 corresponding to the com-

Fig. 5 The variation in the Cooper plot of Sample A with column length

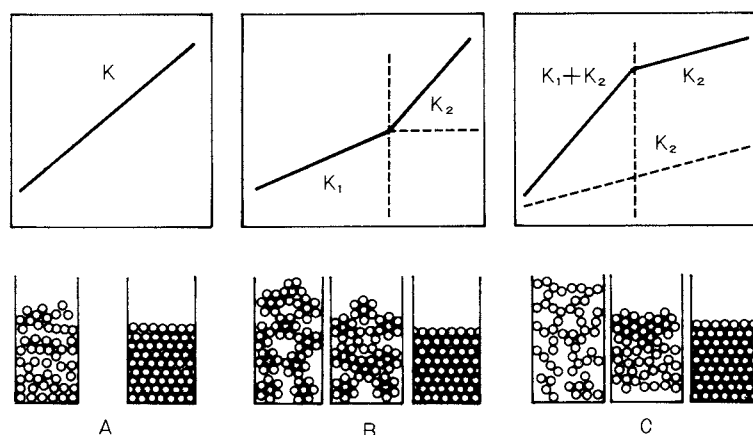Fig. 8 A schematic diagram of the relationship
between the Cooper diagram and the aggregate
structure of fine powders

paction of particles under low pressure and k_2 to the compaction of particles under high pressure.

The particles of a fine powder have a relatively strong tendency to aggregate and necessarily form aggregates of particles under normal conditions. An aggregate of such particles can be considered to act as a unit of motion, where motion occurs under a low force. Such particles not only form aggregates by primary aggregation, but in many cases they also form secondary or tertiary aggregates. The present experiments however, besides dealing with primary particles, are concerned also with tightly clustered secondary aggregates, considering the effect of the kneading given to the samples. The differing stages of k_1 and k_2 in a Cooper plot signify the occurrence of two distinctly different phenomena, for example, the stage at which secondary aggregates of particles are packed without being modified and the stage at which primary particles resulting from the disintegration of particle aggregates are packed.

Type B corresponds to a case in which when one phenomenon under low pressure is finished, and another phenomenon occurs under a higher pressure. Type C is a case in which two different phenomena occur concurrently under low pressure and, at the point of deflection, one of the phenomena terminates but the phenomenon signified by k_2 continues. Type A signifies continuation of the same process

during compaction for the changing pressures in the full range.

A practical example of Type B is the packing of particles that are in part sintered between particles and form aggregates that are fairly firm but somewhat fragile. The aggregates are packed under low pressure without disintegrating but, after being packed to the greatest density, the aggregates disintegrate under pressure into primary particles during subsequent compaction. If the reduction in the volume when a shift occurs from k_1 to k_2 is less than one half the volume in the most close-packed state, it is considered that the aggregates of particles as units of motion in the compacted bodies are so large that the particles in a unit volume are small in number, and the pores between particles amount to a large volume. Type C is considered to show a case in which the particles interact with each other so as to form weakly clustered aggregates that concurrently undergo both disintegration and packing of the resulting primary particles. When the disintegration of the aggregates of particles terminates and only primary particles continue to be packed subsequently, the particles are packed close to the greatest density, and the subsequent reduction in the volume is at a low rate. Type A is typified by relatively small but firmly clustered aggregates of particles that are presumed to undergo compaction without involving disintegration of the aggregates to any significant degree. Although it may be con-

sidered reasonable for primary particles not in the aggregates form to assume Type A, the present experiments can hardly consider that notion, since, as shown in **Figs. 4** and **5**, it is observed that particles may shift from Type B to Type A or from Type A to Type C depending on the degree of kneading to which they are subjected, but the particles do not shift in the reverse order. The reason in that unless it is presupposed that the shift of B $\rightarrow$ A caused by kneading does not signify the disintegration of firmly clustered particles at a stroke into unit particles but means disintegration into smaller aggregates of particles, there is no explanation with respect to the shift of A $\rightarrow$ C. The shift of A $\rightarrow$ C is presumed to occur because an aggregate of particles the momentum of which balances the interaction between particles disintegrates into finer unit particles, and the particles in a unit volume increase in number. As a result, the interaction between them is enhanced, and the behavior peculiar to aggregate particles is seen.

Closer and more accurate observations of such behavior of particles may be possible, if, for example, the pore size distributions of compacted bodies obtained by the application of various degrees of pressure are examined. However, since compacted bodies with low strength easily collapse, it is very difficult to carry out such examination. A method of overcoming this difficulty is now under study.

On the other hand, it is observed, for example, that in **Fig. 5** the Cooper plot of Sample A by the column length shows that the ratio k_2/k_1 becomes smaller with column length and approaches that of Type A. This phenomenon may be explained by the observation that since pressure is applied in only one downward direction in uniaxial compaction, the relaxation of particle stress caused by internal friction or friction against the wall surface becomes large with an increase in the quantity of particles and in the thickness of the compacted body. Also, the stress distribution in the longitudinal direction broadens so that the two-stage change appears continuous. In the case of the Type A sample, such as Sample D in **Fig. 4**, it is considered that the k_1/k_2 ratio does not change with column length because the aggregates of particles easily disintegrate when packed and, therefore, the internal stress is small, and the
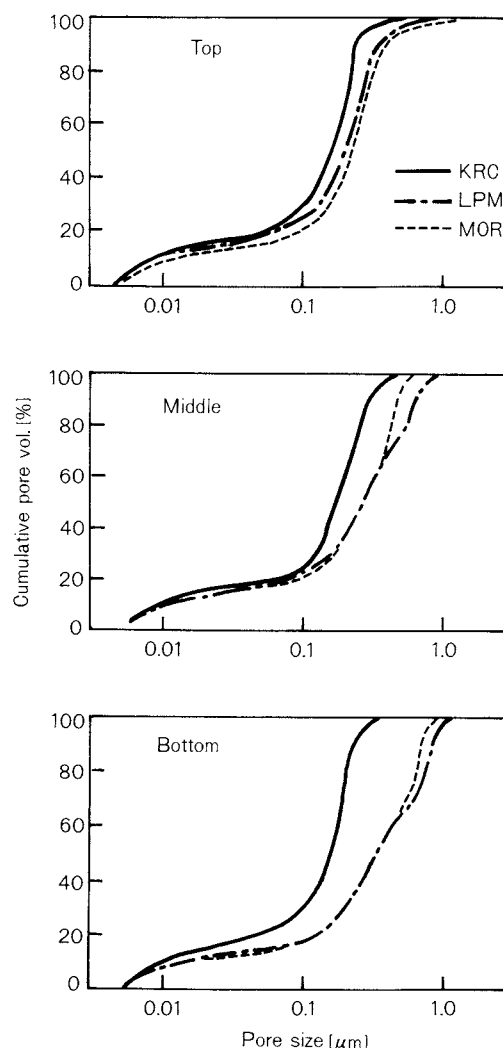
Fig. 9 The pore size distribution of a compacted body

pressure is easily transmitted. These phenomena do not contradict our observations with respect to the aggregate structure of particles and their behavior under compaction.

The pore size distributions of compacted bodies for differing methods of kneading, examined with respect to the top, middle, and bottom parts, respectively, by means of a mercury porosimeter, are observed to be broader and less densely filled toward the bottom, as shown in **Fig. 9**. However, compacted bodies of a sample well kneaded by KRC show pores to be densely and evenly distributed throughout, as shown in **Fig. 10**.

In this way, compacted bodies can be estimated with respect to their pore size distribution, which is dependent on the particle size of the sample powder. The samples U-02, -05,

Fig. 10 The pore size distribution of a compacted body prepared under the best condition

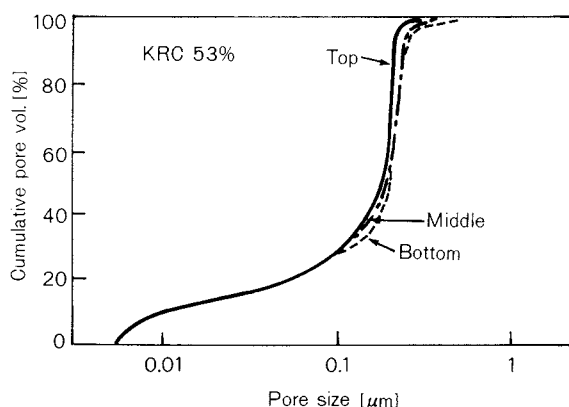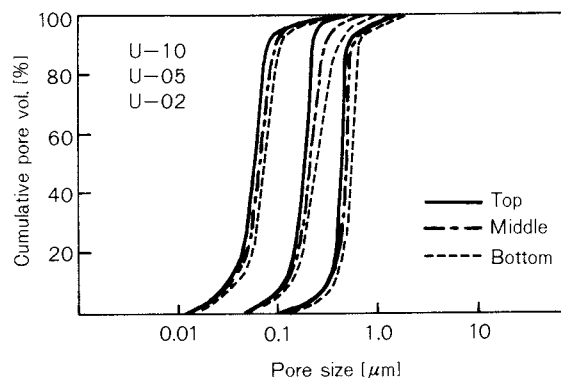Fig. 11 A comparison of pore size distributions for the Sample U-series

and -10 are characterized by the shape of the particles, which is virtually cubic, and narrow particle size distributions with the mean particle sizes as shown in **Table 1**. The pore size distributions of the compacted bodies of these samples show uniformity, as seen in **Fig. 11**, and they correspond to the mean particle sizes calculated from the specific surface areas. Since the mean particle size based on the specific surface area reveals the size of primary particles independent of the aggregate structure, a uniaxial compaction of the order in view, if fine particles are processed, is shown to produce compacted bodies that are densely and evenly packed. An increase in particle size makes it more difficult to obtain an evenly compacted body. It is considered that the particles then becomes less cohesive, and the internal friction increases.

5. Conclusion

Wetted samples of five kinds of industrially used, silicon nitride powders which differed from each other in particle shape, particle size, and method of fabrication, were subjected to simple uniaxial compaction, and the compacting characteristics of the specimens were analyzed using Cooper's formula. The specimens showed three different types of particle be-

havior depending on the method of fabrication of the samples, and the conditions of kneading them with a dispersion medium volume percentage, etc. The aggregate structures of particles of each specimen were capable of being estimated.

Furthermore, by measuring the pore size distributions of the compacted bodies using a mercury porosimeter, the optimal wetting conditions, with respect to volume percentage, kneading method, and compacting conditions, were determined. It was found that since the pore size of the compacted body was more or less relative to the size of the primary particles of the sample powder, fine particles, such as the samples, are capable of being compacted into densely and evenly compacted bodies by controlling the compacting conditions.

Reference

1) Arakawa, M.: *J. Soc. Material Sci., Japan,* **34**, 1245 (1985).
2) Cooper, A.R., et al: *J. Am. Ceram. Soc.,* **45**, 97 (1962).

The Effect of the Ultra-Fine Solid Additives on the Mechanical Properties of a Powder Bed [†]

Makio Naito
Micromeritics Laboratory
Hosokawa Micron Corp. *

Jun-ichiro Tsubaki
Fine Ceramics Center **

Satoru Usuda, Naoki Kato and Genji Jimbo
Dept. of Chemical Engineering,
Nagoya University ***

Abstract

Solid additives are widely used to control the mechanical properties of powders materials in many industries. In this paper, the measurement of the tensile strength of a powder bed with a split-cell type tester was conducted to elucidate the effect of solid additives on the mechanical properties of powders.

Fused alumina powder, silica sand, limestone, lactose and potato starch were selected as the powders. Furthermore, colloidal silica was used as a solid additive.

The relationship between the tensile strength and the porosity of a powder bed containing the additive was proposed to characterize the effect of additives on the mechanical properties of the powders.

Furthermore, the experimental results reported by others were able to be explained by the above relationship.

1. Introduction

Solid additives are widely used in industries as glidants to improve flowability, as lubricants, and as grinding aids, among others. These additives control the mechanical properties of powders. Furthermore, the use of solid additives is considered to be a convenient method for future treatment in the design of various powders. However, an established theory has not yet been developed for the

---

* No. 9, Soudai Tajika 1-chome, Hirakata, Osaka, 573
   TEL. 0720 (55)2220

** 2-4-1, Rokuno, Atsuta-ku, Nagoya, 456
   TEL. 052 (871) 3500

*** Furo-cho, Chikusa-ku, Nagoya, 464
   TEL. 052 (781) 5111

mechanism of their action[5]. Systematic studies have not yet been undertaken on the effect of solid additives on the tensile strength (one basic property) of a powder bed. Thus, there is a lack of experimental studies on the manner in which solid additives act, even though there are a few relevant reports[1,3,8].

In this regard, systematic studies were conducted by the authors[6,7] on the effect of an additive on the tensile strength of a powder bed, starting with colloidal silica (finely divided anhydrous silica), which is in general use as an additive. The results showed[6] that if the additive content is used as a parameter, the tensile strength of a powder bed containing an additive can be represented by the experimental equation[4]

$$\sigma_z = k_{1n} \exp\left(-\epsilon/b_n\right) \tag{1}$$

which has already been proposed. However, these studies did not elucidate the manner in which the additive acted because the coeffi-

cients k_{1n} and b_n in Eq. (1) varied as the additive content changed. They also varied as the powder was changed in kind and in particle size[6].

In this paper, a new characterization method is proposed to evaluate data of the tensile test of a powder bed containing an additive. Furthermore, this characterization methods is applied to the evaluation of the effect of ultra-fine solid additives on other mechanical properties.

2. Experiments

2. 1 Method and apparatus used in the experiments

The experiments consist of the mixing of a powder with an additive and of the tensile test of the mixed powder. The test specimen was mixed in a V-type mixer containing 20 rubber balls, each with a diameter of 30 mm (VJS, product of Tsutsui Physicochemical Instruments Co.). Prior to the mixing of the specimen powder, the material and the additive were made to stand in a thermohygrostat vessel under a specified constant humidity for 24 hours. Then, a batch of the two weighing a total of 0.5 kg was mixed in a mixer at 50 r.p.m. for 2 hours. The resultant mixture was again conditioned in the thermohygrostat vessel and then subjected to the tensile test. A specimen powder containing no additive was also prepared by mixing this way, and the resultant powder was subjected to the test itself.

A split cell type tester (Cohetester, product of Hosokawa Micron Corp.), shown in **Fig. 1**, was employed in the tensile test of the powder beds. The cell had an inside diameter of 50 mm and a depth of 20 mm. The test was carried out

Fig. 1 Split cell type tensile strength tester

by a procedure in which, first, the cell was filled with a specimen powder using a spatula. The specimen was then placed under pressure for 10 minutes for pre-compression to adjust the porosity of the powder bed. Next, the top of the powder bed in the cell was leveled so that the powder bed assumed a set volume, and then the tensile strength was measured by pulling the movable half-cell. The applied pre-compressive stress was within the range of 1.55 ~ 11.5 kPa, and the porosity of the powder bed was measured by weighing the specimen after the tensile test. The apparent particle density ρ_n of the powder containing the additive was calculated by the following equation,

$$\rho_n = \frac{1}{(1-n)/\rho_p + n/\rho_a} \qquad (2)$$

Since additives are generally used in minute ratios, the additive content in the present experiments ranged up to a maximum weight fraction of 0.04. The tensile test was carried out twice for each combination of the same values of the additive content and the pre-compressive stress. The mean values of the tensile strength and of the porosity thus obtained were used in the subsequent analysis. Both the thermohygrostat vessel and the environment in which the tensile test was carried out were conditioned at a constant temperature of 20°C, and a constant relative humidity of 50%.

2. 2 The specimen powders

Table 1 shows the abbreviations used in **Figs. 2 ~ 5** as well as the mean diameter and the true density of the particles of each of the specimen powders and of the additive used. Both the lactose and potato starch conformed to Japanese Pharmacopoeia. The particle size of each specimen powder was measured by a laser diffraction method (CILAS), and the 50% diameter obtained by integration of the volumes was used as the mean particle diameter. **Figure 2** shows the particle size distributions of the specimen powders. Solid additives were available in a variety of types, but as in the previous papers[6,7], a colloidal silica (AEROSIL 130, product of Nihon Aerosil Co.), which is in wide use as an additive to improve
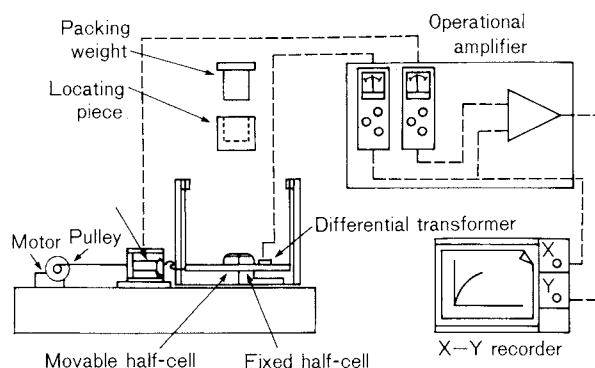
Table 1 Powder materials and additive

Powder		d_p [μm]	$\rho_p \times 10^{-3}$ [kg/m^3]
Fused alumina	(F.A.)	0.9	3.97
		3.3	3.97
Silica sand (JIS 3)	(S.S.)	4.3	2.65
Limestone	(L.S.)	1.7	2.70
		14.2	2.70
Lactose (JPXI)	(La)	38.4	1.53
Potato starch (JPXI)	(P.S.)	37.1	1.50
(Additive) Colloidal silica		d_a [μm] 0.016	$\rho_a \times 10^{-3}$ [kg/m^3] 2.20
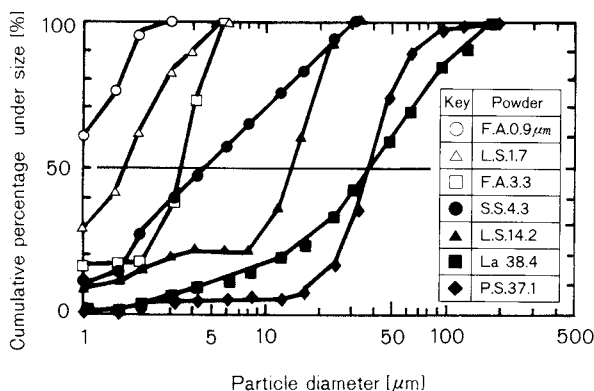
Fig. 2 Particle size distributions of powders

Fig. 3 Relationship between tensile strength of powder bed and additive content
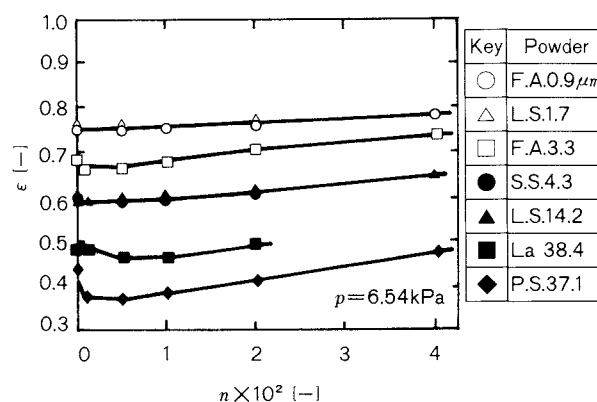
Fig. 4 Relationship between porosity of powder bed and additive content
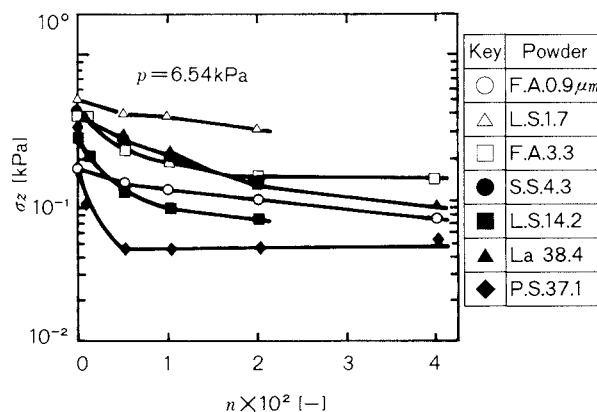
flowability, was used as the solid additive. The mean particle diameter of the additive was the value shown in the catalog.

3. The results of the experiment

Because the data was processed with the additive content n as a parameter in the previous paper[6], the pre-compressive stress p was used as a parameter in this paper. Furthermore, the data was processed into relationships of the additive content n with the tensile strength σ_z and porosity ϵ, respectively. **Figures 3** and **4** show examples of data obtained for a pre-compressive stress p of 6.54 kPa.

With respect to the relationship between the tensile strength σ_z of powder bed and the additive content n, it is seen from **Fig. 3** that the tensile strength σ_z of each powder bed decreased as the additive content n increased. Furthermore, the curves indicate that for additive contents n at the initial stage of the ad-

dition, larger decreases in the tensile strength occurred where the particle diameter of the powder was larger. It was also observed by electron microscopic photography that ultra-fine particles of additive were scattered on the surface of the powder particle and attached to it[6]. Therefore, on the presumption that the rate of change in the tensile strength is correlative to the number of the particles of additive per unit of powder surface area, a conversion of the additive content n into the number of the particles of additive per unit of powder surface area was done by Eq. (3),

$$N = \frac{n / \frac{\pi}{6} \rho_a d_a^3}{(1 - n) \times 6 / \rho_p d_p}$$

The calculation gave no regard to the particle size distributions of the additive or of the powder but was based on the mean particle diameters d_p and d_a. Furthermore, the tensile strength σ_z was normalized as follows so as to
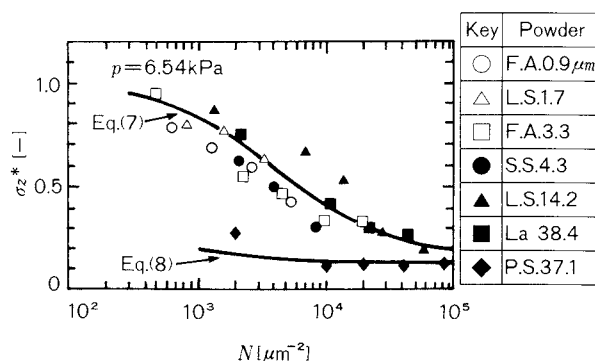
32

Fig. 5 Relationship between $\sigma_z{}^*$ and number of additives per unit powder surface area

Fig. 6 Evaluation of experimental constants a and b of Eq. (5)

simplify the comparison of the tendencies of its changes:

$$\sigma_z{}^* = \sigma_z / \sigma_{zn=0} \tag{4}$$

Using the above process, the relationship in **Fig. 3** is reduced to the relationship between $\sigma_z{}^*$ and N in **Fig. 5**. With the exception that $\sigma_z{}^*$ is distinctly lower in potato starch than in the other powders, it is seen that, although the data shows some scatter, $\sigma_z{}^*$ can be reduced to a one single curve. This curve indicates that $\sigma_z{}^* = 1$ for $N = 0$, and it shows that the decrease in $\sigma_z{}^*$ gradually develops a tendency to level off as N is increased. An approximation of this curve was done by the equation,

$$1 - \sigma_z{}^* = \frac{abN}{1 + aN} \tag{5}$$

To examine the relationship between Eq. (5) and the experimental data, Eq. (5) was transformed into Eq. (6) so that the relationship between $N/(1 - \sigma_z{}^*)$ and N was plotted in a diagram in **Fig. 6**.

$$\frac{N}{1 - \sigma_z{}^*} = \frac{1}{ab} + \frac{N}{b} \tag{6}$$

From **Fig. 6** it is seen that, independent of the pre-compressive stress and except for potato starch, the data of the powders, can be reduced to one straight line. Although the coefficients a and b are different, the data with respect to potato starch can also be represented by Eq. (5). Accordingly, an experimental equation,

$$\sigma_z{}^* = 0.18 + \frac{0.824}{1 + (2.63 \times 10^{-4})N} \tag{7}$$
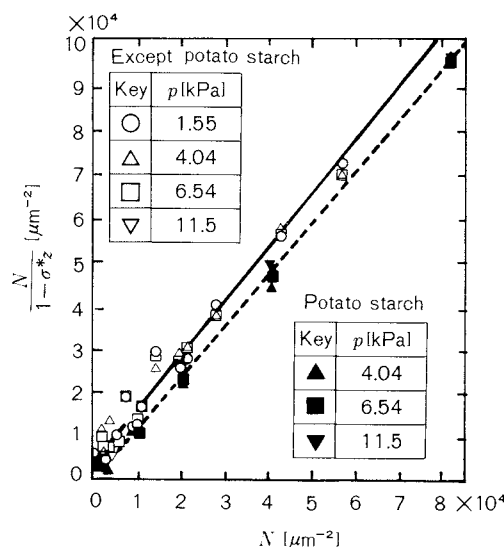
$$(a = 2.63 \times 10^{-4} \mu m^2, b = 0.824)$$

can be proposed for powders other than potato starch. Also, an experimental equation,

$$\sigma_z{}^* = 0.14 + \frac{0.859}{1 + (1.53 \times 10^{-2})N} \tag{8}$$

$$(a = 1.53 \times 10^{-2} \mu m^2, b = 0.859)$$

can be proposed for potato starch. The coefficients a and b were determined by the least-squares method from the data in **Fig. 6**. **Figure 5** shows the results of the calculations using the above experimental equations. It was ascertained that Eqs. (7) and (8) were in fair agreement with the experimental data. From the above processing, it has become clear that the changes in the tensile strength that occur when an ultra-fine powder additive is used can be experimentally represented by Eq. (5).

A study of the relationship between the porosity ϵ of the powder bed and the additive content n in five types of specimen powders has made it clear that, as shown in **Fig. 4**, there is a distinct difference between the inorganic powders (fused alumina, silica sand, and limestone) and the organic powders (lactose and potato starch). With respect to the inorganic powders, the porosity scarcely changes when the additive content is under 0.01, but the porosity of each powder tends to increase as the additive is increased to a content above 0.01. On the other hand, the porosity of each of the organic powders decreases to a mini-

mum at a certain additive content. To make the comparison of this data easier, the porosities were normalized in the same manner as Eq. (4), by Eq. (9),

$$\epsilon^* = \epsilon / \epsilon_{n=0} \qquad (9)$$

Figure 7 shows the resultant data into which data obtained for different pre-compressive stresses has also been incorporated. With respect to the values of ϵ^* of the inorganic powders for each additive content, their respective mean values have been plotted. The ranges of the data are shown by the standard deviation σ in **Fig. 7**. Concerned with the inorganic powders, it can be seen from **Fig. 7** that ϵ^* can be represented by the additive content n rather than by the pre-compressive stress.
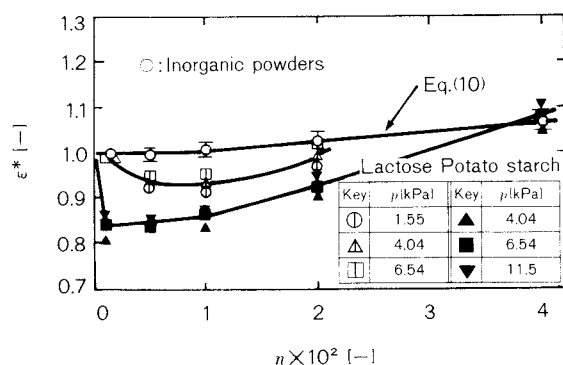
The pre-compressive stress is not observed to influence the data on the organic powders to any significant degree, and ϵ^* can be processed separately so as to be represented by a single curve for each powder. An approximation of the data of the inorganic powders was made by calculating an experimental equation,

$$\epsilon^* = \begin{cases} 1 & (n \leqq 0.01) \\ 1 + 2.27\,(n - 0.01) & (n \geqq 0.01) \end{cases} \qquad (10)$$

This Eq. (10) plotted in **Fig. 7** agrees well with the experimental data.

The relationships of the additive content n with the tensile strength σ_z^* and the porosity ϵ^* of the powder bed have been reviewed, respectively. Next a study of the relationships between σ_z^* and ϵ^*, shown in **Figs. 8 ~ 10**, is done. In these figures, the solid lines represent the calculation of the results obtained by Eqs. (3), (7), (8), and (10), while ϵ^* of the organic powders represents the mean values of ϵ^* at each additive content shown in **Fig. 7**. The calculated values of (ϵ^*, σ_z^*) for each additive content are also shown in **Figs. 8 ~ 10**. From **Fig. 8 ~ 10**, it is seen that, although there are small differences between the data and the experimental equations, they are in close agreement with respect to the representation of the changes in the tendencies of σ_z^* and ϵ^*. This
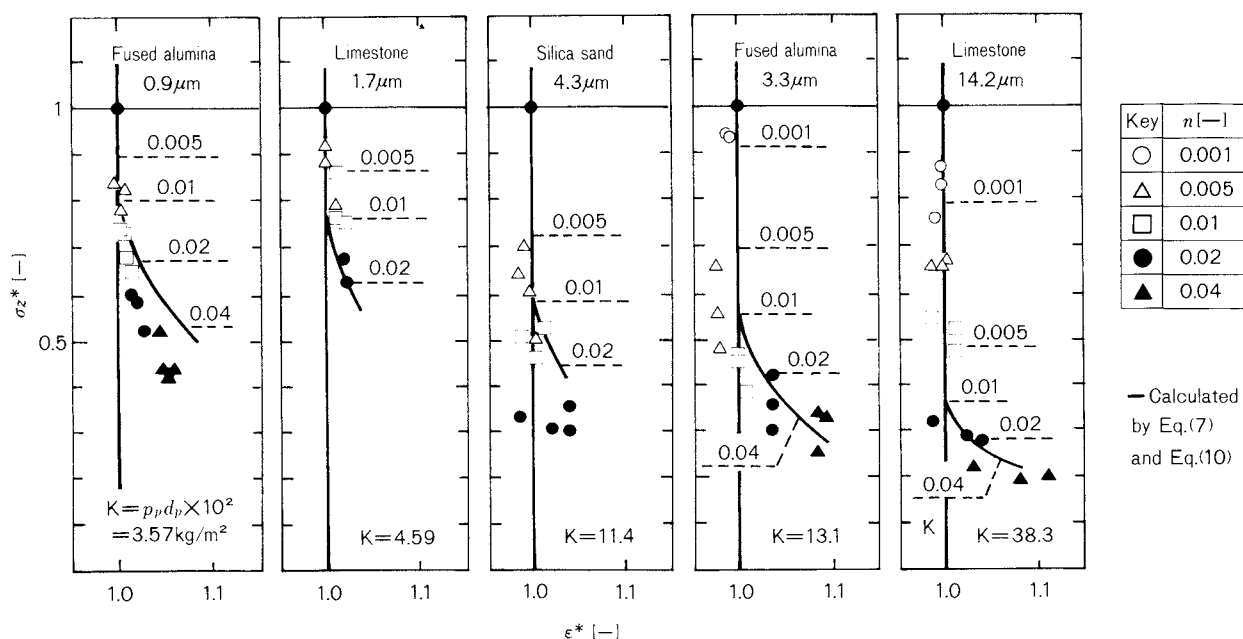

Fig. 7 Relationship between ϵ^* and additive content

Fig. 8 Relationship between σ_z^* and ϵ^* (Inorganic powders) (I: $n \leqq 0.01$, II: $0.01 \leqq n$)
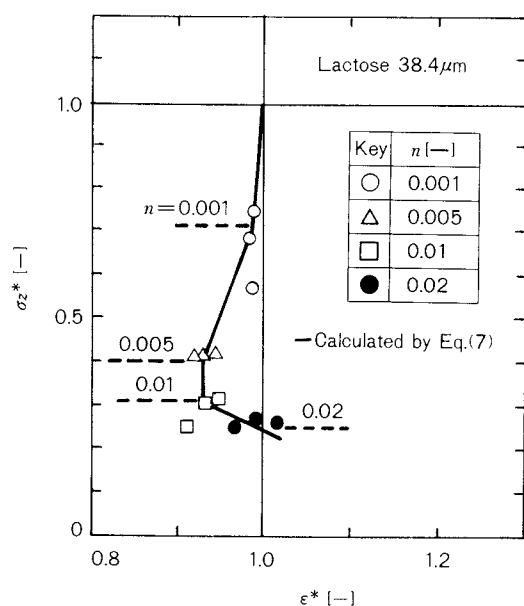
Fig. 9 Relationship between σ_z^*
and ϵ^* (lactose) (I: $n \leq 0.005$,
II: $0.005 \leq n \leq 0.01$, III: $0.01 \leq n$)

Fig. 10 Relationship between σ_z^* and
ϵ^* (Potato starch) (I: $n \leq 0.001$,
II: $0.001 \leq n \leq 0.01$, III: $0.01 \leq n$)

proves that the foregoing experimental equations are applicable to the evaluation of the data in Figs. 8 ～ 10.

4. Discussion

First, consider the scattering of σ_z^* and ϵ^* in Figs. 8 ～ 10. In reviewing the data in Figs. 8 ～ 10, the influence of the additive content n, disregarded the pre-compressive stress p, has been considered so far. Now, reconsider the effect of the pre-compressive stress p on σ_z^* and ϵ^*. Figure 11 shows a portion of the results from the reconsideration of Figs. 8～10. From Fig. 11, it is seen that where the applied pre-compressive stress is relatively large, limestone 14.2 μm and lactose show only a slightly larger increase in ϵ^* as the additive content is increased. On the other hand, fused alumina powder shows that σ_z^* is influenced by the pre-compressive stress. Much of the scatter that the data shows when it is processed by the additive contents only, as shown in Figs. 8 ～ 10, is due to the influence of the pre-compressive stress p, which is large enough not to be entirely disregarded, as shown in Fig. 11. The above-mentioned influence of the pre-compressive stress is a matter of interest when the manner in which additives act is studied. This remains to be studied further in the future. However, we will proceed
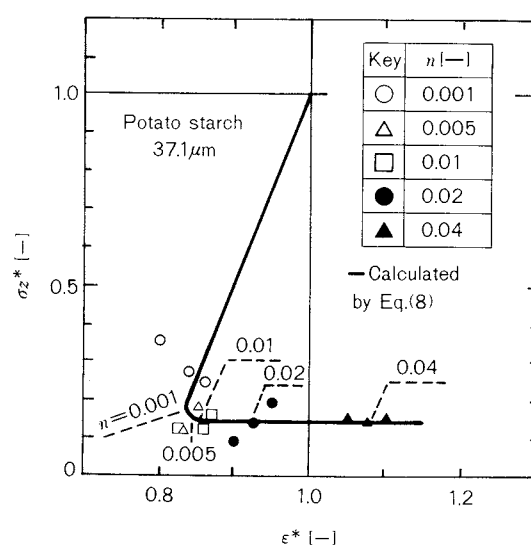
with our studies in this paper without considering the influence of the pre-compressive stress, because of the limited range in which the pre-compressive stress was used in the experiments. Unfortunately, experimental data and data for ascertaining accuracy are lacking in Fig. 11.

As mentioned in the introduction, papers dealing with the effect of additives on tensile strength are extremely limited. Only the results of Hayashi et al.[1] relating to potato starch are adequate. Processing their data[1] in the same manner as was done for Figs. 8 ～ 10, in Fig. 12 is obtained. The experiments were carried out at a constant pre-compressive stress p of 9.99 kPa. This was done using colloidal silica as the additive (d_a = 0.012 μm, AEROSIL 200, product of Nihon Aerosil Co.), which differs in particle diameter from the additive in this paper. In Fig. 12, the solid line represents an experimental equation in which the data was processed using Eq. (5). The experimental equation was,

$$\sigma_z^* = 0.13 + \frac{0.869}{1 + (1.05 \times 10^{-3})N} \qquad (11)$$

$(a = 1.05 \times 10^{-3} \mu m^2, b = 0.869)$

Measured values were used to represent ϵ^* in Fig. 12. The close agreement between the calculated and measured values in this figure suggests the general applicability of the present process.

Fig. 11 Effect of pre-compressive stress on relationship between σ_z^* and ϵ^*
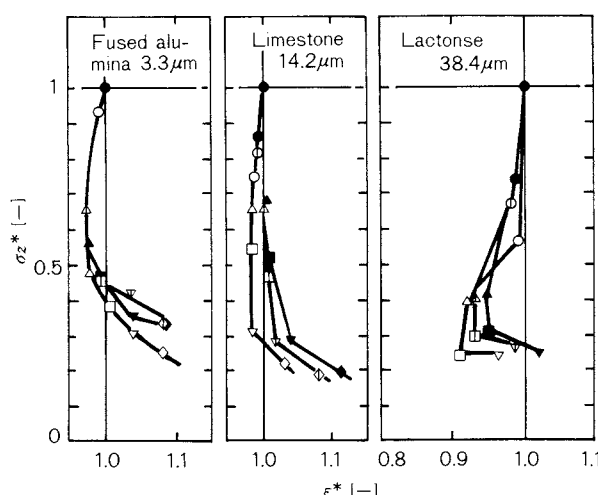
n \ p	1.55kPa	4.04kPa	6.54kPa
0.001	○	◐	●
0.005	△	◭	▲
0.01	□	◫	■
0.02	▽	▼	▼
0.04	◇	◈	◆

The manner in which ultra-fine powder additives act will now be studied by applying the process used in **Figs. 8 ∼ 10** and **Fig. 12**. Since no relevant data is available on inorganic powders, except that in this paper, our study is based on the data obtained in this paper. As shown in **Fig. 8**, the data can be divided into two steps by the additive content as follows:

Step I $(n \leq 0.01)$: $\epsilon^* = 1$, $\sigma_z^* \searrow$

Step II $(n \geq 0.01)$: $\epsilon^* \nearrow$, $\sigma_z^* \searrow$

From a comparison of the differences between different powder materials, it is found that σ_z^* at an additive content n of 0.01 tends to be smaller when K ($=\rho_p d_p \times 10^2$) is larger. In other words, the larger $\rho_p \cdot d_p$ is, the larger the range in which σ_z^* is, assuming Step I.

With respect to organic powder materials, the data, into which the results of Hayashi et al. has been incorporated, can be divided into the following three steps:

Step I $\quad \epsilon^* \searrow \quad\quad$, $\sigma_z^* \searrow$

Step II $\quad \epsilon^* = $ const, $\sigma_z^* \searrow$

Step III $\quad \epsilon^* \nearrow \quad\quad$, $\sigma_z^* \searrow$
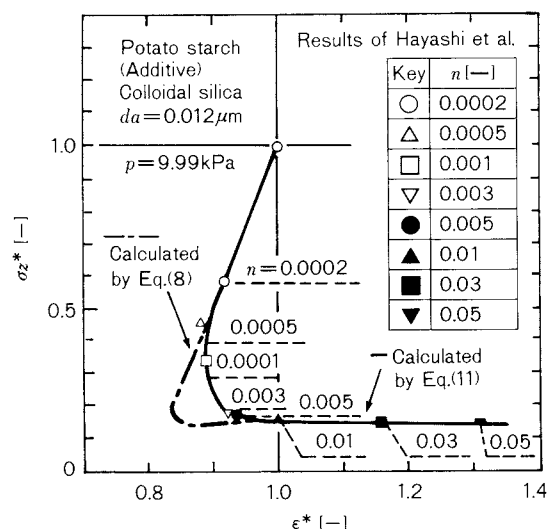
Fig. 12 Relationship between σ_z^* and ϵ^* of experimental results of Hayashi et al.[1]

The data of the lactose shown in **Fig. 9** obtained at an additive content n under 0.005 comes under Step I, that obtained at n within the range of 0.005 ∼ 0.01 comes under Step II, and that obtained at n above 0.01 comes under Step III. As shown in **Fig. 10**, the data on potato starch obtained by the authors comes under Step I for an additive content n under 0.001, under Step II for n within the range of 0.001 ∼ 0.01, and under Step III for n above 0.01. The data obtained by Hayashi et al., as shown in **Fig. 12**, comes under Step I for an additive content n under 0.0005, under Step II for n within the range of 0.0005 ∼ 0.003, and under Step III for n above 0.003.

The characteristics that the organic powders exhibit in each step are as follows: In Step I, as shown by the decrease of σ_z^* more rapidly than of ϵ^*, the additive is seen to have a dominant influence upon the decrease in tensile strength of the powder bed. On the other hand, in Step III, as shown by the increase of ϵ^*, which occurs at a conspiciously higher rate in the case of potato starch than the decrease in σ_z^*, the additive is seen to act dominantly toward the increase in the porosity of the powder bed. Step II is a transition region from Step I to III, where ϵ^* changes only slightly while σ_z^* decreases.

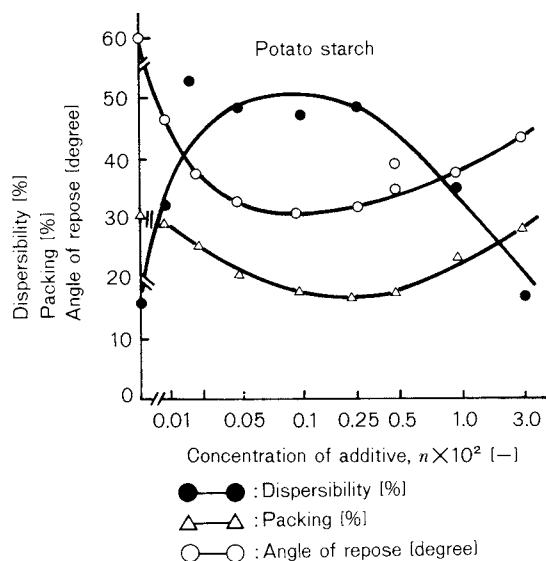We have now characterized the manner in which an additive acts on the tensile test data

36

Fig. 13 Effect of additive on mechanical
properties of potato starch powder
reported by Hayashi et al.[1]

Fig. 14 Relationship between Flow Factor
(FF) and additive content reported
by P. York[10]

of both inorganic and organic powders by the
processing method using the data in **Figs. 8** ~
10 and **Fig. 12**. Next, consider the interrela-
tions between the characteristics that have
been observed and the changes in the other
mechanical properties that are caused by ad-
ditives.

Besides the tensile test shown in **Fig. 12**,
the studies of Hayashi et al.[1] were extended
to the effect of an additive on the dispersibili-
ty, compressibility by tapping, and angle of
repose. The results are shown in **Fig. 13**. In
their paper, they state that on the basis of the
tensile test data, they calculated the adhesive
force for one particle using Rumpf's equation[9]
so that they were able to minimize the adhe-
sion force when the concentration of the ad-
ditive was approximately 0.003. Their paper[1]
states that the adhesion force increases before
and after the above-mentioned concentration,
and that these changes in the adhesion formed
a pattern similar to those of the changes in the
mechanical properties of the powder material,
as shown in **Fig. 13**.

The changes in the mechanical properties
of powder caused by an additive, shown in
Fig. 13, are considered to be composed of
three steps: In one step, ($n \leq 0.0005$) the dis-
persibility increases, and both the compressi-
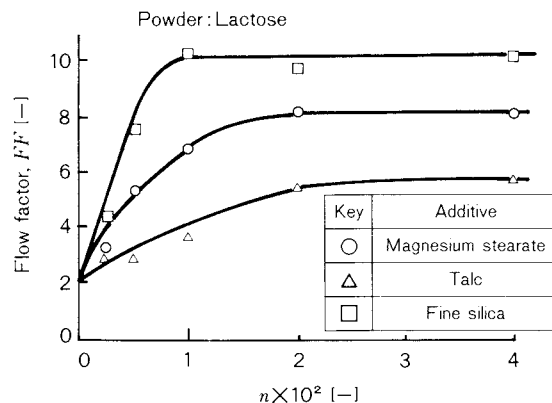bility by tapping and angle of repose decrease

with the concentration of the additive; next,
virtually no change is observed in each of the
three properties ($0.0005 \leq n \leq 0.003$); and in
the third step, ($0.003 \leq n$) the dispersibility
decreases, and both the compressibility by
tapping and angle of repose increase. There-
fore, it is considered impractical to explain the
relationships shown in **Fig. 13** of this paper on
the basis of the observations by Hayashi et al.

However, application of the processing
method that has been proposed by the authors
brings out the correlation of the three steps in
Fig. 13 to the three shown in **Fig. 12**, and it
makes it possible to evaluate the changes in
dispersibility, compressibility by tapping, and
angle of repose in **Fig. 13** on the basis of
Fig. 12.

P. York[10] has reported on his studies re-
garding the relationship between the flow
factor (FF) and the additive content, which
was proposed by A.W. Jenike[2]. **Figure 14**
shows the results reported by York for which
the lactose was used. From this figure, it is
seen that FF increases with the addition of
the additive until the additive content reaches
0.01, and then develops a tendency in which
the additive contents level off above 0.01. In
Fig. 9, on the other hand, the additive content
of 0.01 corresponds to a transition point of an
organic powder from Step II to Step III in the
observations by the authors. This correspond-
ence also suggests the applicability of the char-
acterization method presented in this paper to
the evaluation of changes in FF. From the
above-mentioned observations, the characteri-

zation of the manner in which additives act, which this paper deals with using **Figs. 8 ~ 10** and **Fig. 12**, is also considered to be important in the evaluation of changes in other mechanical properties caused by additives.

5. Conclusion

Our observations on tensile tests, to which powder beds containing colloidal silica as an additive were subjected, are summarized as follows:

1) The changes in the tensile strength of a powder bed containing an additive are experimentally processed by the number of the particles of the additive per unit of powder surface area, and the changes in the porosity of the powder bed are processed by the additive content based on mass.

2) The relationship between the tensile strength and the porosity of a power bed containing an additive, for which 5 kinds of powders were subjected to the experiments in this paper, is characterized in two steps for inorganic powders (fused alumina powder, silica sand, and limestone) and in three steps for organic powders (lactose and potato starch).

3) The above-mentioned characterization has also been found to be important in evaluating the effect of an additive on other mechanical properties of powders.

Nomenclature

a : experimental constant of Eq. (5) $[\mu m^2]$
b : experimental constant of Eq. (5) $[-]$
b_n : experimental constant of Eq. (1) $[-]$
d_a : mean particle diameter of additive $[\mu m]$
d_p : mean particle diameter of powder $[\mu m]$
K : $\rho_p \cdot d_p \times 10^2$ $[kg/m^2]$
k_{1n} : experimental constant of Eq. (1) $[kPa]$
N : number of additives per unit powder surface are $[\mu m^{-2}]$
n : additive weight content $[-]$
p : pre-compressive stress $[kPa]$

ϵ : porosity of powder bed $[-]$
$\epsilon_{n=0}$: porosity of powder bed at $n=0$ $[-]$
ϵ^* : $\epsilon/\epsilon_{n=0}$ $[-]$
ρ_a : true additive density $[kg/m^3]$
ρ_n : apparent particle density $[kg/m^3]$
ρ_p : true particle density $[kg/m^3]$
σ_z : tensile strength of powder bed $[kPa]$
$\sigma_{zn=0}$: tensile strength of powder bed at $n=0$ $[kPa]$
σ_z^* : $\sigma_z/\sigma_{zn=0}$ $[-]$

References

1) Hayashi, H., T. Kasano and K. Suhara: *Yakuzaigaku,* **39**, 187 (1979).
2) Jenike, A.W.: Bull. of the Univ. of Utah, No. 108 (1961).
3) Jimbo, G., S. Asakawa, N. Soga, S. Hatano and T. Uchiyama: *J. Soc. Materials Sci., Japan,* **18**, 541 (1969).
4) Jimbo, G. and R. Yamazaki: Preprints of European Symposium Particle Technology 1980, p. 1064, Amsterdam (1980).
5) Naito, M. and G. Jimbo: *Funsai (The Micromeritics),* No. 29, 104 (1985).
6) Naito, M., N. Kato, G. Jimbo and T. Yokoyama: *J. Soc. Powder Technol., Japan,* **23**, 500 (1986).
7) Naito, M., S. Usuda and G. Jimbo: *Kagaku Kogaku Ronbunshu,* **12**, 495 (1986).
8) Nash, J.H., G.G Leiter and A.P. Johnson: *I & EC, Product Research and Development,* **4**, 140 (1965).
9) Rumpf, H.: *Chem. Ing. Tech.,* **42**, 538 (1970).
10) York, P.: *Powder Technol.,* **11**, 197 (1975).

Measurement of the Dynamic Physical Properties of Solid Particles by a Rotary Shear Tester with a Conical Rotor[†]

Munetake Satoh, Takashi Fujimoto and Kei Miyanami
*Department of Chemical Engineering University of Osaka Prefecture**

Abstract

The transitional torque characteristics of a particle bed have been measured by using a rotary shear tester which is basically a Couette type rheometer. The torque measured on the rotor shaft under constant operating conditions showed the maximum value to be at the initial period. It then decreased exponentially with changes in the packed state of the particle bed around the shearing surface during rotation. The magnitude of the decay coefficient k of the torque indicated some of the dynamic physical properties of the solid particles, such as flowability and surface condition. It was found that the conical rotor was suitable for the more sensitive and accurate measurement of the change in the torque. A dimensionless parameter k/N_R, where N_R is the rotor speed, was introduced and compared with the other flowability indices. It was experimentally shown that this parameter was more sensitive in detecting slight changes in the physical properties of the particles during mixing and coating operations. The coating processes in two different types of mixers and the coating state of the binary mixture were evaluated based on this parameter.

1. Introduction

The flowability characteristics of powder materials are influenced not only by the primary properties of the particles, such as diameter, true density, and physicochemical structure, etc., but also by the inter/exterrelationship among the particles, such as the state of packing and void, size distribution, cohesion force, surface conditions, internal/external friction coefficient, how external forces act thereupon, etc. In addition, the evaluation of flowability may vary according to the method of measurement.

A number of testing methods have been proposed and used to evaluate the flowability. One is the measurement of the internal friction coefficient by methods based on triaxial compression, single shear, ring shear, or by using a rotational double cylinder. Other methods are based on the measurement of the cohesive force, the angle of sliding friction and the flowability index[1,2], the latter including measurements of the angle of repose, the spatula angle, and compressibility, etc. Among others, the rotational double cylinder method has been the subject of study as a relatively convenient method for determining the quasi-static and dynamic frictional characteristics and the rheological properties of solid particles[3~11].

In this paper, the design of the rotor of the rotary shear tester for the powder bed is studied to find the most sensitive shape for detecting the characteristics of the transitional shearing torque with good reproducibility. A decay coefficient of the torque curve as a function of the shearing rate is proposed as a new characteristic parameter to express a dynamic physical property of solid particles. The transitional torque curves for several kinds of solid

---

particles and a mixture of an inorganic particle and a wax powder are measured by using a conical rotor. It has been shown that the new parameter is almost equivalent to the compressibility and is more sensitive to the detection of slight changes in the physical properties of a mixture.

2. Experimental Equipment and Method

Figure 1 shows a schematic diagram of the rotary shear tester used in this work. The tester consists of a cylindrical vessel (ID: 12.5 cm) and round cornered bottom), a rotor placed coaxially within the vessel, and an adjustable speed motor (from 0 to a maximum of 11.7 rps). Three different shapes of rotors were tested, namely, a cylinder, a disk and an inverted cone, with 2 mm-pitched V-shaped cuts on the external surface of each one of them, as
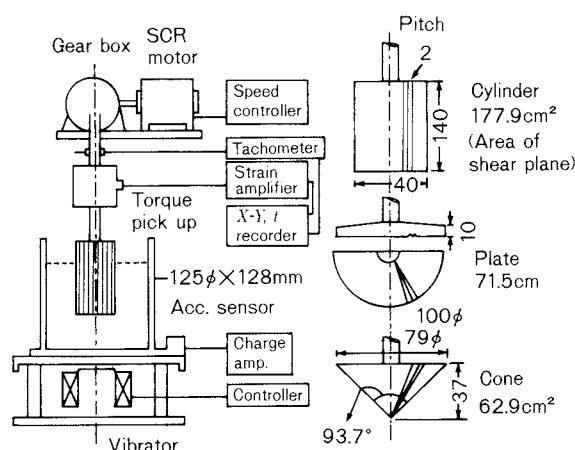

Fig. 1 Schematic diagram of rotary shear tester and rotors

shown in the same figure. The rotational torque was measured by a strain gauge type torque-pickup (capacity: 4.9 Nm) placed between the rotor and the drive shaft.

Table 1 shows the physical properties of the materials used. The bulk density ρ_b was obtained by tapping the powder in a cylindrical vessel of 100 cm^3 under a 5 mm stroke at 0.8 Hz for 5 minutes. The compressibility C was also obtained by the tapping method, the angle of repose ϕ_r by an injection angle method, and the sliding friction coefficient μ_S by an inclining plate method.

In the experiments, a vessel containing a certain amount of the testing material is mounted on an electromagnetic vibrator and vibrated with an intensity of 2.1 G at 60 Hz. Under these conditions, in which the powder bed appears to be in a fluidized state, the vessel is jacked up to an extent such that the rotor penetrates the bed a prescribed distance. The cylindrical rotor was inserted to a depth of h = 65 mm, the conical rotor down to 37 mm, and the disk rotor a depth of 10 mm.

Once the rotor has been properly placed, the vibration intensity is decreased to 1.35 G at 60 Hz and maintained at this value for 5 minutes with the purpose of setting the conditions for the initial packing state of the powder bed. After this preliminary conditioning, the bed is left at rest for 2 to 3 minutes. Then, the rotor is set in motion at a prescribed speed, and the changing transitional torque is measured continuously until the steady state torque is reached.

Table 1 Physical properties of solid particles tested in this work

Material	Symbol	Average diameter d_P [μm]	Density (true) ρ [kg/m^3]	Density (bulk) ρ_b [kg/m^3]	Compressibility C [−]	Angle of repose ϕ_r [deg]	Coeff. of friction μ_r [−]**
Toyoura sand	TS	200	2550	1630	2.45	34.1	0.679
Zircon sand	Zr	130	4650	2950	3.39	33.0	0.610
Silicon carbide # 46*	SiC 46	360	3240	1680	3.63	33.8	0.651
Silicon carbide # 80*	SiC 80	259	3240	1744	9.98	33.2	0.644
Silicon carbide #120*	SiC 120	130	3240	1652	10.29	37.0	0.641
Silicon carbide #180*	SiC 180	80	3240	1611	15.83	37.2	0.670
Silicon carbide #320*	SiC 320	57	3240	1537	17.50	39.1	0.678
Mica #2000	Mica	4.7	2865	485	49.28	43.0	0.831
Alumina powder	Al$_2$O$_3$	3.8	3980	1767	28.92	46.9	0.827
Calcium carbonate	CaCO$_3$	2.5	2700	1072	33.77	46.9	0.832
Talc	Talc	1 $\sim$ 10	3050	509	35.95	46.8	0.797

*) JIS R 6111, **) sliding friction

3. Experimental Results and Discussion

3. 1 Torque curve and rotor shape

The characteristic curves of the change in the torque with time for two different powders and for the three types of rotors are shown in **Fig. 2.** When using the conical rotor in silicon carbide (#120), the flowability of which is relatively good, the torque showed the maximum value T_1 to be at the start and then gradually decreased until reaching the steady torque T_S. When the disk rotor was used, the maximum value of the torque was several times larger than that of the conical rotor, and it took a long time to reach the steady value. Besides, the disk rotor exhibited an irregular torque curve and a poor reproducibility of T_S. As for the cylindrical rotor, which has been widely used, the torque showed no clear difference between T_1 and T_S and no clear peak either. Rather, the torque increased with time and, in some cases, it was difficult to find a definite value of T_S. The reasons for this behavior may
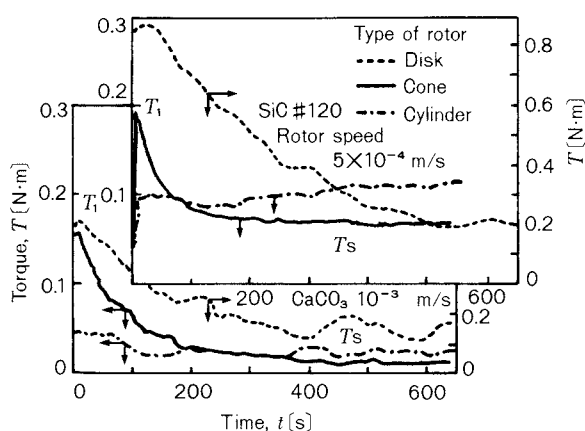
be found in the changing of the local packing state of the particles bed closed to the rotor during rotation. Observing the motion of the particles by using colored tracer particles, it was found that, unlike the cone or disk, the movable regions in the particles bed were formed only at and near the surface of the rotor. On the other hand, the cylindrical rotor was surrounded by flowable regions developing a funnel form.

For calcium carbonate, which is cohesive and has poor flowability although changes in the torque showed a behavior similar to that in silicon carbide, the steady torque of both disk and cylindrical rotors showed conspicuous cyclic changes such that no definite value could be appropriately assigned to T_S. On the other hand, using a conical rotor, the torque decayed relatively smoothly, and after the experiment it was found that there was no consolidation of the powder bed at or near the rotor.

These results proved the conical rotor to be the most suitable shape for the measurement of the transitional torque.

3. 2 The decay coefficient of torque

Assuming that the torque has its maximum value T_1 at time $t = 0$, and decays continuously until it reaches the steady torque T_S, the following expression was used to fit the experimental data,

$$T = (T_1 - T_S) \cdot \exp(-kt) + T_S \qquad (1)$$

The exponent k can thus be evaluated from the slope of a semilog plot of torque T versus time t.

Figure 3 shows the relationship between the torque ratio $(T - T_S)/(T_1 - T_S)$ and the time t for coarse and fine materials using the conical

Fig. 2 Effect of rotor shape on the torque curve
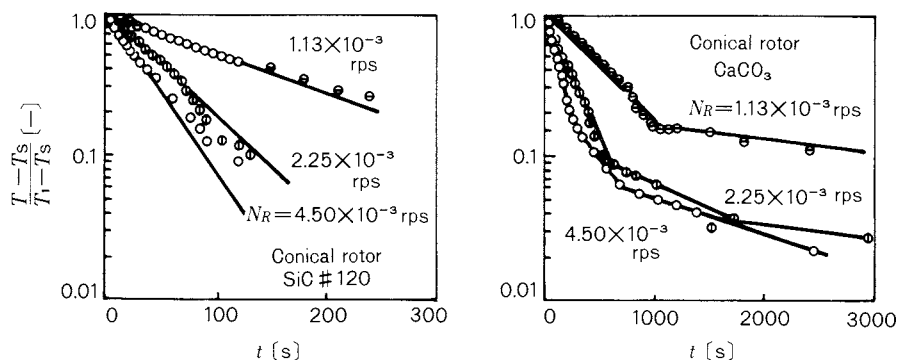
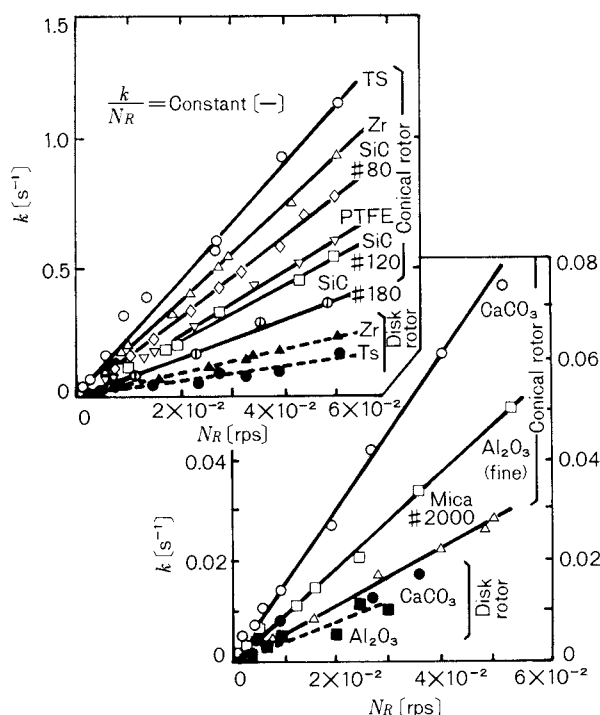Fig. 3 Semilogarithmic plotting of the experimental data

Fig. 4 Decay coefficient of torque

rotor at different rotational speed, N_R. It is seen that, in the case of the coarse powder, T approximately follows Eq. (1). However, the decreases of T in the fine powder take place in two or more steps. For both materials, the slope k of the curve at the initial stage increases with the rotational speed N_R.

The relationship of k and N_R for a number of different powders is shown in **Fig. 4**. It was found that k is directly proportional to N_R and the ratio, k/N_R represents a peculiar value for each material tested. The value of k/N_R turned out to be large for relatively large-size particles, i.e., particles which can be easily replaced and rearranged the region of the surface of the rotor so that the torque can reach a steady state in a relatively short time. On the other hand, the value of k/N_R is small for fine powders which are more difficult to disperse into single particles because of their tendency to cohere and form agglomerates. Therefore, the parameter k/N_R gives information about the flowability and packing characteristics of a powder material[6,7]. k and N_R also showed a linear relationship when the disk rotor was used, but in some cases the ratio k/N_R failed to show clear differences among different materials. For this reason, only the results corre-

sponding to the conical rotor will be discussed here.

3. 3 Comparison of k/N_R with other characteristic values

Average particle diameter $\overline{d_P}$: **Figure 5** shows the relationship between the value of k/N_R and the average particles diameter $\overline{d_P}$ of silicon carbide SiC. k/N_R increases with $\overline{d_P}$. It is clear that the flowability of powders increases as the particle size increases. However, k/N_R is not more sensitive to particle size for large sized particles (more than 250 μm), as shown in the figure.

Coefficient of sliding friction μ_S : The relationship between k/N_R and the friction coefficient μ_S (measured by a tilting plate method) for various powders is shown in **Fig. 6**. For
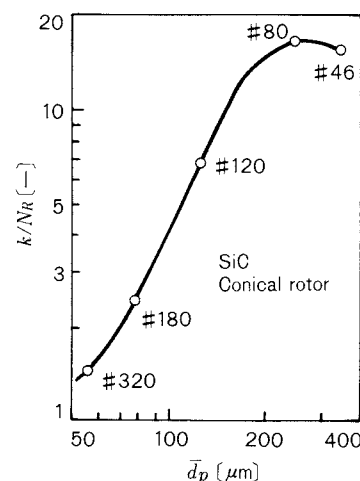

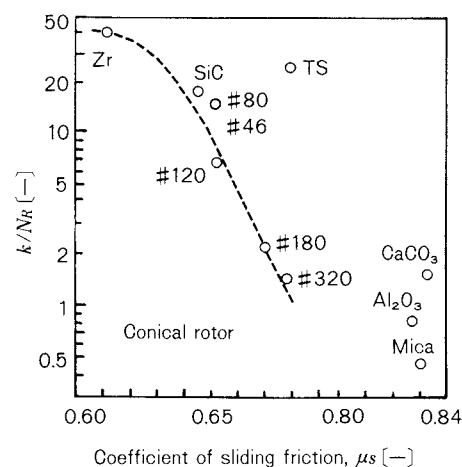Fig. 5 Relationship between parameter k/N_R and average diameter d_P

Coefficient of sliding friction, μ_S [—]

Fig. 6 Relationship between parameter k/N_R and coefficient of sliding friction μ_S
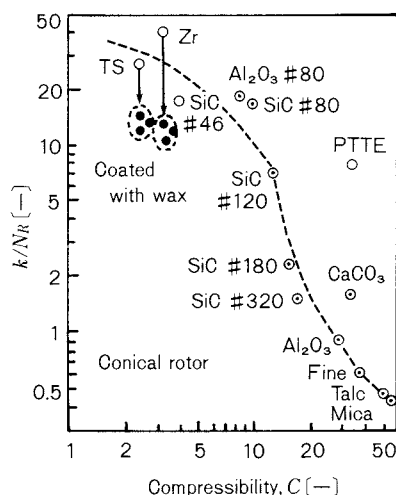
Fig. 7 Relationship between parameter k/N_R and compressibility C

large particle sizes, as μ_S increases k/N_R decreases, that is the flowability becomes lower. It is also seen that in experiments with fine powders, although there was no appreciable change in μ_S, k/N_R showed significant differences. Since k/N_R exhibits a wide variation range despite the narrow variation range of μ_S, k/N_R is considered to be effective for detecting minute changes in physical properties.

Compressibility C: The relationship between the parameter k/N_R and the compressibility C (measured by a tapping method in a 100 mℓ cylindrical vessel) is shown in **Fig. 7**. As for silicon carbide, C increases with a decrease in particle diameter, but the changes in C were within a limited range compared with those of k/N_R. For fine powders, such as calcium carbonate, alumina, talc and mica, C was so likely to be influenced by the measuring conditions that C varied within a wide range; however, k/N_R was obtained with a relatively good reproducibility.

4. Binary Powder Mixtures and k/N_R

The parameter k/N_R was used to characterize the mixtures of inorganic powders with small amounts of a synthetic wax having a relatively low melting point. In the mixing process, the coarse inorganic powders are coated by the fine wax powders. As a result, the physical properties and surface condition of the powders are modified. Using the subscripts O and M to designate before and after mixing, respectively, a dimensionless parameter, K is defined as,

$$K = (k/N_R)_M / (k/N_R)_O \qquad (2)$$

K is used to account for the changes in physical properties that occurred throughout the mixing process.

4. 1 Influences of mixer type and operating conditions

A V-type mixer with an effective capacity of 5 ℓ, and a high speed stirred type mixer (1.5 ℓ) with a device to vibrate the vessel were used. The coating wax used consisted of glycerol-monostearate in powder form ($\overline{d_P}$ = 390 μm, m.p. = 60.5 ± 2.5°C).

4. 1. 1 V-type mixer

It is known that in this type of mixer, the time required for complete mixing is about 6.5 minutes for relatively flowable powders.

Figure 8 shows the variation of K with time for three different mixtures (the rotational speed of the mixer vessel for all runs: 1 rps). In the mixing of 1.5 g of wax with 1.5 kg of zircon sand (having the highest density amont the materials tested), K decreased sharply during the first 5 minutes, and thereafter it maintained a constant value of about 0.43 (see ● in the figure). With Toyoura and (0.3 g of wax mixed with 1.4 kg), K showed no noticeable change even after 30 minutes of mixing (see ○ in the figure). A similar trend was shown by a glass powder, the physical properties of which were almost equal to those of the Toyoura sand. In the mixtures of silicon
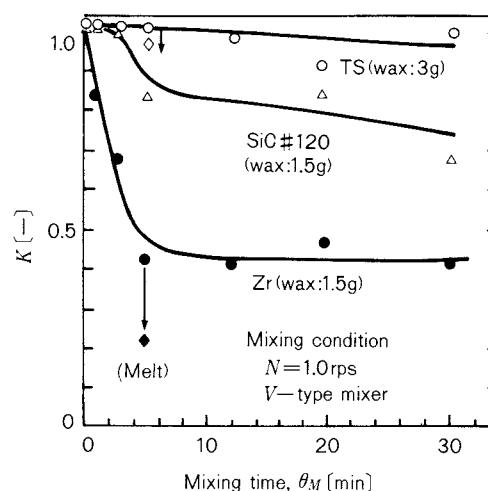

Fig. 8 Relationship between parameter ratio K and mixing time θ_M (V type mixer)

carbide (1.5 g of wax mixed with 1.0 kg), K showed an intermediate behavior between those of zircon sand and Toyoura sand (see △ in the figure). These results suggest that the shearing effect between particles resulting from their circulating flow in the mixer vessel varies depending on the density and friction coefficient of the material. During mixing, the temperature of the powder bed was constant (20 ~ 25°C), and the wax remained in a granular form even after 30 minutes of mixing.

To examine the effect of the melting of wax on K, the mixed samples were placed in a thermostatic vessel for 2 to 3 hours at a temperature above the melting point of the wax. In these conditions, the melted wax adhered onto the particles surface. After cooling, K was measured again. The symbols ◇ and ◆ in **Fig. 8** represent zircon sand and Toyoura sand, respectively. K showed a further decrease in the zircon sand but only a slight decrease in the Toyoura sand. It was presumed that the degree of adhesion of the wax differed between the two samples.

4. 1. 2 High speed stirred type mixer[12]

The mixing vessel used here was vibrated at a frequency of 33.3 Hz in order to improve the flowability of the powder bed and to eliminate the stagnant zone in the mixer. It has been shown that the mixing of coarse particles was complete in the first period of 3 ~ 4 minutes. The final degree of mixing was found to be approximately equal to the degree of mixing attainable in a V-type mixer.

The wax powder was added while the vessel was vibrating, and the mixture was stirred by a knife-like impeller rotating at 16.7 rps.

Figure 9 shows the variations in the mixing torque T, the parameter k/N_R and the temperature of the mixture with time.

When using zircon sand (1.5 kg), the torque decreased immediately after the addition of the wax (0.25 g) attaining a steady-state value in about 3 minutes. The temperature of the mixture rose to close to the melting point of the wax in about 27 minutes. As a result of the increased adhesion by the softened wax, the torque increased slightly. On the other hand, the decreasing tendency of k/N_R with time continued for up to 25 minutes.
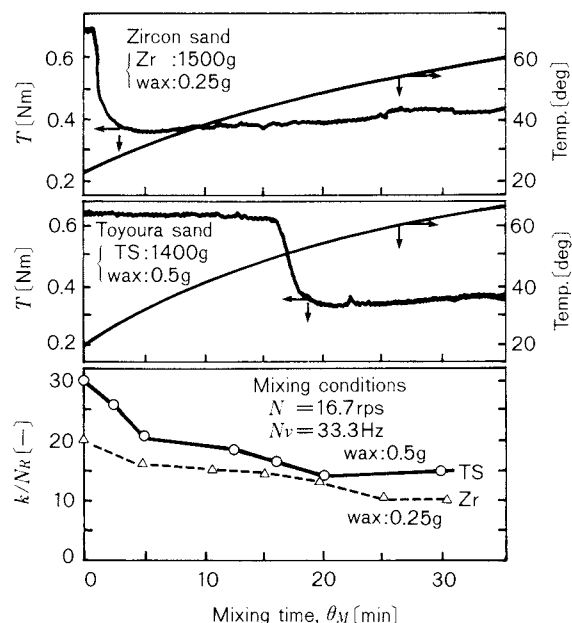
When Toyoura sand (1.4 kg) was mixed with

Fig. 9 Coating process of particles with wax. Changing of torque, temperature and parameter k/N_R (high speed mixer)

the wax (0.5 g), the temperature also rose markedly from the beginning, but the torque did not change until 16 minutes after the beginning of mixing. At this point, the torque decreased sharply and became steady. k/N_R decreased from the beginning of mixing, at room temperature, until the temperature reached the melting point and then attained a constant value of steady state.

According to these experimental results, the mixing mechanism of the binary powders with a coating process is estimated. In the first stage, a rearrangement of the relative positions of sand and wax particles takes place, and as mixing proceeds, the particles of wax are ground and melt as a result of the heat generated by interparticle friction. The melted wax adheres to the surface of the inorganic particles which thus become coated. It was observed that the color of the mixture changed from yellowish brown to dark brown, which proves that the coating process is occurring within the mixer. The compressibility C was almost the same before and after coating, as shown in **Fig. 7** enclosed within dotted lines. On the other hand, k/N_R showed clearer changes, thus reflecting the differences in flowability caused by the modification of the surface condition of the particles.
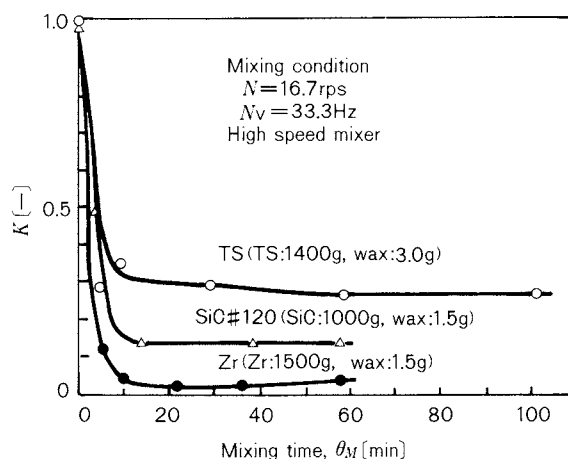
Fig. 10 Relationship between parameter ratio K and mixing time θ_M (high speed mixer)

Fig. 11 Effect of wax quantity on the coated state

Figure 10 shows the relationship between K and the mixing time θ_M. K decreased gradually for each material in about 10 minutes. In every case, the value of K was smaller than that obtained with the V-type mixer. These results show that the shearing force exerted by the impeller and the interparticle friction effect enhance a remarkable change in the surface condition.

4. 2 Effect of the amount of wax on the parameter K

The effect of the amount of coating agent on the parameter K was investigated by adding different amounts of wax to silicon carbide (#120) in the high speed stirred type mixer. In the experiments, 1 kg of silicon carbide was mixed within the weight range of wax of 0.1 to 3.0 g, at a vibration frequency of 33.3 Hz and an impeller velocity of 16.7 rps, during a period of 40 minutes. The mixture was maintained at a temperature above the melting point of the wax and then gradually cooled to the room temperature. K decreased as the amount of wax increased and attained a constant value for concentrations of wax greater than 1.5 g/kg., as shown in **Fig. 11**.

The cosine of the contact angle β, which was determined by a penetration rate method using acetone, is also shown in the same figure. It is seen that the changes of $\cos\beta$ and those of K show the same trend. In this figure, the decay coefficient of torque measured by using a cylindrical rotor[6,7] have also been plotted. The results for the mixtures of glass:oleic-acid
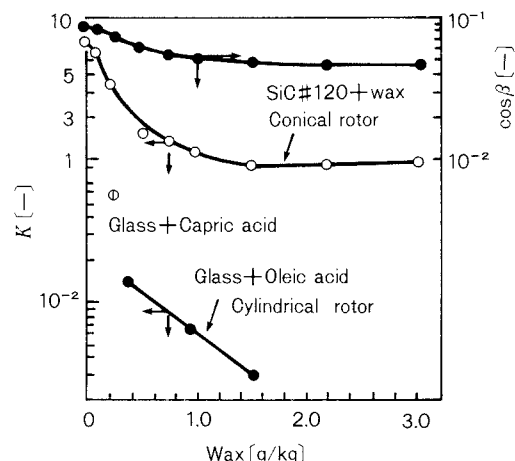
and glass:capric-acid show that K decreases as the amount of the oleic/capric-acid is increased. This trend is in agreement with the results of the present experiments.

5. Conclusion

The dynamic physical properties of solid particles were evaluated in a rotary shear tester by measuring the changes in the torque with time. Three types of rotors were compared, and the conical rotor was found to be the most sensitive in detecting the characteristics of the transitional torque, the decay of which was approximated by an exponential function. A dimentionless decay coefficient k/N_R intimately related to the flowability of the powder, was proved to be effective in detecting minute changes in the physical properties of the solid particles. This parameter was also shown to be useful in the following up of the coating process of inorganic powders by a wax. It also made clear the influence of the mixer type, i.e. difference in mixing mechanisms, on the coating state of the mixture. Furthermore, the change in k/N_R was related to the change in the contact angle of the solid particles.

Nomenclature

C	: compressibility	[−]
$\overline{d_P}$	: average particles diameter	[μm]
K	: coefficient defined by Eq. (2)	[−]
k	: rate constant	[s^{-1}]
N_R	: rotational speed of rotor	[rps]
N_V	: frequency of mixer vessel	[Hz]
T	: agitating torque	[Nm]

T_i	:	maximum torque	[Nm]
T_S	:	torque at steady state	[Nm]
t	:	time	[s]
β	:	contact angle	[deg]
θ_M	:	mixing time	[s]
μ_S	:	coefficient of sliding friction	[−]
ρ	:	true density of particle	[kg/m³]
ρ_b	:	bulk density of particles bed	[kg/m³]
ϕ_r	:	angle of repose	[deg]

References

1) Carr, R.L.: *Chem. Eng., Jan.,* **18**, 163 (1965).
2) Yokoyama, T. and K. Urayama: *J. Res. Assoc. Powder Tech. Japan,* **6**, 264 (1969).
3) Benaric, M.M.: *British J. Appl. Phys.,* **12**, 514 (1961).
4) Shimizu, K. and K. Yashiro: *Funtai Kougaku,* **4**, 283 (1969).
5) Shimizu, K. and K. Yashiro: *J. Soc. Materials Science, Japan,* **18**, 505 (1963).
6) Taneya, S.: *Jap. Appl. Phys.,* **2**, 728 (1963).
7) Taneya, S.: *Ouyou Buturi (Appl. Phys.),* **33**, 887 (1964).
8) Kuno, Y.: *"Symposium of Powder Technology, Soc. of Powder Metallurgy"* (preprint), **12**, (1965).
9) Arakawa, M.: *J. Soc. Materials Science, Japan,* **20**, 776 (1971).
10) Terashita, K., K. Miyanami, T. Yano and S. Uno: *J. Soc. Powder Tech., Japan,* **16**, 394 (1979).
11) Terashita, K., K. Miyanami and T. Yano: *Ibid.,* **16**, 406 (1979).
12) Satoh, M., Y. Deguchi, S. Komura and K. Miyanami: *Ibid.,* **22**, 79 (1985).

Velocity Discontinuity of Particles Flowing
in a Mass-Flow Hopper and the Analysis of Its Characteristics[†]

Hiroshi Takahashi, Eiji Obata
and Takao Takeuchi
Department of Chemical Engineering
Muroran Institute of Technology *

Abstract

The velocity distribution of particles flowing in a two-dimensional mass-flow hopper under gravity was obtained for the entire region of a hopper by measuring the position of tracer particles against time. The characteristic regions of discontinuity or rapid change in velocity and flow direction were found from a detailed analysis of the velocity distribution obtained. On the other hand, an approximate calculus for the estimation of the "velocity characteristic curve" and "stress characteristic curve" (i.e., slip line) was proposed on the basis of the plasticity theory. Theoretically, discontinuity in velocity is possible across the velocity characteristic curve. It was confirmed that both the characteristic regions estimated and obtained experimentally were identical. Also, it was confirmed that the slip lines appear in the flow field that developed immediately after the yield of material occurred.

Introduction

One of the important requirements in designing moving beds and storage bins for granular materials is to estimate the velocity characteristics of the particles. Measuring the particle velocity requires difficult techniques. The flow characteristics of granular materials have gradually been uncovered by research[2~8]. Perry et al.[6] have experimentally discovered that particles flow with velocity discontinuity in a mass-flow hopper. One of the present authors observed the flow patterns of particles flowing in a hopper and suggested that, in the incipient stage of particle flow immediately after the yield of material occurred, the flow was discontinuous and accompanied by slip lines (a stress characteristic curve and discontinuous curve of stress and velocity). Also, it was observed that another type of discontinuous flow, differing from that observed in the

incipient stage, developed with the advance of the flowing stage. In this case, the discontinuous flow characteristics appearing in the advanced flow stage are estimated to be identical to the ones reported by Perry. Thus, the discontinuity of particle flow has two different forms, but the particle behavior has not yet been sufficiently investigated.

In this investigation, two types of two-dimensional hoppers having a different angle of hopper cone were used, and the moving velocity of the samples (coal particles) was measured through the observation window. The velocity in the entire hopper was analyzed in detail, experimentally confirming that a discontinuity in the velocity did in fact occur. The movement characteristics of particles flowing with a velocity discontinuity were investigated to obtain the velocity characteristic curve, i.e. the regions where rapid change in the velocity occurred, for the respective hopper. An approximate calculus for estimating this characteristic curve and the slip line characterizing the incipient stage of particle flow was proposed on the basis of the plasticity theory in order to attempt to estimate the discontinuity of particles flowing in a hopper.

1. The equipment and method used in the experiment

The hoppers used were two-dimensional, and the inclination surfaces were made of steel plates. The parallel front and rear surfaces were made of transparent acrylic sheets. Two hoppers of the following dimensions were used:

(1) angle of the hopper cone $2\theta = 20°$
     diameter of the hopper outlet $D = 5$ cm
     height $H = 1.1$ m
     distance between the parallel
     sheets $l = 12.5$ cm

(2) angle of the hopper cone $2\theta = 40°$
     diameter of the hopper outlet $D = 10$ cm
     height $H = 1.5$ m
     distance between the parallel
     sheets $l = 20$ cm

Coal particles, the diameters of which were arranged within a range of 0.8 to 1.0 cm, were used as specimens. The specimens were rinsed using water, then packed into the hopper channel through a 2 x 2 cm screen provided in the upper portion of the hopper, so that the particles were packed in a uniform and horizontal manner in the channel cross section. At this time, a layer of tracer particles that were colored white and a layer of specimen particles were horizontally and alternately provided. Thus packed coal particles were made to discharge at a constant flow velocity by an electromagnetic feeder situated below the outlet at a right angle to the observation window of the hopper. Photographs of the motion of respective tracer particles in the entire area of the hopper were taken simultaneously and over a specific time interval using three or four cameras. The flow velocity was set to approximately 1.1 kg/min when a hopper of $2\theta = 20°$ was used, and to approximately 4.4 kg/min when a hopper of $2\theta = 40°$ was used. To facilitate the easy reading of the coordinates of tracer particles, squares at 4 cm intervals were provided in the front acrylic plate, as shown in **Fig. 1**. As described below, a pseudo-steady flow of particles, which was the feature of the mass-flow hopper, was obtained at these flow velocities. As a result, the obtained particle behavior could be explained using a theory which assumes steady flow.

In general, when the motion of particles is observed through a transparent plate, as de-
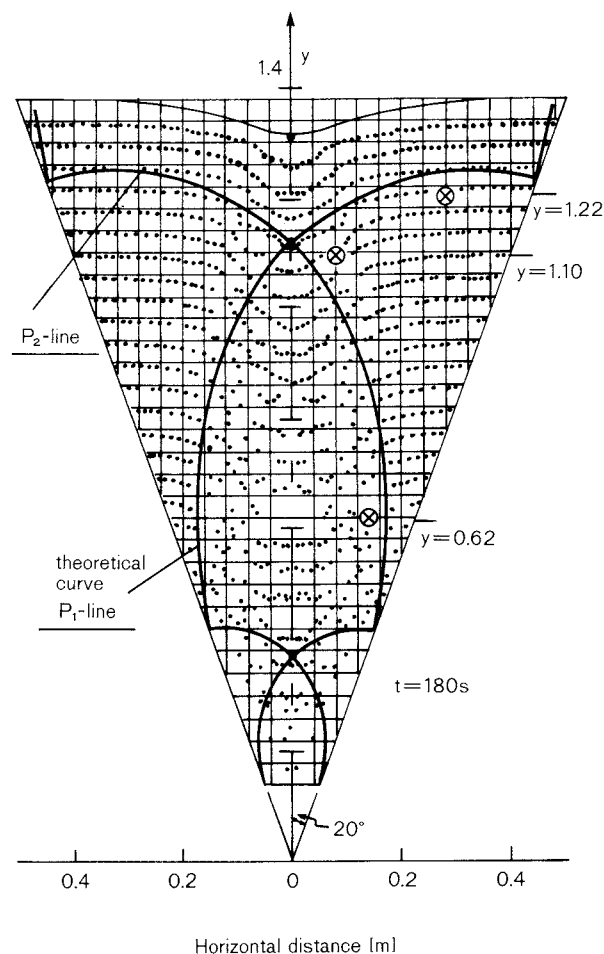

Fig. 1   Flow pattern and velocity characteristics calculated with $\phi = 37°$ and $\phi_w = 25°$

scribed in this paper, the 1- to 2-particle layer that contacts the transparent plate suffers from the wall effect. This results in such a poor expression that the obtained velocity characteristics cannot sufficiently describe the motion of the interior particles. In this case, the tracer contacting the wall surface abruptly disappears into the interior particles, or it abruptly appears from the interior particles as a result of the shearing effects between particles, thereby making it impossible to estimate the velocity through the observation window. In our experiments, the wall effects described above were not observed, and so the particles were assumed to move at an equal velocity perpendicular to the observation window.

The angle of friction between the coal particles and the hopper inclination surface was measured as follows:

○ A container, devised so that the contained particles contact the steel plate but do not move inside the containers, was placed on the steel plate.

○ The plate was gradually inclined to obtain the angle between the plate and the horizontal line when the container started sliding.

The obtained angle was determined as the angle of wall friction, and $\phi_w = 26°$ to $27°$.

In addition, the angle of discharge (ϕ_d) was measured using the method described below (the method is the same as that described in the previous report[7]), obtaining $\phi_d = 38°$.

○ Colored particles were packed into a two-dimensional box container that had a slit-shaped outlet provided in the center of the horizontal base.

○ The packed colored particles were discharged from the outlet while continuously supplying non-colored coal particles from the upper portion of the container.

○ When the particle flow reached a steady status, photographs of the stationary shape of the colored particles were taken.

○ The angle between the horizontal base and the stationary layer of the colored particles at the outlet, was determined to be ϕ_d. The angle of discharge approximately equals the angle of internal friction of the particles.

2. The results and discussion of the experiment

The moving distances Δr and Δz of the target particle in the horizontal and vertical directions during a time elapse Δt starting from an arbitrary time were obtained. The horizontal and vertical velocities u_r and u_z, and also, the angle between the direction of flow of the particles and horizontal plane were calculated from Eqs. (1) and (2), respectively.

$$u_r = -\Delta r/\Delta t, \quad u_z = \Delta z/\Delta t \tag{1}$$

$$B = \tan^{-1}(u_z/u_r) \tag{2}$$

Using these equations, the velocity distribution and the distribution in the direction of flow at any moment was calculated over the entire area of the hopper.

2. 1 The flow pattern and velocity characteristics

Figure 1 shows one example of the flow patterns that was obtained in a hopper having a cone angle of $2\theta = 40°$, and 180 seconds after the start of the flow operation. Each black dot in Fig. 1 indicates one tracer particle that was initially placed in the horizontal layer. The solid curves indicate the velocity characteristics calculated by the method described below. The figure represents two regions in the hopper: one is a region expanding upward from the discharge outlet where the deformation of the tracer layers is significant; the other is a region expanding outside the above-mentioned region toward the hopper wall surface where the deformation of the tracer layer is small. The boundary of these two regions is easily discernible as the points at which the deformation of the tracer layers suddenly changes. In a hopper having a cone angle of $2\theta = 20°$, the moving velocity of the tracer layers in the region contacting the hopper wall was larger than that shown in Fig. 1. In this case, two regions having different velocity characteristics could be determined on the flow pattern, though the boundary was not as clear as that shown in Fig. 1. The relationship between the observed results obtained from the flow patterns and the velocity characteristics of the particles calculated using Eqs. (1) and (2) will be discussed next.

Figure 2 shows one example of the horizontal distribution of the calculated horizontal and vertical velocities u_r and u_z and flow direction defined by Eq. (2). Three different distances from the hopper apex ($y = 1.22$, 1.10, 0.62 m indicated on Fig. 1) were selected. The velocities in Fig. 2 were calculated from the moving distances during a period of from 60 to 120 seconds after the start of the flow operation. Therefore, the distribution was obtained at a time when the tracer deformation was smaller than that shown in Fig. 1. A maximum u_z was obtained at the center line of the hopper at all levels. However, the shapes of the horizontal distribution of u_z differed from each other depending on the distance from the hopper apex. At $y = 0.62$ m, the region in which the value of u_z is approximately the same as that on the center line is spread out from the center line
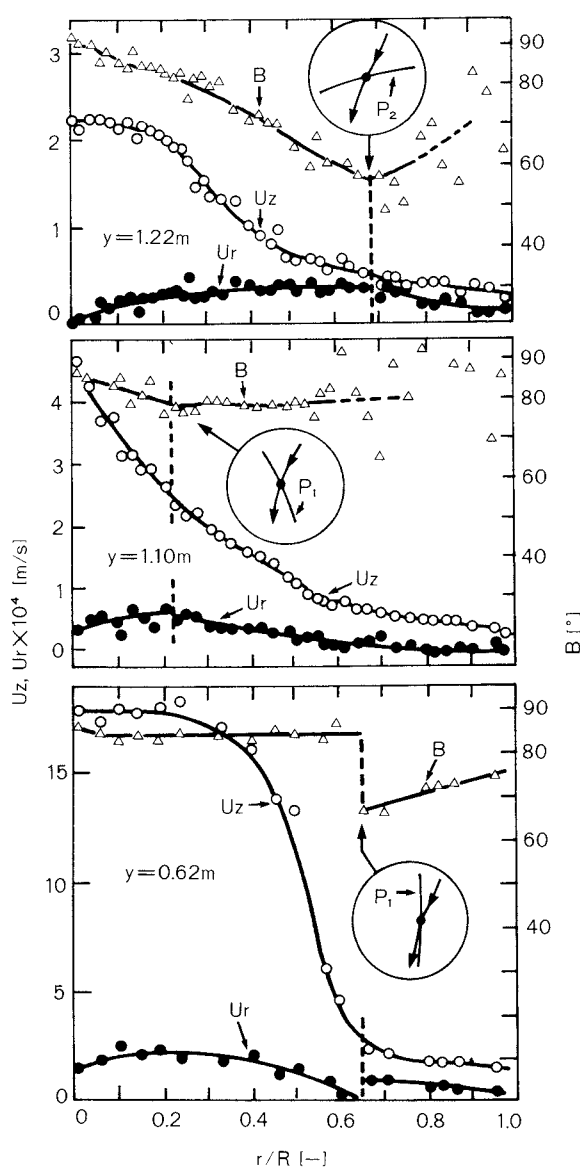
Fig. 2 Horizontal distributions of u_r, u_z and B

Fig. 3 Distribution of the position of discontinuity in flowing direction of particles

to r/R = 0.4. However, when y = 1.10 m, the u_z value sharply decreases with an increase in the distance from the center line of the hopper. On the other hand, u_r on the center line of the hopper is theoretically zero because of the symmetry of the flow. The value of u_r increases with the increase in the distance from the center line of the hopper and reaches a maximum value at a specific point. This point differs depending on the y level. Thus, it is revealed that the similarity rule cannot be applied to the variation with height in the velocity distribution in the horizontal direction within the hopper. Jenike[2] assumed a radial velocity
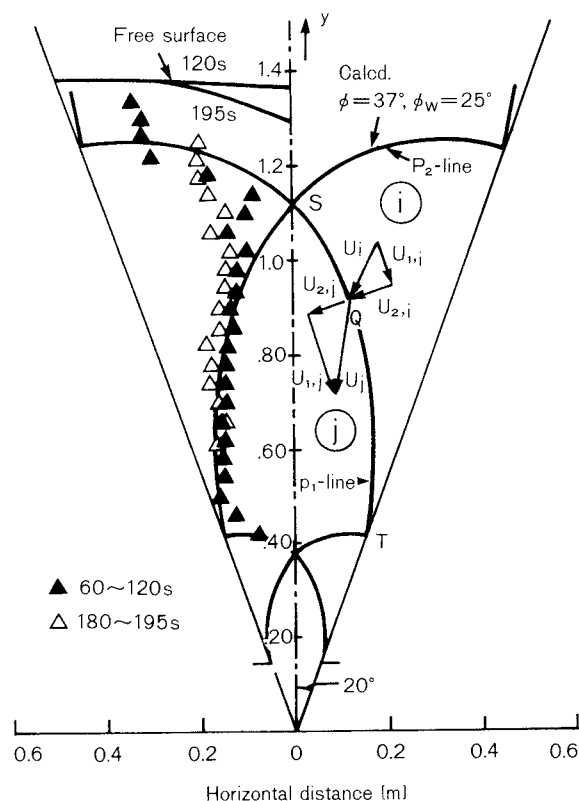
field where each particle in a mass flow hopper linearly moves toward the imaginary apex. According to this assumption, the velocity distribution at each height should be similar. The results of our experiment revealed that this assumption is not correct. Perry et al.[6] also pointed out that the measured velocity field did not coincide with the radial velocity field. The deviation from the radial velocity field was most significant in the horizontal distribution of B (flow direction of particle). For instance, in **Fig. 2**, when y = 1.22 m, the particle on the hopper center line moves toward the gravity direction (that is, B = 90°), B values gradually decrease as the distance from the center line increases, indicating that the particles in these areas move inwards toward the hopper center line. However, B values increase in the region of $r/R \geq 0.68$. The graphs of the levels of y = 1.1 m and y = 0.62 m clearly indicate that two regions of different flow directions exist. In particular, in the graph of y = 0.62 m, a discontinuous change in B values clearly appears. The change in the flow direction of the particle

passing through this point, where the inclination of the B distribution curve changes abruptly or discontinuously (indicated by the broken lines in **Fig. 2**), can be quantitatively illustrated in the circles in **Fig. 2**. In these circles, p_1 and p_2 are velocity characteristic curves that are defined according to the method of calculation described below. Clearly, these discontinuous points are not on a specific straight line leading to the virtual apex of the hopper. Experimentally, these points correspond to the points where a maximum value of u_r is obtained or u_z starts to increase. Furthermore, it has not been experimentally confirmed but it is mathematically possible that $\partial u_r/\partial r$ need not necessarily be zero at the point where a maximum value of u_r is obtained. That is, it is possible that the differential coefficient may not be defined, and the inclination of the velocity distribution curve can discontinuously change. For the $2\theta = 20°$ hopper, the same characteristics as the velocity field described above were obtained by analyzing the velocity characteristics.

The positions where B or the inclination of the B curve discontinuously changes, which were obtained at each height in **Fig. 2**, are indicated by the ⊗ marks in **Fig. 1**. **Figure 3** a plot of these points of discontinuity obtained for various different heights. The ▲ marks indicate the distribution of discontinuity at the same time as in **Fig. 2**. The △ marks indicate the distribution of discontinuity obtained using $\Delta t = 15$ seconds at the time when 180 seconds has elapsed from the start of flow. After the flow begins, the free surface of the sample in the upper portion of the hopper continuously changes in shape. However, the distribution of the position of discontinuity remains approximately the same shape independent of the time that has elapsed. This may be regarded as one characteristic of a mass flow. In a funnel flow, a flow region surrounded by a static region gradually expands from the outlet and propagates upwardly, in contrast to the steady behavior that appears in the mass flow. As can be seen by comparing **Figs. 1** and **3**, two regions of different velocity characteristics that appear in the flow pattern correspond to the two regions that are defined by the distribution of the position of discontinuity. To investigate the reproducibility of the results obtained, the same experiments were repeatedly carried out,

thus obtaining the same flow patterns and the same distribution of the positions of discontinuity as those shown in **Figs. 1** and **3**.

2. 2 Discontinuity in velocity

In this section, the velocity characteristics will be discussed using the distribution of u_z in the vertical direction. **Figure 4** shows the axial distributions of u_z at distances of $r = 0.02$, 0.06, and 0.1 m, from the central axis. These distributions were obtained in a hopper of $2\theta = 20°$. The u_z was calculated based on the movement of the particles 180 to 210 seconds after the start of the flow operation. As can be seen in the figure, the axial distribution of u_z is complicated in shape. Especially at the positions of $r = 0.02$ and 0.06 m, significant velocity discontinuities appear at $y = 0.6$ m. The same behavior was observed in the hopper of $2\theta = 40°$, so significant velocity discontinuity
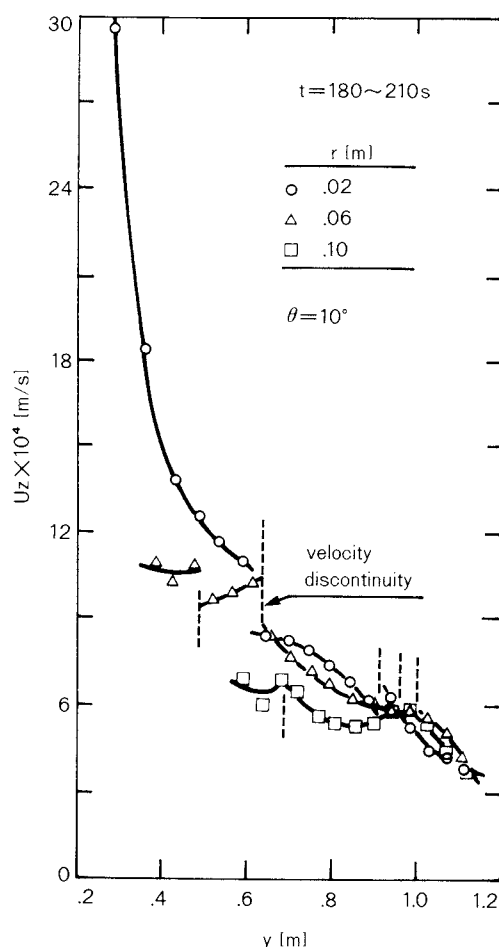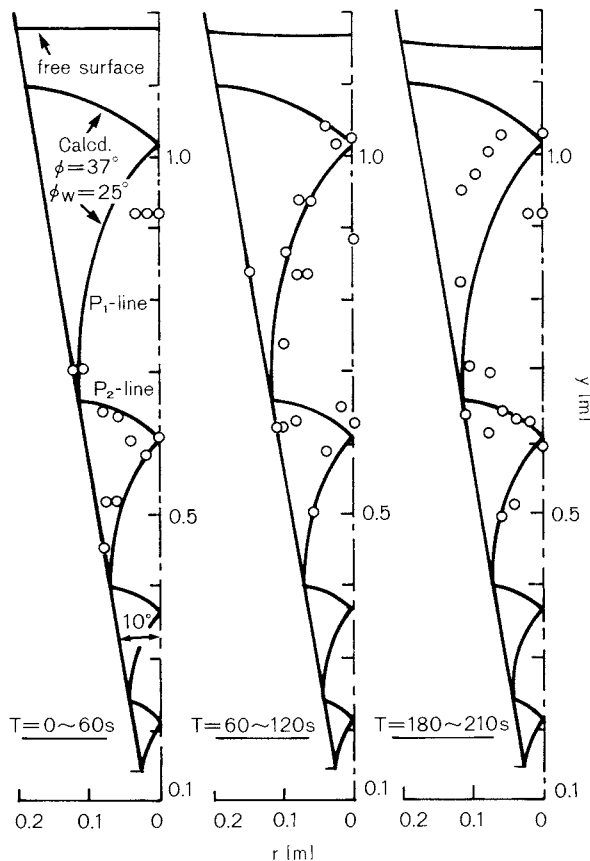

Fig. 4 Axial distribution of u_z, $\theta = 10°$

Fig. 5 Distribution of the position of discontinuity in u_z and network of velocity characteristics

in u_z appeared at $y = 0.4$ to 0.5 m. The broken lines in **Fig. 4** indicate the positions where u_z or $\partial u_z/\partial y$ changes discontinuously. The same velocity analysis was carried out for many positions, excluding the positions shown in **Fig. 4**. Thus, the distribution of the position of discontinuity in u_z was obtained over the entire hopper as shown by the ○ marks in **Fig. 5**. The solid lines in the figure indicate the theoretical velocity characteristics described below. Each graph was obtained based on a velocity analysis executed at the times shown in the figure. These graphs show the experimental data from 0 to 210 seconds after flow started. The shape of each distribution curve is substantially the same independent of the time when the data was obtained thus indicating that the flow characteristics are pseudo-steady. The velocity distribution when the amount of particles was reduced to a low level was not obtained. However, the following assumption may be made: the particle flow in a hopper cannot be steady

because the amount of particles in the hopper gradually decreases. However, it may be assumed that the velocity characteristics do not change as long as the stress conditions in the particle layer remaining in the hopper are the same as in the initial state (defined by Eq. (10) described below). As described in the preceding section, the distribution of the points of discontinuity of the B value was regarded to be pseudo-steady. Therefore, it is necessary to discuss whether the discontinuity observed in B, u_z or the inclination of these curves is caused by the same particle behavior.

2. 3 Analysis of the characteristic curves of particle behavior

The flow behavior of the particles will be discussed from the viewpoint of plasticity theory. The basic items theoretically supporting this research, such as the equations for the slip lines and the velocity characteristic curve, introduced from plasticity theory, are listed in the Appendix.

1) Discontinuity in the tangential velocity along the velocity characteristic curve

Assume that at the point Q on the characteristic curve (p_1-line) in the hopper shown in **Fig. 3**, both the velocity and direction of movement change discontinuously, as shown in the figure, when particles pass from region i to region j. (It will be indicated by the result of the calculation described below that the characteristic curve ST equals p_1.) At this time, the tangential and normal velocities along the p_1-line in regions i and j are defined as shown in the figure. By applying the equations along the p_1-line (that are included in Geiringer's equations [Eq. (A-4)] to the regions i and j, and assuming $\alpha^* = \alpha_Q^*$ at point Q:

$$\left.\begin{array}{l} \text{Region } i : \quad du_{1,i} + u_{2,i}d\alpha_Q^* = 0 \\ \text{Region } j : \quad du_{1,j} + u_{2,j}d\alpha_Q^* = 0 \end{array}\right\} \qquad (3)$$

Even when a discontinuity in the velocity is permitted, at least the normal velocity that is at a right angle to the discontinuous line p_1 must be continuous, that is $u_{2,i} = u_{2,j}$[10]. Therefore,

$$d(u_{1,i} - u_{1,j}) = 0 \qquad (4)$$

and $\quad u_{1,i} - u_{1,j} = C$ (constant)

52

C represents the amount of discontinuity in the tangential velocity along the p_1- line. Assuming the normal axis of the p_1-line to be n, the equation indicates that a discontinuity is permitted in the shear strain velocity $\partial u/\partial n$ when exceeding the p_1-line. Thus, the velocity and the direction of movement of particles can change discontinuously when passing through the velocity characteristic curve (Eq. (A-3)).

2) Estimation of the velocity characteristic curve and the slip line

It was implied[8] that the direction of the failure (slip) was given by the stress characteristic curve (Eq. (A-1)) in the incipient flow status immediately after the particles reached yielding (failing) conditions. From the characteristics of the slip phenomena between the particle layers, a discontinuity in the tangential velocity components along the stress characteristic curve may be permitted in both sides of the curve. Thus, two types of discontinuities in particle flow exist: one related to the stress characteristic curve and the other related to the velocity characteristic curve. To estimate these discontinuities, it is first necessary to determine the stress parameter α (angle between the direction of the major principal stress and the horizontal plane) as a function of the position in the hopper.

Assuming two slip lines (a and b) passing through an arbitrary point P in the hopper as shown in **Fig. 6**, the change in α along the respective slip line can be approximately estimated using Eqs. (A-5) and (A-6) and Eqs. (A-7) and (A-8). The boundary conditions of are given as follows:

$\alpha = \alpha_c$ at $r = 0$ (on the central axis)

$\alpha = \alpha_R$ at $r = R$, $y = y_R$ (on the wall surface)

$$(5)$$

After applying Eq. (5) to the a-slip line and Eqs. (A-5) and (A-6) to eliminate the integration constant, introduce r/R and y/R as functions of α. By taking the ratio between the above functions, the relationship between the coordinates (r, y) of the point P on the a-slip line is given as follows:

$$y/r = \cot\psi$$
$$= \frac{\cot\theta \cdot f(\alpha_R, \alpha_c, \eta) + g(\alpha_R, \alpha, \eta)}{f(\alpha, \alpha_c, \eta)} \quad (6)$$
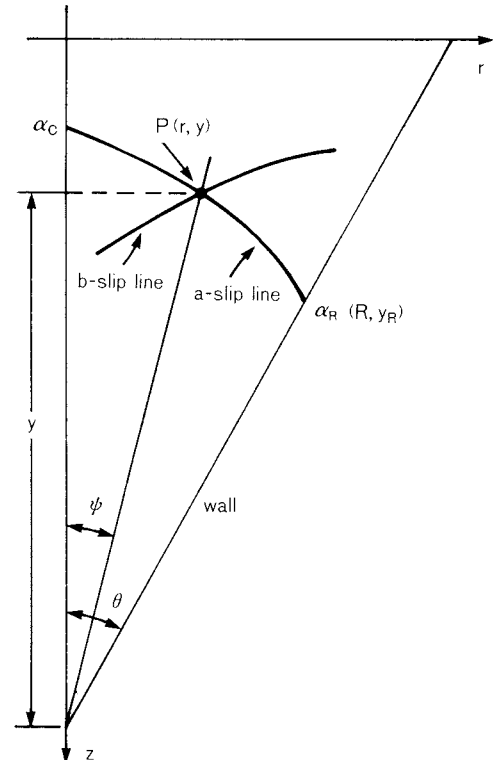

Fig. 6   Schematic diagram showing slip lines and boundary values of α

where functions f and g are defined as follows:

$$
\left.
\begin{aligned}
f(X, Y, \eta) &= (X - Y)\cos 2\eta - \sin 2\eta \\
&\quad \times \ln|\cos(Y - \eta)/\cos(X - \eta)| \\
g(X, Y, \eta) &= (X - Y)\sin 2\eta + \cos 2\eta \\
&\quad \times \ln|\cos(Y - \eta)/\cos(X - \eta)|
\end{aligned}
\right\} \quad (7)
$$

Since the α value can be calculated at any point P in the hopper by assuming an a-slip line passing through the said point P, the distribution of α over the entire hopper can be estimated using the above equations. Likewise for the point P on the b-slip line in **Fig. 6**, by applying the boundary conditions (Eq. (5)) to Eqs. (A-7) and (A-8), the distribution of α can also be obtained. The result is expressed by the following equation that is obtained by replacing η with $-\eta$ in Eq. (6).

$$y/r = \cot\psi$$
$$= \frac{\cot\theta \cdot f(\alpha_R, \alpha_c, -\eta) + g(\alpha_R, \alpha, -\eta)}{f(\alpha, \alpha_c, -\eta)}$$

$$(8)$$

If α_a is the value of α at point $P(x, y)$ obtained from Eq. (6) and α_b is the value obtained from

Eq. (8), their values do not necessarily coincide with each other. Rather, they are normally slightly different because Eqs. (A-5) through (A-9) are approximate equations. In the present research, the average values of these were used to estimate the distribution of α.

$$\alpha = (\alpha_a + \alpha_b)/2 \qquad (9)$$

Jenike[2] called the stress field where α is a function of only ψ shown in **Fig. 6** a "radial stress field". From Eqs. (6) and (8), the approximate solution of α obtained in the present research is also the solution for a radial stress field. To execute the calculation, the boundary conditions are given by the following equations[8] based on the assumption that the horizontal stress within the particles in a mass-flow hopper is at a maximum on the center axis, that is, the particles are in the so-called passive state or arched field.

$$\alpha_c = 0$$
$$\alpha_R = \left\{\phi_w + 2\theta + \sin^{-1}(\sin\phi_w/\sin\phi)\right\}/2 \qquad (10)$$

The network of velocity characteristic curves obtained using Eqs. (6) through (10) and Eq. (A-3) is represented by the solid lines in **Figs. 1**, **3**, and **5**. The calculation was executed starting from the hopper wall on the discharge outlet. The friction characteristics of $\phi = 37°$ and $\phi_w = 25°$ were used in the calculation. These values are considered to be reasonable compared with the experimentally obtained values: the angle of discharge $\phi_d = 38°$, and the angle of static friction $= 26$ to $27°$. The theoretical velocity characteristics coincide approximately with the position where the deformation quantity of the tracer layers abruptly changes (shown in **Fig. 1**) and the position where the direction of particle flow changes discontinuously (shown in **Fig. 3**). Slight disagreement between the calculated and experimental results are observed in the upper portion of the hopper. This disagreement is considered to be caused by applying the theory (that is only effective when it is applied to regions which are not affected by the free surface) to the upper portion of the hopper without any modifications. From **Fig. 5**, it is seen that the calculated velocity characteristics coincide with the distribution of the position of discontinuity in u_z determined by the experi-
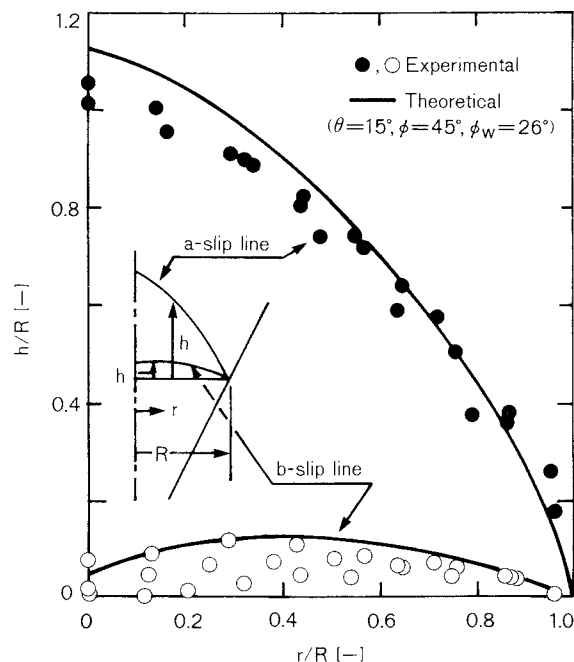

Fig. 7 Comparison between the breaks found at incipient flow of sawdust[8] and theoretical slip lines

ments. According to Yamada[10], the velocity discontinuity curve is equivalent to the limiting case, where the width of the narrow transitional region in which the velocity changes suddenly is infinitesimally small. This implies that it is reasonable for the velocity characteristics to be measured as two phenomena: discontinuity in u_z and B; and abrupt change in the slope of these curves. In the flow pattern of sawdust given in the preceding report[8], the existence of discontinuities in both the direction of flow and velocity, which did not appear in the incipient flow immediately after the start of flow, was implied in the velocity field of relatively advanced flow. The above described velocity characteristics may be considered to appear in the flow pattern. Thus, the theory described in Section 2.3.1), which predicts the existence of discontinuous change in the velocity vector at the boundary of the velocity characteristic curve, was proved to be effective when applied to the analysis of the flow behavior of the particles.

It was described above that the characteristics of the initial and subsequent flows were observed to be different. The breaks found in an incipient flow of sawdust and in the theo-

54

retical slip lines obtained using Eqs. (A-1), (6) through (10) are compared in **Fig. 7**. The experimental data in **Fig. 7** were obtained by reading the positions of the breaks from several sheets of photos similar to those shown in the previous report[8]. In the previous report, these break surfaces were assumed to correspond to the slip lines. In the previous report[8], $\phi = 40°$ to 45°, and the angle of static friction $\phi_w = 30°$ were estimated. By assuming the angle of friction shown in the figure, the calculated results coincided approximately with the measured values. Although indefinite factors concerning the angle of friction remain, it may be concluded that the development of breaking surfaces in the incipient flow can be expressed by the slip lines.

In the above analysis, it was assumed that the passive stress conditions (Eq. (10)) developed with the start of flow. The results described above indicate that the particle flow under the conditions used in this experiment satisfies the passive stress field. However, according to a recent report by Moriyama and Jimbo[4], the state of consolidation of packed particles depended on the method by which they had been fed into the hopper, and this affected the dynamic behavior of the wall pressure during discharge. Assuming that the stress conditions differ according to the method of supplying the particles into the hopper, the velocity characteristic curve and slip line generation will differ based on the stress conditions. Investigating this will be our objective in the future research.

Conclusion

By measuring the velocity of coal particles flowing under gravity in a two-dimensional hopper and by analyzing the obtained velocity in detail, the following results were obtained:

1) The existence of the positions where the direction of particles flow and the velocity changed discontinuously or abruptly was confirmed experimentally, and the distribution of these positions in the hopper was determined. Judging from this distribution, the radial velocity field proposed by Jenike cannot be applied.

2) The particle flow characteristics obtained in the above 1) remained without any

changes as time elapsed. That is, the flow was pseudo-steady.

3) The experimentally obtained distribution of velocity characteristics coincided with the velocity characteristic obtained using the plasticity theory. An approximate estimation method was described.

4) It was confirmed that the flow immediately after the particles yielded was characterized by the slip line.

Appendix

In the rz plane stress problems, the direction in which the yielded material initiates failure is given by the following equation for the stress characteristic line (slip line) if Coulomb's yield condition for non-adhesive particles is applied[1,3,7,8].

$$dz/dr = \tan (\alpha \pm \eta) \qquad \text{(A-1)}$$

α is a variable indicating the angle between the plane perpendicular to the r-direction and the major principal plane. Breaking (slip) is possible in two directions, and these are called the a- and b-slip lines. The following equations can be applied to the particles that have already begun to deform only when it is assumed that the axes of major strain and major principal stress coincide[10].

$$
\begin{aligned}
&\partial u_r/\partial r + \partial u_z/\partial z = 0 \\
&\quad \text{(Equation expressing continuity)} \\
&(\partial u_z/\partial r + \partial u_r/\partial z)/(\partial u_r/\partial r - \partial u_z/\partial z) = \tan 2\alpha
\end{aligned}
$$
$$\text{(A-2)}$$

The velocity characteristic line can be given by the following two curves as the solution of the above simultaneous equations[10]. Designating each of them as p_1 and p_2:

$$
\begin{aligned}
&p_1 : dz/dr = -\cot\alpha^*, \quad p_2 : dz/dr = \tan \alpha^* \\
&\quad 2\alpha^* = 2\alpha - \pi/2 \qquad \text{(A-3)}
\end{aligned}
$$

Between the components of the strain velocity along the velocity characteristic line, the following equation is satisfied.

$$
\begin{aligned}
&p_1 : du_1 + u_2 d\alpha^* = 0 \\
&p_2 : du_2 - u_1 d\alpha^* = 0
\end{aligned}
\qquad \text{(A-4)}
$$

Where u_1 and u_2 are tangential velocities along lines p_1 and p_2, respectively.

In the previous reports[7,8,9], the distribution of α was estimated from the following approxi-

mations for the changes in α along the slip line, Eq. (A-1).

a-slip line

$$r \text{ vs. } \alpha \quad A\{(\alpha - \eta)\cos 2\eta + \sin 2\eta \\ \times \ln \mid \cos(\alpha - \eta) \mid \} = r + c_1 \quad \text{(A-5)}$$

$$y \text{ vs. } \alpha \quad A\{(\alpha - \eta)\sin 2\eta - \cos 2\eta \\ \times \ln \mid \cos(\alpha - \eta) \mid \} = -y + c_2 \quad \text{(A-6)}$$

b-slip line

$$r \text{ vs. } \alpha \quad A\{(\alpha + \eta)\cos 2\eta - \sin 2\eta \\ \times \ln \mid \cos(\alpha + \eta) \mid \} = r + c_3 \quad \text{(A-7)}$$

$$y \text{ vs. } \alpha \quad A\{(\alpha + \eta)\sin 2\eta + \cos 2\eta \\ \times \ln \mid \cos(\alpha + \eta) \mid \} = y + c_4 \quad \text{(A-8)}$$

where c_1 through c_4 are integration constants and

$$A \equiv 2\,\sigma_m \,\sin\phi\,/\,(-\rho_b g) \quad \text{(A-9)}$$

Acknowledgement

Nomenclature

B : flow direction of particle, defined in Eq. (2) [°]

R : distance from center axis to hopper wall [m]

r, z : coordinates defined by **Fig. 6** [m]

t : time [s]

u_r, u_z : horizontal and vertical velocities [m/s]

u_1, u_2 : velocities tangential and normal to p_1-line [m/s]

y : distance from hopper [m]

α : angle between the plane perpendicular to the *r*-direction and major principal plane [rad]

α_c, α_R : values of α at $r = 0$ and $r = R$ [rad]

η : $\pi/4 - \phi/2$ [rad]

θ : hopper half-angle [°]

ρ_b : density [kg/m³]

σ_m : mean principal stress [Pa]

ϕ : angle of internal friction [°]

ϕ_d : angle of discharge [°]

ϕ_w : angle of wall friction [°]

ψ : radial angle defined by **Fig. 6** [rad]

References

1) Hoshi, K. and K. Sato: "Statics of Soil Media", p. 22, Ohm-sha, Tokyo (1964).

2) Jenike, A.W.: *J. Applied Mechanics, Trans. of the ASME,* 5/March (1964).

3) Johanson, J.R.: *ibid.,* 499/September (1964).

4) Moriyama, R. and G. Jimbo: *Kagaku Kogaku Ronbunshu,* **12,** 63 (1986).

5) Pariseau, W.G.: *Powder Technology,* **3,** 218 (1969/1970).

6) Perry, M.G., E. Rothwell and W.T. Woodfin: *ibid.,* **14,** 81 (1976).

7) Takahashi, H. and H. Yanai: *Kagaku Kogaku,* **38,** 746 (1974).

8) Takahashi, H., H. Yanai and T. Tanaka: *J. Chem. Eng. Japan,* **12,** 369 (1979).

9) idem: *ibid.,* **12,** 376 (1979).

10) Yamada, Y.: "Sosei Rikigaku (Plasticity Mechanics)", p. 218, Nikkan Kogyo Shinbunsha, Tokyo (1982).

On the Stress Distribution of Granular Materials Conically Piled on the Ground[†]

Takaaki Nagao, Yotaro Hatamura,
Takatsugu Takeuchi and Nobuyuki Nakajima
Dept. of Mechanical Engineering for Production,
Faculty of Eng.,
University of Tokyo*

Abstract

Two-directional stress cells which can measure the small normal and friction stress of granular materials on a wall were recently developed. With these cells, the stress distributions of granular materials (silica sand and millet grain) piled conically on a plate are measured and compared with the results of theoretical analysis. The results are as follows:

1) The maximum normal stress occurs at a distance of a quarter of the outer radius of the cone of the pile, which is about $(0.7 \sim 0.8)\gamma H$, where γ is the apparent specific gravity, and H denotes the height of cone.

2) The normal stress at the center is rather small, about $(0.4 \sim 0.6)\gamma H$.

3) The maximum frictional stress also occurs at the same position as the maximum normal stress.

4) Theoretical analysis gives a maximum normal stress of $0.5\gamma KH(\sqrt{2/K-k} - \sqrt{k})^2/ (1 - kK)^2$ at a radius of $r = H/\sqrt{k(2/K-k)}$ and a normal stress at the center of $\gamma H [1 - K^2(\bar{f} - k)(2/K - k - \bar{f})/(1 - kK)^2]$. k denotes the friction coefficient, and K denotes the friction coefficient between granular material and the surface of plate. $\bar{f}$ is given by the formula (40). This agrees well with the experimental result.

1. Introduction

Granular materials are often stocked by being piled conically on the ground in steel-making, cement and other industries. In this case, the state seems to be very brief and the stress distribution might be expected to be simple, but it is unexpectedly complicated. There is a paper by Jotaki and Moriyama which treats this matter experimentally. The authors developed a new two-directional stress cell which can experimentally measure small normal and frictional stresses of granular materials on a wall. They theoretically analyzed this case, and investigated the possibility of applying these results to the stock control of

granular materials.

This paper reports on these results.

2. The structure of a stress cell

The structure of a stress cell is given in **Fig. 1**. It is made of a parallel plate and can measure the two-directional load (in normal and tangential directions) separately. The rate stress and strain in the normal direction are 5080 Pa and 500×10^{-6}, respectively, and those in the tangential direction are 1270 Pa and 500×10^{-6}, respectively. It is sensitive enough to measure very low stresses, and it has a contact plate of 10 mm in diameter. Phosphor bronze parallel plates (0.2 mm thick) are stuck onto the main brass body. These plates are so sensitive that they have been kept in a non-stress state during their making. The thin plates of the main body were later cut.

The characteristic curve of this sensor is very linear, though it has a small hysteresis. Interference is too small to measure. The natural
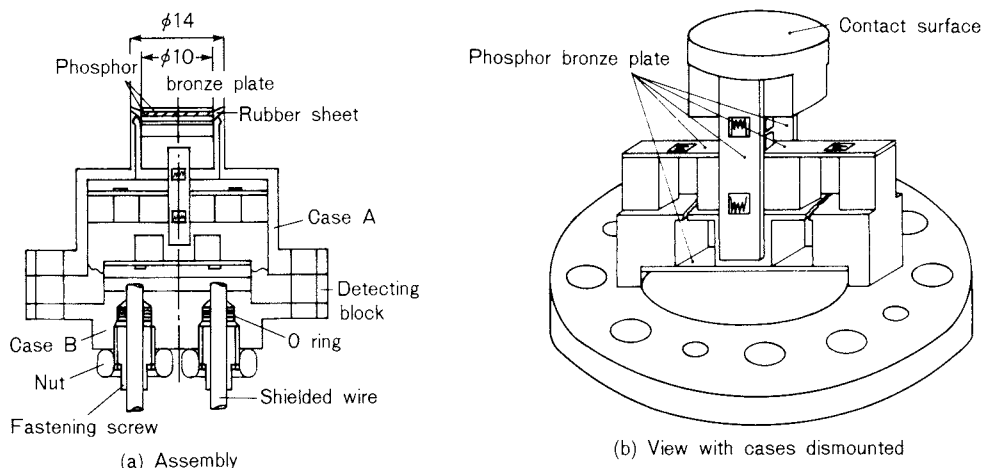

Fig. 1 Two-way stress cell (rated stress normal 5080 Pa (50 gf/cm^2) frictional 1270 Pa (12.5 gf/cm^2))

frequencies are 380 ~ 490 Hz in normal direction and 170 ~ 250 Hz tangentially.

Eight cells of this kind have been made.

3. Experiment and results

As shown in **Fig. 2**, the experimental apparatus consists of a steel plate (600 mm × 600 mm × 3 mm) and a steel bar for mounting stress cells. Stress cells are put on them in a row 60 mm from each other, with their surfaces kept at the same level as the steel plate. Silica sand and millet grains were used for the experiments. Their properties are shown in **Table 1**. Granular material has been dropped from the nozzle which is always kept about 10 mm higher than the top of the pile. 12 kg of silica sand

Table 1 Properties of used grains

Grain	Apparent density r[g/cm^2]	Mean diameter d[mm]	Angle of repose θ	Internal friction coefficient k
Silica sand	1.39	0.18	34°	0.657
Millet grain	0.68	1.3	29°	0.554

and 7 kg of millet grains were dropped with stresses measured at every 1 kg and 0.5 kg dropped, respectively. Data was obtained from the means of the experiment done five times.

The states and weights of the pile and the stress distributions are shown in **Figs. 3 ~ 6**. The stress cells No. 1 and No. 2 did not give any data because of the small number of channels
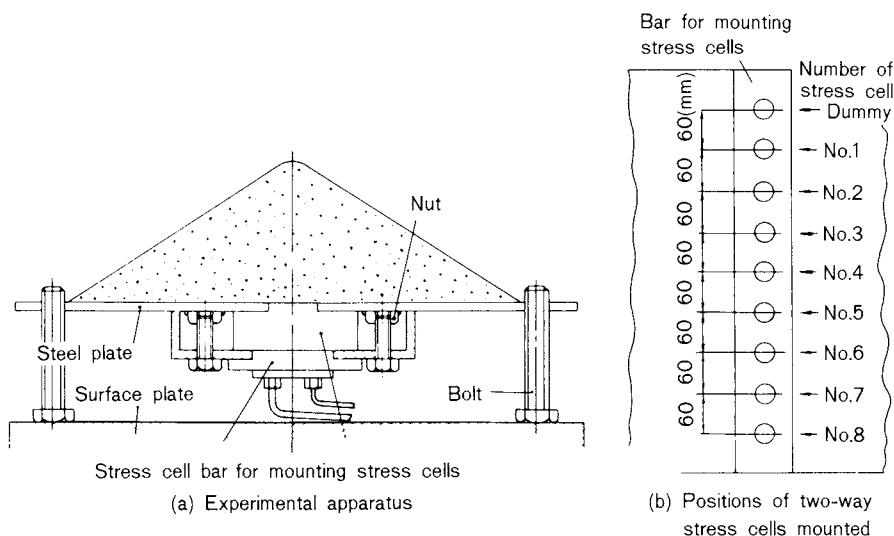
Fig. 2 The experimental apparatus
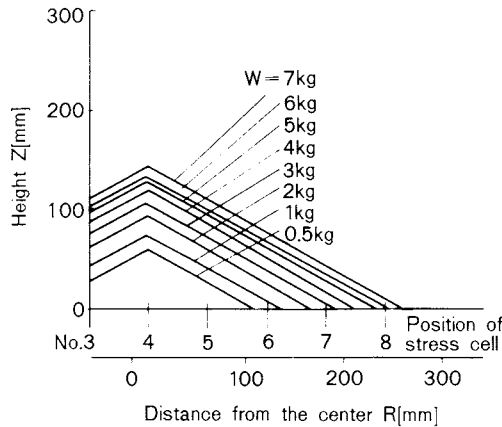
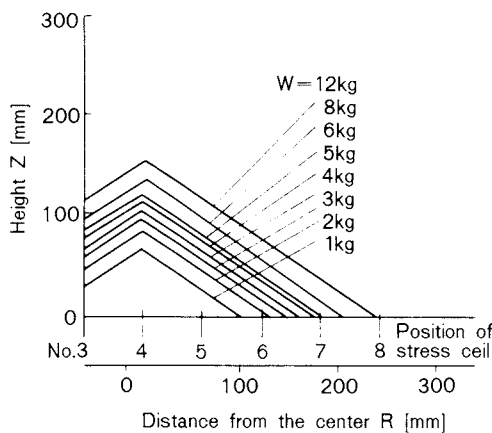Fig. 3 The state of the pile of silica sand
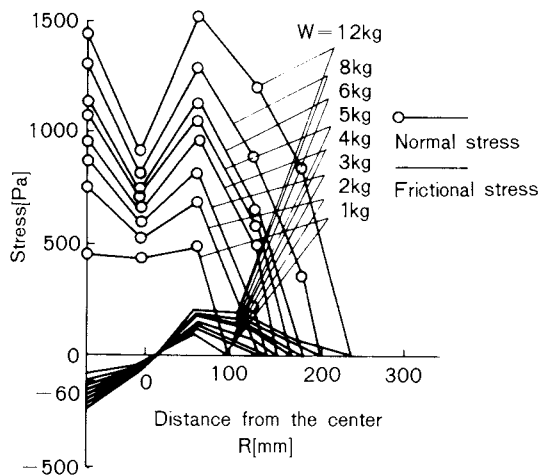

Fig. 4 The state of the pile of millet grain

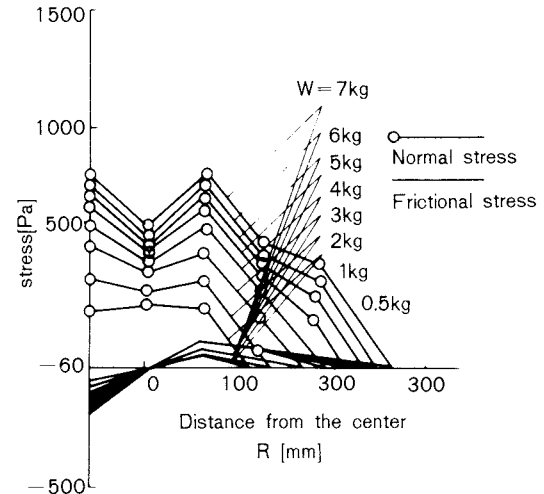Fig. 5 The stress distribution at the bottom of the piled silica

Fig. 6 The stress distribution at the bottom of the piled millet grain
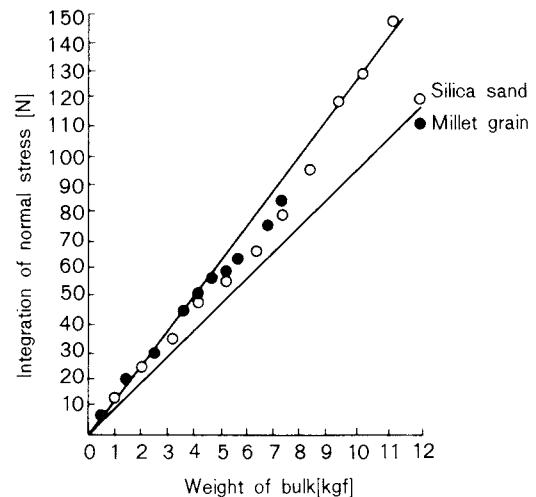
Fig. 7 The relationship between the weight of the bulk and the integration of the normal stress

in the data recorder.

These data show that the normal and frictional stresses reach their peaks slightly outside the radial distant from the center. This seems to be caused by "arching", in which granular material at the periphery supports the upper part. This has already been reported on by Jotaki[1].

These data show that the peak of the normal stress always occurs at a radius of 60mm from the center. The distributions of the normal and frictional stresses in one stage do not seem to be similar with those at another. This is because of the positions of the stress cells, so that the positions of the peaks must move.

Figure 7 shows the comparison of the integration of the normal stresses at the bottom with the weight of the pile. The former is about 112 ~ 136% of the latter, i.e. roughtly in

proportion.

This seems to be caused by the rough arrangement of the stress cells or by the rough integration method. This relationship, however, can be industrially useful to roughly calculate the weight of a pile by the integration of normal stresses.

4. Stress analysis

In analyzing the stress of granular material conically piled on the ground, the pile must be divided into two regions, I and II, as shown in Fig. 8. When θ denotes the angle of repose ($k = \tan\theta$; the internal friction coefficient of the granular material), the free surface $\overline{HB}$ can be considered to be piled at the inclination angle θ. Then, if the region II is at the state of limiting equilibrium, the maximum principal stresses must occur in the direction parallel to $\overline{HD}$ which forms the angle η ($= \pi/4 - \theta/2$) with the free surface. Consequently, it is reasonable to divide the regions I and II at the boundary $\overline{HD}$.

Although there is room for a discussion as to whether the angle of repose is equal to the internal friction angle, it is assumed to be so in this paper.

4. 1 Analysis I — when $K \geq k/(1 + 2k^2)$

Consider the case of $K \geq k/(1 + 2k^2)$, where K denotes the friction coefficient between the plate and the granular material, and k is its internal friction angle.

σ_r, σ_θ and σ_z denote the principal stresses in the radial, peripheral and axial directions, and τ_{rz} is the shearing stress in the plane perpendicular to the axial direction in the cylindrical coordinates (r, θ, z). Presuming axi-symmetry, the principal stresses are positive in compres-

Fig. 8 A pile of granular material

sion, and τ_{rz} is positive when the granular material rubs the surface of the plate in the direction radially to the center. When r denotes the specific gravity of a granular material (the product of the apparent density and the acceleration of gravity), the equations of stress equilibrium are given as follows:

$$\frac{\partial \sigma_r}{\partial r} + \frac{\partial \tau_{rz}}{\partial z} + \frac{\sigma_r - \sigma_\theta}{r} = 0 \tag{1}$$

$$\frac{\partial \tau_{rz}}{\partial r} + \frac{\tau_{rz}}{r} + \frac{\partial \sigma_z}{\partial z} = -\gamma \tag{2}$$

In region II, it is presumed that,

$$\sigma_z = Ar(H - z - kr) \tag{3}$$

where $\sigma_z = 0$, $\tau_{rz} = 0$ and $\sigma_r = 0$ at the free surface, where $z = H - kr$, and σ_z is proportional to the height of granular material above the concerned point.

Substituting this relationship into Eq. (2), integrating it and letting $\tau_{rz} = 0$ at $z = H - kr$, Eq. (4) is obtained.

$$\tau_{rz} = -\frac{(A-1)\gamma}{2k^2 r}\{(H - z)^2 - k^2 r^2\} \tag{4}$$

Next, the solution in region I is sought. In this region, if τ_{rz} is proportional to the distance from the center, presume that,

$$\tau_{rz} = -\gamma Br \tag{5}$$

Substituting this into Eq. (2) and connecting this solution with that from Eq. (3) at the boundary of regions I & II $\overline{HD}$ (expressed as $z = H - fr$), Eq. (6) is obtained,

$$\sigma_z = -(2B - 1)\gamma(H - z - fr) + A\gamma(f - k)r \tag{6}$$

As for τ_{rz}, by equalizing Eqs. (4) and (5) by making $z = H - fr$, Eq. (7) is obtained.

$$B = \frac{A-1}{2}\left\{(\frac{f}{k})^2 - 1\right\} \tag{7}$$

When $\overline{HD}$ is the boundary of regions I and II, f is given as follows:

$$1/f = \tan\eta \quad (\eta = \pi/4 - \theta/2, \tan\theta = k)$$

$$\therefore f = k + \sqrt{1 + k^2} \tag{8}$$

The granular material at the boundary $\overline{HD}$ is considered to be in limiting equilibrium, so that,

$$\frac{\sigma_r}{\sigma_z} = \frac{1}{1 + 2k^2}, \quad \frac{\tau_{rz}}{\sigma_r} = -k$$
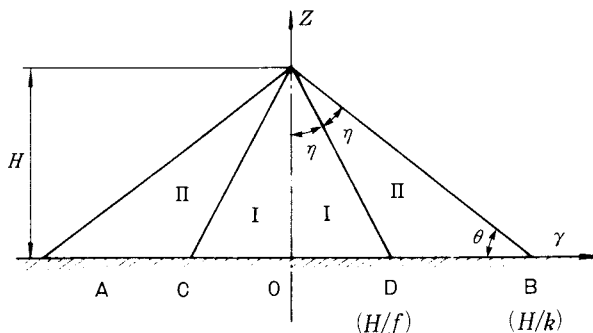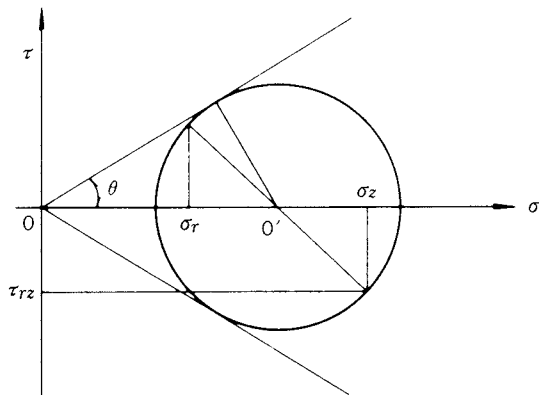
Fig. 9 The Mohr stress diagram in Domain II

$$\therefore \frac{\tau_{rz}}{\sigma_z} = -\frac{k}{1+2k^2} \qquad (9)$$

Substituting Eqs. (5), (6) and (7) into Eq. (9), Eq. (10) is obtained,

$$A = \frac{1}{1 - \dfrac{2k^3}{(1+2k^2)(f+k)}} \qquad (10)$$

Next, consider σ_r and σ_θ to be in region II where Eq. (9) does not generally hold. According to **Fig. 9**, Eq. (11) is obtained.

$$(\frac{\sigma_r + \sigma_z}{2} \sin \theta)^2 = (\frac{\sigma_z - \sigma_r}{2})^2 + \tau_{rz}{}^2$$

$$\therefore \ \sigma_r = (1 + 2k^2)\sigma_z - 2\sqrt{1+k^2}\sqrt{k^2\sigma_z{}^2 - \tau_{rz}{}^2} \qquad (11)$$

and σ_θ can be calculated from Eq. (1).

Next, consider σ_r and σ_θ to be in region I. Let,

$$\sigma_r = \gamma (P + 2Qr + Rz) \qquad (12)$$

As $\tau_{rz} = -\gamma Br$, substituting these relationships into Eq. (1), Eq. (13) is obtained.

$$\sigma_\theta = \gamma (P + 2Qr + Rz) \qquad (13)$$

On the other hand, provided that the state of stress near the boundary $\overline{HD}$ is in limiting equilibrium and Eq. (9) holds, from Eqs. (3) and (1), Eqs. (14) and (15) are obtained.

$$\sigma_r = \frac{A\gamma}{1+2k^2} (H - z - kr) \qquad (14)$$

$$\sigma_\theta = (\frac{A-1}{k^2} + \frac{A}{1+2k^2})\gamma (H-z) - \frac{2A\gamma kr}{1+2k^2} \qquad (15)$$

Then, considering the relationship of Eqs. (12) and (14) as well as Eqs. (13) and (15)

at $z = H - fr$. Comparing the coefficient of r Eq. (16) is obtained.

$$\left. \begin{array}{l} Q = \dfrac{(A-1)f}{R^2} + \dfrac{Ak}{1+2k^2} \\[4mm] R = \dfrac{A-1}{k^2} - \dfrac{A}{1+2k^2} \\[4mm] P = H(\dfrac{A}{1+2k^2} - \dfrac{A-1}{k^2}) \end{array} \right\} \qquad (16)$$

4. 2　Analysis II − when $K \leqq k/(1+2k^2)$

Let,$\qquad \tau_{rz} = -k\sigma_z \qquad (17)$

in region II. Letting,$\qquad T = r\tau_{rz} \qquad (18)$

from Eq. (2) the following partial differential equation is obtained:

$$\frac{\partial T}{\partial r} - \frac{1}{K} \frac{\partial T}{\partial z} = -\gamma r \qquad (19)$$

To solve this equation, it is necessary to solve the following characteristic equation:

$$\frac{dr}{1} = \frac{dz}{-1/K} = \frac{dT}{-\gamma r} \qquad (20)$$

The following solutions are obtained:

$$dr + Kdz = 0 \qquad \therefore \ r + Kz = a$$

$$\gamma rdr + dT = 0 \qquad \therefore \ T + 1/2\gamma r^2 = b$$

Consequently the following general solution of Eq. (19) is obtained:

$$T + 1/2\gamma r^2 = F(r + Kz) \qquad (21)$$

Then letting,

$$F(r + Kz) = A(r + Kz)^2 + B(r + Kz) + C$$

$$T = 0 \quad \text{at } z = H - kr$$

and comparing the coefficient of r, it is possible to obtain,

$$A = \gamma/2(1 - kK)^2, \quad B = -\gamma KH/(1 - kK)^2,$$

$$C = \gamma K^2 H^2/2(1 - kK)^2,$$

$$F = \frac{\gamma}{2(1 - kK)^2} \{r + K(z - H)\}^2$$

Consequently Eqs. (22) ～ (24) are obtained,

$$T = \frac{\gamma K^2}{2(1 - kK)^2} (H - z - kr)\{H - z - (\frac{2}{K} - k)r\} \qquad (22)$$

$$\tau_{rz} = \frac{\gamma K^2}{2(1 - kK)^2 r} (H - z - kr)\{H - z - (\frac{2}{K} - k)r\} \qquad (23)$$

$$\sigma_z = \frac{-\gamma K}{2(1-kK)^2}\frac{1}{r}(H-z-kr)\left\{H-z-\left(\frac{2}{K}-k\right)r\right\} \tag{24}$$

It is evident that σ_z is at its maximum value at

$$r/H = 1/\sqrt{k(2K-k)} \tag{25}$$

from $\partial T/\partial r = 0$. The value is,

$$(\sigma_z)\max = \frac{\gamma KH}{2(1-kK)^2}\left(\sqrt{\frac{2}{K}-k}-\sqrt{k}\right)^2 \tag{26}$$

In region I, letting,

$$\left.\begin{array}{l} \tau_{rz} = -Dr \\ \sigma_z = E+Fr+Gz \end{array}\right\} \tag{27}$$

from Eq. (2), Eq. (28) is obtained.

$$-2D+G = -\gamma \qquad \therefore \ G = 2D-\gamma \tag{28}$$

Let $H-z=fr$ be the border of regions I and II. Considering the connection of τ_{rz} and σ_z at this border, from Eqs. (23), (24) and (27), Eq. (29) is obtained.

$$\begin{aligned} G &= \gamma\left\{K^2(f-k)(2/K-k-f)/(1-kK)^2-1\right\} \\ F &= \gamma\left\{K(2Kf+1)(f-k)(2/K-k-f)/\right. \\ &\quad \left. 2(1-kK)^2-f\right\} \\ E &= -\gamma H\left\{K^2(f-k)(2/K-k-f)/(1-kK)^2-1\right\} \end{aligned} \tag{29}$$

The stress σ_z at $r=0$, $z=0$ is given as follows:

$$\sigma_z \mid \text{center} = E \tag{30}$$

Next, σ_r and σ_θ are sought. In region II, which is considered to be limiting equilibrium, the normal stress σ on the slip surface is given from **Fig. 10** as follows:
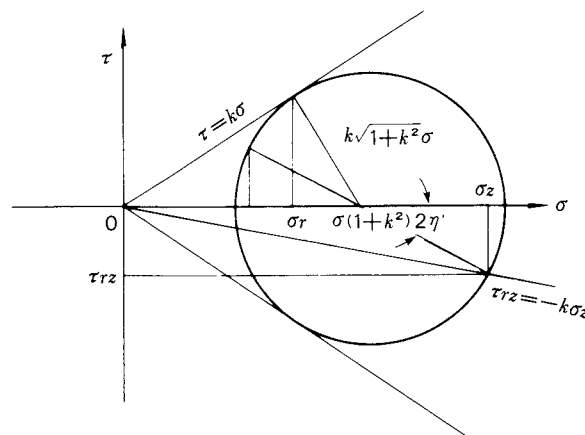

Fig. 10 The Mohr stress diagram in Domain II

$$\left\{\sigma_z-(1+k^2)\sigma\right\}^2+\tau_{rz}{}^2 = k^2(1+k^2)\sigma^2$$

$$\therefore \ \sigma = \sigma_z-\sqrt{(k^2\sigma_z{}^2-\tau_{rz}{}^2)/(1+k^2)}$$

$$\therefore \ \sigma_r = 2(1+k^2)\sigma-\sigma_z$$

$$= \left\{1+2k^2-2\sqrt{(1+R^2)(R^2-K^2)}\right\}\sigma_z$$

$$\equiv K'\sigma_z \tag{31}$$

Then, from Eqs. (1) and (19), Eq. (32) is obtained.

$$\begin{aligned} \sigma_\theta &= (1-K'/K^2)\left\{\gamma K^2/(1-kK)^2\right\} \\ &\quad \times \left\{-(H-z)+r/K\right\}+K'\gamma r/K \end{aligned} \tag{32}$$

In region I, as $\partial\tau_{rz}/\partial z = 0$ providing that,

$$\sigma_r = L+Mr+Nz \tag{33}$$

Eq. (34) is obtained from Eq. (1).

$$\sigma_\theta = L+2Mr+Nz \tag{34}$$

Connecting Eqs. (31) and (33) as well as Eqs. (32) and (34) at the boundary $z=H-fr$ and comparing the coefficient of r, Eq. (35) is obtained.

$$\begin{aligned} M &= \left\{\gamma/(1-kK)^2\right\} \\ &\quad \times \left\{K-K^2f-K'k+K'K(k^2+f^2)/2\right\} \\ N &= \gamma(1-Kf)(K-K'f)/\left\{(1-kK)^2f\right\} \\ L &= -\gamma H(1-Kf)(K-K'f)/\left\{(1-kK)^2f\right\} \end{aligned} \tag{35}$$

At the center

$$\sigma_r \mid \text{center} = \sigma_\theta \mid \text{center} = L \tag{36}$$

and at the connecting point,

$$\sigma_r = L+MH/f, \qquad \sigma_\theta = L+2MH/f \tag{37}$$

These distributions for silica sand and millet grain are plotted in **Figs. 11** and **12**, respectively. In this case, σ_θ is negative in the range of r/H above a certain value, which, however, does not seem true. σ_θ must be nearly zero in this range. If $\sigma_\theta = 0$ is assumed, substituting Eq. (22) into Eq. (1) and integrating it, the following is obtained:

$$r\sigma_r = \left\{\gamma K^2/(1-kK)^2\right\}\left\{(H-z)r-r^2/2K+F(z)\right\}$$

Determining $F(z)$ as $\sigma_r = 0$ at $r = (H-z)/k$, Eq. (38) is obtained.

$$F(z) = (H-z)^2/(2Kk^2)-(H-z)^2/k$$

$$\therefore \ \sigma_r = \frac{\gamma K}{2k^2(1-kK)^2}\frac{1}{r}(H-z-kr)$$

$$\times \left\{(1-2kK)(H-z)+kr\right\} \tag{38}$$

The difference between this solution and Eq. (31) is negligibly small, though Eq. (38) is slightly smaller. Consequently, Eq. (31) can be used practically.

Then, how can the boundaries of regions I and II be determined? When $1/f = \tan\eta'$, the angle between the principal stress direction and σ_z is $2\eta'$ in **Fig. 10**. Then, from Eqs. (17) and (31), Eq. (39) is obtained.

$$\tan 2\eta' = \frac{2\tau_{rz}}{\sigma_z - \sigma_r} = \frac{2K}{1-K'} = \frac{2\tan\eta'}{1-\tan^2\eta'} = \frac{2f'}{f'^2-1}$$

$$\therefore f' = \frac{1}{2}\left(\frac{1-K'}{K} + \sqrt{(\frac{1-K'}{K})^2 + 4}\right) \quad (39)$$

This value of f' is too large, which means that region I is narrow. It is, in fact, most probable that the tangent in the principal stress direction is given by f (Eq. (8)) at the free sur-
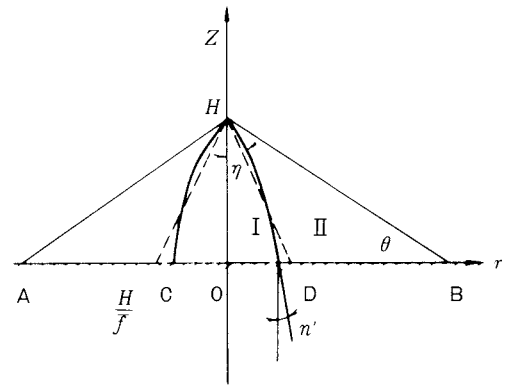
Fig. 13 The boundary of Domain I and II

face (near the top), and by f' (Eq. (39)) at the bottom. Consequently, the following $\bar{f}$ given as,

$$\frac{2}{\bar{f}} = \frac{1}{f} = \frac{1}{f'} \quad (40)$$

This should be used as f in Analysis II. The results are plotted in **Figs. 11** and **12** together with those from Analysis I.

The experimental values are those in **Fig. 5** and **Fig. 6**, non-dimensionalized and divided by γH. The results from Analysis II agree well with the observed values.

It is most probable that the medium state between Analysis I and Analysis II occurs. This state is near to Analysis I at the free surface, while it is near to Analysis II at the bottom. Consequently, the result of Analysis II might be used to seek the stress distribution at the bottom.

5. Conclusion

The stress distribution of granular materials piled conically on the ground has been theoretically analyzed and compared with the experimental data. The following are the results:

(1) Two-directional wall stress cells for low stress (rated normal stress 5080 Pa (50 gf/cm²) and rated frictional stress 1270 Pa (12.5 gf/cm²) have been developed. These perform well.

(2) Using the stress cells mentioned above, a series of experiments using silica sand and millet grains have been carried out. Those have been piled conically on a plate and the stress distribution at the bottom have been observed. It has been found that the normal stress is rather low at the center,
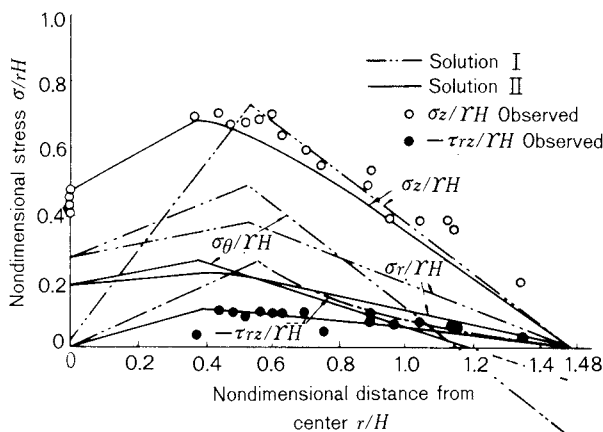

Fig. 11 Bottom stress distribution for Silica Sand
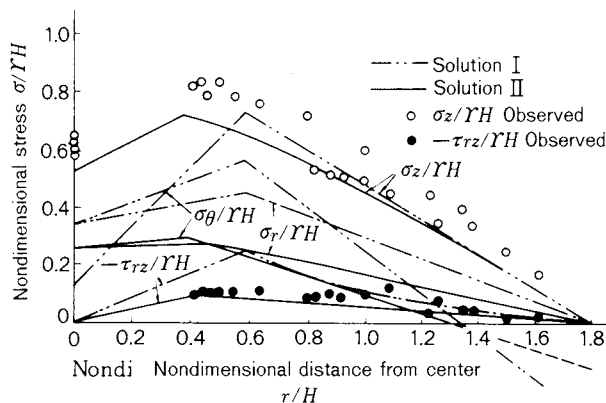$k = 0.675$, $\bar{f} = 2.607$, $K = 0.167$, $d = 0.18$ mm, $r = 1.39$ g/cm³

Fig. 12 The bottom stress distribution for millet grain
$k = 0.554$, $\bar{f} = 2.551$, $K = 0.125$, $d = 1.3$mm, $r = 0.68$g/cm³

and the maximum value appears at about a quarter of the outer radius, which is about 0.7 γH for silica sand and 0.8 γH for millet grains, where γ denotes the apparent specific gravity, and H is the height of the pile. The frictional stress is maximized in the same place, which is about 0.11 γH for silica sand as well as for millet grains.

(3) The theoretical stress analysis agrees well with the experimental data. The analysis has revealed the following:

The maximum value of the normal stress appears at

$$r/H = 1/\sqrt{k(2/K - k)} \text{ and}$$

$$\sigma \max = 0.5\gamma KH(\sqrt{2/K - k} - \sqrt{k})^2/(1 - kK)^2$$

The normal stress at the center is

σ center

$$= \gamma H [1 - K^2(\bar{f} - k)(2/K - k - \bar{f})/(1 - kK)^2]$$

The maximum value of the shearing stress is given by,

$$-\tau \max = K\sigma \max$$

where K denotes the friction coefficient between the granular material and the plate, and k is the internal friction coefficient of the granular material. $\bar{f}$ is given by Eq. (40).

(4) The weight of the pile is proportional to the integration of the normal stress at the bottom. This means that the former can be calculated approximately from the latter. This could be helpful in controlling the stock of granular materials.

6. Acknowledgement

References

1) Jotaki, T. and R. Moriyama: *J. Soc. Powder Technol., Japan*, **16**, 184 (1979).

The Production of Some Ultrafine Particles by Gas Phase Reactions in Aerosol Reactors[†]

Shigeharu Morooka and Katsuki Kusakabe
Department of Applied Chemistry,
*Kyushu University**

Abstract

This paper summarizes the authors' recent studies on properties of TiO_2 and nickel powders produced by gas phase reactions in aerosol reactors.

The weight-average diameter and polymorphism of TiO_2 particles at temperatures lower than 1200°C were virtually unchanged 5-cm downstream from the nozzle mouth, and the effects of the residence time of gas and the reaction temperature were not dominant. However, the mean diameter of nickel powders produced by the hydrogenation of $NiCl_2$ at 1380°C was close to the theory assuming instantaneous fusion of coagulated particles. The fraction of rutile was maximum at ca. 1000°C. These results imply the importance of the fusion rate of particles and the heterogeneous deposition rate from the gas phase.

1. Introduction

Gas phase reactions have been used to produce ultrafine particles with novel functions. Although overall stoichiometric reactions are normally simple, complicated kinetic steps such as nucleation, deposition and fusion are involved. The synthesis of ultrafine particles have been investigated by many authors[4~6, 10~12, 15~17, 20~24], but there are many aspects which require further research.

Titania usually exists in two polymorphic forms; anatase and rutile. The anatase phase is preferentially obtained at lower temperatures, while the rutile phase is the most stable at any temperature and pressure. Matsumoto et al.[10], George et al.[5] and Suyama et al.[20~22] studied the influence of experimental conditions and additives in the gas phase on the properties of TiO_2 particles.

The present paper summarizes studies[11,12] on the production of TiO_2 and nickel particles by gas phase reactions. In particular, the effects of various operating conditions on the particle size and the polymorphic composition of TiO_2 produced by the oxidation of $TiCl_4$ without additives have been investigated[11]. The growth mechanism of nickel particles produced by the hydrogenation of $NiCl_2$[12] is also cited in relationship to TiO_2 particles.

2. Experiment apparatus and procedure

2. 1 TiO_2 production

The first series of the experiment[11] was carried out by using a reactor consisting of two mullite tubes with an inside diameter of 30 mm and length of 600 mm connected in series. The temperature inside the tubes was measured with 0.1 mm diameter platinum/platinum rhodium thermocouples. The reactor was heated by means of a resistance heater. The heated length of each furnace was 390 mm. Nitrogen and oxygen were dried over silica gel and in an ethanol-dry ice trap. $TiCl_4$ was of reagent grade quality. The $TiCl_4$ vapor was fed into the center of the reactor through an alumina nozzle of inside diameter 4 mm and outside diameter 6 mm, and it reacted with the oxygen
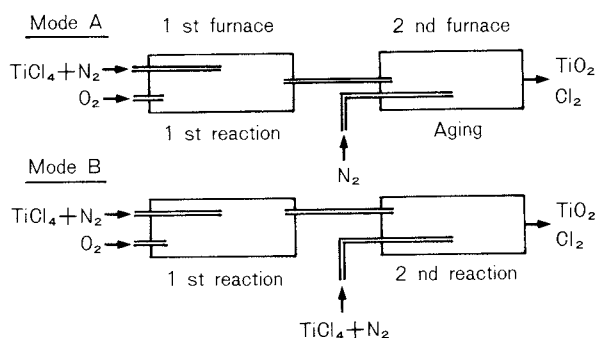
Fig. 1 Reactor modes for aging and 2nd reaction.
$d_T = 30\,\text{mm}$, $d_N = 4\,\text{mm}$: $Q_a(\text{O}_2) = 10\ \text{cm}^3\text{s}^{-1}$,
$Q_n(\text{N}_2) = 3.3\ \text{cm}^3\text{s}^{-1}$, $Q_n(\text{TiCl}_4) = 0.073 - 0.169\ \text{cm}^3\text{s}^{-1}$

which entered through the annular inlet to the reactor. The reaction was carried out at temperatures above 850°C where the TiCl_4 conversion was 100%. The particles produced were trapped on a filter paper in a dust collector. The concentration of TiCl_4 was determined by absorbing Cl_2 formed in the reaction in an aqueous potassium iodide solution.

The following investigation was performed: (1) the effects of the reaction temperature and the TiCl_4 and O_2 concentrations on the TiO_2 particle size and the weight fraction of rutile; (2) the transformation from anatase to rutile when the powder produced in the first furnace was aged in the second furnace (mode A); (3) the growth and transformation of the crystallites when not only the particles produced in the first furnace but also TiCl_4 was fed into the second furnace (mode B).

The experiments of mode A and B are illustrated in **Fig. 1**[11]. The flow rates of N_2 and O_2 in the two modes were constant at 3.3 cm³/ s and 10 cm³/s, respectively, based on 25°C. The particle size was measured by X-ray diffraction (Cu-K_α) and transmission electron-microscopy. The weight fraction of the anatase and rutile particles was calculated from the ratio of the X-ray diffraction intensities by Spurr and Myers'[19] method.

The second series experiment was done by using a reactor with mullite tubes having an inside diameter of 52 mm arranged vertically or horizontally. The TiCl_4 vapor diluted with nitrogen was fed into the center of the reactor via an alumina nozzle of inside diameter 6 mm
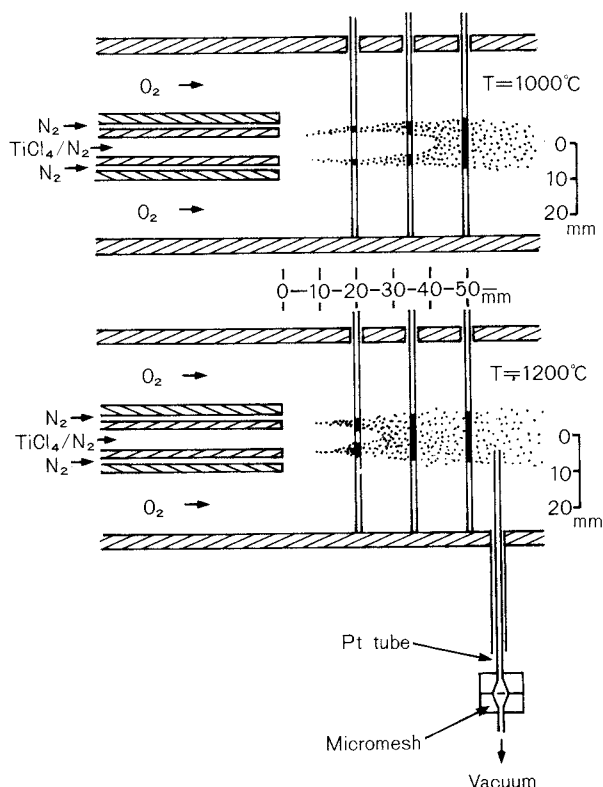

Fig. 2 Examples of reaction zones. $d_T = 52$ mm, $d_N = 6$ mm, horizontal: $Q_a(\text{O}_2) = 25\ \text{cm}^3\text{s}^{-1}$, $Q_s(\text{N}_2) = 13.4\ \text{cm}^3\text{s}^{-1}$, $Q_n(\text{N}_2) = 6.7\ \text{cm}^3\text{s}^{-1}$, $Q_n(\text{TiCl}_4) = 0.24\ \text{cm}^3\text{s}^{-1}$: $t = 0.12$ s

and outside diameter 10 mm. In some runs, particles were sampled by evacuation through a 1 mm i.d. platinum tube from different parts of the reactor, and they directly impinged on the electron microscope grid mounted in a small holder. **Figure 2** shows the direct sampling system. The lateral distribution of the reaction zone was visualized by inserting alumina rods of 1 mm in diameter across the flame.

2. 2 Production of nickel particles

Nickel powders were produced in a vertical reactor of inside diameter of 35 mm[12]. The nozzle was a mullite tube with an inside diameter of 9 mm connected to a mullite tube of 24 mm i.d. The nickel vapor was generated by heating pelletized anhydrous nickel chloride in the evaporating chamber of the nozzle side. The nickel chloride vapor was blown into the reactor through the nozzle using argon as a carrier gas, and it reacted with the hydrogen

66

introduced through the annular space enclosing the nozzle. The rate of vaporization of the nickel chloride was determined by measuring the amount of HCl which was absorbed in aqueous NaOH at the outlet of the reactor.

3. Results and discussion

3. 1 Reaction zone

Figure 2 illustrates a map of the reaction zone in the 52 mm i.d. reactor. Since the concentration of $TiCl_4$ was low, the reaction was controlled by the diffusion of oxygen toward the core of the jet. The length of the unreacted core decreased with increasing reaction temperature. The lateral expansion of the jet was not remarkable because the diffusion of particles was very slow compared to that of gas.

3. 2 Particle size

TiO_2 particles

Figure 3 shows a transmission electron micrograph of the TiO_2 particles collected at the outlet of the furnace. Most particles were round or cubic. The mean diameter of crystallites, calculated from the X-ray diffraction with Si as an internal standard agreed closely with the value obtained by electron-microscopy. This indicates that the particles were single crystals with few defects.

Figure 4[11] reveals the effect of the reaction temperature on the size of the TiO_2 particles. The concentration of $TiCl_4$ is the value in the gas leaving the nozzle. The size of the particles produced in the first furnace (o) decreased somewhat with increasing temperature. The results obtained with the 52 mm i.d. reactor show the same tendency. The mean size of TiO_2 particles sampled 5 cm downstream from the nozzle mouth was nearly equal to that at the reactor outlet. The symbols ● in Fig. 4 represent the particle size in mode A, in which particles were aged at 1000°C in the second furnace, while the symbols ■ denote the particle size in mode B, in which the feed gas was also introduced into the second furnace. There was no change in the particle size when the particles issuing from the first furnace were simply aged at 1000°C in the second furnace.

Figure 5[11] indicates that the particle size increases with increasing initial $TiCl_4$ concentration. The oxygen concentration is the value
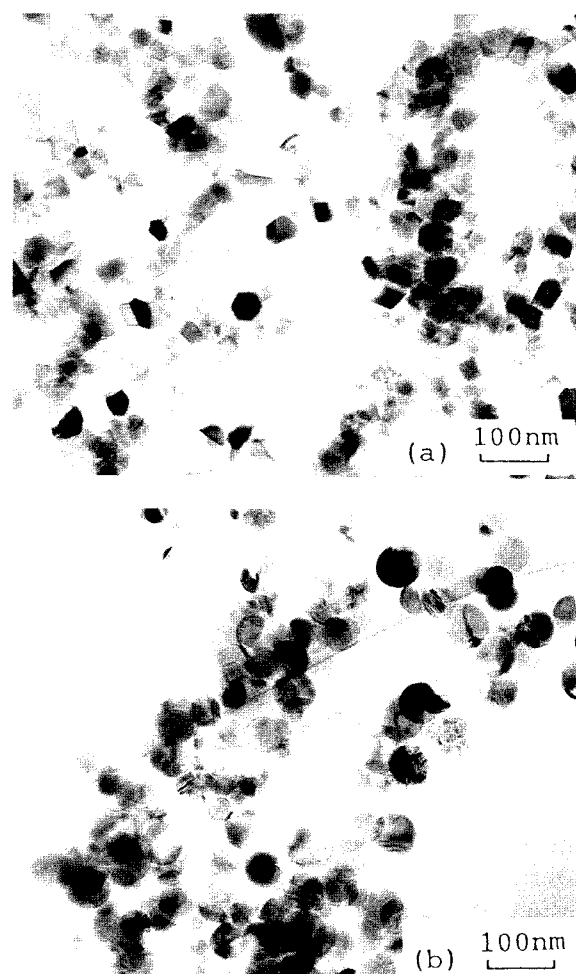

Fig. 3 Examples of TiO_2 particles. (a) 1000°C; (b) 1200°C: The conditions are the same as in Fig. 2: Sampling point = 5 cm downstream from the nozzle mouth

in the gas entering the annular space. The contact time was calculated from the gas velocity through the nozzle, and was roughly 0.4 s.

Assuming that all of the $TiCl_4$ reacts at the nozzle mouth ($t = 0$), and that fresh crystals are produced by instantaneous fusion as a result of interparticle collisions due to the Brownian motion, the mean particle size is given by[7]

$$d_p = 1.88 \ (6kT/\rho_s)^{1/5} \psi^{2/5} t^{2/5} \tag{1}$$

where the effective residence time in the furnace, t, is calculated at the reaction temperature. The experimental data of d_p is 5 times smaller than Eq. (1) at 1000°C and 3 ~ 4 times smaller at 1100°C, respectively. The above results show that the growth of TiO_2 particles
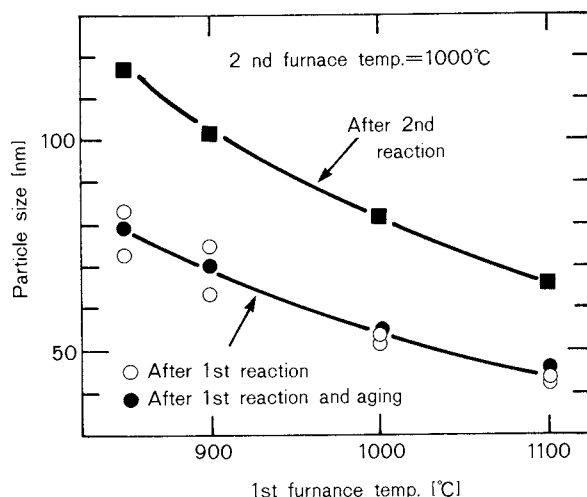
Fig. 4 The effect of 1st furnace temperature on weight-mean particle diameter. $d_T = 30$ mm, $d_N = 4$ mm: 1st furnace; Q_n (TiCl$_4$) = 0.14 − 0.17 cm^{3}s^{-1}, 2nd furnace; Q_n(TiCl$_4$) = 0.10 − 0.13 cm^{3}s^{-1} (in case of 2nd reaction), other flow rates are the same as in Fig. 1.

ended within 5 cm downstream from the nozzle mouth. The growth by intra-aggregate fusion of coagulated particles[23,24] at 1000°C hardly occurred after the particles grew beyond 50 ~ 60 nm under the condition tested. Similar results were reported by Suyama and Kato[21] at 1100°C.

The fusion of TiO$_2$ particles is controlled by the surface diffusion of oxygen ions[1,2,13,14]. Nichols and Mullins[13] simulated the coalescence of a sphere onto a wall. The surface diffusion coefficient of TiO$_2$ was given by Anderson[1] as follows:

$$bD_B/(\text{m}^3.\text{s}^{-1}) = 3.5 \times 10^{-16} (T/\text{K})$$
$$\times \exp(322\text{kJ}.\text{mol}^{-1}/RT) \quad (2)$$

The calculation indicates that the fusion of TiO$_2$ crystals larger than serveral nm in diameter is not significant in the range of $T < 1200°$C under the present experimental conditions.

When a second reaction was carried out at 1000°C, however, the particle diameter increased by about 1.5 times (equivalent to a 3.3-fold increase in the volume) as shown in **Fig. 4**[11]. Therefore, the growth of larger particles is considered to proceed via the heterogeneous deposition of TiCl$_4$ as well as the coalescence of very small particles. The coincidence of the
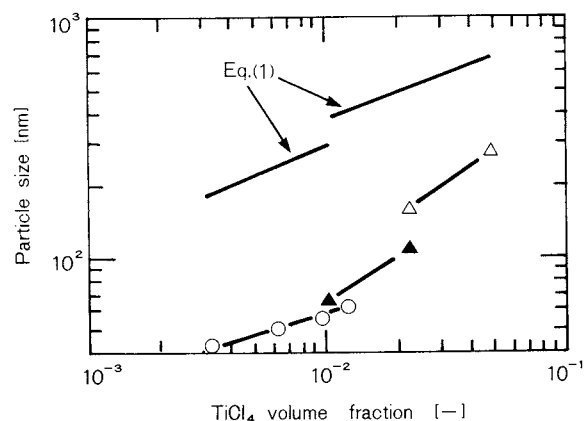

Fig. 5 The effect of TiCl$_4$ concentration on weight-mean particle diameter after 1st reaction. Q_a(N$_2$ + O$_2$) = 10 cm^{3}s^{-1}, Q_n(N$_2$) = 3.3 cm^{3}s^{-1}: ○, C_{o2} = 0.50, T = 1000°C, t = 0.4 s; △, C_{o2} = 0.48, T = 1100°C, t = 0.46 s, Suyama et al.[21], ▲, C_{o2} = 0.97, T = 1100°C, t = 0.46 s, Suyama et al.[21]
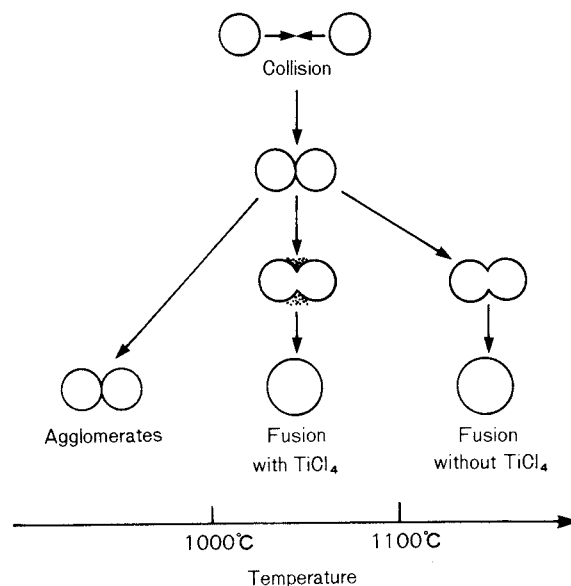

Fig. 6 Schematic concept of particle growth

data of George et al.[5] with Eq. (1) is due to the high temperature of their reaction. Particle growth by simple aging was also observed when the second furnace was kept at 1200°C.

The growth mechanism of TiO$_2$ particles is summarized in **Fig. 6**[11]. The residence time of the particles in the reactor was in the range of 0.05 ~ 0.3 s in the present experiment. This was not long enough for agglomerated particles
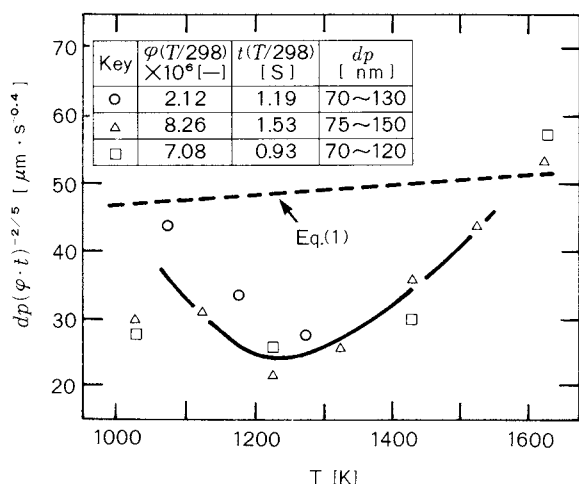
Fig. 7 The effect of temperature on weight-mean particle diameter of nickel. $d_T = 35$ mm, $d_N = 9$ mm: O, $Q_n(Ar) = 11$ cm^{3}s^{-1}, $Q_a(Ar) = 39$ cm^{3}s^{-1}, $Q_a(H_2) = 1.7$ cm^{3}s^{-1}, $Q_n(NiCl_2) = 0.13$ cm^{3}s^{-1}; □, $Q_n(Ar) = 11$ cm^{3}s^{-1}, $Q_a(Ar) = 39$ cm^{3}s^{-1}, $Q_a(H_2) = 1.7$ cm^{3}s^{-1}, $Q_n(NiCl_2) = 0.20$ cm^{3}s^{-1}; △, $Q_n(Ar) = 6.7$ cm^{3}s^{-1}, $Q_a(Ar) = 16.7$ cm^{3}s^{-1}, $Q_a(H_2) = 1.7$ cm^{3}s^{-1}, $Q_n(NiCl_2) = 0.20$ cm^{3}s^{-1}

Fig. 8 The effect of 1st furnace temperature on rutile fraction. The experimental conditions are the same as in Fig. 4

to fuse into larger particles at temperatures below 1100°C. However, when some unreacted titanium chloride was present, filling the space between the attached particles, fusion occurred at temperature of 1000°C. This is also valid for particles larger than a few tens of nm. Any smaller particles would probably have coalesced at lower temperatures.

Nickel particles

Figure 7[12] shows the effect of temperature on the mean size of nickel particles. The mean particle size is virtually equal to the theoretical value of Eq. (1) at 1380°C which is close to the melting point of nickel (1450°C).

3. 3 Fractional rutile content

Figure 8[11] shows the effect of the reaction temperature on the weight fraction of rutile in the TiO$_2$ particles. Suyama et al.[20] reported that the weight fraction of rutile increased with increasing reaction temperature. However, the present results as well as those of Matsumoto et al.[10] indicate that the weight fraction of rutile was at a maximum when the temperature of the first reactor was 1000°C. The existence
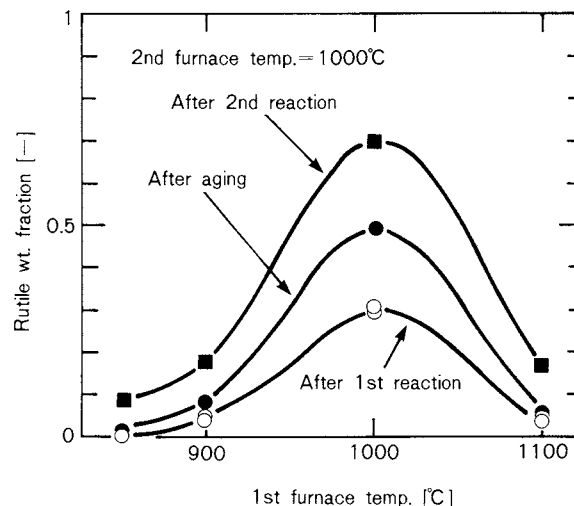
of this maximum in the rutile content was observed irrespective of reactor dimensions and whether or not an aging or a second reaction took place in the second furnace. The rutile fraction in the particles sampled at 5 cm downstream from the nozzle coincides with that at the exit of the reactor. It was reported that the rutile content in a flame reactor operated at 1450 ∼ 1650°C was very low[4].

Shannon and Park[18] and others[3,8,9] have indicated that the rutile phase is nucleated on the surface and then spreads in the anatase body. The anatase-rutile transformation rate is given by,

$$(1 - \alpha)^{1/3} = c - 2k_r t/(\rho_s d_p) \qquad (3)$$

where α is the fraction of transformation completed. **Figure 9** shows the coefficient of the transformation on the basis of Eq. (3). Even at 1200°C, the transformation rate is very slow, and the spreading rate of the rutile phase is in the order of 0.1 nm·s^{-1}. Thus, within the residence time of the present experiment (0.05 − 0.3 s), only several layers of the anatase structure could be transformed into the rutile. The decrease in the rutile content at higher temperatures can be explained by the following mechanisms.

(I) Competitive reaction model[11,22]

Figure 10 illustrates this model[11]. The first

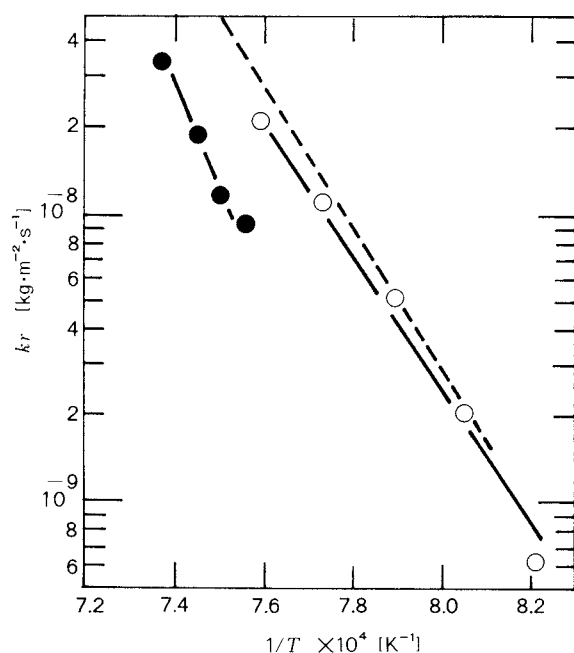Fig. 9 Arrhenius plot of anatase-rutile transformation.
○, calculated from ref. 8 and 9; ●, U-110 ref. 18;
broken line, ZSD ref. 18

Fig. 10 Schematic concept of transformation
(Model I)

stage of the reaction is the preferential forma-
tion of clusters of anatase. The clusters of
anatase either grow into anatase particles or
else are transformed into clusters of rutile. As
soon as the anatase clusters grow into anatase
particles, the transformation virtually stops.
With increasing reaction temperature, the rate
of transformation of the anatase particles into
rutile decreases because the rate of fusion in-
creases.

(II) Heterogeneous deposition model

As shown in **Fig. 8**, the rate of formation of
rutile particles in the second reaction is strong-
ly affected by the polymorphic phase composi-
tion of the particles entering the second fur-
nace. This implies the heterogeneous deposi-
tion of rutile from gaseous $TiCl_4$ on the parti-
cle surface which is already transformed to
rutile is important. At higher temperatures,
$TiCl_4$ reacts with oxygen more quickly to form
TiO_2 particles. Thus, $TiCl_4$ disappears at an
earlier stage of the reaction. After the con-
sumption of $TiCl_4$, an increase in the rutile
fraction may not be expected.

To specify the mechanism for the formation
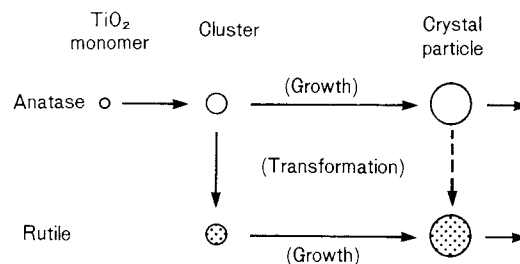of rutile particles, it is important to evaluate

the mass transfer rate of oxygen into the core
of the jet and the reaction rate of $TiCl_4$ with
oxygen[21]. Future research must focus on this
point.

4. Conclusion

Ultrafine TiO_2 particles were produced by
gas phase oxidation of $TiCl_4$ without additives
in aerosol reactors operated in the laminar
regime. The weight-average diameter of TiO_2
particles increased with an increase in the $TiCl_4$
concentration. The reaction terminated within
5 cm downstream from the nozzle mouth, and
the effects of the residence time of gas and the
reaction temperature were not dominant. The
mean diameter of nickel powders produced by
the hydrogenation of $NiCl_2$ at 1380°C was
close to Eq. (1). The intra-aggregate fusion was
strongly related to the heterogeneous deposi-
tion and the temperature.

The fraction of rutile took a maximum at ca.
1000°C. Models were proposed for the expla-
nation, but more research is needed to eluci-
date the exact mechanism.

Nomenclature

b	:	thickness of diffusion
C_{o2}	:	volume fraction of oxygen
c	:	constant
D_B	:	surface diffusion coefficient
d_T	:	inside diameter of reactor
d_N	:	inside diameter of nozzle
d_p	:	weight-mean diameter of primary particles
k	:	Boltzmann constant
k_r	:	reaction rate coefficient defined by Eq. (3)
L	:	length of reaction space
$Q_a(i)$	:	flow rate of i-component in annular space. The volume of gas is measured at 25°C
$Q_n(i)$	:	flow rate of i-component in nozzle space. The volume of gas is measured at 25°C

$Q_s(N_2)$: flow rate of sheath gas measured at 25°C. The velocity is equal to that of nozzle gas.

R : gas constant

T : reaction temperature

t : residence time of nozzle gas calculated at reaction temperature

α : fraction of rutile

ρ_s : density of particles

ψ : volume fraction of solids at reaction temperature

References

1) Anderson, H. U.: *J. Am. Ceram. Soc.,* **50**, 235 (1967).

2) Brailsford, A.D. and N.A. Gjostein: *J. Applied Phys.,* **46**, 2390 (1975).

3) Criado, J. and C. Real: *Chem. Soc. Farad. Trans.* 1, **79**, 2765 (1983).

4) Formenti, M., F. Juillet, P. Meriaudeau, S.J. Teichner and P. Vergnon: *J. Colloid Interface Sci.,* **39**, 79 (1972).

5) George, A.P., R.D. Murley and E.R. Place: *Symp. Farad. Soc.,* No. 7, 63 (1973).

6) Kirkbir, F. and H. Komiyama: *Can. J. Chem. Eng.,* **65**, 759 (1987).

7) Lai, F.S., S.K. Friedlander, J. Pich, and G.M. Hidy: *J. Colloid Interface Sci.,* **39**, 395 (1972).

8) Mackenzie, K.J. D. and P.J. Melling: *Trans. J. Brit. Ceram. Soc.,* **73**, 23 (1974).

9) Mackenzie, K.J.D.: *Trans. J. Brit. Ceram. Soc.,* **74**, 77 (1975).

10) Matsumoto, A., S. Sakamoto, J. Shiokawa, H. Tamura and T. Ishino: *Kogyo Kagaku Kaishi,* **70**, 2115 (1967).

11) Morooka, S., T. Yasutake, A. Kobata, K. Ikemizu and Y. Kato: *Kagaku Kogaku Ronbunshu,* **13**, 159 (1987).

12) Morooka, S., A. Kobata, T. Yasutake, K. Ikemizu and Y. Kato: *Kagaku Kogaku Ronbunshu,* **13**, 481 (1987).

13) Nichols, F.A. and W.W. Mullins: *J. Applied Physics,* **36**, 1826 (1965).

14) O'Bryan, Jr., H.M. and G. Parravano: *Mater. Sci. Eng.,* **1**, 177 (1966).

15) Okuyama, K., Y. Kousaka, N. Tohge, S. Yamamoto, J.J. Wu, R.C. Flagan and J.H. Seinfeld: *AIChE J.,* **32**, 2010 (1986).

16) Otsuka, K., H. Yamamoto and A. Yoshizawa: *Nippon Kagaku Kaishi,* **1984**, 869 (1984).

17) Pratsins, S.E., T.T. Kodas, M.P. Dudukovic and S.K. Friedlander: *Ind. Eng. Chem. Process Des. Dev.,* **25**, 634 (1986).

18) Shannon, R.D. and J.A. Park: *J. Am. Ceram. Soc.,* **48**, 391 (1965).

19) Spurr, R.A. and H. Myers: *Anal. Chem.,* **29**, 760 (1957).

20) Suyama, Y., K. Ito and A. Kato: *J. Inorg. Nucl. Chem.,* **37**, 1883 (1975).

21) Suyama, Y. and A. Kato: *J. Am. Ceram. Soc.,* **59**, 146 (1976).

22) Suyama, Y., K. Ohmura and A. Kato: *Nippon Kagaku Kaishi,* **1976**, 584 (1976).

23) Ulrich, G.D. and J.W. Riehl: *J. Colloid Interface Sci.,* **87**, 257 (1982).

24) Ulrich, G.D. and N.S. Subramanian: *Combust. Sci. Technol.,* **17**, 119 (1977).

The Agglomeration Mechanism of Phenytoin (Antiepileptic) by a Novel Agglomerated Crystallization Technique[†]

Yoshiaki Kawashima, Tetsurou Handa,
Hirofumi Takeuchi and Motonari Okumura
Dept. of Pharmaceutical Engineering
Gifu Pharmaceutical University *

Abstract

Novel agglomerated crystallization techniques, i.e., neutralization and solvent change, methods, were devised in order to design phenytoin (antiepileptic) crystals so as to be directly compounded during their formulation. The proposed techniques could directly transform the fine precipitated crystals into free-flowing spherical agglomerates during crystallization. Agglomeration by neutralization and solvent change was described in terms of a random-coalescence model and a mixed model with layering, respectively. The micromeritic properties of the agglomerates, e.g. surface topography, particle density and mechanical strength, depended on the agglomeration mechanism. The consolidation of the agglomerates in the neutralization process was represented by a function of the agglomeration rate constants.

1. Introduction

The quality of a powder product and the efficiency with which it is prepared are dependent upon the physical properties of the powder subjected to processing. The primary properties of a powder determine the quality of the product; the secondary properties determine the efficiency with which it is prepared. For example, when a drug that is not easily soluble is prepared, it is desirable to have it done so in a fine crystalline form from the viewpoint of bioavailability. Indeed, the reduction of a powder to finer particles markedly improves its primary properties, such as solubility. On the other hand, it increases the tendency of the particles to cohere so much that their secondary properties, such as flowability and ease of packing, deteriorate. As a result, it becomes necessary to process the powder through a series of additional steps, such as

forming a mixture of the ground product with a filler so to become granules. It would be a significant accomplishment if a particle-design method developed whereby powder particles simultaneously assumed both of the desired primary and secondary properties. With a view to developing such a compounded process, these researchers had sought a way[1,2] to control the secondary properties of crystals by agglomeration, simultaneously controlling the primary properties during crystallization. The primary properties are crystal form, particle size, and the like, while the secondary properties are those of the agglomerates formed from the precipitated crystals. Such a dual control has not been feasible by any of the conventional crystallization methods. The processes dealt with in this paper should extend the crystallization technology.

These researchers previously observed[1] that when a mixed solvent composed of chloroform, ethyl alcohol, and water was used in the crystallization of salicylic acid, a phase separation was forced to occur by adjusting the composition of the solvent and by liberating a slight amount of chloroform in a phase which caused the precipitated crystals to agglomerate into

---

* 5-6-1, Mitahorahigashi, Gifu, 502
  TEL. 0582 (37) 3931

spherical granules. This phenomenon is due to the capability of the liberated chloroform to function as a bridging liquid[2], which forms a liquid-bridge between hydrophobic salicylic acid crystals. The resultant capillary attraction causes the crystals to agglomerate. In this paper, this theory was expanded to introduce new methods for designing phenytoin in particles, a drug which is not easy to dissolve and the bioavailability of which varies strikingly according to the method used for its preparation. It is known that[3] the concentration of phenytoin in blood, when orally administered, is heavily dependent upon the particle size, and its bioavailability is enhanced by upgrading the fineness of the particles[3]. It is desirable, therefore, to develop a new method for designing phenytoin in particles with a view to overall improvement. With this objective in mind, the present research focussed on the development of a new crystallization process by which very fine crystals of phenytoin could be precipitated and directly agglomerated, simultaneously, without the use of any additive, such as a binder. To do this, a neutralization method and a solvent change method were both devised. The agglomerates thereby obtained were subjected to the measurement of their micromeritic properties — particle size, density, and

mechanical strength (friability) — and the mechanisms of the agglomerated crystallization in the two methods and the process of consolidation of the agglomerates were analyzed.

2. Experiments

2. 1 Agglomerated crystallization

Two methods — a neutralization method and a solvent change method — were devised for the agglomerated crystallization.

The neutralization method

Many drugs show either an acidic or a basic property. As an effective method for reducing such a drug to finer particles, there is a neutralizing technique[4] in which the drug is converted into a salt, and then an alkali or acid is added. In the present research, phenytoin (Aleviatin, a product of the Dainippon Pharmaceutical Co.) was dissolved in 1N sodium hydroxide at 40°C, while an aqueous solution of hydrochloric acid in which isopropyl acetate was dispersed as a bridging liquid was prepared and maintained at 20°C in a glass-made cylindrical stirring vessel (diameter 8.4 cm, height 10.8 cm). This solution, which contained isopropyl acetate, was stirred with a 6-vane turbine type stirrer (diameter 4.8 cm, at

(a) Neutralization method   (b) Solvent change method

Isopropyl acetate was miscible (M) in the left region and immiscible (I) in the right region to the solid line.
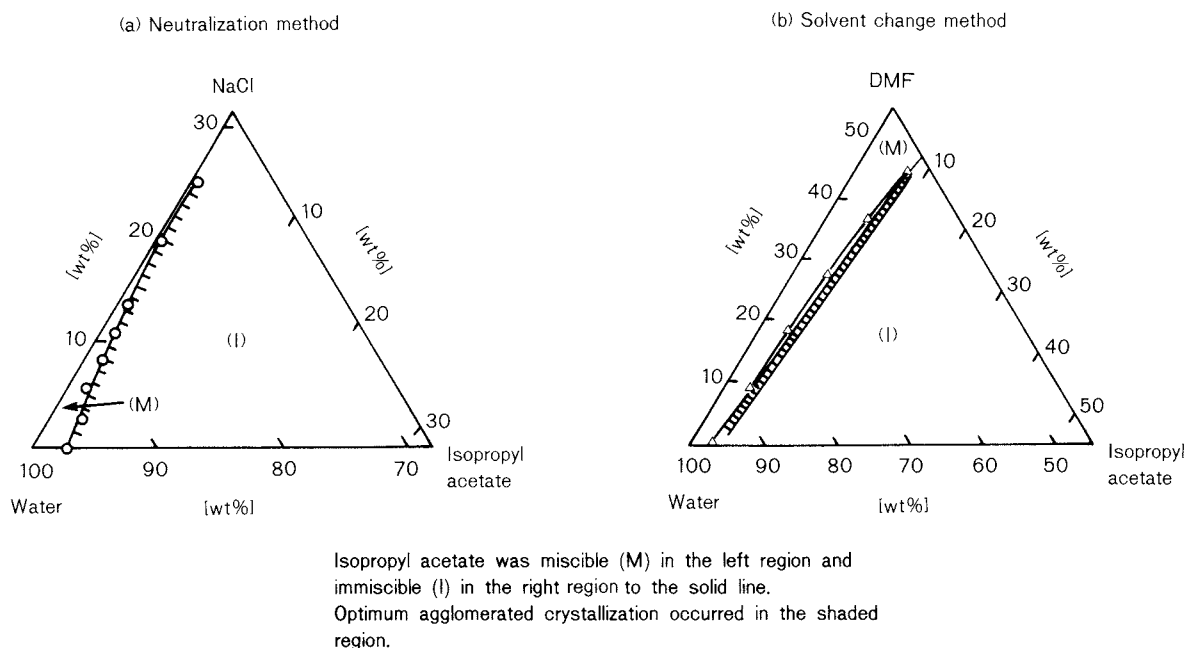Optimum agglomerated crystallization occurred in the shaded region.

Fig. 1 Solubility diagram of isopropyl acetate in agglomerated crystallization system

600 rpm) after the addition of the aqueous NaOH solution of phenytoin so as to cause the phenytoin to precipitate in fine crystals by neutralization. Then, depending on the proportion of the isopropyl acetate in the composition, the mixture was observed either to become a homogeneous solution or to separate into an aqueous phase and a phase of isopropyl acetate. Also, it was observed that whereas the crystals which precipitated from the homogeneous solution were dispersed, the crystals which precipitated in the presence of free isopropyl acetate in slight amounts immediately agglomerated by forming a liquid-bridge with the isopropyl acetate. The quantity of isopropyl acetate necessary to cause the agglomerated crystallization was determined by a solubility diagram of isopropyl acetate in a three-component system of common salt, water and isopropyl acetate (**Fig. 1 (a)**), which was formed separately in consideration of the formation of common salt by neutralization. The agglomerated crystallization was possible in the region along the phase separation curve. The crystals precipitating in a dispersed state were in the left (M) region where the solution formed a homogeneous phase, and the crystals forming agglomerates or slurries were in the right (I) region. **Table 1** shows the compositions formulated accordingly. In this research, the agglomerated crystallization was examined both for varied and fixed concentrations of phenytoin, that is, for varied loading quantities of phenytoin against fixed quantities of the liquids used in combination, and for fixed proportions in which the respective quantities of sodium hydroxide and the liberated bridging liquid were adjusted to varied loading quantities of phenytoin. The aqueous hydrochloric acid solution was used in concentrations necessary for the neutralization. Upon the termination of the agglomeration, the pH of the crystalization solvent was examined (pH = 3 ~ 4) so as to confirm that crystallization had been completed. Experiments showed that, in this method, the quantity or concentration of the medicament in the feeding solution could be adjusted relatively easily by changing the concentration of the alkali or acid. Moreover, unlike the solvent change method described next, there was no need to consider whether or not increases in the solubility of the medica-

Table 1 Formulation for agglomerated crystallization

Neutralization method

Phe* [g]	1N NaOH [mℓ]	Hydrochloric acid [N, mℓ]	Isopropyl acetate [mℓ]
3.0	20	0.071, 280	13.5
3.5	20	0.071, 280	13.5
4.0	20	0.071, 280	13.5
2.0	10	0.034, 290	12.0
8.0	40	0.154, 260	16.5

Solvent change method

Phe* [g]	DMF* [mℓ]	Water [mℓ]	Isopropyl acetate [mℓ]
4.0	8	292	14.5
4.0	8	292	15.0
4.0	8	292	15.5
2.0	4	296	12.8
8.0	16	284	19.5

* Phe : phenytoin
DMF : dimethylformamide

ment and bridging liquid were attributable to the use of the mixed solvent. Therefore, the conditions for agglomerated crystallization could be set easily by means of the solubility diagram shown in **Fig. 1 (a)**.

Solvent change method

One commonly known method to reduce crystals to finer particles is to pour a solution of a medicament in a good solvent into a poor solvent[4]. The present experiments incorporated a process for agglomerating the fine crystals into this known method. Dimethylformamide (DMF) was used as a good solvent, and water was used as a poor solvent. Isopropyl acetate was used as a bridging liquid. In the experiments on the solvent change method based on DMF, agglomeration was examined in two ways: by varying the quantities of bridging liquid against fixed quantities of loading phenytoin, DMF and water; and by varied the quantities of phenytoin against a fixed loading concentration of phenytoin in a DMF solution. A solubility diagram of isopropyl acetate in the mixed solvent (**Fig. 1 (b)**) was drawn in a manner similar to that in the neutralization method so as to determine the composition in which a crystallization solvent consisting of DMF, water and isopropyl acetate was pre-

pared. **Table 1** shows the formulated compositions, which are in the shaded region indicating the possibility of agglomeration in **Fig. 1**. The conditions of the experiments, such as the method of stirring and temperature, were the same as those for the neutralization method.

In order to clarify the agglomeration mechanism of the crystals in the solvent change method, the experiments used a system containing no bridging liquid to compare the results. Crystals were made to precipitate without the addition of a bridging liquid, and then immediately, 5 mℓ of the suspension of the crystals was sampled and put into a stoppered measuring cylinder (25 mℓ). To this sample was added an aqueous solution of a surface-active agent [0.1% Tween 80 (polyoxyethylene sorbitan monooleate)] saturated with phenytoin to make 25 mℓ of the sample. After being stirred by shaking upside down, the sample was left to stand for 30 seconds. Then the top 8 mℓ portion of the sample was removed, and the same aqueous solution of Tween 80 saturated with phenytoin was added to the remaining sample to make 25 mℓ of the sample. This same procedure was carried out ten times so as to separate the crystals into dispersed and agglomerated ones. The collected agglomerated crystals were measured with respect to weight and particle diameter under a microscope.

2. 2 The micromeritic properties of agglomerated crystals

The agglomerated crystals were evaluated with respect to their micromeritic properties. This was done by measuring the particle diameters of both the agglomerates and the crystals constituting the agglomerates, as well as the apparent density and the friability of the agglomerates.

The particle diameters of the agglomerates were obtained by sieve analysis and those of their constituent crystals by dispersing them in liquid paraffin and using a microscope. The apparent density ρ_{ap} of the agglomerates was obtained with respect to samples, the weight W of which was known by first calculating the volume from the diameter d of the projected area and then by using the equation,

$$\rho_{ap} = \frac{W}{\Sigma \frac{\pi}{6} d^3} \tag{1}$$

The evaluated micromeritic properties included, the friability of the agglomerated crystals because since such agglomerates are assumed to be subjected immediately to drug preparation, pharmaceutical industries attach importance to friability as a mechanical strength. The friability was determined by a procedure in which agglomerates (W_o = approx. 3 g) correspond to the granule size range (297 ~ 1,410 μm) specified in the Japanese Pharmacopoeia. These were loaded onto a No. 80 sieve (sieve opening 177 μm) and given continuous impacts by a low tap type sieving machine (Model ES-65, product of Iida Manufacturing Co.) to periodically measure the weight (W_p) of the particles which pass through the sieve. The friability was obtained as $X = W_p/W_o$.

3. Observations

3. 1 The micromeritic properties of agglomerated crystals

The obtained agglomerated crystals were observed to be spherical and to have a free-flowing property. Their particle size was seen to be controlled by the amount of the bridging liquid added to the crystallization system. **Figure 2** shows the relationship between the average particle diameter of the agglomerated
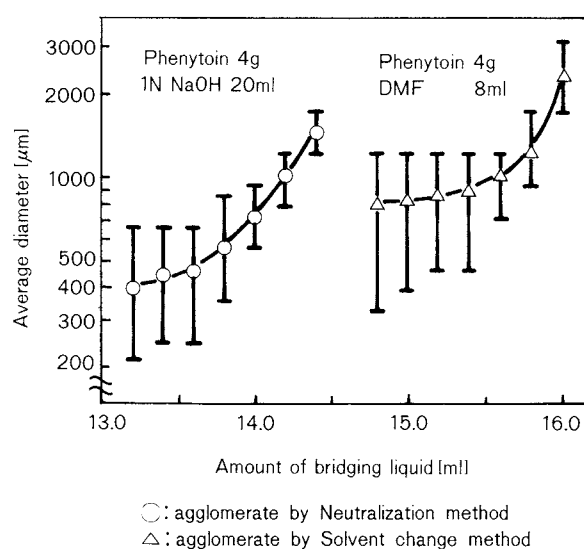
Fig. 2　Average diameter of agglomerates as a function of amount of bridging liquid
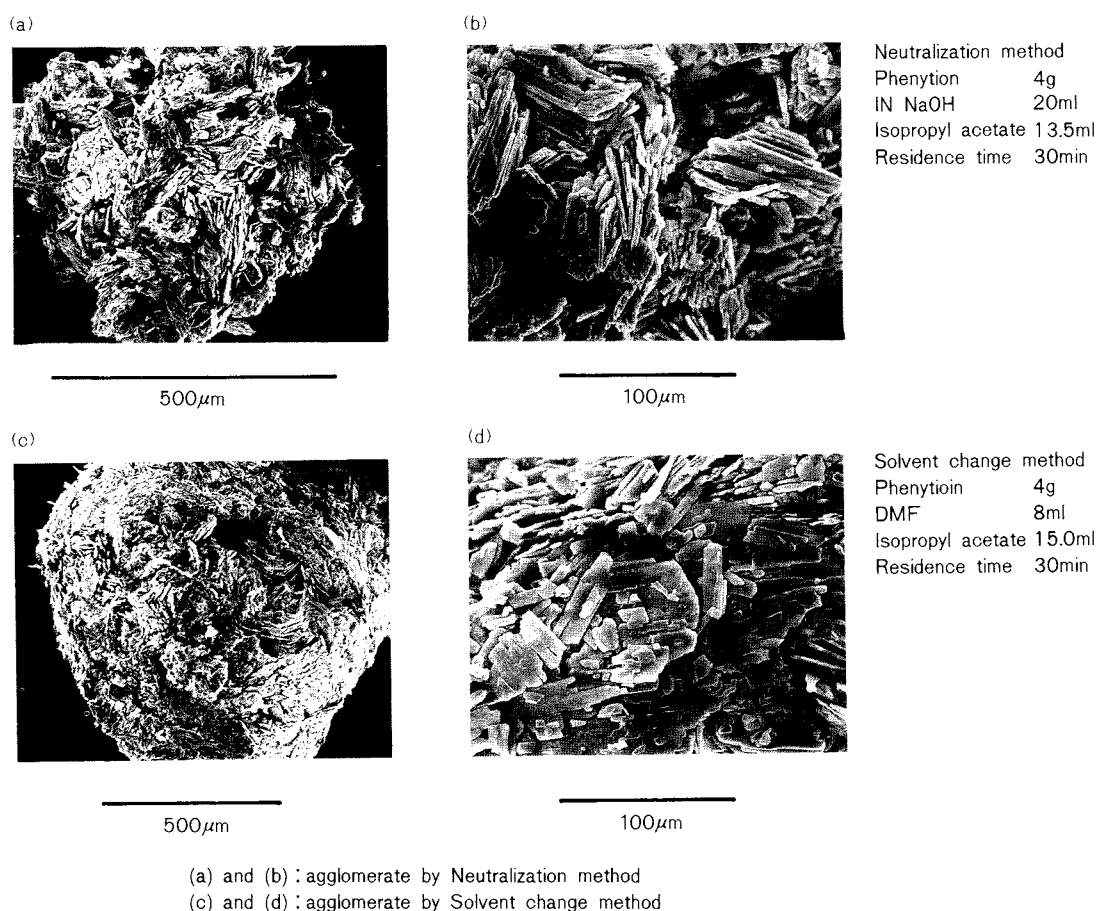
(a)

(b)

Neutralization method
Phenytion   4g
IN NaOH   20ml
Isopropyl acetate 13.5ml
Residence time   30min

500μm

100μm

(c)

(d)

Solvent change method
Phenytioin   4g
DMF   8ml
Isopropyl acetate 15.0ml
Residence time   30min

500μm

100μm

(a) and (b) : agglomerate by Neutralization method
(c) and (d) : agglomerate by Solvent change method

Fig. 3 Scanning electron microphotographs of agglomerates

crystals and the amount of the bridging liquid used for 30 minutes in a process of agglomerated crystallization. In both methods, an increase in the amount of the bridging liquid used caused the particle diameter of the agglomerates to increase, as already reported[5]. As was predicted from the solubility diagrams of the bridging liquid in **Fig. 1**, the amount of bridging liquid required to yield agglomerates of an equal particle size was more in the solvent change method than in the neutralization method. As shown in **Fig. 2**, the particle size distributions indicated by a standard deviation had a broad range, and the particle diameters as a whole were larger in the solvent change method than in the neutralization method. The solvent change method presented a solid-liquid interfacial phenomenon which was not observed in the neutralization method because DMF was mixed in the crystallization solvent and bridging liquid.

Figure 3 shows photographs of agglomerates

taken by a scanning electron microscope (JSM-T20, product of Nihon Electronics Co.). No difference was observed between the two methods with respect to the shape and particle diameter of the primary crystals that constituted the agglomerates (see **Fig. 4**), but there were differences in the surface features of the agglomerates and the patterns in which crystals agglomerated. Sub-units of sizes ranging from 40 to 90 μm, that probably formed by coalescence, were observed in the agglomerates in the neutralization method, however, the agglomerates in the solvent change method were shown to be favorably spherical in shape. Their surfaces were densely built of plate-shaped crystals, and their structures suggested the agglomeration of crystals by the layering agglomeration mechanism.

Figure 4 shows the particle size distributions of agglomerates of crystals and crystals constituting the agglomerates, determined by a microscopic method. The particle sizes were,
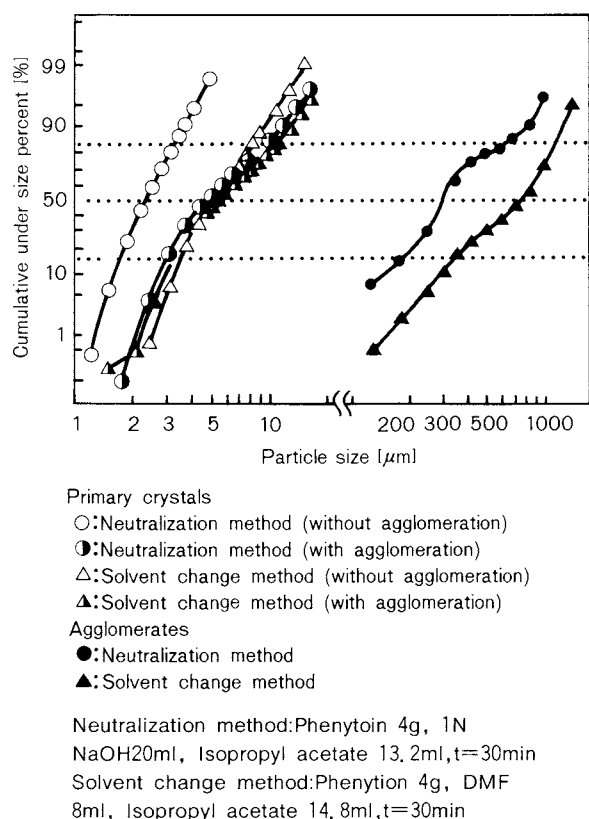
Fig. 4 Particle size distributions of agglomerates and
primary crystals composing agglomerates

Primary crystals
○:Neutralization method (without agglomeration)
◑:Neutralization method (with agglomeration)
△:Solvent change method (without agglomeration)
▲:Solvent change method (with agglomeration)
Agglomerates
●:Neutralization method
▲:Solvent change method

Neutralization method:Phenytoin 4g, 1N
NaOH20ml, Isopropyl acetate 13.2ml,t=30min
Solvent change method:Phenytion 4g, DMF
8ml, Isopropyl acetate 14.8ml,t=30min

larger with respect to the crystals which constituted agglomerates in both methods. The crystals which did not agglomerate in the solvent change method were also larger than the crystals which did not agglomerate in the neutralization method. It is considered that the solubility of phenytoin in the crystallization solvent was enhanced because of the addition of DMF and isopropyl acetate, so that the degree of supersaturation of phenytoin was lowered, and the particle diameter of the precipitated crystals consequently increased[6]. In fact the solubility of phenytoin in the crystallization solvent was increased by 1.4 ~ 1.7 times more than the solubility in cases where no briding liquid was used in the neutralization method. As is clear from Figs. 3 and 4, there was no difference between the neutralization method and the solvent change method with respect to the size of the crystals that constituted the agglomerates; nor was there any difference in the shape or the crystals between the two methods.

Although there were differnces in particle diameters and surface features of the agglom-

erates depending on the method of crystallization described above, the experiments produced spherical agglomerates which were free-flowing, each having a diameter of 0.2 ~ 1 mm and composed of fine crystals with a diameter in the range of 3 ~ 11 μm. It was also observed that the particle diameter of the agglomerates could be changed as desired by adjusting the amount of the bridging liquid used.

Next, the friability of the agglomerates was examined. As shown in **Fig. 3**, it was observed that whereas the surface of an agglomerate obtained by the neutralization method was jagged and thinly composed of crystals, the surface of an agglomerate by the solvent change method was densely composed of crystals. This structural difference was considered to have a bearing upon the mechanical strength of the agglomerate. The friability of the agglomerates was examined by a test in which they were impacted with a low tap, type sieving machine. The results are shown in **Fig. 5**. These data were processed[7] by the equation,

$$R_n(x) = R_0(x) \cdot (1 - Pr)^n \qquad (2)$$

where Pr represents the probability of breakage per impaction due to abrasion and destruction and is estimated for each number of times (n) dropped, and $R_n(x)$ is the cumulative weight percent over size x on a sieve with a sieve opening of x (80 mesh). In the friability test of spherical agglomerates, the relationship between the pulverized fraction X and the time t_f is expressed by Eq. (3), which was formulated on the reasoning that the rate of friability is proportional to the surface area of the agglomerates:

$$\sqrt[3]{1-X} = 1 - \frac{2k\phi}{\rho_{ap}D_0} t_f \qquad (3)$$

where k is the friability rate constant, D_0 is the diameter of the agglomerates prior to the test, ρ_{ap} is the apparent density of the agglomerates, and ϕ is the shape factor. The agglomerates obtained by the neutralization method were pulverized in accordance with Eq. (2) and Eq. (3). As a result, the agglomerates obtained by that method were observed to be progressively pulverized from the surface through abrasion, and the cohesive force (= strength) acting between the constituent crystals was
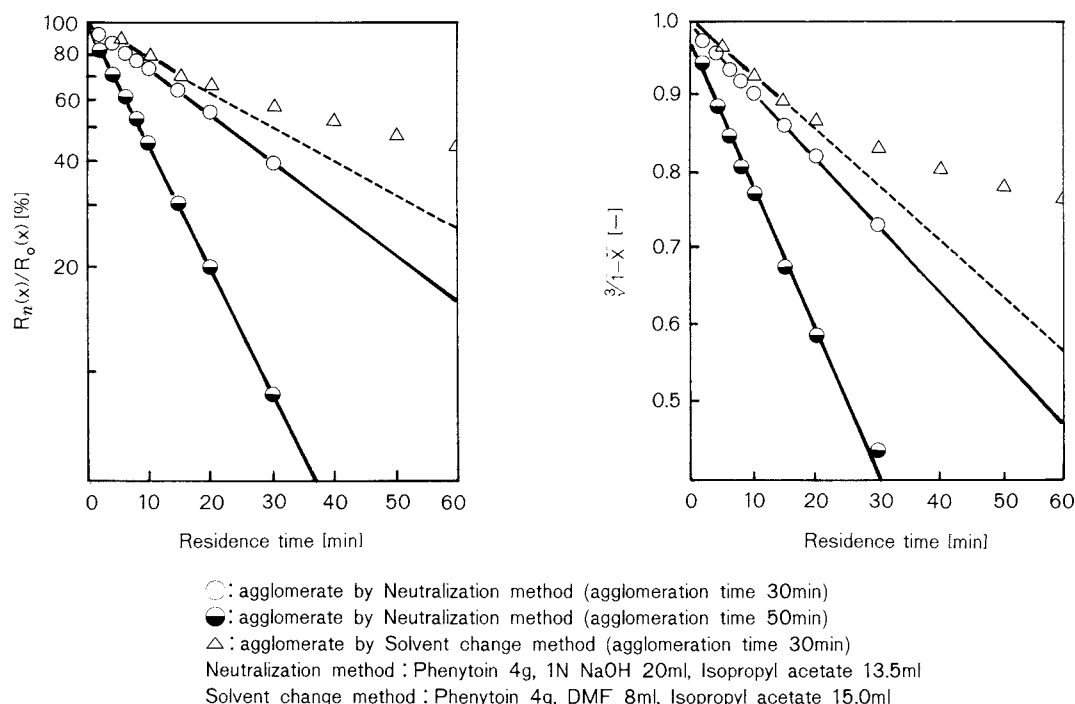
○ : agglomerate by Neutralization method (agglomeration time 30min)
◑ : agglomerate by Neutralization method (agglomeration time 50min)
△ : agglomerate by Solvent change method (agglomeration time 30min)
Neutralization method : Phenytoin 4g, 1N NaOH 20ml, Isopropyl acetate 13.5ml
Solvent change method : Phenytoin 4g, DMF 8ml, Isopropyl acetate 15.0ml

Fig. 5 Friability of agglomerates

seen to be uniform. The agglomerates which had been allowed a longer time for agglomeration (t = stirring time) were found to be easier to pulverize, even though they were thought to have become more consolidated. This observation is based on the difference in average particle diameter between the specimens examined (t = 30 min. 586 μm, t = 50 min. 741 μm). In contrast, the agglomerates obtained at t = 30 min. by the solvent change method (average particle diameter = 776 μm), although larger than those obtained by the neutralization method (586 μm), were hard to pulverize and satisfied neither of the equations. Since they were pulverized as easily as those obtained by the neutralization method in the initial stage ($<$ 15 min.) of the test and became hard to pulverize later, a hard nucleus was considered to exist in the interior of the agglomerate obtained by the solvent change method.

From these results it was determined that the mechanical strength of the agglomerates is dependent on the mechanism which is active in the agglomerated crystalization.

3. 2 The process of agglomerated crystallization and the mechanism of agglomeration

Figures 6 (a) and (b) show the relationship

between the average particle diameter and the residence time of the agglomerates obtained by the neutralization method. As shown in **Fig. 6 (a)**, the changes in the concentration of phenytoin in the feeding solution had no bearing upon the average particle diameter of the agglomerates extrapolated for the residence time t = 0. Subsequently, however, differences were observed in the growth rates of the agglomerates. On the other hand, when phenytoin was fed at a constant concentration but in varied quantities, as shown in **Fig. 6 (b)**, the particle diameters of the agglomerates at the initial stage showed increases corresponding to increases in the quantity of phenytoin but the growth rate of the agglomerate did not change.

The data from the neutralization method in **Fig. 6** was rearranged in **Figs. 7 (a)** and **(b)**. The linear relationships were found between the logarithmic particle diameters and the residence time in the two diagrams. They agreed with the coalescence model[8] formulated by P.C. Kapur. These results also agreed with the results of the electron-microscopic observations shown in **Fig. 3**.

$$\ln l = k_1 t + C_1 , \quad \frac{dl}{dt} = k_1 l \qquad (4)$$
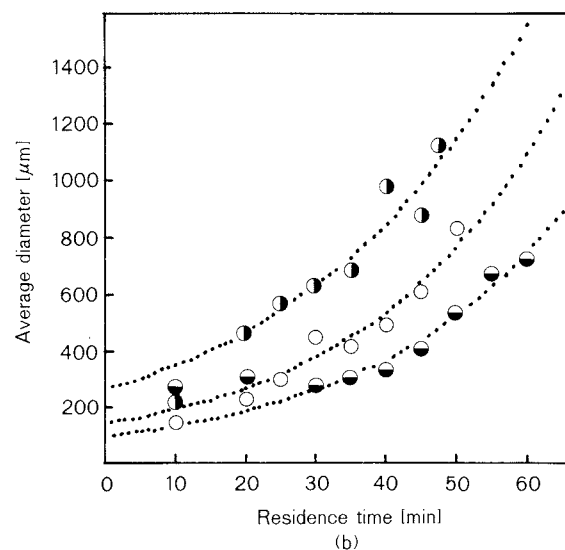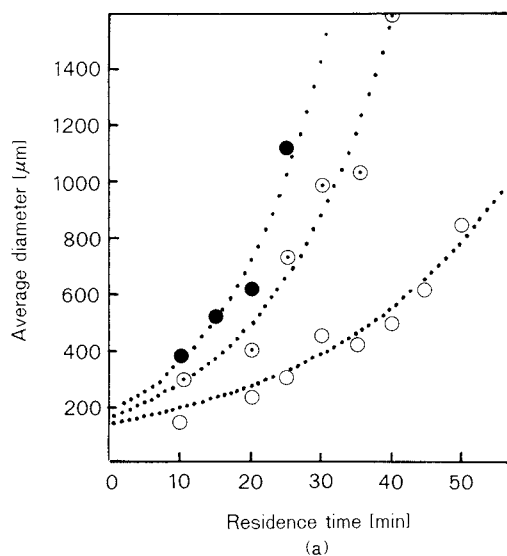
Phenytoin (g)/1N NaOH [ml] : ●3/20, ⊙3.5/20, ○4/20, ◒2/10, ◐8/40

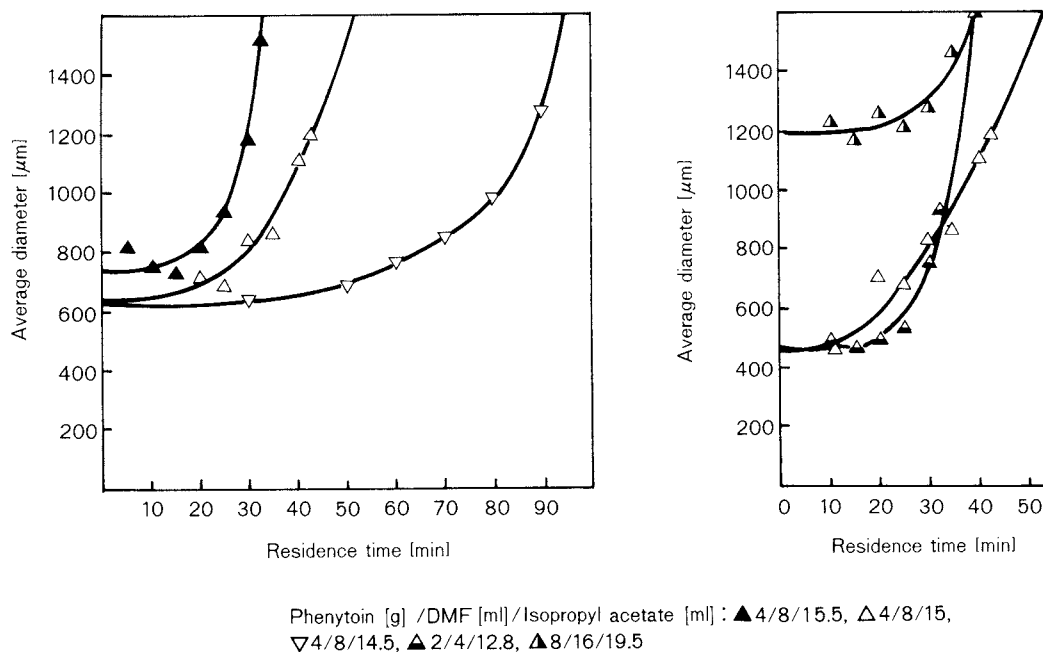Fig. 6 Average diameter of agglomerates as a function of residence time

where l represents the average particle diameter of agglomerates, and k_1 and C_1 are constants. When phenytoin was fed in varied concentrations [(a) in **Figs. 6** and **7**], the phenytoin crystals which precipitated decreased in relationship to the decrease in the concentration of phenytoin, but no change was observed in the quantity of the liberated bridging liquid. It is

therefore considered that the rate of the agglomeration of crystals, that is, the growth rate, increased because of increases in the quantity of the bridging liquid per unit weight of the crystals, and that, when pheytoin was fed in varied quantities against a fixed concentration [(b) in **Figs. 6** and **7**], the presence of the bridging liquid in a changeless quantity per unit
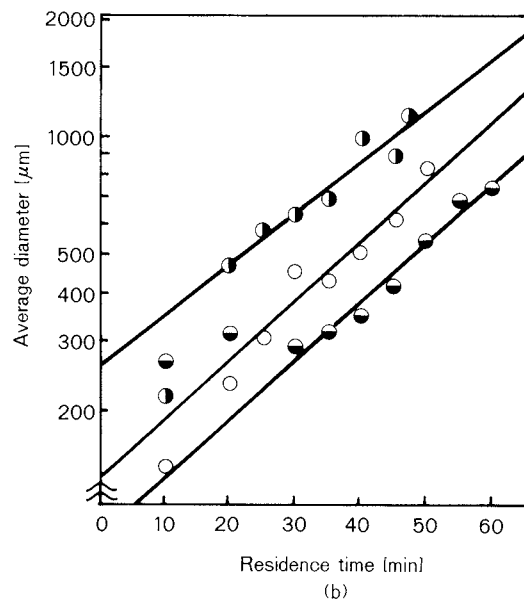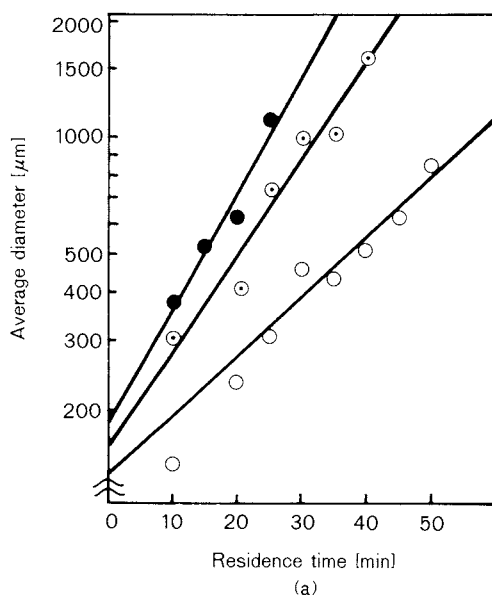
Phenytoin (g)/1N NaOH [ml] : ●3/20, ⊙3.5/20, ○4/20, ◒2/10, ◐8/40

Fig. 7 Average diameter of agglomerates as a function of residence time

Phenytoin [g] /DMF [ml]/Isopropyl acetate [ml] : ▲4/8/15.5, △4/8/15,
▽4/8/14.5, ▲2/4/12.8, ▲8/16/19.5

Fig. 8 Average diameter of agglomerates as a function of residence time

weight of the crystals caused the crystals to agglomerate at a constant rate.

Figures 8 (a) and (b) show the growth process of the agglomerates in the solvent change method. No difference was observed between this method and the neutralization method with respect to the shape and particle diameter of the crystals constituting the agglomerates (see Fig. 4), but the particle size of the agglomerates produced at the initial stage was more than twice as large as that of a comparable diameter in the neutralization method. As shown in Fig. 8 (a), the increased use of the bridging liquid enhanced the growth rate of the agglomerates of the crystals. When phenytoin was fed at a fixed concentration, the particle diameter of the agglomerates produced at the initial stage increased for 8 g of phenytoin but showed no difference for 2 g and 4 g, respectively, of phenytoin, as shown in Fig. 8 (b). As described in the aforementioned experiments, an increase in the proportion of DMF in the crystallization solvent results in the bridging liquid as well as the phenytoin having increased solubility in the crystallization solvent. Therefore, a slight change in the recipe strikingly affects the rate of the agglomeration and makes it difficult to set the conditions of the experiments on the basis of the solubility diagram in Fig. 1. The

agglomerating process in the solvent change method did not agree with Kapur's Eq. (4) or the layering mechanism[8] of the agglomeration expressed by Eq. (5):

$$\ln l = k_2 \cdot \ln t + C_2 \tag{5}$$

Figure 9 shows the relationship between the residence time and the size distribution of the agglomerates of the crystals. It was observed that the size distributions of the agglomerates obtained by the neutralization method agreed with the so-called "self-preserving" principle[9]. According to this principle, a logarithmic normal distribution is shown, and the agglomerate maintains a constant geometrical standard deviation while it grows. In the solvent change method, small agglomerates (<12 μm) were found to exist in fairly large proportions with large agglomerates ($100 \sim 300$ μm) at the initial stage of the agglomerated crystallization, but small agglomerates were seen to exceed large agglomerates as the agglomeration progressed. On the other hand, scarcely any change was observed in the maximum diameter of the agglomerates.

With a view to clarifying the agglomeration mechanism of the crystals in each of the two methods, the behavior of crystals was examined in the crystallization where no bridging liquid

Neutralization method

Solvent change method

Phenytoin 3.5g,1N NaOH 20ml

Phenytoin 4g, DMF 8ml,
Isopropyl acetate 15.0ml

Residence time [min] : ▲20, ○25, ●30, □35, ■40
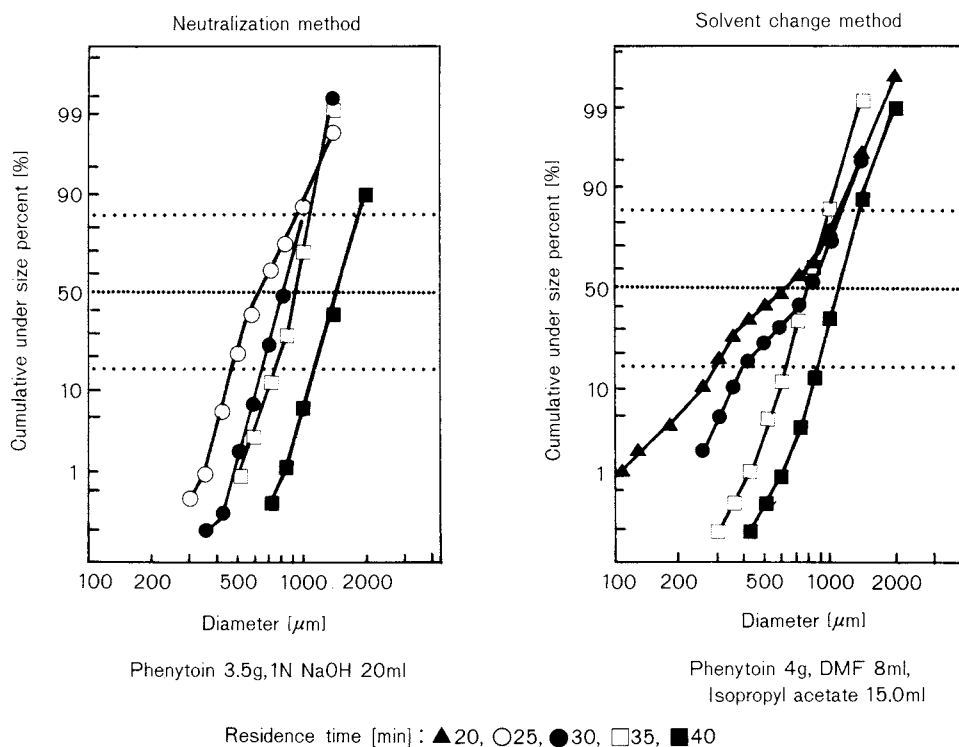
Fig. 9 Size distribution of agglomerates

was used. Most of the crystals produced by the two methods were of sizes up to several μm, as shown in **Fig. 4**, but particles as large as 100 ~ 300 μm were also seen to exist in the solvent change method. Scanning electron micro-photography [**Figs. 10 (a) and (b)**] showed them to be agglomerates of fine crystals. No such agglomerates were seen to exist in the neutralization method. By dropping a DMF solution of phenytoin into the water in a petri dish, it was possible to examine how crystals precipitated and gathered [**Fig. 10 (c)**]. As soon as the liquid drop touched the surface of the water, a crystal cluster resulting from solid-based cross-linking was formed and fell to the bottom. Furthermore, fine crystals precipitated at the surface of the water as the DMF spread. At first, this clustering mechanism was considered to be due to localization of DMF at the surface of the precipitated phenytoin crystal and to the function of the localized DMF as a bridging liquid. However, this assumption was disproved by the facts that, 1) the concentration of DMF in bulk showed no difference whether phenytoin was present or not, 2) phenytoin dispersed in water did not agglomerate when DMF was added,

and 3) when the crystallization solvent already contained DMF, the solubility of phenytoin increased, the recovery of the clusters decreased and, furthermore, the average diameter of the crystal clusters decreased [**Fig. 11 (a)**]. **Figure 11 (b)** shows the relationship of the loading weight of phenytoin in DMF to the recovery of the crystal clusters and their average diameter. As the concentration of phenytoin in DMF was increased, the recovery and average diameter of the crystal clusters increased accordingly. On the other hand, the crystals which precipitated formed no cluster when exposed to ultrasonic waves. These results show that when stirring is weak, a new crystal nucleus is formed among precipitated crystals before they are dispersed, and the crystal nucleus acts as a bridging solid among the crystals to from a crystal cluster.

With respect to friability, agglomerates of crystals obtained by using a bridging liquid were compared with clusters of crystals obtained without using any bridging substance, the results being shown in **Fig. 12**. The specimens were of sizes ranging from 250 to 270μm. The comparison clearly showed the clusters to be much firmer than the agglomerates. This

(a)

(b)

(c)

(a) and (b) : SEM photos
(c) : appearance of forming
crystal cluster by dropping
DMF solution of phenytoin
into water
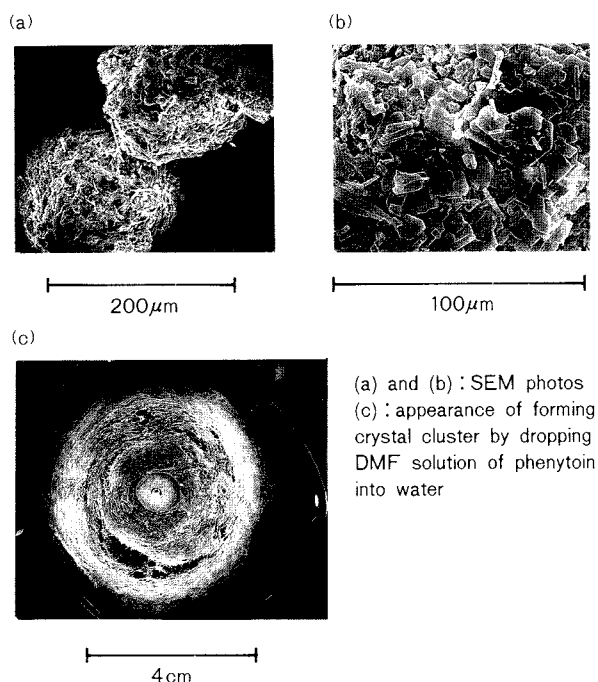
Fig. 10 Crystal cluster obtained in solvent change
method

Residence time [min]
● : agglomerate
○ : cluster
Phenytoin   4g
DMF   8ml
Isopropyl acetate 14.8ml
Residence time   30min
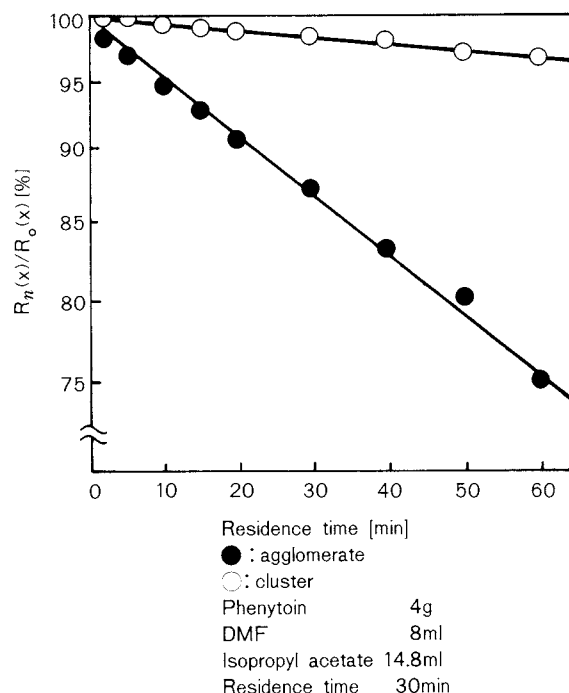
Fig. 12 Friabilities of agglomerate and cluster

corroborated the observation that crystals clustered by solid-bridging. From the results shown in **Fig. 5**, it was learned that the agglomerates obtained by the solvent change method gradually became more difficult to pulverize as the pulverization progressed. In connection with this, the results of the comparison in **Fig. 12** suggests the presence of a hard cluster in the interior of such an agglomerate which

resulted from solid-bridging at the initial stage of agglomeration.

Considering the above-mentioned results, the agglomeration mechanisms of crystals in the two methods may be reduced to the diagrams shown in **Fig. 13**. In the neutralization method, agglomeration takes place by the coalescence mechanism which is based on a bridging liquid, whereas agglomeration developed by the sol-

DMF concentration in crys-
tallization solvent [%]
(a)

Loading weight of phenytoin
in 8ml of DMF [g]
(b)
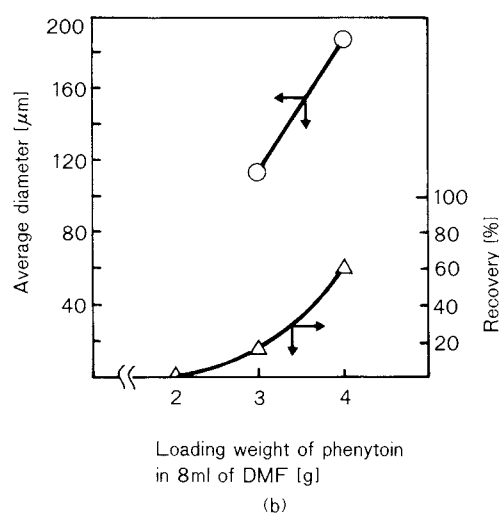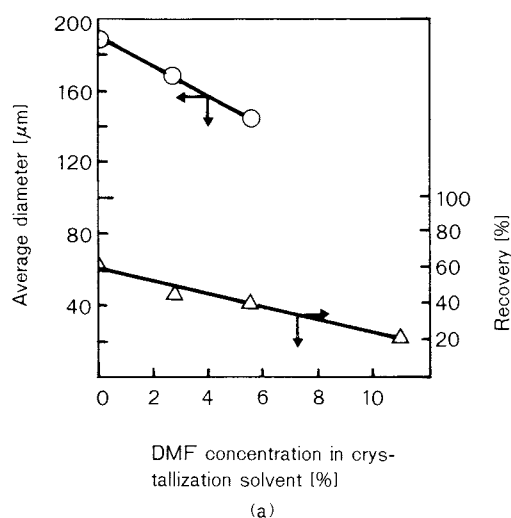
feeding solution : Phenytoin 4g, DMF 8ml

Fig. 11 Average diameter and recovery of crystal cluster
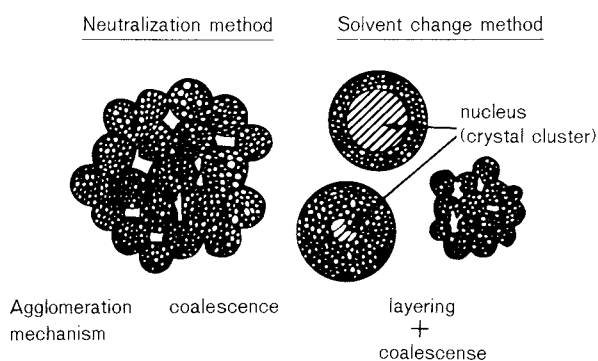
Fig. 13 Schematic internal structure of agglomerate and mechanism of agglomeration

vent change method is considered to be a concurrence of the coalescence mechanism, as in the neutralization method. The layering mechanism which consists of the agglomeration of fine crystals was caused by liquid-bridging on the surface of a cluster formed by solid-bridging.

3. 3 The consolidation of agglomerated crystals

The agglomeration mechanism of particles in agglomerated crystallization consists of the growth of an agglomerate which, as is now clear, allows the bridging liquid to exude from the interior to the surface under pressure of consolidation and becomes tied to another par-

ticle by forming a liquid bridge. It is important, therefore, to analyze the process of consolidation of agglomerated crystals when the process and rate of the agglomeration are considered.

Figure 14 shows the relationship between the particle size and the apparent density of the agglomerates determined by a microscopic technique. With respect to agglomerates obtainable in the neutralization method, a positive correlation was shown to exist between the two scales; that is, it is seen that by the neutralization method the agglomerates grow by coalescence while they undergo consolidation. With respect to agglomerates obtainable by the solvent change method, however, no clear relationship was shown to exist between the particle size and the apparent density, probably because a mixed model of coalescence and layering, as described earlier, controlled the growth mechanism of the agglomerates.

Next, the process of consolidation was analyzed with respect to agglomerates in the neutralization method, which showed a correlation between the particle size and the apparent density. The total weight W of the precipitated crystals is expressed by the following equation,

$$W = \frac{\pi}{6} \cdot l^3 \cdot \rho_{ap} \cdot N \tag{6}$$

where ρ_{ap} is the apparent density of the agglomerate, and N is the total number of ag-
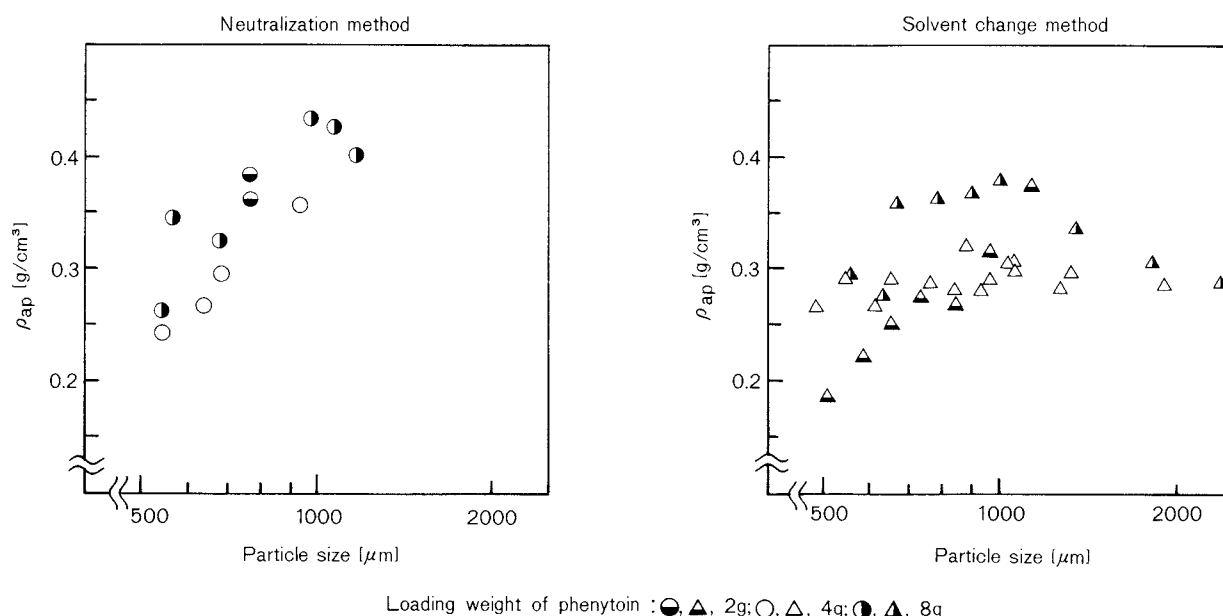
Loading weight of phenytoin : ◑, ▲, 2g; ○, △, 4g; ◐, ▲, 8g

Fig. 14 Relationship between particle size and apparent density of agglomerates

Phenytoin (g)/1N NaOH [ml] : ●3/20, ☉3.5/20, ○4/20, ◓2/10, ◑8/40
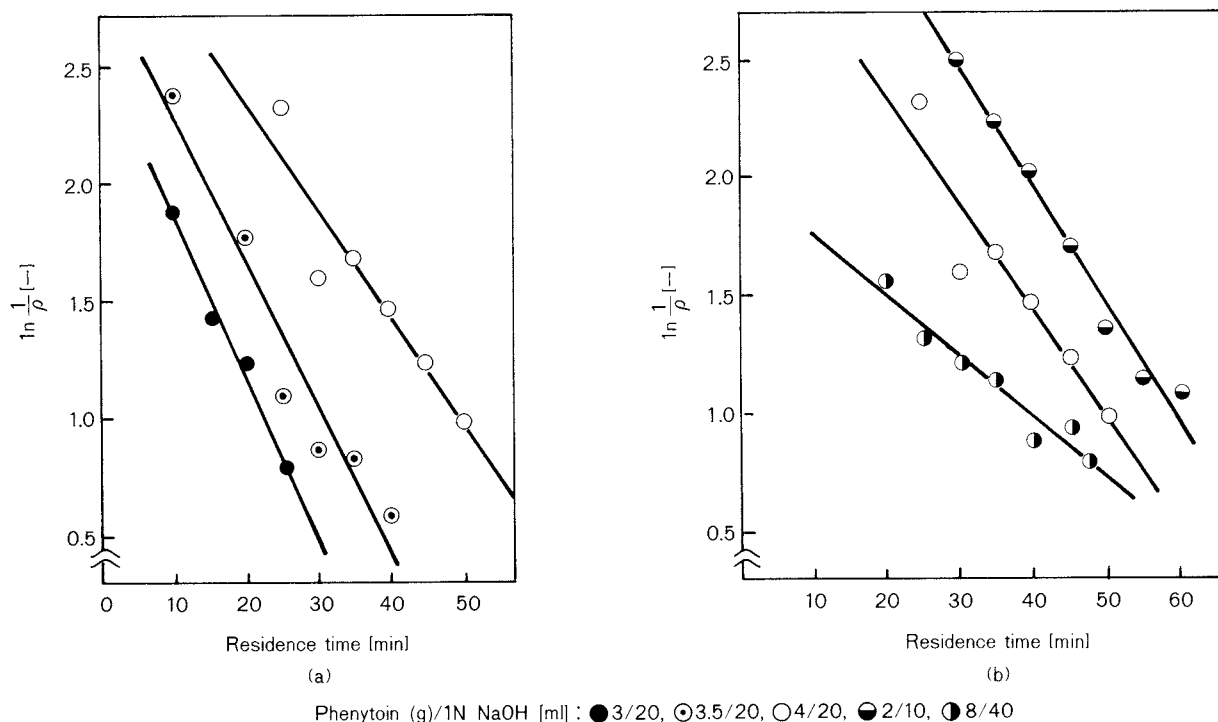
Fig. 15 Consolidation process of agglomerated crystals during crystallization

glomerates in the system. The crystallization ended as soon as an alkali solution of phenytoin was introduced into the system. W remained unchanged during agglomeration. N is expressed by Eq.(7) and l is expressed by Eq.(4), as shown before, so that Eq. (8) can be formed from Eq. (4), (6) and (7).

$$N = N_0 \cdot \exp\left[-k_3 t\right] \tag{7}$$

$$\frac{1}{\rho_{ap}} = \frac{\pi l_0^3 N_0}{6W} \cdot \exp\left[(3k_1 - k_3)t\right] \tag{8}$$

Figure 15 shows the relationship between $\ln(1/\rho_{ap})$ and t. The data formed straight lines so that Eq. (8) was satisfied. Accordingly, it has become clear that the incline of each straight line (consolidation rate constant of agglomerates) was dependent upon the agglomeration rate constants k_1 and k_3.

4. Conclusion

The results of the present study can be summarized as follows:

1) Agglomerated crystallization techniques, i.e., neutralization and solvent change techniques, which enable the primary and secondary properties of phenytoin crystals to be si-

multaneously controlled and as desired, were devised as novel particle-design techniques. The methods were capable of producing free-flowing agglomerates of high mechanical strength composed of fine phenytoin crystals.

2) The differences between the two methods in the agglomeration mechanism of phenytoin crystals were clarified. It was determined that whereas it was the coalescence mechanism by liquid-bridging that controlled the agglomeration of crystals in the neutralization method, clusters of crystals were formed by solid-bridging at the initial stage by the solvent change method, and the agglomeration developed into a concurrence of the clustering and layering agglomeration in which fine crystals agglomerated on the surface of the cluster by liquid-bridging. As a result, the agglomerates developed by both methods were shown to differ in the manner in which they were pulverized. The agglomerates developed by the solvent change method had a hard nucleus formed by solid-bridging in the interior, so that they were relatively hard to pulverized compared with the agglomerates developed by the neutralization method.

84

3) Whereas the agglomerates in the neutralization method showed a positive correlation between particle size and apparent density, the agglomerates developed by the solvent change method showed no such relationship because of the difference in the agglomeration mechanism. It became clear that the rate of consolidation of the agglomerates of crystals in the neutralization method was dependent upon the agglomeration rate constants in the crystallization.

Acknowledgement

Nomenclature

C_1, C_2 : constants [—]
d : Heywood diameter of agglomerate [μm]
D_0 : diameter of agglomerate before pulverization [μm]
k : pulverization rate constant [g·cm^{-2}·min^{-1}]
k_1, k_2 : growth rate constant [min^{-1}]
k_3 : agglomeration rate constant [min^{-1}]
l : diameter of agglomerate [μm]
l_0 : diameter of agglomerate at $t = 0$ [μm]

N : total number of agglomerate in system [—]
N_0 : total number of agglomerate in system at $t = 0$ [—]
n : impaction number [—]
Pr : probability of breakage per impaction [—]
$R_n(x)$: cumulative weight percent over size(x) [%]
t : time [min]
W : total weight of crystal precipitated in system [g]
X : pulverized fraction [—]

ρ_{ap} : apparent density of agglomerate [g·cm^{-3}]
ϕ : shape factor of agglomerate [—]

References

1) Kawashima, Y., M. Okumura and H. Takenaka: *Science*, **216**, 1127 (1982).
2) Kawashima, Y., M. Okumura, H. Takenaka and A. Kojima: *J. Pharm. Sci.*, **73**, 1535 (1984).
3) Chakrabarti, S., E. Moerman and F. Belpaire: *Pharmazie*, **34**, [4], 242 (1979).
4) Hirakawa, Y. and K. Harada: *Yakugaku Zasshi*, **102**, 951 (1982).
5) Kawashima, Y., S. Aoki and H. Takenaka: *Chem. Pharm. Bull.*, **30**, 1900 (1982).
6) Elworthy, P.H. and H.E.C. Worthington: *J. Pharm. Pharmacol.*, **23**, 101S (1971).
7) Sekiguchi, I.: *Pharmaceutical Factory, Japan*, **3**, 417 (1983).
8) Kapur, P.C.: *Chem. Eng. Sci.*, **27**, 1863 (1972).
9) Vanangamudi, M. And T.C. Rao: *Powder Technology*, **41**, 29 (1984).

The Wetting Properties of Powders and Devices for Measuring Them

Noriyoshi Kaya
*Micromeritics Laboratory, R & D Div.
Hosokawa Micron Corporation**

Masumi Koishi
*Faculty of Industrial Science and Technology,
Science University of Tokyo***

1. Introduction

Once a solid comes into contact with liquid, a phenomenon known as "wetting" occurs. Wetting is an interfacial phenomenon where liquid molecules are adsorbed onto the surface of a solid. According to interfacial chemistry textbooks[1]~[3], it is defined as a phenomenon where the gas-solid interface is disrupted, and a liquidsolid interface occurs.

This phenomenon appears responsible for the adhesion and the affinity of liquid molecules relative to a solid surface. Both the interaction between the liquid molecules and the solid surface can be evaluated by using this phenomenon. The wetting measurement technique is a long-established means[4] for evaluating the surface properties of various materials in which certain liquids penetrate. This technique has been basically studied, especially in fabrics technology[5]~[7].

The many applications of wetting include at one extreme the laundering of clothes. Other applications are industrial bases, ore floatation, impregnation with insulator oil, the molding of plastics, and the dispersion of various pigments in liquids. Recently, applications such as liquid penetration into a paper filter for paper chromatography[8], and the preparation of composite materials by adjoining ceramics to metals have been found. In essence, this phenomenon has indispensable roles of modern technology.

The discussion in this paper is mainly about powders, especially on studies the measurement of wetting in Japan.

* No. 9, 1-chome, Shoudai Tajika, Hirakata, Osaka, 573
TEL. (0720) 55-2220

** 102-1, Oshamanbe-cho, Yamagoe, Hokkaido, 049-35
TEL. (01377) 2-5111

In studying the measurement of the wetting of a powder, unlike that of solid matter, there are several technical difficulties that are not readily solved: data taken on a specific powder by one researcher may be different from that taken by another researcher; replicability of the wetting measurement of powders can be poor, and measurement values may be unstable. These problems are mainly attributable to the high surface energy of the powder, and partly to the number of uncertain factors in measuring the wetting of a powder bed. These factors include uncompacted structures within a powder bed, the presence of ultrafine particles, and uneven moisture content.

2. Expression of wettability

As previously defined, wetting is a phenomenon where the gas-solid interface is disrupted, and a liquid-solid interface occurs. A quantitative evaluation of this phenomenon has been discussed on the basis of the energy balance. The change in this energy is expressed in **Fig. 1**[9].

The change in the surface energy during wetting is analyzed into two relationships: one based on free energy, and the other based on total energy.

As shown in **Fig. 2**, a droplet of a liquid with good wetting, placed on the solid surface, produces a smaller angle of contact. The angle formed between the droplet and the solid surface is smaller, whereas the droplet of the liquid with poor wetting indicates a larger angle.

In this figure, γ indicates surface tension, that represents the work necessary to form a unit area of the additional interface. It is expressed as the free energy of the phenomenon, where, the suffix S represents the solid, and L,

Disruption of liquid surface
Wetting
Disruption of solid surface
Liquid-Solid interface occurs
Change in energy

Change in energy
① Change in free energy
▷ Adhesion tension, Angle of contact
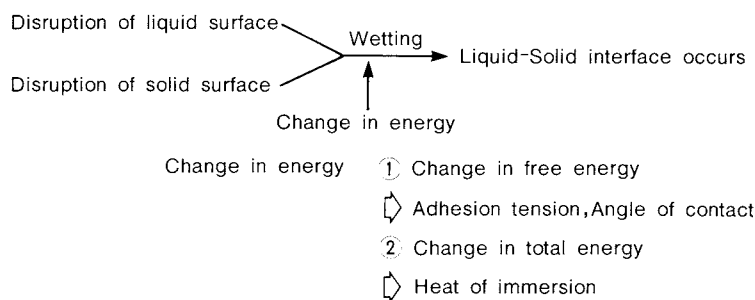② Change in total energy
▷ Heat of immersion

Fig. 1 Change in energy of the wetting process

the liquid.

Considering the balance of the horizontal component of the forces, the widely known Young's equation can be deduced as follows.

$$\gamma_S = \gamma_{SL} + \gamma_L \cos\theta \qquad (1)$$

$\gamma_L \cos\theta$ in Eq. (1) is called the adhesive tension, which is equivalent to the free energy of a solid being immersed in a liquid.

For this reason, the adhesive tension is obtained by the measurement of a surface tension γ_L of liquid and the angle of contact θ. Generally, however, a value θ is used to indicate the wettability of solid matter.

Generally speaking, once a liquid comes into contact with solid matter, heat generates even in the absence of a chemical reaction, caused by the interaction between the solid and the liquid in which the solid is immersed. When the enthalpy of the solid surface is H_S, and that of the liquid-solid interface is H_{LS}, the heat of immersion Q is indicated as the difference between these enthalpies.

$$Q = H_{LS} - H_S = \Delta H \qquad (2)$$

Furthermore, there is a correlation between the enthalpy and the total energy as shown below;

$$\Delta H = \Delta E + p\Delta V \qquad (3)$$

Since the volumetric change ΔV can be negligible in the wetting process;

$$\Delta H = E_{SL} - E_S = \Delta E \qquad (4)$$

The heat of immersion corresponds with the total energy. Under a constant pressure, the interrelationship between the total energy and the free energy gives the Gibbs-Helmholtz equation. Applying this equation to the wetting, the following equation can be obtained;

$$\Delta E = \Delta\gamma - T\left[\frac{\partial(\Delta\gamma)}{\partial T}\right]_{P=\text{const}} \qquad (5)$$

Where the change $\Delta\gamma$ in the interfacial free energy is;

$$\Delta\gamma = \gamma_S - \gamma_{SL} = \gamma_L \cos\theta \qquad (6)$$

Combining Eqs. (2), (4), (5), and (6);

$$Q = \gamma_L \cos\theta - T\left[\frac{\partial(\gamma_L \cos\theta)}{\partial T}\right] \qquad (7)$$

Thus, the angle of contact θ can be obtained by the measurement of the heat of immersion Q, the surface tension of the liquid γ_L and the estimation of $\partial\gamma_L/\partial_T$. As can be understood from expression (7), the determination, as-

γ_L

θ

γ_S γ_{SL}

(a)

γ_L

θ

γ_S γ_{SL}

(b)
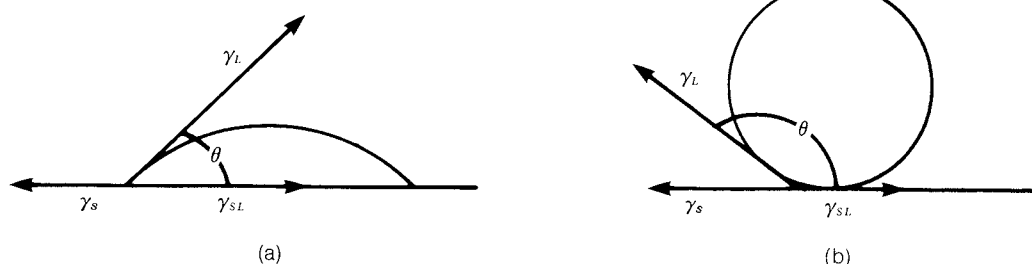
Fig. 2 Wetting with liquid on a solid surface

sumes that the angle of contact is constant relative to the temperature T.

Meanwhile, the temperature dependency of the surface tension $(\partial \gamma_L / \partial \gamma_T)$ can be calculated by using various methods for estimating the properties of constants[10].

3. Wettability measurements

Table 1 summarizes methods commonly used for determining the wetting of powders.

(1) The heat-of-immersion method

This method gives the most fundamental values on the wettability of powder. The generation of heat of immersion is attributable to the surface areas of particles, the polarities of particles and liquid, and to the formation of an electrical double layer on the individual particle surface. This method is an important means for analyzing the surface properties of powders. As the method of determining the angle of contact based on the heat of immersion, was previously described, no attempt is made to explain here.

Usually, the magnitude of heat of immersion is considerably small. The resultant temperature level is still low even with inorganic powder having higher energy. Therefore, measuring the heat of immersion of a powder having small specific surface area or a sample with low energy takes significant difficulties or requires long measuring time.

At the cost of inconvenience in measuring, the heat-of-immersion measurement promotes the analysis of the dispersion force caused by the interaction between a powder and liquid, the mechanism of induced dipoles and permanent ones, and the change in the surface conditions of a powder that will occur by heat treatment or chemical reaction.

Recently, Arakawa[11], Arai[12] and others discussed the correlation between the heat of immersion and the dipole moment, with various powders. Measurement data on the heat of immersion were also disclosed[13].

(2) The dripping method[14]

The angle of contact with a powder not readily wetted can be measured by packing the powder into a specific formation, placing a droplet onto the powder and directly observing the droplet with a microscope. This technique is theoretically based on the assumption that the liquid does not penetrate into the powder bed. However, in actual operations, measurement can be accomplished after the penetration of the liquid into the powder bed is saturatedly attained.

First, the distance h from the apex of a droplet to the surface of a powder is measured. Using the following expression, the angle of contact θ is calculated.

$$\cos \theta = 1 - \sqrt{\frac{\beta h^2}{3(1-\epsilon)}} \qquad (8)$$

Table 1   Methods for measuring the wetting of powders

Method	Measuring principle
The heat-of-immersion method	Measures the heat of immersion generating when a powder is dispersed in liquid.
The dripping method	A powder is formed into a specific shape onto which a droplet is applied, and the angle of contact is measured with a microscope.
The capillary method	Using a compacted powder bed as composite capillaries, the adhesion tension and angle of contact are determined by the penetration of the liquid medium. (1) The penetration rate method: wetting is evaluated based on the penetration of the liquid medium. (2) The pressurizing method: pressure is exerted onto one and of a liquid medium penetration a compacted powder layer. Wetting is evaluated based on the pressure that attains equilibration.
The liquid phase distribution method	Two liquids not readily blended together are maintained in a dual liquid phase to which powder is added. Wetting is evaluated by observing the migration into the powder.

where $\beta = \rho_L g/2\gamma_L$, ρ_L represents the density of the liquid, and ϵ denotes a volumetric void fraction.

Murata[15] examined Kossen's formula and gave an expression that is valid under the assumption that capillaries are saturated around a droplet on a compacted powder. He then measured the wettability of a formed coal powder using the equation.

(3) The penetration rate method

Using this method, a cylinder is filled with powder. The angle of contact θ is then determined by measuring the proceeding rate of the gas-liquid interface formed by the liquid penetrating into the powder layer, or by measuring the change in the amount of the liquid penetrated into the layer.

When a liquid penetrates through the powder bed, the penetration rate can usually be determined by the Hagen-Poiseuille equation as follows:

$$\frac{d\ell}{dt} = \frac{r^2}{8\eta\ell}\Delta p \qquad (9)$$

where ℓ represents the distance of penetration, r denotes the average radius of capillaries formed by particles in the powder layer, and η is the viscosity of the liquid. Meanwhile, the pressure Δp is the addition of the external pressure Δp and the tension Δp_c.

The pressure Δp_c of the capillary tension is defined as:

$$\Delta p_c = \frac{2\gamma_L \cos\theta}{r} \qquad (10)$$

The penetration rate of the powder bed is obtained as:

$$\frac{d\ell}{dt} = \frac{r^2}{8\eta\ell}\left(\frac{2\gamma_L \cos\theta}{r} + \Delta p\right) \qquad (11)$$
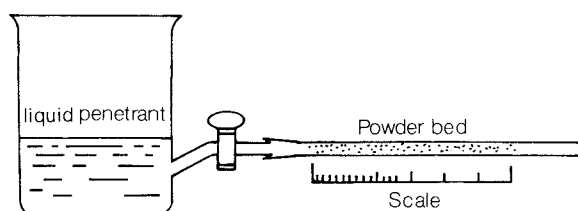
Using the penetration rate method, when Eq. (11) is solved under the assumption that the external pressure $\Delta p = 0$ and the distance $\ell = 0$ at $t = 0$ (initial condition of penetration) then the expression is solved:

$$\ell^2 = \frac{r\gamma_L \cos\theta}{2\eta}t \qquad (12)$$

Eq. (12) is known as the Washburn equation and has often been applied to measure the penetration rates[16].

In this expression, r represents the mean radius of the path (capillaries) in the powder bed. The value r can be estimated using an amount of liquid that completely wets the powder, and by determining the ℓ^2 versus t relationship at $\cos\theta = 1$.

In some cases, the value r can be simplified by assuming that the value is half of the average particle size of the powder[17,18].

One example of the measuring apparatus in compliance with the Washburn equation is illustrated in **Fig. 3**. Instead of the visual observation in **Fig. 3**, Tanaka et al. invented the apparatus in **Fig. 4**[19].
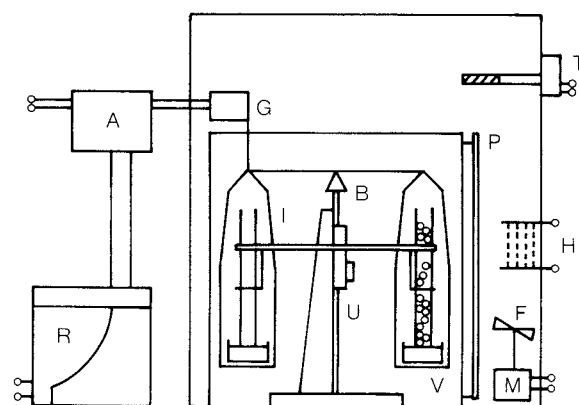
I : Glass cylinders, Left reference cell, Right sample cell
B : Balance
U : Vertical micrometer
V : Liquid vessel
G : Strain gauge
R : Recorder
T : Thermocontroller
H : Heater
F : Fan
M : Motor
P : Heat protector

Fig. 4 Apparatus for measuring the penetration rate used by equilibration balance

Fig. 3 Apparatus for measuring the penetration rate
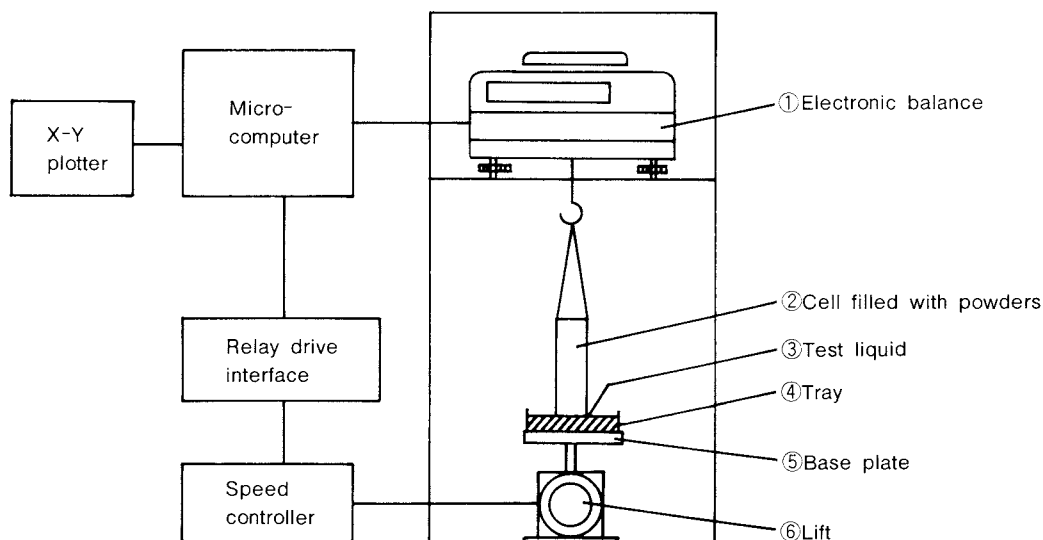
Fig. 5 A measurement apparatus based on electronic balance

Using this apparatus, the powder is poured into one of a pair of cylinders, each having a paper filter on the bottom, while the other cylinder is left empty. A tray filled with a liquid is equilibrated with the other similarly filled tray on the balance. Then the pair of cylinders is allowed to simultaneously come into contact with the liquid. Next, the volume reduction in the liquid caused by liquid penetration into the powder bed is converted into electrical signals by a strain gauge and is recorded for evaluation.

The authors[20] developed a measuring ap-

paratus employing an electronic balance schematically illustrated in **Fig. 5**. With this apparatus, a cell filled with a powder bed is suspended from the electronic balance, and a tray filled with test liquid is automatically moved with a lift. A microcomputer detects the contact of the cell with the liquid surface by the change in weight of the cell, and then the microcomputer stops lifting of the cell and automatically measures the weight of the penetrated liquid. The change in the weight of the cell during the operation is summarized in **Fig. 6**. As shown in this figure, once the cell
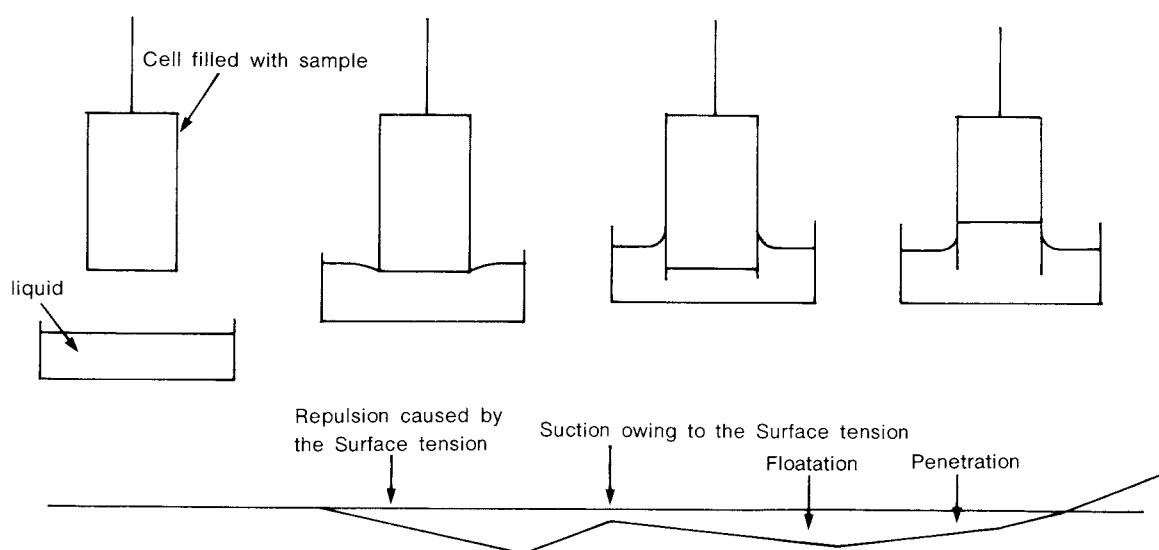
Fig. 6 A method for detecting the contact with liquid surface
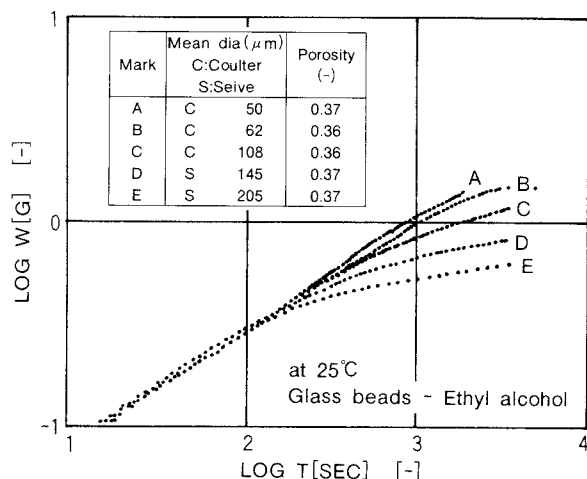
Fig. 7 Weight of ethyl alcohol that penetrated into glass beads

Fig. 8 Comparison of penetrated liquid levels by visual observation and by using the weighing method

filled with powders comes into contact with the liquid surface, the surface tension of the liquid excludes the cell from the surface. In contrast with this action when the tray is further lifted, the cell receives a suction force by the surface tension, and, then, the cell also receives floatation from the portion immersed in the liquid. After the tray is stopped lifting, the liquid penetrates through the powder layer. The apparent weight of the cell thereby increases again. Sasaki noted that such a penetration process is not limited to powders but is valid even where solid matter is immersed in a liquid[21].

The distance of penetration ℓ and the weight W_L of the liquid penetrated has the following interrelationship:

$$W_L = \epsilon S \ell \rho_L \tag{13}$$

substituting from Eq. (13) in Eq. (15), the relationship is given:

$$\frac{W_L^2}{t} = (S\epsilon\rho_L)^2 \frac{r\gamma_L \cos\theta}{2\eta_L} \tag{14}$$

where S is the cross-sectional area of the powder layer, ϵ denotes the void fraction, and ρ_L, γ_L, and η_L represent the density, surface tension, and viscosity of the liquid, respectively.

Figure 7 shows the results of logarithmic plotting correlated between the weight of penetrated liquid W_L and the time t. This relationship was obtained by the apparatus shown in Fig. 5, where W_L^2 is apparently proportional to time t for a specific duration. Murata[22] ob-

tained the similar relationship with both coal powder and SiO_2 powder. Using an electronic balance connected with a recorder, Fujitani et al.[23], also measured the weight of liquid that penetrated into a glass tube filled with a powder sample.

These methods of measuring the weight of penetration are simple and accurate, whereas conventional methods of visually observing the surface of penetrated liquid are inherently inconvenient and relatively inaccurate. This is because of the irregular rate of the penetration through the powder bed, and because of a greater penetration rate of liquid along the internal wall of the cell filled with powder. The authors[24], simultaneously performed a visual inspection and weight-measurement to determine the penetration rate of ethyl alcohol into glass bead layer. The resultant data was plotted in Fig. 8. Once the weights of the cell and paper filter were eliminated from the raw weight data in this figure in order to determine the height of penetrated alcohol, the results were virtually identical for both measuring techniques. However, the results of visual observation were always higher. Therefore, that the penetration rate relative to the inner wall of the cell is always greater than that relative to the powder layer can be deduced from this fact. The authors also found that the liquid traveling along the inner wall affects the scattering of measured data on the penetration rate.

Morishima et al.[25] developed a system for measuring the penetration distance by detect-
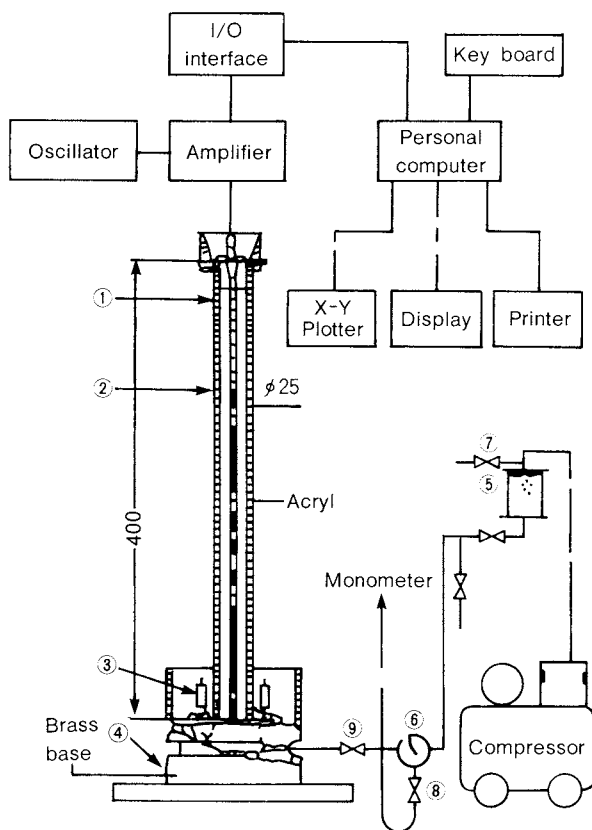
Fig. 9 Schematic diagram of the testing apparatus

(Formation of powder bed)

Fig. 10 Apparatus for measuring the horizontal penetration rate

ing the electrical conductivity as shown in **Fig. 9**. In it, electrodes are placed in the cell to determine the vertical position of the penetrated liquid.

Furthermore, Matsumoto et al. developed an apparatus shown in **Fig. 10**[26]. This apparatus also principally uses electrodes for measuring electrical conductivity in order to determine the horizontal position of the penetrated liquid. Optionally, this apparatus can incorporate a photosensor to detect change in the refraction of light caused by the penetrated liquid. This apparatus is advantageous in that a thinner powder layer makes uniform compaction, which means a stable void fraction.

Though simple and easy to operate, the position detection method using an electrode or photosensor has difficulty in measurement. This is because the discontinuous measuring points cannot cope with uneven penetration of the liquid.

(4) The pressurizing method

This type of measuring technique was initially invented by Bartell[27], where a cylindrical

cell filled with powder is placed horizontally. The inside of the cell is depressurized to make liquid to penetrate from one end, while from the other end a pressurized suitable gas is introduced, and then, the cell is sealed off. Next, a pressure Δp is determined where the penetration stops and reaches equilibration with the liquid. In this technique, the angle of contact is estimated by Eq. (10).

Though it is difficult to verify the equilibration, the pressurizing method has an advantage. It can be used to evaluate a liquid-liquid system the liquids of which are not readily blended with each other.

Matsumoto et al.[28] developed a constant flow rate method, where liquid is supplied into the powder bed at a constant flow rate. At the same time, the pressure applied on the powder bed is measured to determine wettability.

One example of the constant flow rate method is schematically illustrated in **Fig. 11**. If the evaluated liquid-solid system is that of anhydrous powder and water, the water level in column A is identical to that of column B until the water level reaches plane 0-0'. Once passing through the perforated plate that supports the powder bed, the water temporarily remains stagnant. Then, when the water level in column B reaches a specific point, water again penetrates through the powder layer in column A. Finally, water exceeds the top of the powder layer as shown in **Fig. 11 a)**. In contrast, the pressure pattern of a hydrophilic powder is shown in **Fig. 11 b)** since water is sucked by the powder bed.
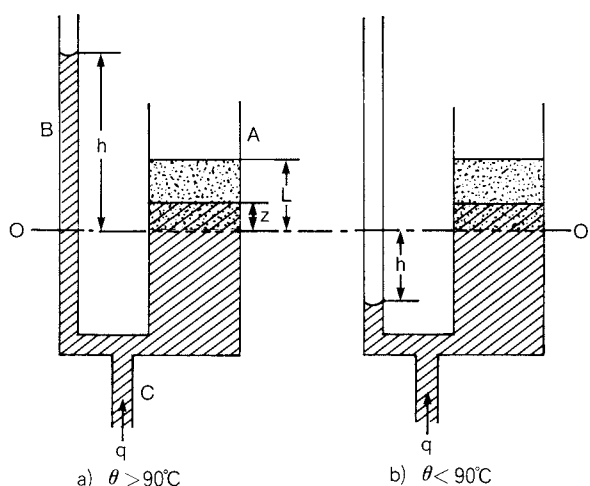
Fig. 11 Schematic of the constant flow rate method (principle)

Fig. 12 Some examples of the penetration rate with TiO$_2$

This technique has limitation with a lyophilic sample in that liquid is rapidly absorbed, and liquid supply is disrupted, giving data with poor replicability. Nevertheless, this technique is regarded as an appropriate means for evaluating the penetration rate of lyophobic powder, the penetration rate of which is otherwise difficult to measure.

4. Discussion on the penetration rate

Figure 12 summarizes the penetration rate data measured on various liquids and expressed in weights, using titanium oxide as a powder sample. An angle of contact can be determined using Eq. (14), based both on a linear gradient of this penetration rate diagram, and on theoretical capillary radius determined with the same powder having the same void fraction. In other words, the hydrodynamic radius is determined by the specific surface area measurement using the air permeability method. The resultant angles of contact are not less than 80°, unrealistic values.

The possible reason is that unlike the ideal rapillaries of the straight path, the actual capillaries of the powder bed, which is subjected to the penetration rate measurement, have meandering paths. This must be considered in order to obtain a more realistic angle of contact.

Accordingly, in conjunction with the air permeability method for determining the capillary radius r, another method for evaluating the wettability is available. In it, using the penetration rate of a reference liquid with a $\cos\theta = 1$

and the penetration rate of the liquid being evaluated, the ratio of the rates is determined in order to evaluate the wettability of the liquid.

For evaluating the penetrations of different liquids into the powder sample, the sample is prepared in the same manner, then the void fraction ϵ and capillary radius r remain constant. Therefore propsitioning the equations for each cases, the expression reduces to

$$\frac{(W_{L2}^2/t_2)}{(W_{L1}^2/t_1)} = \frac{\rho_{L2}^2 \eta_{L1} \gamma_{L2} \cos\theta_2}{\rho_{L1}^2 \eta_{L2} \gamma_{L1} \cos\theta_1} \quad (15)$$

The left side of Eq. (15) can be determined by actual measurement, while the density of liquid ρ_L, viscosity η_L, and surface tension γ_L can be determined by the literature. The wettability of liquid can thus be evaluated.

Meanwhile, Koishi[29] derived the formula based on Poiseuille's equation (9), by incorporating the tortuosity of the capillaries in the powder bed and the fluid friction as follows:

$$\frac{d\ell}{dt} = \frac{r^2\rho_L g}{8\eta_L k^2}(\frac{\ell_\infty}{\ell_t}-1)+\frac{r\rho_L g}{2\epsilon k^2}(\frac{\ell_\infty}{\ell_t}-1) \quad (16)$$

where k represents a ratio of capillary paths that corresponds to an actual distance and the apparent distance, while ℓ_∞ is a distance of penetration attained when the equilibration of a penetration rate $\frac{d\ell}{dt} = 0$ is reached.

Converting Eq. (16) to the weight base, the penetration rate leads to the following expression:

$$\frac{dW_t}{dt} = K_1 \left(\frac{W_\infty}{W_t} - 1 \right) + K_2 \left(\frac{W_\infty}{W_t} - 1 \right)$$

where,

$$K_1 = \frac{\epsilon S \rho_L^2 g r^2}{8 \eta_L k^2} \qquad K_2 = \frac{\epsilon S \rho_L^2 g r}{2 \epsilon k^2} \qquad (17)$$

In Eq. (17), for a larger radius, the first term on the right side alone can be approximated, while for a smaller radius it can be simplified by the second term alone.

Using Eq. (17), Koishi et al.[30] plotted (dW_t/dt) and ($1/W_\varrho$). By the resultant plotting, they determined the coefficients K_1, K_2, and W_∞, in order to evaluate the wettability of powder.

There is a problem in the penetration rate method, however. It is that with powder of good wettability, the liquid is rapidly permeated in the particle surface, and the voids in the powder layer are not completely filled with the liquid. Therefore, some voids remain unfilled as bubbles.

Nakagawa et al.[31] studied this phenomenon by evaluating the void structures in powder bed.

5. The evaluation of surface properties

To improve dispersion in liquid, SiO_2 or TiO_2 powder is often subjected to a physical adsorption technique where a compound having an oil-attracting radical is allowed to be fixed onto the particles. Also, a surface treatment technique may be used where the surfaces of the particles are modified by a chemical reaction.

For instance, it is known[32] that once polyvinyl alcohol (PVA) is adsorbed onto the surface of SiO_2 particles, the OH group on the SiO_2 surface is strongly bonded to the OH group of the side chain on the PVA, hydrophobic hydrocarbon groups are thereby oriented on the particle surface, and the SiO_2 surface become hydrophobic.

Figure 13 indicates the example of the evaluation on the effects of the surface modification. The data was obtained by the penetration rate measurement[33].

The powder samples used had a virtually identical particle size distribution and void fraction, where the effects of the surface modification were evaluated. As shown in the electromicrographs of **Fig. 14**, the surface of individual TiO_2 particles modified with alumina Al_2O_3, etc. has minute ruggedness compared to that of non-modified particles. The specific surface area by the air-permeability method revealed that the modified particles had a surface area four times as large as that of unmodified particles. It seems that such a change in surface properties of the particles affected the data the resulted from penetration rate measurement.

Recently, methods of combining different types of powders in order to develop new materials has gained researchers' attention. One such method is known as the "mechanofusion system"[34].

According to this method, the extremely powerful mechanical energy of "Angmill", which is an ultrafine milling machine using grinding and shearing forces as an operational principle, makes the surfaces of the particles to be fused with another material in order to obtain particles that have unconventional physical properties.

Fig. 13 Effect of the surface coating
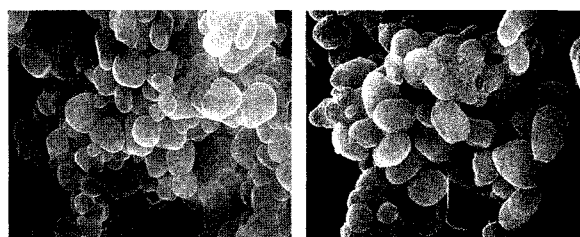
Titaninm ox;de untreated

Fig. 14 Photomicrographs of the surface of titan dioxide samples
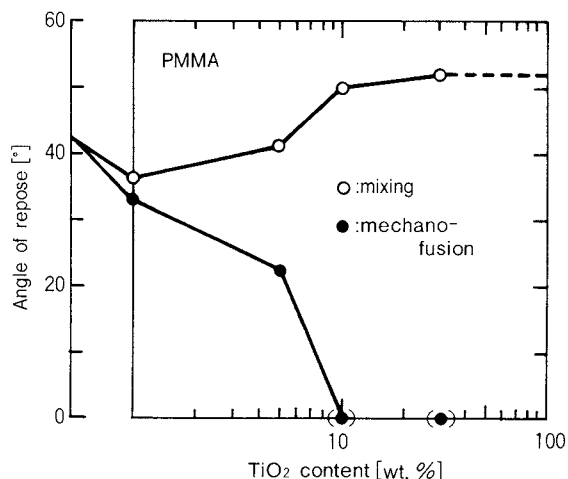
Fig. 15　The mixing ratio and angle of repose of TiO_2

Fig. 16　The penetration ratio measurement with mechanofusion-processed materials

Once fused, the resultant particles have surface properties different from those of the original powder materials. The penetration rate method has capable of evaluating this change.

Figure 15 illustrates the variation in the angle of repose, where one sample type was prepared by fusing TiO_2 particles onto PMMA particles. The other sample was prepared by mixing. A smaller angle of repose means better fluidity of powder, and this relationship is comparable to the previously mentioned relationship. The smaller angle of contact shows that a liquid medium has better affinity with a solid. The mechanofused type of sample exhibits better fluidity that corresponded to the content of added TiO_2 than a non-modified parent material lacking TiO_2 particles. The angle of repose reached 0° with 10 wt% of TiO_2 added. In contrast, the mixture type of sample showed the smallest angle of repose with 1 wt% of TiO_2 mixed. The angle of repose of this type of sample became again greater with a larger ratio of TiO_2 mixed, the pattern showed different from that of the mechanofusion-modified type of sample.

Figure 16 illustrates the results of the penetration rates of water into the mechanofusion-modified type of sample. The mother material, PMMA, has no water penetration. However, the larger the rate of TiO_2 added was, the larger the penetration rate became. The individual samples used, however, had different void fractions. Therefore, correction had to be incorporated.

Accordingly, taking the previously described

ratio of the Washburn equation, and using, as reference, the data of the mechanofused sample (1 wt%), the data listed in **Table 2** was obtained. Obviously, the larger the rate of TiO_2 added, the greater the wettability of the sample and the smaller the angles of contact.

Figure 17 illustrates electromicrographs of unmodified PMMA particles, and of mechanofusion-modified (1 wt% TiO_2 particles) PMMA particles, respectively.

● 1 μm　PMMA　　● 1 μm　PMMA-TiO_2
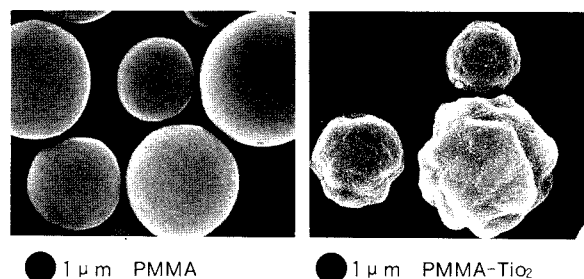
Fig. 17　Mechanofusion of PMMA particles

Table 2　Evaluation of mechanofused materials for wettability

Sample		$\dfrac{\cos\theta}{(\cos\theta)\,1\%}$	Angle of contact	Wettability
Mechanofusion-processed material	1%	1		
Same as above	5%	1.52	Small →	Large →
Same as above	10%	3.09		
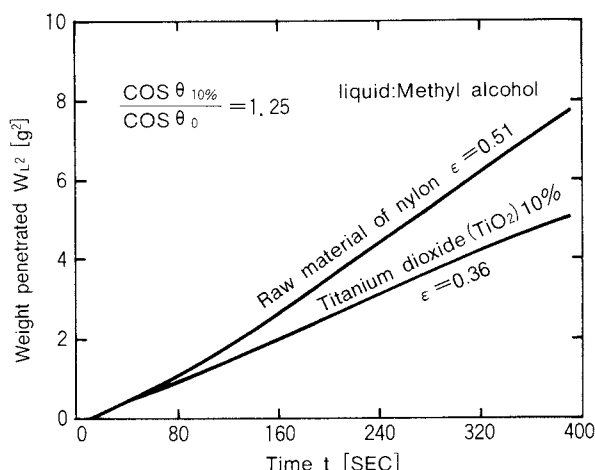
Fig. 18 The penetration rate of ordinary nylon and that of nylon the surface of which is being fused with titanium dioxide

Figure 18 indicates the penetration rates of methyl alcohol into nylon particles having mechanofusion treatment with TiO_2 particles on the surface of the nylon particles, and unmodified one. In this figure, the penetration rate with the unmodified nylon particles is greater than that of mechanofusion modified sample. Since nylon powder had a larger void fraction than that of TiO_2 particles, it was impossible to directly evaluate the affinity of methyl alcohol and nylon.

To solve this problem, the same evaluation method as used for the previously mentioned PMMA particles was performed. Thus, void fractions of the respective sample were sub-
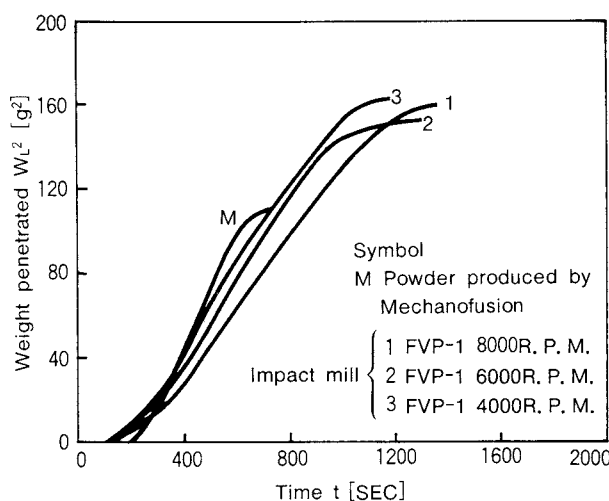
Fig. 19 Penetration ratios of PMMAs the surface of which is fused respectively with different methods

Table 3 Comparison of wettability treated by mechanofusion and impact mill

Preparation method	Conditions	$\cos\theta/\cos\theta_{8000}$ [-]
Impact mill	8000 r.p.m.	1
FVP	6000	0.99
	4000	1.24
Mechanofusion		1.91

stituted in the Washburn equation in order to determine the ratio between the two samples. The mechanofusion-modified particles have good wettability with methyl alcohol compared to the unmodified nylon sample.

An another method for obtaining a new material without the mechanofusion technique, is an application of a mechanical impact mill. Figure 19 illustrates the penetration rate measurement data obtained by various pulverization conditions with a fine-micron mill this is one type of the impact mill, as well as the corresponding data of the modified material by the mechanofusion.

Obtained by this penetration rate measurement, the void fraction and particle size were corrected using relative comparison based on the Washburn equation. The result is summarized in Table 3.

On the affinity with the powder and water conditions 1 and 2 is deemed identical with respect to fluctuation in measured values. Affinity is better with condition 3, and the mechanofusion modified sample has the best affinity.

With the samples treated with the impact mill, and in particular with samples on the condition of 8,000 and 6,000 rpm, fusion onto the parent material seems to be attributable primarily to impact; while a sample treated at 4,000 rpm, includes frictional crushing mechanism marginally so that affinity is improved than those of higher rotations.

The mechanofusion process seems to involve not only impact but also strong friction or frictional grinding. It appears that the frictional grinding makes ultrafine particles to firmly deposit onto the surface of the parent material, and the interaction between the coarser particles and ultrafine particles generates. Thus, "fusion" acts on the individual particle-particle

interface.

For this mechanism, applying mechanofusion to various powders, whether they be organic, inorganic, or metallic, can create novel materials.

6. Conclusion

In this paper, the technique for evaluating wettability with powders in Japan has been summarized. Penetration rate measurement techniques were especially focused on.

Wettability evaluation is an important technique not only in conventional powder dispersion in liquid but also in the creation of composite particles[35] which has been attracting the attention of researchers recently.

Mounting attention is being given to the wettability of powder. This is a continuous source of topics in various conferences and seminar meetings[36].

It is hoped that this report helps promote further research on this theme.

References

1) D.J. Show: Introduction to Colloid and Surface Chemistry, 3rd. Ed., Butterworths (1980) Translated into Japanese by F. Kitahara and K. Aoki, Hirokawa Shoten (1983).
2) M. Nakagaki: "Hyomenjotai to Koroidojotai", Tokyo-Kagaku-Dozin (1969).
3) Jpn. Chemical Society: "Shin Jikken Kagaku Kouza 18, 'Kaimen to Koroido", Maruzen (1977).
4) E.W. Washburn: *Phys. Rev.,* **17**, 273 (1921).
5) R.L. Peek and D.A. McLean: *Ind. Eng. Chem. Anal Ed.,* **8**, 85 (1934).
6) H. Sanuki: Fiber Engineering, **24**, 467 (1971).
7) H. Sanuki: *Ibid.,***25**, 496 (1972).
8) K. Kurematsu: "Zairyo Gijutsu", **5**, 34 (1987).
9) M. Koishi and M. Tsunoda: "Funtai no Hyomen Kagaku", Nikkan-Kogyo-Shimbun (1975).
10) K. Sato: "Bussei Teisu Suizanho", Maruzen (1954).
11) M. Arakawa: "Saishin Funtai no Zairyo Sekkei", Tekuno shisutemu (1988).
12) Y. Arai: "Funtai no Zairyo Kagaku", Baifukan (1987).
13) H. Murayama and K. Meguro: *J. Japan Soc. Colour Mat.,* **43**, 461 (1970).
14) N.W. Kossen and P.M. Heertjes: *Chem. Eng. Sci.,* **20**, 593 (1955).
15) T. Murata: "Funtai to Kogyo", No. 4, 26 (1981).
16) H. Kuno and R. Abe: *Ind. Chem.* **61**, 1445 (1958).
17) *Ibid.,* 11).
18) M. Nishino and M. Arakawa: *J. Soc. Mat. Sci., Japan,* **22**, 663 (1973).
19) Y. Tanaka and M. Koishi: *J. Japan Soc. Colour Mat.,* **49**, 22 (1976).
20) H. Honda, Y. Taniguchi, T. Ishizaka, T. Yokoyama, N. Kaya, T. Matsuno and M. Koishi: "Zairyo Gijutsu", **3**, 489 (1985).
21) N. Sasaki: "Zairyo Gijutsu", **5**, 298 (1987).
22) T. Murata: *J. Japan Mining Soc.,* **98**, (1982).
23) T. Fujita and T. Sato: *J. Japan Soc. Colour Mat.,* **55**, 459 (1982).
24) T. Yokoyama and N. Kaya: Preprints of 1984 Autumn Research Presentation, p. 13 (1984).
25) N. Morishima, K. Maehara and Y. Nomura: Preprints of 1983 Autumn Research Presentation, p. 40 (1983).
26) K. Matsumoto, Y. Tabata, G. Hong and K. Watanabe: *J. Soc. Powder Tech., Japan, Soc.* **25**, 365 (1988).
27) F.E. Bartell, L.S. Bartell: *J. Am. Chem. Soc.,* **56**, 2208 (1934).
28) K. Matsumoto, H. Akutsu, A. Yoshimidzu, G. Hong and K. Watanabe: *J. Soc. Powder Tech., Japan, Soc.,* **25**, 359 (1988).
29) M. Koishi and Y. Tsuriya: "Bunsan Gijutsu Nyumon", Nikkan-Kogyo-Shimbunsha (1972).
30) Y. Tanaka and M. Koishi: *J. Japan, Soc. Colour Mat.,* **49**, 473 (1976).
31) M. Nakagawa, M. Furuuchi, K. Miwa and G. Gotoh: *J. Soc. Powder Tech., Japan of Pow. Tech. Soc.,* **23**, 845 (1986).
32) Y. Arai: "Funtai no Zairyo Kogaku", Baifukan (1987).
33) M. Koishi, N. Kaya, T. Yokoyama and H. Kitai: Preprints of the 24th Discussion on Powder, p. 182 (1983).
34) T. Yokoyama, K. Urayama, M. Naito, M. Kato and T. Yokoyama: KONA [5], 59 (1987).
35) H. Honda, T. Matsuno and M. Koishi: "Zairyo Gijutsu", **6**, 186 (1988).
36) M. Koishi, K. Kurematsu, M. Kuwa and N. Kaya: "Ganshin Gijutsu to sono Ouyo" Seminar, Manuscripts, Tekuno Shisutemu (1988).

Review

An Introduction to Standard Powders in Japan

Ken-ichi Yamashita
Mechanical Engineering Laboratory
*Agency of Industrial Science and Technology**

1. Preface

The uses of standard powders have increased sharply in the past several years, and industrial tests and studies relevant to them have increased accordingly. The application that once chiefly comprised tests on the filterability of air cleaners in motor vehicles and on the abrasion resistance and antidust ability of automotive engine parts has recently expanded to cover labor hygiene, medicine, pharmacology and the food industry, besides mining and manufacturing industries. The demand has been increasing steadily in diversified uses which now include, calibration in monitoring airborne microfine particles in a clean or bioclean room, contamination control, the examination of dust respirators, durability tests of seat belts in motor vehicles, and experimental administration to mice.

This paper attempts to provide introductory information on standard powders which have hitherto been handled by The Association of Powder Process Industry & Engineering, Japan (APPIE)**, giving an outline of their properties with the purpose of serving as a reference.

2. Kinds of standard powders

Generally, the properties of a bulk solid may be specified in terms of four elements, true density, particle size distribution, chemical composition, and particle shape. Specifications standardizing bulk solids in foreign countries

as well as in Japan show that it is an ordinary practice to define their properties in terms of the above-mentioned four elements or three excluding particle shape. It is necessary for the properties of a standard powder to be specified defined, for its constant stable supply to be ensured, and for the material itself to be applicable to the performance tests of instruments and machinery, etc. as a means of evaluating the efficiency of their mechanical operation.

According to the practice by The Association of Powder Process Industry & Engineering, Japan, standard powders are generally divided into three categories on the basis of the properties of bulk solids for convenience, as shown in **Table 1**; that is, standard particles for basic properties, testing grade standard powders, and dusts for industrial testing.

Table 1 shows the classification of standard powders arranged by Prof. Masafumi Arakawa of Kyoto Institute of Technology, in which a "standard particle for basic properties" refers to one to be used for research on basic properties, having a particle shape and particle size which are ideal in simplifying the complexity that the powder itself essentially has; a "test grade standard powder" refers to one which

* 1-2 Namiki, Tsukuba-shi, Ibaragi, 305
  TEL. 0298 (54) 2758

Received June 23, 1988

** The Association of Powder Process Industry & Engineering, Japan (APPIE)
  Headquarters: No. 33 Shibunkaku Kaikan
  2-7 Tanakasekiden-cho, Sakyo-ku,
  Kyoto, 606
  Tel. (075) 761-7123, 751-0195

  Tokyo Office: No. 401 Tohshin Building
  2-27-2 Hongo, Bunkyo-ku, Tokyo, 113
  Tel. (03) 815-3955

Table 1 Classification of standard powders

	Heading	Description
Standard powders	Standard particles for basic properties	Has a particle size and shape ideal for simplifying statistical features that complicate the phenomena
	Testing grade standard powder	With a particle size and shape close to uniformity, used for basic research on powders, grains or the calibration of measuring devices
	Dusts for industrial testing	Such as a dust used for testing specified in JIS Z 8901, used for performance tests of dust-related apparatuses in commercial plants, etc.

has a particle shape and size both of which are close to uniformity next only to a standard powder in terms of basic properties, to be used for basic research on bulk solids or granular materials, or for the calibration of devices for measuring physical properties of bulk solids; a "dust for industrial testing" refers to one specified by JIS[1] and used for performance tests of apparatuses handling dust in mining or manufacturing industries and corresponding to industrial dusts in particle shape, size and composition.

3. Standard powders

3. 1 Standard particles for basic properties

Table 2 shows the mean particle diameter, true density, uses respectively of a standard particle and the basic properties of which are designated by The Association of Powder Process Industry & Engineering, Japan. Figure 1 shows the particle shapes of the standard particles.

Table 2 Basic properties of standard particles

Heading	Mean particle diameter D_p (μm)		True density ρ_p (g/cm^3)	Uses
Poly-styrene latex	0.1 μm	5 μm		Calibration of fine particle-measuring devices (for both
	0.2	7		
	0.3	10		
	0.4	15		
	0.5	20	1.50	gases and liq-uids); as a
	0.6	41		
	0.7	66		standard for samples under a microscope
	1.1	92		
	2.0			

As shown clearly in Fig. 1, polystyrene latex is a standard particle that consists of almost perfectly spherical particles. There are many variants with particle diameters ranging from 0.1 μm to 7 μm, each prepared in the form of about 2 ~ 3 mass percent solution and packed in a container of about 5 cm^3 in volume. Some of the uses of this series of polystyrene latex are for calibration in the measurement of air-bone particles in a clean room, as a standard

① Latex(transmission electron micros-cope)× 31000   0.5 μm

② Lycopodium, (scan-ning electron microscope) × 1000   20 μm

③ Precipitated cal-cium carbonate, (scanning electron microscope)× 500   20 μm

④ Glass beads,(scan-ning electron microscope)× 3000   4 μm

⑤ White fused alumina,(scan-ning electron microscope)× 1000   20 μm

⑥ Talc,(scanning electron microscope)× 1000   20 μm
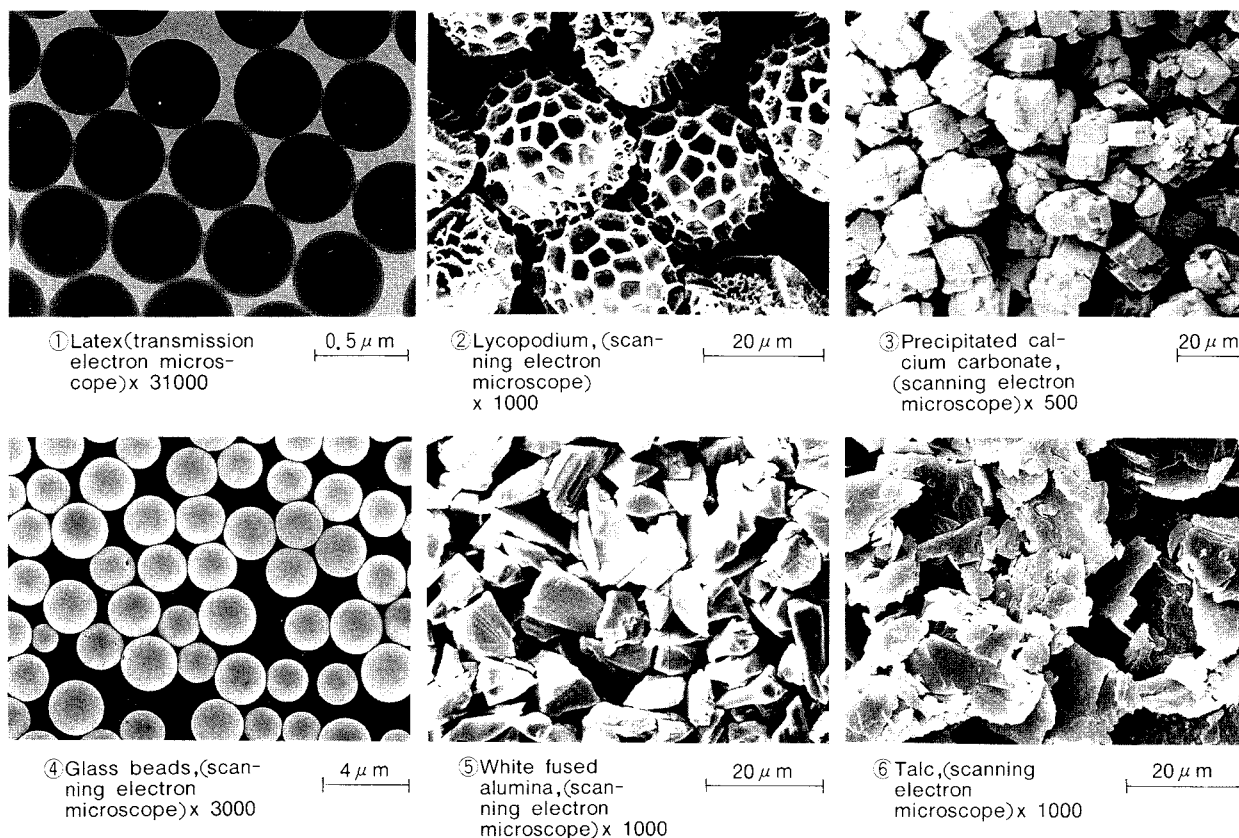
Fig. 1 Particle shapes of standard powders

sample in the measurement of surface contamination in a clean room, and for the determination of magnifications or for the comparison of the dimensions with the sample when added to samples for use in electron microscopy.

3. 2 Testing grade standard powders

Table 3 shows the properties and uses of the testing grade standard powders designated by The Association of Powder Process Industry & Engineering, Japan. Figure 1 shows the particle shapes of the testing grade standard powders.

(1) Lycopodium powder

Lycopodium powder, besides being a product of nature, is characterized by virtual evenness in particle size and by excellent fluidity. Being a pollen occurring in nature and having an outstanding dispersibility in the air, lycopodium powder has uses in tests on fluidity, clinical tests for pollinosis, and the like.

(2) Precipitated calcium carbonate

As seen in Fig. 1, precipitated calcium carbonate comes in a configuration and size characteristic of the rhombohedron. Such

an evenness characterizes a size which makes the crystals useful for basic experiments on devices for measuring powder properties.

(3) Glass beads

Glass beads are transparent spherical particles with evenness in particle size. There are six variants with an average particle size of 10, 20, 30, 40, 60 and 80 μm. They are used for calibration in the measurement of particle sizes of powders and as standard samples in, for example, efficiency tests of filters for hydraulic equipment.

(4) White fused alumina

White fused alumina is a product of refining available in six variants with a mean particle diameter of 2, 5, 10, 20, 40 and 80 μm (each doubles to the next in progression). The properties, i.e. true density, particle size distribution, specific surface area, fluidity, particle shape, and composition etc., are known with respect to each of these variants. The white fused alumina is considered to be most suited for calibration in measuring the properties of bulk solids.

Table 3   Standard powders

	Heading		Mean particle diameter D_p (μm)	Main ingredient (%)	True density ρ_p (g/cm^3)	Uses
Standard powders	Lycopodium powder		30 ~ 40	Fatty oil about 50 (oleic acid 80, arachic acid 8)	1.05	Test on fluidity and diffusion
	Precipitated calcium carbonate		12 ~ 15	CaCO$_2$	2.71	Calibration of particle size measurement
	Glass beads	No. 1	10	○ Soda lime · Silicate glass SiO$_2$ ... 70 ~ 73 ○ Titanium · Barium glass TiO$_2$ ... 32 ~ 38 BaO ... 43 ~ 48	2.72	Calibration of a fine particle counter
		No. 2	20			
		No. 3	30			
		No. 4	40			
		No. 5	60			Fluidity test
		No. 6	100			
	White fused alumina	No. 1	2	Al$_2$O$_3$ 98	3.92	Calibration of particle size measurement of bulk solid
		No. 2	5		3.94	
		No. 3	10		3.95	Test on wear, durability of machinery
		No. 4	20		3.96	
		No. 5	40		3.97	
		No. 6	80		3.98	Test on fluidity
	Talc		0.5	SiO$_2$ ... 60 ~ 63 MgO ... 30 ~ 34	2.80	Performance test of high efficiency filter, etc. Calibration of particle size measurement

(5) Talc

Talc consists of very minute particles with a mean particle diameter of 0.5 μm, the particle diameter being the smallest of all powders prepared by pulverization and classification. The particle is a flake shaped. Talc is expected to become increasingly in demand for uses in research on the surface contamination of wafers in clean rooms, and for tests on the filterability of fine filters. Talc, together with Class 4 and Class 9 as dusts for industrial testing, comes in three grades of particle sizes, i.e. fine, very fine, and ultrafine.

3. 3 Dusts for industrial testing (JIS Z 8901)

The standardization of dusts for industrial testing dates back to 1958, when the six classes from 1 (silica sand powder) to 6 (cement) were initially designated. In compliance with the desires in various fields of mining and manufacturing industries and in the instrumental control of environmental pollution and labor hygiene, the number of dusts used for industrial testing was increased during the next thirty years, to the present 17 classes, which are shown in **Table 4.**

The particle size distributions and the particle shapes of the dusts for industrial testing are shown in **Fig. 2** and **Fig. 3,** respectively. A general idea of all 17 dusts used in industrial testing can be obtained from **Table 4** which shows the median diameters, principal components and true densities, and from **Figs.** 2 and 3 which show the particle size distributions and particle shapes.

(1) Classes 1, 2 and 3 (silica sand powder of the coarse, fine, and very fine grades, respectively)

Silica sand powder is composed mainly of SiO_2, characterized by hard quality and irregularity in particle shape. The particles become finer in the order of from Class 1 to Class 3. Its characteristic of being able to accelerate abrasion is used in tests on the durability and wear of dust-related instruments and machinery.

(2) Classes 4 and 9 (talc of the very fine and ultrafine grades)

Talc pulverized and prepared to have a specified particle size is used. The particles
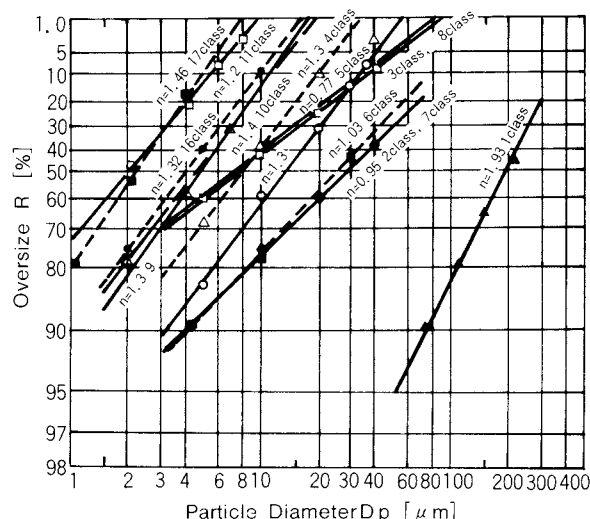
Fig. 2 Particle size distributions of dusts used for industrial testing

are fine flakes in shape. The main use is for testing the filter cloth in a dust-collecting system.

(3) Classes 5 and 10 (fly ash of the very fine and ultrafine grades)

Particulates obtained from the pulverized coal-burning furnace of a thermal power plant is used. The collected fly ash is prepared by classification so as to have specified particle size distributions. Most of the particles are spherical in shape, though irregular particles are also included. The main use is for testing dust collectors.

(4) Class 6 (ordinary portland cement)

An ordinary concrete-forming cement is used for tests on the airtightness of lamps in motor vehicles as specified by the SAE-recommended standard[3] and JIS[4]. Care must be taken in handling it because of its hygroscopicity.

(5) Classes 7, 8 and 11 (Kanto loam powder of the fine, very fine, and ultrafine grades)

Also called Kanto loam dust, these classes of dust come from Kanto volcanic ash soil which is distributed widely in the south-western part of the Kanto district of Japan, and is produced by calcination followed by pulverization. The products have coherency with both "fine" and "coarse" dusts in the SAE-recommended standard[5]. They are used for testing various dust-collecting devices, for testing the durability of instru-

Table 4 Dusts for industrial testing specified by JIS Z 8901

Kind	Substance		Medium diameter D_p 50 (μm)	Main ingredient (%)		True density ρ_p (g/cm³)	Uses
Class 1	Silica sand powder	(coarse)	195	SiO_2	over 97	2.6 ~ 2.7	○ Efficiency test of powder apparatus ○ Tests on the wear and durability of instruments and machinery
Class 2	Silica sand powder	(fine)	30				
Class 3	Silica sand powder	(very fine)	8				○ Dust collector test
Class 4	Talc	(very fine)	8	SiO_2	57 ~ 63	2.7 ~ 2.9	○ Dust collector test ○ Chemical apparatus efficiency test
Class 9	Talc	(ultrafine)	4.6	MgO	28 ~ 32		
Class 5	Fly ash	(very fine)	15	SiO_2	over 45	2.0 ~ 2.3	○ Test of a dust collector ○ Test of the airtightness of containers, Dust elimination test
Class 10	Fly ash	(ultrafine)	5	Al_2O_3	over 20		
Class 6	Ordinary portland cement	(very fine)	26	C_2O SiO_2	63 ~ 73 21 ~ 24	3.1 ~ 3.2	○ Test of the airtightness of motor vehicle lamps
Class 7	Kanto loam powder	(fine)	30	SiO_2	34 ~ 40	2.9 ~ 3.1	○ Dust collector test ○ Machinery wear test ○ Oil pressure filter test
Class 8	Kanto loam powder	(very fine)	8	Fe_2O_3	17 ~ 23		
Class 11	Kanto loam powder	(ultrafine)	1.9	Al_2O_3	26 ~ 32		
Class 12	Carbon black	(ultrafine)	—	DPB absorption, iodine absorption		—	○ Dust elimination test
Class 13	Aerosol	(ultrafine)	0.27	Dioctyl phthalate		—	○ Test of high efficiency air filter ○ Calibration of a fine particle counter
Class 14	Aerosol	(ultrafine)	0.86	Stearic acid			
Class 15	Dust mixture		—	Dusts for industrial testing Class 8, Class 12 and linters		—	○ Prefilter test
Class 16	Heavy calcium carbonate	(very fine)	4.1	CaO	54 ~ 56	2.7 ~ 2.9	○ Test of adhesion/aggregation, Dust collector test
Class 17	Heavy calcium carbonate	(ultrafine)	2.2	Heat reduction	42 ~ 54		

Silica sand powder
(optical microscope)
x 130   100 μm

Talc (scanning
electron
microscope) x 3200   10 μm

Fly ash (scanning
electron microscope)
x 130   20 μm

Cement (optical
microscope)   100 μm

Kanto loam powder
(optical microscope) x130   100 μm

Carbon black (scan-
ning electron micro-
scope) x 11000   0.2 μm

Dust mixture (optical
microscope) x 130   100 μm

Heavy calcium car-
bonate (scanning
electron microscope)
x 3500   5 μm

Fig. 3 Shapes of dusts used for industrial testing

ments and machinery, etc. This dust is the one most used for testing.

(6) Classes 9, 10 and 11 (talc, fly ash, and Kanto loam powder respectively of an ultrafine grade)

Classes 9, 10 and 11, which have already been referred to, were developed at the request of the Standard Department of the Agency of Industrial Science and Technology in connection with enactment of Notification No. 1 of the Envrionment Agency and the Health and Welfare Ministry Ordinance in the Public Buildings Sanitary Administration Law. Aptly called "10 μm cut dusts" informally, these three classes of dusts have particle diameters of less than 10 μm and differ in particle shape — Class 9 is flakes, Class 10 is spheres and Class 11 is irregular particles.

(7) Class 12 (carbon black of the ultrafine grade)

This one corresponds to the dust that falls from the smokestacks of a factory and is used in tests on dust collection in a large scale dust collection system. The particles are extremely fine with a particle diameter range of 0.03 ~ 0.20 μm, and they exist as spheres linked together.

(8) Classes 13 and 14 (aerosols of the ultrafine grade)

Two kinds of aerosols are specified in terms of particle size distribution — a monodispersed system and a polydispersed system — with submicron particles as the liquid drops in both cases. Each class of aerosol is produced by using stearic acid or dioctyl phthalate (DOP), as specified in JIS, and by means of an aerosol generator. As currently specified by JIS[6], the monodisperse aerosol is used for testing the filterability of the air filter, and an polydisperse aerosol is used for the air leakage test of the same air filter.

(9) Class 15 (dust mixture)

The product is a mixture of Class 8 dust (Kanto loam powder corresponding to road dust), Class 12 dust (carbon black corresponding to dust fall), and linters (fibrous particles corresponding to indoor dust), which corresponds to polluted urban air. It is used mainly for testing the filterability of prefilters (filters in advance or for coarse dust).

(10) Classes 16 and 17 (heavy calcium carbonate in very fine and ultrafine grades)

These two classes were added to the dusts for industrial testing in the revised standards in fiscal 1982. They are used for testing dust-collecting devices and as standard samples in testing the adhesive and aggregative properties of bulk solids. A constant stable commercial supply of products characterized by virtual evenness in particle size, though irregular in shape, can be ensured.

3. 3. 1 Physicochemical properties of dusts for industrial testing

(1) Items of measurement

Table 5 shows the items and methods of measurement with respect to the physicochemical properties of the dusts used in industrial testing. Besides true density, particle size distribution and chemical composition as specified by JIS[1], the items of measurement included, are bulk density, specific surface area, fluidity and particle shape.

The true density was measured by vacuum deaeration using a pycnometer in accordance with the relevant specification of the JIS[1].

As a means of determining particle size distributions, the standard sieves[7] are used in the production of Class 1 dust, in the screening of dusts with a particle diameter of over 75 μm in the production of Classes 2, 3, 6, 7 and 8, and in the screening of dusts with a particle diameter of over 106 μm in the production of Classes 5 and 10.

The specific surface area was determined by using a constant pressure air-permeable type of measuring device and the automatic device in the BET method.

The fluidity was measured by using the powder tester, which was a product of Hosokawa Micron Corporation.

As to particle shapes, an optical microscope was mainly employed, but an electron microscope of the scanning type or the transmission type was also employed where the particle size was finer.

The chemical compositions are those

Table 5 Items and methods of the measurement of powder properties

Measurement item	Measurement method	Remarks
True density	(1) Pycnometer method	Specified in JIS[1]
Particle size distribution	(1) Andreasen pipette method (2) Sedimentation balance method (3) Standard sieve method	Specified in JIS[1]
Specific surface area	(1) Automatic measurement (2) Constant pressure air-permeable measurement	ISO standard (provisional)[5]
Fluidity	(1) Power tester	
Shape	(1) Optical microscope (2) Scanning type electron microscope (3) Transmission type electron microscope	Partly specified in JIS[1]
Composition	(1) Chemical analyses (2) Others	Specified in JIS[1]

obtained by chemical analyses, and the standards[1] of the dusts for industrial testing are shown in the following list.

3. 3. 2 Physicochemical properties

(a) True density

Table 6 shows the results of the actual measurement of the true densities of dusts for industrial testing in comparison with the respective standards. The table shows the conformance of each measured value to the respective standard.

(b) Particle size distribution

To determine the particle size distribution, Class 1 dust was subjected to standard screening[8] by introducing standard sieves[7], whereas the Andreasen pipette method was introduced with respect to Classes 2, 3, 4, 5, 7, 8, 9, 10, 11, 16 and 17.

As a result, the particle size distributions of the above-mentioned classes of dusts for industrial testing were all found to conform to the specifications in JIS[1] and to satisfy the value of median diameters in **Table 4**

Table 6 True density and specific surface areas of dusts for industrial testings

Dust	True density ρ_p [g/cm^3]		Specific surface area S_W [m^2/g]	
	Measured value	Standard value	BET method	Air-permeable method
Class 1 (silica sand powder, coarse)	2.65		–	0.0685
Class 2 (silica sand powder, fine)	2.64	2.6 ~ 2.7	0.80	0.405
Class 3 (silica sand powder, very fine)	2.7		1.94	0.752
Class 4 (talc, very fine)	2.74	2.7 ~ 2.9	7.51	1.534
Class 9 (talc, ultrafine)	2.78		7.14	1.866
Class 5 (fly ash, very fine)	2.08	2.0 ~ 2.3*	1.51	2.664
Class 10 (fly ash, ultrafine)	2.07		2.64	3.920
Class 6 (cement, very fine)	3.16	3.10 ~ 3.18**	1.30	0.325
Class 7 (Kanto loam powder, fine)	2.96		10.6	0.513
Class 8 (Kanto loam powder, very fine)	2.96	2.9 ~ 3.1	10.4	0.897
Class 11 (Kanto loam powder, ultrafine)	2.9		–	1.897
Class 16 (heavy calcium carbonate, very fine)	2.72	2.7 ~ 2.8	3.74	1.110
Class 17 (heavy calcium carbonate, ultrafine)	2.72		6.12	1.657

* Specified in JIS A 6201 (fly ash)
** Specified in JIS R 5210 (portland cement)

and the particle size distributions in **Fig. 2**.

(c) Specific surface area

Table 6 shows the specific surface areas of dusts for industrial testing.

In the BET method, the specific surface area showed increases with decrease in particle size with respect to the silica sand powder, fly ash and heavy calcium carbonate, whereas the particle size of talc and Kanto loam powder were found to be independent of the specific surface areas. The likely reason for this difference is that talc and Kanto loam powder crumble easier than the others when tapped.

(d) Fluidity

The fluidity of a dust for industrial testing was evaluated in terms of Carr's flowability index[10] based on the apparent bulk density, compressibility, angle of repose, angle of spatula, cohesiveness, and uniformity as determined by a Powder Tester (Model PT-E)[9].

Table 7 shows the results of the measurement. From this, it is observed that the fluidity of the dusts for industrial testing is not satisfactory; where dusts with the same composition are compared, there is a tendency for the fluidity to decrease with decrease in particle size.

When Classes 1, 2 and 3 (silica sand powder of the coarse, fine, and very fine grades) are compared, it is seen that the fluidity of Class 1 is good, but it becomes poor with decrease in particle size as shown by Classes 2 and 3.

This degradation of the fluidity influenced by enhancement of the fineness of the particles is also obvious when Classes 4 and 9 (talc of the very fine and ultrafine grades) are compared.

Classes 5 and 10 (fly ash of the very fine and ultrafine grades) are relatively better in fluidity than Class 4; the likely reasons are that fly ash is relatively coarser in particle size than the talc and that fly ash is an aggregate of spherical particles which are easily dispersed.

Of Classes 7, 8, and 11 (Kanto loam powder of the fine, very fine, and ultrafine grades), the fluidity of Class 7 is as good as that of Class 5, but that of Class 8 and Class 11 is unsatisfactory. The fluidity of

Class 12 (carbon black of the ultrafine grade) is very poor.

Fluidity is very poor with respect to Classes 16 and 17 (heavy calcium carbonate of very fine and ultrafine grades), differing little independent of the particle size in between.

A glance at the constituent values of the measurement by a Powder Tester reveals that between dusts of the same composition there is a decrease, dependent on particle size, in the apparent bulk density (g/cm^3), the compressibility, the angle of spatula, the cohesiveness, and the uniformity. An exception is heavy calcium carbonate which has a high cohesiveness and shows little difference in characteristics between Class 16 and Class 17 which differ in particle size.

(e) Particle shape

Figure 3 shows the particle shapes of the dusts for industrial testing which were observed by an optical microscope and electron microscope. Silica sand powder, i.e. Classes 1, 2 and 3, is irregular in particle shape and has rigid angular configurations.

Talc, i.e. Classes 4 and 9, is an aggregate of flake-shaped particles which easily exfoliate. The photograph also shows the talc to be relatively crumbly.

Fly ash, i.e. Classes 5 and 10, consists mostly of spherical particles, although some particles are irregular in shape.

Ordinary portland cement, i.e. Class 6, consists of somewhat roundish particles.

Kanto loam powder, i.e. Classes 7, 8 and 11, consists of particles which are not angular but rather roundish in shape.

Carbon black, i.e. Class 12, is an aggregate of spherical particles. Practically none of the individual particle exist by themselves but rather are linked to one another.

Dust mixture, i.e. Class 15, consists primarily of Class 8 (Kanto loam powder of the very fine grade), contains added linters and Class 12 (carbon black of the ultrafine grade). The particles of Class 12 exist in part separate from one another and in part forming aggregates closely filling the interspaces.

Heavy calcium carbonate, i.e. Class 16 and Class 17, consists of somewhat roundish particles which exist in part separate from

Table 7 Results of the measurement of the fluidity of dusts for industrial testing

Dust	Apparent bulk density [g/cm³]			Compressibility		Angle of repose		Angle of spatula			Cohesiveness/ uniformity		Total flow- ability index	Evaluation of flowability
	loosed	packed	working	%	points	deg.	points	deg.		points	%/units	index		
Class 1 (silica sand powder coarse)	1.503	1.612	1.577	6.8	23	40	17.5	Before 45 / After 43	44	18	△3.1	23	81.5	Good
Class 2 (silica sand powder, fine)	0.992	1.613	1.231	38.5	2	52	12	Before 70 / After 67	68.5	12	65	2	28	Very poor
Class 3 (silica sand powder, very fine)	0.650	1.307	0.980	50.3	0	41	17	Before 82 / After 79	80.5	7	65	2	26	Very poor
Class 4 (talc, very fine)	0.288	0.561	0.421	48.7	0	50	12	Before 72 / After 78	75	10	17	12	34	Very poor
Class 5 (fly ash, very fine)	0.747	1.192	0.913	37.3	5	43	16	Before 82 / After 78	80	7	5	15	43	Poor
Class 6 (cement, very fline)	0.926	1.693	1.273	45.3	0	54	12	Before 82 / After 71	76.5	7	65	2	21	Very poor
Class 7 (Kanto loam powder, very fine)	0.734	1.142	1.008	35.7	7	49	12	Before 69 / After 66	67.5	12	26	12	43	Poor
Class 8 (Kanto loam powder, very fine)	0.563	1.145	0.859	50.8	0	46	14.5	Before 70 / After 69	69.5	12	57	2	28.5	Very poor
Class 9 (talc, ultrafine)	0.258	0.523	0.392	50.7	0	49	12	Before 77 / After 72	74.5	10	43	7	29	Very poor
Class 10 (fly ash, ultrafine)	0.595	1.052	0.790	42.8	2	47	12	Before 83 / After 79	81	7	10	12	33	Very poor
Class 11 (Kanto loam powder, ultrafine)	0.395	0.891	0.589	46.7	0	35	20	Before 76 / After 68	72	12	55	5	37	Very poor
Class 12 (carbon black, ultrafine)	0.302	0.571	0.504	47.1	0	41	17	Before 67 / After 63	65	12	51	7	36	Very poor
Class 16 (heavy calcium carbonate, very fine)	0.520	1.030	0.770	49.1	0	44	16	Before 84 / After 82	83	7	87.5	0	23	Very poor
Class 17 (heavy calcium carbonate, ultrafine)	0.480	0.940	0.700	48.1	0	45	15	Before 86 / After 84	85	7	87.8	0	22	Very poor

△ Measured degree of uniformity

one another and in part in the form of aggregates. Using a transmission type electron microscope, the contours of the separate particles and aggregates of the particles can be relatively clearly distinguished. However, when using a scanning type electron microscope, the particles overlying one another in an aggregation can be distinguished.

(f) Chemical composition

Table 8 shows the chemical compositions of the dusts for industrial testing.

The silica sand particles forming Classes 1, 2 and 3 are obtained by pulverizing standard Soma sand[1] and preparing it to have specified particle size distributions and a chemical composition of hard SiO_2 particles in a proportion of over 97%.

The talc forming Classes 4 and 9 is obtained by pulverizing natural talc and preparing it to have specified particle size distributions and a chemical composition consisting mainly of SiO_2 and MgO.

The fly ash forming Classes 5 and 10 consists mainly of SiO_2 and Al_2O_3, and the cement forming Class 6 consists mainly of CaO.

The Kanto loam powder forming Classes 7, 8 and 11 consists mainly of SiO_2, Al_2O_3 and Fe_2O_3.

The physicochemical properties of carbon black forming Class 12 are specified on the basis of both DBP and iodine absorption.

The dust mixture forming Class 15 is composed of Class 8 Kanto loam powder, Class 12 carbon black and linters which are mixed in a specified proportion.

The heavy calcium carbonate forming Classes 16 and 17 consists mainly of CaO.

3. 4 Dusts used for industrial testing that meet other than JIS specifications

The Association of Powder Process Industry & Engineering, Japan besides specifying standard particles, also specifies testing grade standard powders, dusts for industrial testing JIS Z 8901, and the dusts used for industrial testing, which are shown in Table 9. The particle shapes of these additional dusts are shown in Fig. 4.

(1) Standard Soma sand

The standard Soma sand is silica sand

(a)
Standard Soma Sand
(Optical microscope)×5
2mm

(b)
Quarts powder
(Optical microscope)×150
100 μ mm

(c)
The three-component Mixture
(SEM)×40
20 μ mm

(d)
AC dust Coarse
(Optical microscope)×130
100 μ mm
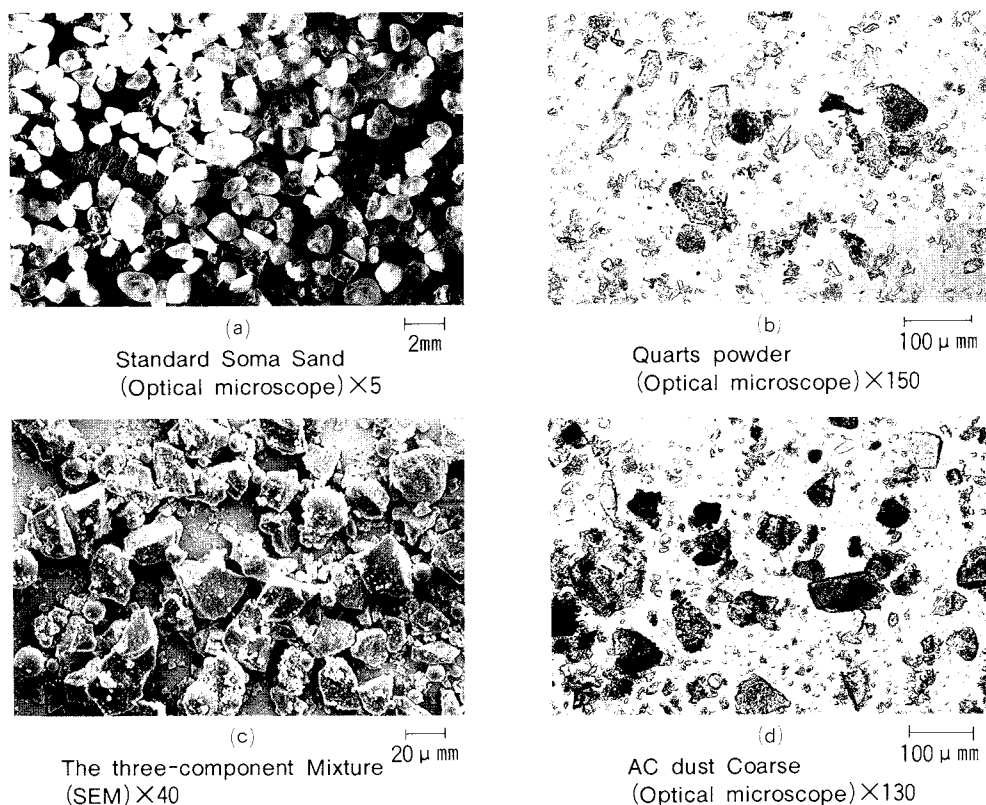
Fig. 4 Particle shapes of dusts for industrial testing that meet other than JIS specifications

Table 8 Chemical composition of dusts for industrial testing

(Unit: %)

| Kind | Composition | | | | | | | Undissolved residuum | Reduction by heating |
	SiO₂	Al₂O₃	Fe₂O₃	CaO	MgO	TiO₂	SO₃		
Class 1, 2 and 3 (silica sand powder)	Over 97	Under 3, including reducing portion by heating						—	—
Class 4, 9 (talc)	60 ~ 63	0 ~ 3	0 ~ 3	0 ~ 2	30 ~ 34	—	—	—	3 ~ 7
Class 5, 10 (fly ash)	Over 45	Over 20	—	—	—	—	—	—	—
Class 6 (ordinary portland cement)	20.5 ~ 23.7	4.0 ~ 7.0	2.5 ~ 4.5	63.0 ~ 65.6	0.6 ~ 3.2	—	0.3 ~ 2.0	0.1 ~ 1.0	0.3 ~ 2.0
Class 7, 8 and 11 (Kanto loam powder)	34 ~ 40	26 ~ 32	17 ~ 23	0 ~ 3	3 ~ 7	0 ~ 4	—	—	0 ~ 4
Class 12 (carbon black)	DBP absorption 25 ~ 34%, iodine absorption 22 ~ 30% Note 1)								
Class 13 and 14 (aerosol)	Dioctyl phthalate (D.O.P.), stearic acid Note 2)								
Class 15 (dust mixture)	Mixture of Class 8 and Class 12 dusts and linters Note 3)								
Class 16 and 17 (heavy calcium carbonate)	0 ~ 4	0 ~ 3	0 ~ 1	54 ~ 56	0 ~ 3	—	—	—	42 ~ 45

Note 1) physicohemical properties
Note 2), Note 3) indicates quality

Table 9 Dusts used for industrial testing that meet other than JIS specification

Heading	Medium dia.	Main ingredient	True density	Uses
Standard Soma sand	170	SiO₂ ..... over 97%	2.63	○ Raw material for dusts for industrial testing, classes 1, 2 and 3. Efficiency test of powder apparatus
Quarts ultra fine powder	0.44	high pure quarts	2.45	○ Performance test of dust respirators
Quarts powder				○ Durability testing of sent belts (Australian Standard, ASE, Part II)
Quarts dust	1.58			
the three component mixture	—	Class 3 (specified in JIS) 75% / Class 5 (specified in JIS) 16% / Iron powder (under 75 μm) 15%	—	○ Test of a dust collector / ○ Tests on the durability
Fine	8	SiO₂ 68%		○ Test of air cleaner
AC dust		Al₂O₃ 16%	2.62	
Coarse	30	Fe₂O₃ 4%		○ Tests on the wear of instruments and machinery

naturally occurring in the Soma district of Fukushima Prefecture; the particles do not have an angular configuration but are roundish in shape and are characterized by virtual evenness of particle size with a range of 590 ~ 840 μm and very good fluidity. Standard Soma sand is used as the raw material for dusts for industrial testing, namely, Classes 1, 2 and 3, as well as in the manufacture of glass and cement, and in civil engineering, etc. Some of its characteristic uses are for research on comminution, the performance testing of pulverizers, and tests on characteristics such as fluidity in powder-related machinery.

(2) Quartz powder

Quartz powder is produced by pulverizing in a ball mill from high purity quartz naturally occurring in the Ishikawakami district of Fukushima Prefecture and prepared in two grades of particle sizes — very fine and ultrafine.

Very fine grade quartz powder is used for the durability testing of seat belts in motor vehicles, and that of the ultrafine grade is used for the performance test[12] of dust respirators. The first-mentioned test is being specified in a related Australian standard[11] and in the latter-mentioned test by the JIS.

(3) The three-component mixture

The three-component mixture is a dust used for industrial testing and prepared by combining Class 3 (silica sand powder of the very fine grade), Class 5 (fly ash of the very fine grade), and iron powder of the ultrafine grade, the first-mentioned two components being dusts for industrial testing specified in JIS Z 8901.

This mixture is unique in that its components differ from each other in true density, particle size distribution, and chemical composition. It is used for tests on wear

and on the durability of machinery.

(4) AC Dust

Air cleaner (AC) testing dust consists of natural sand from the Arizonan desert and is a typical American testing dust for motor vehicles specified by the SAE-recommended Standard[5]. ISO Standard[13] AC Dust has also come into use for performance tests of automative air cleaners in Europe. The product has always been a high quality dust.

AC Dust is available in two grades — fine and coarse. The fine grade corresponds in particle size distribution to Class 3 (silica sand powder of the very fine grade) and Class 8 (Kanto loam powder of the very fine grade) and the coarse grade corresponds in particle size distribution to Class 2 (silica sand powder of the fine grade) and Class 7 (Kanto loam powder of the fine grade) (the four classes are dusts used for industrial testing specified by JIS).

References

1) Dusts for Industrial testing, JIS Z 8901 (1984).
2) Arakawa, Lycopodium, Powders and Properties Illustrated, Revised & Enlarged, P599, The Powder Technology and Ind. Assoc., Micromeritics society (1985).
3) SAE Handbook, J575, June 8 (1982).
4) Lamps for Motor Vehicles, JIS D 5500 (1969).
5) SAE Handbook, P829 (1973).
6) Air Filter Unit for Ventilation, JIS B 9908 (1977).
7) Standard Sieve, JIS Z 8801-1987.
8) General Principles of Screening, JIS Z 8815-1987.
9) Fujiyama, Fujihara, Trial Model of Powder Properties Measuring Device, Comminution No. 14, 102107 (1969).
10) Ralph, L. Carr, Chemical Engineering, Jan. 18, 163-185 (1965).
11) Australian Standard E35, Part II (1970).
12) Dust respirators, JIS T 8151 (1970).
13) Performance Testing of Inlet Air, Cleaning Equipment for IC Engineers and Compressors, ISO 5011.

The Symposium on Powder Technology

The Party of Powder Technology (Japan) held its 21th Symposium at the Foundation of Osaka Science & Technology Center in Osaka on August 28, 1987. This symposium focused on ultra-fine powder that has been recently at- tracting attention. Its production and the ar- rangement of ultra-fine powder was chosen as the main theme of this meeting to which many people (approximately 250) attended and enthu- siastically contributed to the lively discussions.

Session 1   Production of Ultra-fine Powder

Chairmanship: Masafumi Arakawa (Kyoto Institute of Technology)

- Production of ultra-fine powder using the liquid phase process — Shinichi Hirano (Nagoya University)
- Production of ultra-fine powder using the gas phase process — Chihiro Kaito (Kyoto Institute of Tech.)

Session 2   Arrangement of Fine Powder

Chairmanship: Yasuo Kousaka (Univ. of Osaka Prefecture)

- Mechno fusion system and its applications — Tohei Yokoyama (Hosokawa Micron Corp.)
- Measurement of electrostatic charge distribution of toner particles for copying machines by EST-1 — Yasuo Kitabatake (Sharp Corp.)
- Mulling process of fine powders and its applications — Kei Miyanami (Univ. of Osaka Prefecture)
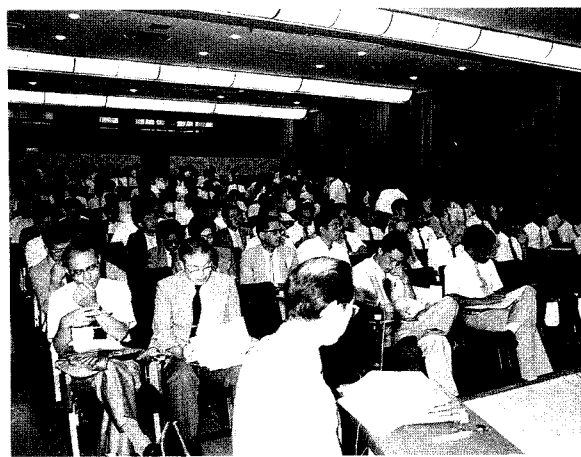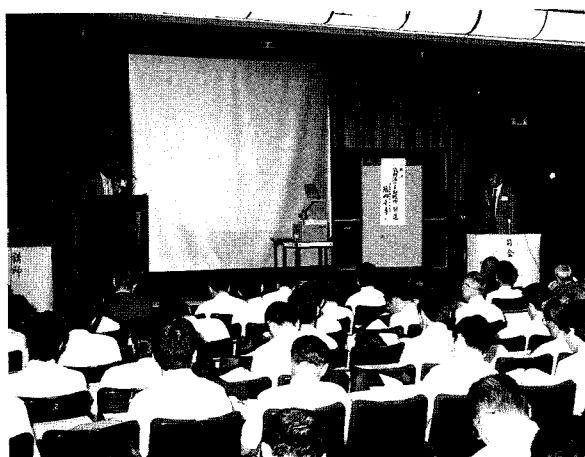
23rd Technical meeting

promoted by the Society of Powder Technology, Japan
held at Tokyo on June 23–24, 1988

At the latest technical symposium, a new technique and method for the evaluation of particle design were taken up and studied with their application not only to the pharmaceutical industry but also to ceramics, toner, electronic materials, chemicals and food industry making this symposium a global one with common problems. 18 lectures, 3 special lectures and the demonstration of some equipments and catalogs showing were carried out. The main lectures were:

- The relationship between powder characteristics and phermaceutical preparations — (Yoshinobu Nakai, Chiba University)

- Technology and methods for evaluation in particulate design — Wetting and dispersion — (Masumi Koishi, Science University of Tokyo)

- The formation and dispersion state of multiple emulsions — (Yukio Matsumoto, University of Osaka Prefecture)

24th Summer seminar

promoted by the Society of Powder Technology, Japan
held at Atami on July 12–14, 1988

Theme: The preparation and handling of ultra-fine powders

The peculiar problems related to ultra-fine powders were discussed along with the process from the preparation to the handling operation of these powders from many points of view. The meeting included 14 lectures. The main lectures were:

- Evaluation and control of the preparation process of ultra-fine powders using gas phase process — (Kikuo Okuyama, University of Osaka Prefecture)

- The preparation of mono dispersed particles using the liquid phase process — (Nobuyasu Mizutani, Tokyo Institute of Technology)

- The preparation of crystalline fine particles using the amorphous solid phase process — (Tadashi Kokubo, Kyoto University)

4th Symposium on medicine production and particle design

promoted by the Society of Powder Technology, Japan (Particle preparation and Design Dept.) and the Association of Powder Process Industry & Engineering (Division Meeting on Particulate Modification Technology)
held in Atami on Oct. 29–30, 1987

Ordinary lectures: 17, Special lectures: 4 as indicated below.

- Feature and technique for the preparation of seamless capsules — (Toshiyuki Suzuki, Morishita Medicine Co.)

- Drying technique for particulate design — Drying speed and product quality — (Morio Okazaki, Kyoto University)

- Cyclodextrins derivative as a medicinal carrier — (Kaneto Kamigawa, Kumamoto Univ.)

- Preparation of powders with good pharmaceutical qualities by inclusion in cyclodextrins — (D. Duchene, Pari University)

Panel discussions: 11, Forums: 3

Academic publication concerning powder technology in Japan (1987)

Journal of the Society of Powder Technology, Japan   Vol. 24 (1987)

Funsai (The Micromeritics)   No. 32 (1988)

Kagaku Kogaku Ronbunshu   Vol. 13 (1987)

Journal of the Society of Materials Science, Japan   Vol. 36 (1987)

Title	Author(s)	Page
• Submicron Grinding of $BaTiO_3$ by Ball Milling — Effect of Specific Gravity of Balls and Concentration of Powder —	K. Tanaka, K. Minai, K. Wakino and I. Uei	29–34
• Preparation of Ultrafine Nitride Particles by Applying Microwave Plasma to Gas Evaporation Technique	S. Iwama	1162–1166
• Surface-Treatment of Silicon Carbide and its Surface Properties	N. Suzuki, A. Komori, A. Endo and H. Utsugi	1176–1180
• Surface Treatment of Natural Zeolite by Dye and and its Characterization	A. Takasaka, S. Yoshino, H. Kono and Y. Matsuda	1181–1184
• Effects of Powder Characteristics on Kneading and Flow Properties of Highly Filled Alumina — Thermoplastic Resin Systems —	M. Takahashi, S. Suzuki, E. Arai and H. Nitanda	1185–1191
• Measurement of Initial Porosity Distribution in a Powder Cell by X-Ray Radiograph	K. Kuramitsu and K. Makino	1192–1197

Journal of the Japan Society of Powder and Powder Metallurgy   Vol. 34 (1987)

Title	Author(s)	Page
• Superconductivity of the Composite Consisting of Nb_3Sn Particles Dispersed in Silver — Effect of the Size of Nb_3Sn Particle —	T. Watari, T. Takasu, S. Nakamura and A. Kato	18–21

Proceedings of the Institute of Electrostatics Japan   Vol. 11 (1987)

Title	Author(s)	Page
• Analysis of Electric Field at Boundary of Complex Dielectries by Fluid Flow Visualization	K. Kaneko, J. Fukuoka, T. Matsumoto, H. Ohmura and T. Tateno	29–36
• Effects of Ripples in Voltage on Corona V-I Characteristics in ESP	A. Iijima and S. Masuda	110–118
• Effects of Ripples in Voltage on Particle Charge in ESP	A. Iijima	351–360
• A Program to Develop Engineering Data for Fabric Filtration with Integral Particle Charging and Collection in a Combined Electric and Flow Field	N. Plaks	445–452
• Dummy Load Equipment with Similar Characteristics by using Electron Beam for Electrostatic Precipitator	A. Iijima and T. Tsukamoto	453–461

Hosokawa Micron Corp. presents two of its new products.

HOSOKAWA/MIKRO ACM PULVERIZER, CERAMIC TYPE

The HOSOKAWA/MIKRO ACM PULVER-IZER is a classifier-pulverizer which incorporates a unique, directed internal circulation of material for the production of a fine grind at a high capacity.

The newly developed HOSOKAWA/MIKRO ACM PULVERIZER, CERAMIC TYPE is a metallic, clean type pulverizer which uses partially stabilized zirconium (PSZ) and alumina at its powder-contacting portions, thereby preventing the material from being contaminated. The shapes and sizes of the components of the ceramic type pulverizer are in accordance with those of the metallic standard type specifications. Therefore, the components of both types are interchangeable.

Models : ACM-10, ACM-30,
Power required :

Grinding rotor	: 7.5 − 22 kW
Separating element	: 0.75 − 3.7 kW
Feeder	: 0.2 − 0.4 kW

Air volume : 15 − 45 m³/min.

Features:
- No contamination of material
- Enhanced wear resistance capability
- No problems caused by corrosion or chemical reaction.
- Component interchangeability with the metallic standard type pulverizer.
- Easy maintenance
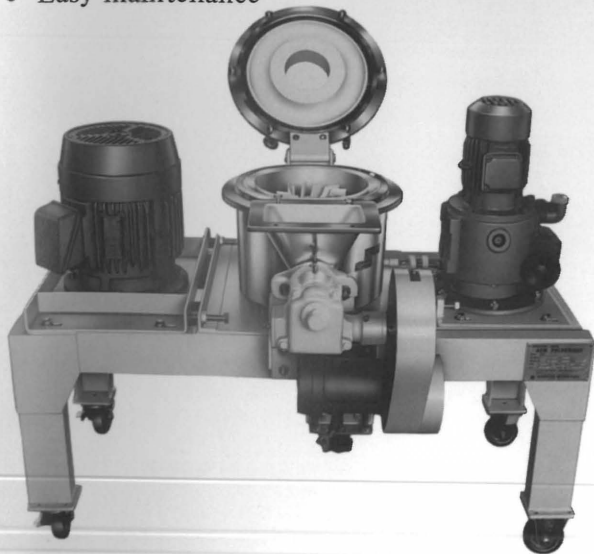
HOSOKAWA MICRON PENETOANALYZER

The HOSOKAWA MICRON PENETOANA-LYZER measures the wettability of powder and the angle of contact between powder and solvent. The PENETOANALYZER allows you to instantaneously evaluate the wettability or surface characteristics of powder materials using a computer. The PENETOANALYZER also can measure the penetration rate for paper, fiber, and porous materials in addition to powder materials.

Specifications:
- Measuring method : Penetration rate method
- Accuracy : 10 mg
- Optional accessories
  - (1) Microcomputer (2) Tapping machine
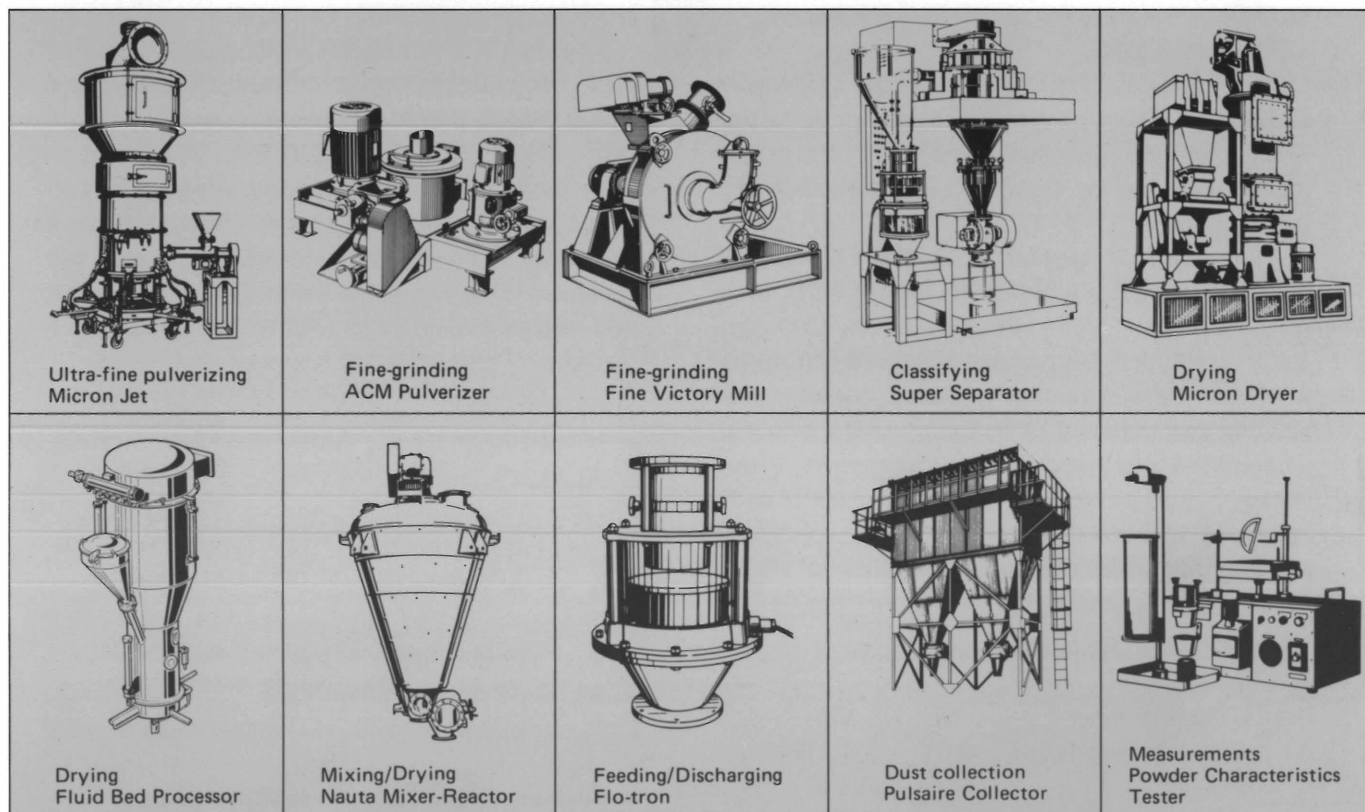 - (3) X-Y recorder (4) Mantle heater

Features:
- Easy measurement
- Accurate measurement data
- Surface tension (of liquid) measurement available
- High repeatability of measurement data